Title

Synthesis and Characterization of Hybrid Metal-Metal and Metal-Oxide Nanostructure Decorated Single Walled Carbon Nanotube Devices

Author

Hernandez, Sandra Catalina

Publication Date

2010

UNIVERSITY OF CALIFORNIA
RIVERSIDE

Synthesis and Characterization of Hybrid Metal-Metal and Metal-Oxide Nanostructure Decorated Single Walled Carbon Nanotube Devices

A Dissertation submitted in partial satisfaction
of the requirements for the degree of

Doctor of Philosophy

in

Chemical and Environmental Engineering

by

Sandra Catalina Hernández

December 2010

Dissertation Committee:
	Dr. Nosang V. Myung, Co-Chairperson
	Dr. Ashok Mulchandani, Co-Chairperson
	Dr. Wilfred Chen

The Dissertation of Sandra Catalina Hernández is approved:

Committee Co-Chairperson

Committee Co-Chairperson

University of California, Riverside

DEDICATION

I would like to take the time to thank the entire faculty that have shaped, motivated and inspired their students to peruse their dreams and if necessary, to aim higher particularly Dr. Myung and Dr. Mulchandani for guiding and working with me for the last five years. I appreciate their efforts and long hours dedicated to helping me navigate through my research and come atop with a finished and comprehensive creation. Furthermore, I am grateful for their full support and understanding in my balancing of monumental life changes, family and research. To Dr. Myung I am without words of gratitude for believing in me when I was an undergraduate student seeking for opportunities in a foreign area of education. Thank you for seeing potential in me, for helping me achieve it and for demanding me to aim higher.

I was fortunate to work and learn from many talented and knowledgeable people, including BY, Kumar, Young, Debu, Aravinda, Ming and Mahendra. Aside from all of the lab techniques and research insights they shared, I am most grateful for the research values, research persistence, and imaginative thinking they unconsciously instilled in me.

I am thankful for sharing so many good and stressful times with my lab mates who became a second family to me, Mangesh, Fang, Max, Silvie, Mubeen, Paul, Hyungsun, Nicha, Feng, James, Sira, Tapan, Miso, Milou, and Charles. Many of which I spent long late hours with in the lab and office, and all of which I shared joyous moments, stressful sighs, and hopeless tears. I will miss our get-togethers eating Thai food, our secret movie nights [not so secret now] and our BBQ potlucks. And of course the little undergrads that have worked with me and helped me grow in different ways, Nicha, Pilar, Tracey, Chris, and Yoyo. Although over whelming at times, I am thankful to have aided in their research experience and am grateful for their contributions in my work. I wish them all the best in their future endeavors and hope to continue building on our friendships. I am grateful for my long lasting friends who have shared my pains, listened to my whining, and gave me emotional strength. Thank you for always being a phone call way Temi, Andrew, Perla, Maria, Lety, Susanna, and Sanjua.

Although I have always held a very special place for my family, this year in particular was world shaking for me and it goes without saying that they have always been and will always be very important to me. To my parents Sergio and Martha, I cannot express how thankful I am for all of their sacrifices, hard work and good examples made throughout their lives. I thank them for their selflessness sacrifice in leaving everything they knew behind in hope of providing their children better opportunities. I hope to make them happy with my decisions and I to never let them down. I was very blessed to have in my life my best friend and younger sister Carmen as well as my younger brothers Yoyo and Ivan. More often than not, those closest to you see the worst of you, so I appreciate that even on my most difficult moments they were there to put up with me, make fun of me, and for just keeping things real. Growing up with them has made me more aware of life’s riches values. I also want to thank my in-laws Rosalie and Paul Santos for supporting me and always being quick in helping me in anything I needed… who ever said in laws were hard to get along with don’t know mine!

And of course, there is no one bigger to acknowledge than my husband Carlos who has held me together, been by my side and worked hand in hand with me throughout this journey. I admire, respect and am proud to have him in my life and want to thank him for motivating me to pursue this degree and pushing me to finish till the end. For bestowing me with unconditional love and understanding, and for making me complete. And my little Tatiana who shook my world upside down and put everything in perspective. She gives each day more meaning makes each sacrifice more worthwhile and fills me with unimaginable happiness. I thank God to have put such great opportunities in my path and for being present in every step I took, for clearing my mind and heart in all those many days when nothing else made sense. No one battle is ever won alone.

ABSTRACT OF THE DISSERTATION

Synthesis and Characterization of Hybrid Metal-Metal and Metal-Oxide Nanostructure Decorated Single Walled Carbon Nanotube Devices

by

Sandra Catalina Hernández

Doctor of Philosophy, Graduate Program in Chemical and Environment Engineering
University of California, Riverside, December 2010
Dr. Nosang V. Myung, Co-Chairperson
Dr. Ashok Mulchandani, Co-Chairperson

The overall objective of this work is the development of a high density sensor array using singe wall carbon nanotube (SWNT) hybrid structures as the platform material for the realization of highly sensitive, selective and discriminative gas sensors for monitoring of industrial and automotive emissions in the environment. To conceive such desired sensor characteristics SWNTs were surface functionalized with metal and metal oxide active materials [i.e. ZnO, Ag, Pt, Pd, Au] to target specific analytes. Detailed analysis of ZnO electrodeposition on to SWNTs was performed to investigate structure property relations between ZnO particle size, density, material quality, catalyst type, and combination thereof, towards the sensing performance and analyte specificity.

Room temperature gas sensing performance of environmentally significant gases such NH_3, SO_2, H_2S, NO_2, CO, CO_2, benzene derivatives, alkanes, and alcohols was evaluated using the metal and metal oxide hybrid structures. The ZnO-SWNT hybrid structures exhibited characteristic selectivity towards H_2S, with enhanced sensitivity, response and recovery time contingent of crystal orientation; additionally as synthesized ZnO-SWNT hybrid structures displayed conductance response cognizance of xylene

isomers (*ortho, para, meta*). Furthermore, at the hand of sequential incorporation of a metal catalysts (Au, Ag, Pt, and Pd), the ZnO-SWNT system showed distinct charge dependant pattern recognition towards less detectable analytes such as SO_2 and NO_2; metal-SWNT hybrid structures with Pd as the second deposited metal demonstrated enhanced sensitivity towards NO_2 and NH_3 due to the enhanced dissociation of the molecular adsorbate on the catalytically active Pd nanoparticle surface.

Understanding of the deposition process was then extended to the deposition of binary metals Au, Pd, Pt, followed by sequential deposition of a combination of metals. Emphases was placed on both the gas sensing aspect of the resultant hybrid structures, and also on the ability to site specifically control the deposition of the second metal. A detailed examination of these hybrid nanostructures and the nature of their responses towards different gaseous environments was studied and compared with the performance of unfunctionalized carbon nanotubes.

TABLE OF CONTENTS

LIST OF FIGURES

CHAPTER 1:

INTRODUCTION

1.1 Introduction

Sensors are existing and emerging components in a spectrum of fields, ensuring emission compliance of greenhouse gases in the industrial sector as well as worker safety. On the homeland security front gas sensors can provide an early warning to vaporized or aerosoled toxins, and they can also be used to ensure the freshness of perishables, detecting alcohols, aldehydes, and other volatile organic compounds (VOCs) characteristic of food and produce decomposition. With higher level analysis we can use gas sensors as a screening tool for early medical diagnostics and equally important, increase our understanding and predicting power of fate and transport for emission in our environment by making these sensors ubiquitous components.

Chemical sensors are devices that can detect the presence or absence of of analytes in a qualitative and / or quantitative manner by changing a material property when the material interacts with the analyte of interest. When a sensor interacts with gaseous chemical compound it then changes its electrical property in term of resistance, or current, mass, color, to output signals that can be quantified directly or in directly. Figure 1.1 shows important components of a thin film based gas sensor. The main components consist of a sensitive layer and a transducer material. The sensitive material directly interacts with the gaseous compound and is responsible for recognizing the analyte gas while the transducer, interfaced with proper electronics, will transfer the material property change of the sensing element to a measurable signal. Throughout the longevity of this work, efforts were made in engineering the sensory element of a gas sensor. A typical sensor response is depicted in figure 1.1, where key sensor characteristics are defined as the following:

1. Sensitivity: The change in measurement signal per concentration of the analyte.
2. Selectivity: The ability to discriminate or preferentially detect/ interact with a specific compound.
3. Response Time: The time required for the sensor to respond to an exposure of gaseous compound.
4. Recovery Time: The time required for the sensor to return to 90% of the original state of the measurable signal.
5. Upper Detection Limit (UDL): The maximum concentration of an analyte gas that can be reliably detected by the sensor.
6. Lower Detection Limit (LDL): The minimal analyte concentration that produces a signal change 3X greater than the sensor's intrinsic noise.
7. Dynamic Range: The concentration range where the sensitivity shows a linear behavior between the lowest possible detection limit to the upper limit concentration.

Metal oxide semiconductors have found their niche in today's society owing to their diverse properties and functionalities. For example, metal oxide semiconductors have a broad range of electronic, chemical and physical properties that are sensitive to changes in their chemical environment rendering them good candidates as a sensing material. Past research has focused on exploiting the material's sensitivity towards differing analytes to make simple, robust, solid-state sensors whose operation is based on a measurable signal created from the interaction of an analyte with the sensing material; where the output signal is in the form a change in the resistance, capacitance, temperature or luminescence. The idea of implementing metal oxides as semiconducting sensors dates back to the 1950's and the realization of these sensors has been labeled as Taguchi-type sensors. Traditional semiconducting sensors have been made of pristine or doped polycrystalline, thin or thick films, and compressed powers of metal oxides most, commonly SnO_2, however other important metal oxides for sensing applications are listed in figure 1.2. Figure 1.3 provides images of commercially available metal oxide gas sensors, the typical operation properties are described in figure 1.4. Although available commercially, highly selective and sensitive sensors are not yet attainable.

The underlying problem hindering metal oxide sensor selectivity and sensitivity is that when synthesizing sensors with bulk material in the form of films and compressed powders, there is little control over the particle size, crystallinity and phases that constitute that sensor. To aggravate the situation, commercial metal oxide sensors operate at elevated temperatures and thus the different phases and crystallites translate into different reactivities within one sensor. Consequently the resultant sensor response to a certain analyte can be a median of individual responses. If desired material conditions are known, the sensor response can be improved by engineering the metal oxide sensing element with optimal material characteristics. Therefore, knowledge of the interplay between material properties and sensing characteristics is crucial in developing an enhanced sensor. Traditional thin film based sensors also have inherent limitations in terms of the sensitivity. When a charged analyte binds to the sensor surface, a zone of charge accumulation or depletion is created. When the current flows through the thin film, the current can bypass the region of charge accumulation or depletion because the affected region is a small fraction of the total cross sectional area. This leads to attenuation in the signal and lowers the sensitivity of the sensor.

To overcome these challenges, one dimensional nanostructures have been proposed and rigorously investigated in recent years for a number of reasons. The first being the exponential increase in the percentage of surface atoms as we decrease the diameter of a wire into the nanoscale regime. This is important because there is a larger fraction of atoms involved in the surface processes whether it be adsorption or catalytic in nature. And with these diminutive structures, particularly in the case of semiconductors, carriers become increasingly sensitive to fields produced by charged entities, as depicted in figure 1.5. Since these nanomaterials are so small, it is also easier to synthesize single crystalline structures with controlled orientations and faceting, which opens up a slew possible studies. Furthermore, sensors based upon more crystalline materials provide greater long tern stability compared to their thin film counterparts, due to the reduction of instability associated with hopping conduction [140].

1.2 Zinc Oxide

ZnO is an n-type semiconductor that has gained interest as a nanostructured gas sensor due to its sensitivity to small molecules and volatile organic compounds (VOCs). Although numerous metal oxides have been studied for gas sensing, ZnO has also attracted attention as a nontoxic, abundant material that can be easily synthesized with well controlled nanoscale morphologies. ZnO is an *n*-type material with a large direct band gap of ~3.3 eV at room temperature. Electron mobility of ZnO strongly varies with temperature and has a maximum of ~2000 $cm^2/(V\cdot s)$ at 80 K, hole mobility values have been reported in the range 5–30 $cm^2/(V\cdot s)$. Advantages associated with a large band gap include higher breakdown voltages, ability to sustain large electric fields, lower electronic noise, and high-temperature and high-power operation.

Zinc oxide crystallizes in three forms, hexagonal wurtzite, cubic zinc blend, and the rarely observed cubic NaCl type. The wurtzite structure is most stable at ambient conditions and thus most common, schematic of the structure is represented in figure 1.6. The zinc blend form can be stabilized by growing ZnO on substrates with cubic lattice structure. In both cases, the zinc and oxide centers are tetrahedral, typical growth morphologies of nanostructured ZnO are demonstrated in figure 1.7. The hexagonal structure has a point group 6 mm (Hermann-Mauguin notation) or C_{6v} (Schoenflies notation), and the space group is $P6_3mc$ or C_{6v}. The lattice constants are a = 3.25 Å and c = 5.2 Å; their ratio c/a ~ 1.60 is close to the ideal value for hexagonal cell c/a = 1.633.

Additionally, improvement of electronic properties and enhancement of selectivity towards VOCs can be achieved with selective doping. This opens up the possibility of multiple ZnO sensing elements with dopant tailored selectivity and selectivity for analysis of analyte mixtures with real time detection. Furthermore, the low cost, wide, direct band gap (3.35eV) and large exciton binding energy (60 meV) of ZnO have roused interest in developing light emitting diodes, solar cells, and UV detectors [141], applications of one dimensional ZnO structures are summarized in figure 1.8.

These devices typically exploit nanostructured ZnO, including nanowires, nanoparticles, and hierarchical nanostructures [142]. Demonstrations of more complex constructs have been fabricated to enhance the surface area of ZnO across multiple length scales, however hierarchical ZnO nanostructures do not exhibit designs that maximize both nanoscale surface processes and electronic signals. ZnO nanowires are perhaps the most studied as their small diameters produce significant enhancement and their lengths enable two point electrical contact with relative ease. Alternatively, nanoparticles provide the greatest potential for size imposed enhancement with confinement in three dimensions, but are more difficult to electrically interface. However, hybrid materials that utilize the advantages of both metal oxide nanoparticles and ultra high aspect ratio carbon nanotubes is promising route to advanced sensing systems.

1.3 Single Walled Nanotubes

Single walled carbon nanotubes (SWNT) are promising nanomaterials largely responsible for the “nano-revolution” due to their small size, incredibly high aspect ratio, unique electronic properties, thermal stability, and mechanical flexibility. SWNTs consist of a single grapheme sheet seamlessly wrapped into a cylindrical tube while multiwalled carbon nanotubes (MWNTs) are composed of an array of such concentric nanotubes figure 1.9 shows a representation of SWNTs and MWNTs. SWNTs are an important variety of carbon nanotube because they exhibit electric properties that are not shared by the multi-walled carbon nanotube (MWNT) variants. In particular, their band gap can vary from zero to about 2 eV and their electrical conductivity can show metallic or semiconducting behavior, whereas MWNTs are zero-gap metals. The existence of a crystallographic defect affects the material properties, which can occur in the form of atomic vacancies. Another form of carbon nanotube defect is the Stone Wales defect, which creates a pentagon and heptagon pair by rearrangement of the bonds. Crystallographic defects also affect the SWNT's electrical properties, with a common result being a lowered conductivity through the defective region of the tube. A defect in armchair-type tubes (which can conduct electricity) can cause the surrounding region to become semiconducting, and single monoatomic vacancies induce magnetic properties.

Although, carbon nanotubes are composed entirely of surface atoms and have an exceptional high surface area available for interaction with molecular adsorbates their chemical inertness limits their role as stand-alone gas sensors. Dai, Kong et al and Collins et al demonstrated the conductance change of SWNTs with exposures to NH_3 and NO_2 gaseous compounds, attributing the detection to direct charge transfer between the gaseous molecule and the p-type semiconducting SWNT. Later Snow et al. demonstrated capacitance based gas sensing using SWNT networks with lithographically patterned top-contact interdigited electrodes. The group's reported capacitance based detection resulted in high sensitivity with fast response and recovery times towards polar alcohols, ketones, and non-polarizable hydrocarbons. But even more, it demonstrated the high potential for SWNT based electronics and sensitive gas sensing devices.

Moreover, work developed by Star et al. demonstrated that the sensitivity and selectivity towards certain analytes can be induced when the carbon nanotubes are covalently or non-covalently functionalized [143-150]. Therefore, SWNTs can be powerful transducing elements for gas sensors as functionalization can impose nanoparticles dependent sensitivity and selectivity upon the electronic structure of SWNTs. Furthermore, several groups have reported utilizing semiconductor nanoparticles for optical sensitization of SWNT networks.

1.4 Research Objectives

The global objective of this work is to develop a high density sensor array using ZnO and metal nanostructure decorated SWNT networks as the platform material for the realization of highly sensitive, selective and discriminative gas sensors. To conceive such desired sensor characteristics, an electrochemical route was developed to synthesize ZnO nanostructures with optimized structural and electrical properties. The specific aims of this work were the following:

1. Establish a simple and scalable method to fabricate hybrid ZnO/SWNT network devices for room temperature detection of small gaseous molecules. Characterize the structural features of these composites based on the ZnO electrolyte composition, temperature, and deposition potential. Investigate the sensing performance as a function of particle size/density and particle crystalline quality.
2. Study the performance of ZnO/SWNT networks for the detection of volatile organic compounds. Elucidate the impact of molecular functional groups on the sensing response of ZnO/SWNT devices. Explore the ability to distinguish isomers or structurally similar compounds in a conductometric fashion.
3. Investigate the potential of ZnO/SWNT networks as UV photodection systems. Ascertain the effect of ZnO functionalization with electrical measurements of bare and decorated SWNT networks. Describe the impact of crystallinity and nanoparticle size/density on the conductometric response of these devices.

4. Formulate conditions to electrochemically decorate SWNT networks with Au, Pt, Pd, and Ag catalysts. Measure the electrical properties of these devices before and after catalyst coatings. Explore selectivity and sensitivity modulations to gaseous compounds induced by catalyst overlayers.
5. Study the influence of ZnO nanoparticles on the site-selectivity of catalyst electrodeposition on the SWNT networks. Investigate the effect of applied potential on the site-selectivity of catalyst electrodeposition on ZnO/SWNT networks.
6. Investigate synthesis conditions to selectively control the positioning of sequential metal nanoparticles, as well as the effect of sequence in metal deposition.

1.5 Thesis Organization

The presentation of this thesis is as follows:

Chapter 2 will detail the development of a bath and electrodeposition conditions to synthesize ZnO on the surface of SWNTs with precise control over particle formation, size and density. Chapter 3 will follow with more detailed real time room temperature gas sensing performance of the ZnO/SWNT hybrid structures towards gaseous compounds of interest. In chapter 4, UV photoconduction behavior of electrochemically synthesized ZnO-SWNT hybrid structures will be presented.

Sequential functionalization of ZnO/SWNT hybrid structures with metal catalyst (Au, Pt, Ag and Pd) is described in chapter 5, where the surface morphology, growth mechanism and room temperature sensing performance were investigated as a function of charge, and presence or absence of seeded metal oxide.

Chapter 6 will deal with the deposition of multiple metals to understand the behavior of binary/dual metal catalyst and metal catalyst sequence on sensing performance. Furthermore, manipulation of site specific electrodeposition to control the positioning of the sequential metal catalyst will be explained.

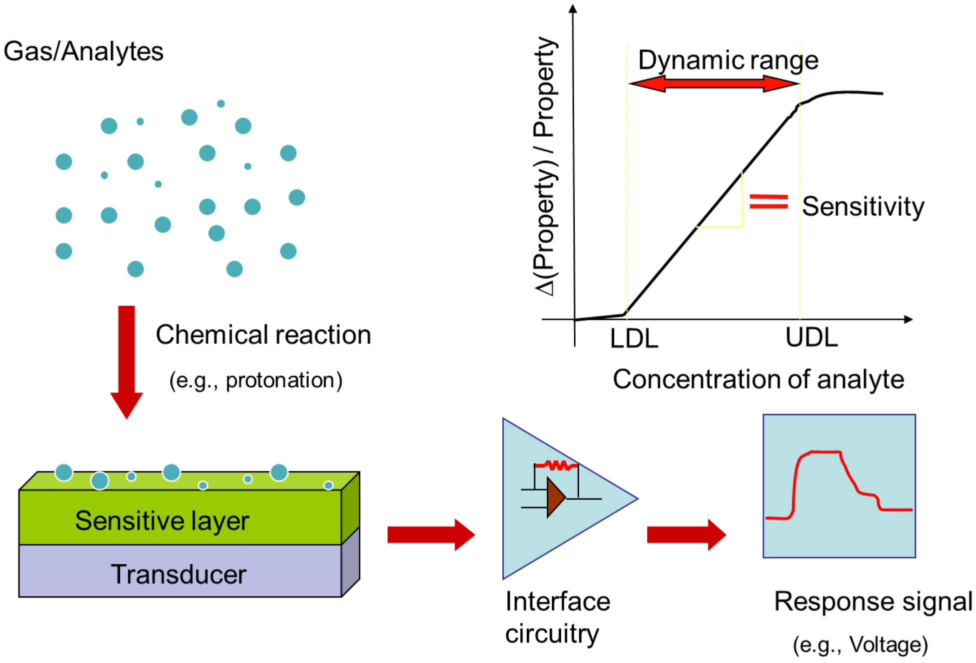

Figure 1.1. Properties of a sensor.

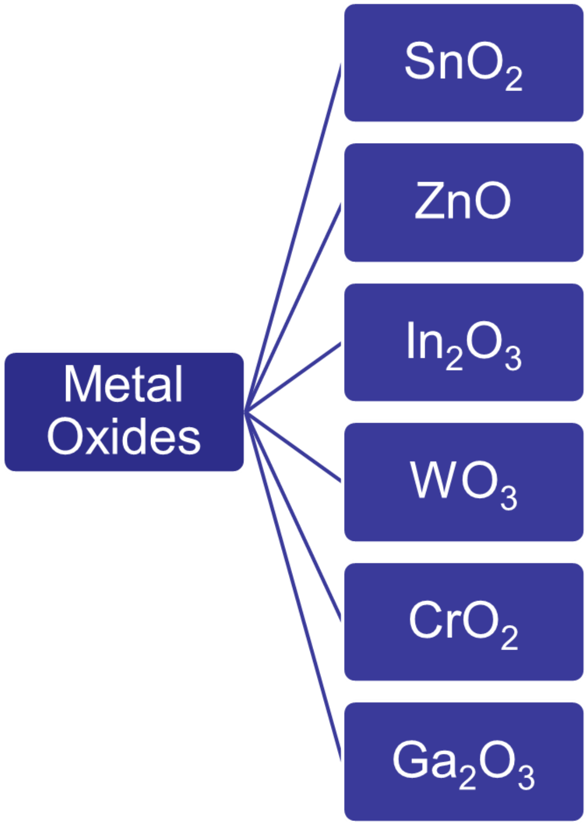

Figure 1.2. Important metal oxide materials for gas sensing applications.

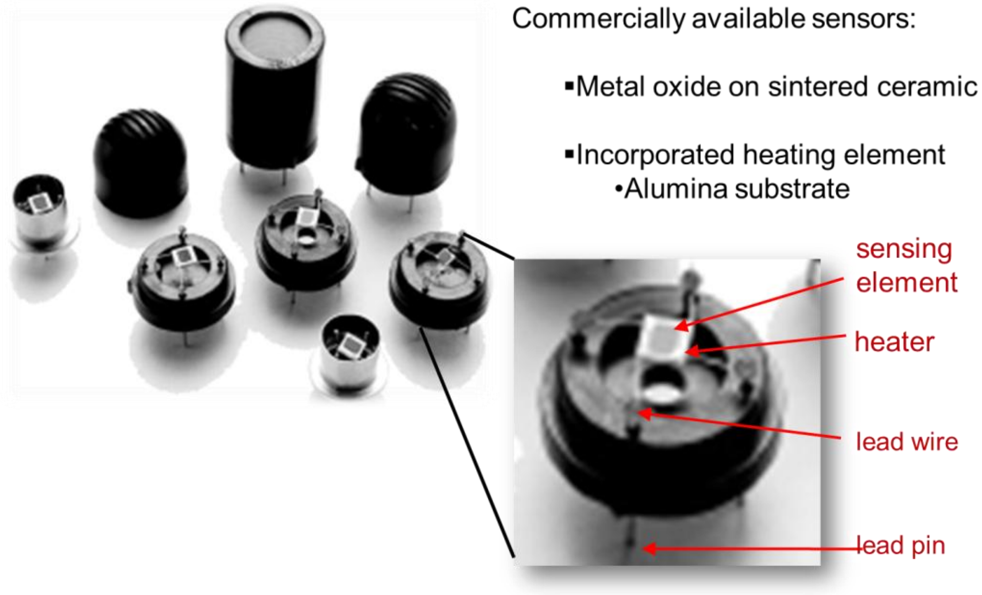

Figure 1.3. Image showing conventional commercially available gas sensors.

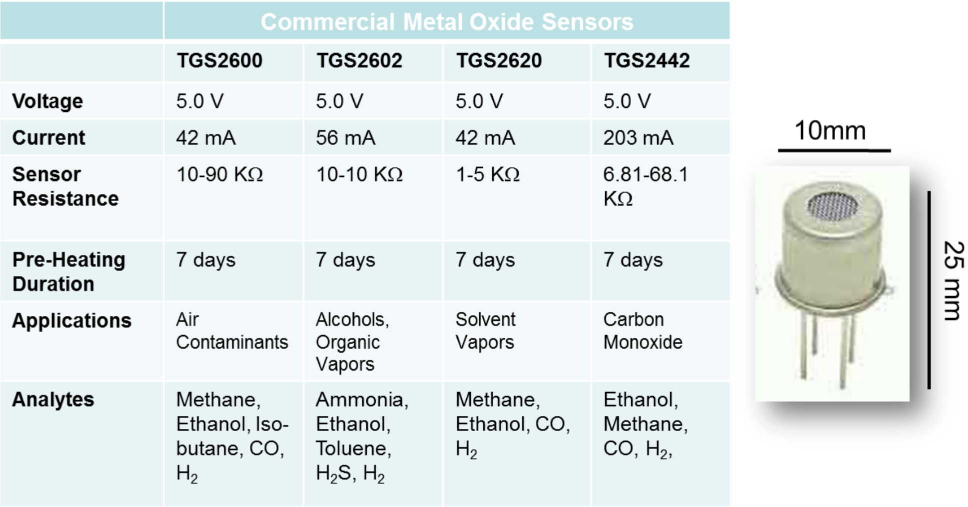

	Commercial Metal Oxide Sensors			
	TGS2600	**TGS2602**	**TGS2620**	**TGS2442**
Voltage	5.0 V	5.0 V	5.0 V	5.0 V
Current	42 mA	56 mA	42 mA	203 mA
Sensor Resistance	10-90 KΩ	10-10 KΩ	1-5 KΩ	6.81-68.1 KΩ
Pre-Heating Duration	7 days	7 days	7 days	7 days
Applications	Air Contaminants	Alcohols, Organic Vapors	Solvent Vapors	Carbon Monoxide
Analytes	Methane, Ethanol, Iso-butane, CO, H_2	Ammonia, Ethanol, Toluene, H_2S, H_2	Methane, Ethanol, CO, H_2	Ethanol, Methane, CO, H_2,

Figure 1.4. Table showing operation requirements of commercially available metal oxide gas sensors.

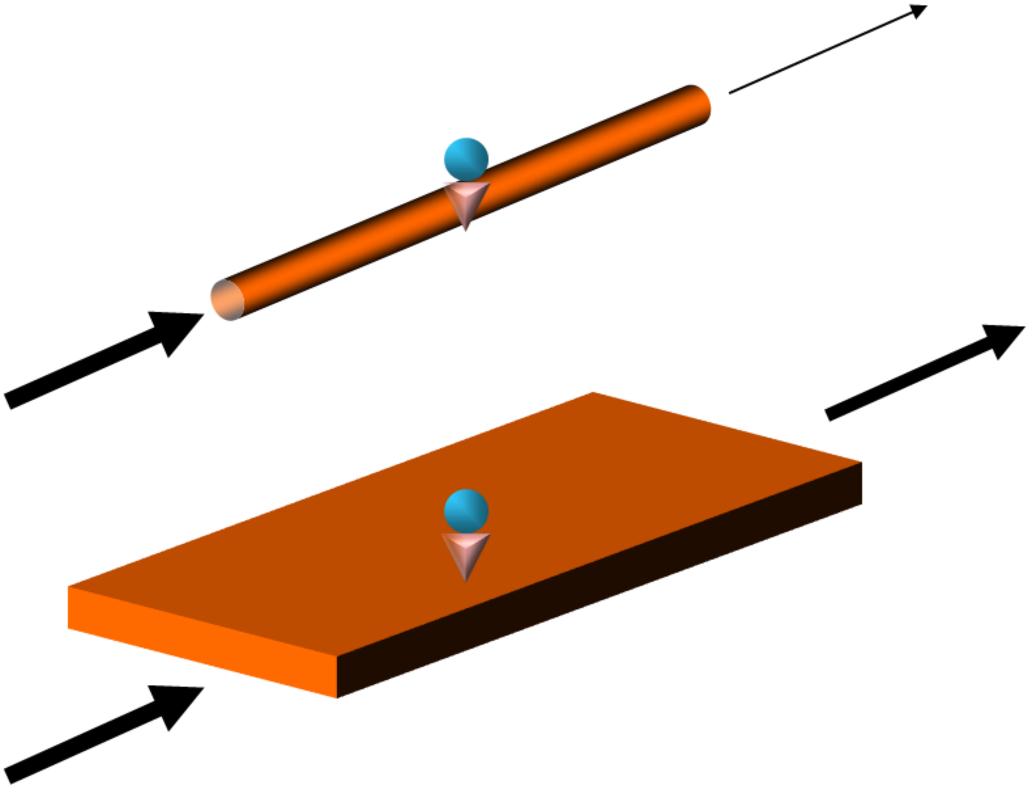

Figure 1.5. Schematic depicting 1-D nanostructure versus 2D thin film, where arrows represent the charge carriers and density, blue sphere denotes the analyte and cone shapes correspond to the depletion region.

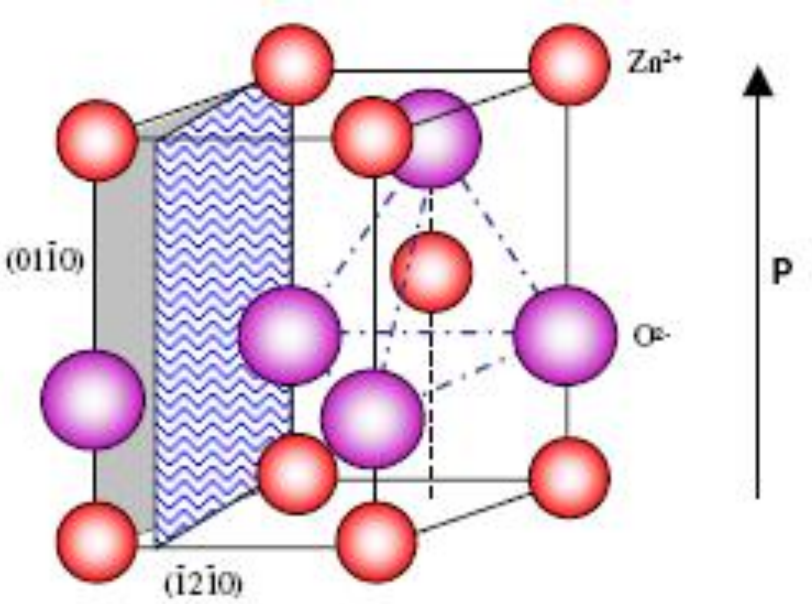

Figure 1.6. Schematic showing typical ZnO wurzite structure.

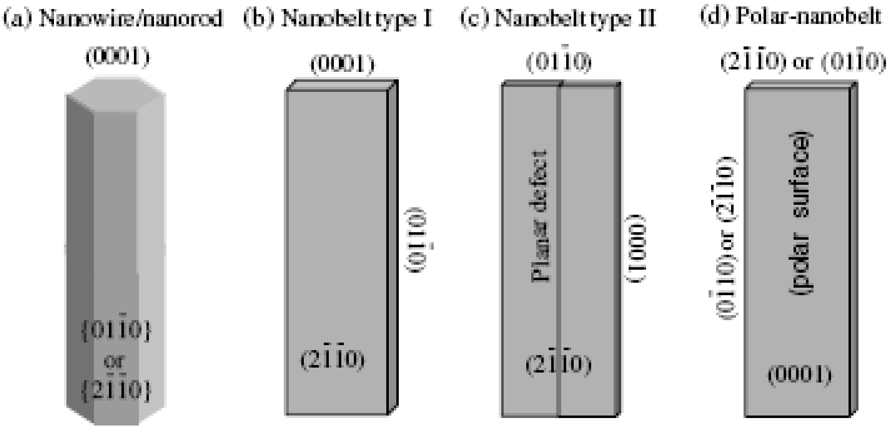

Figure 1.7. Typical growth morphologies of one dimensional ZnO nanostructures and their corresponding facets.

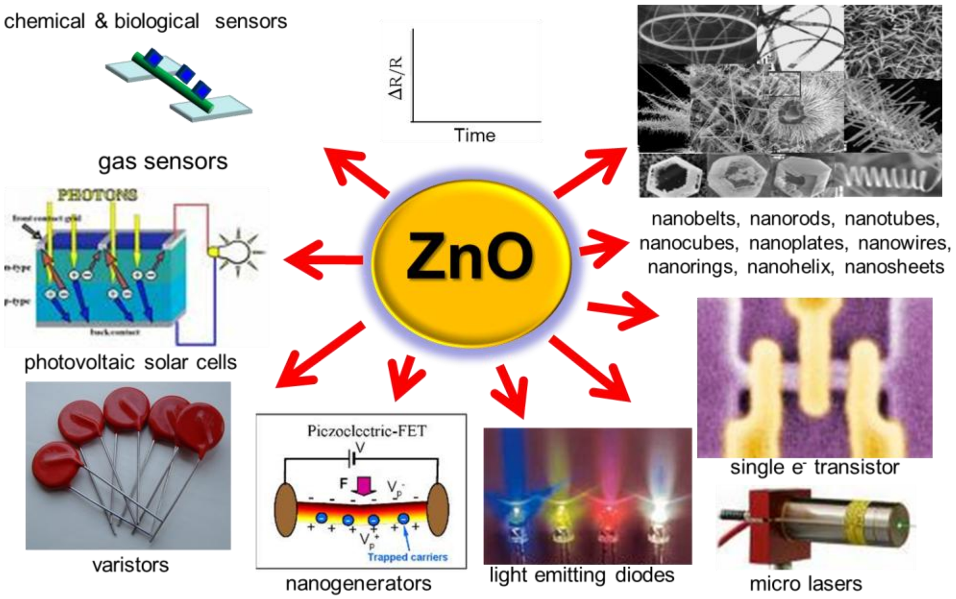

Figure 1.8. Image showing the multitude of applications for one dimensional ZnO nanostructures.

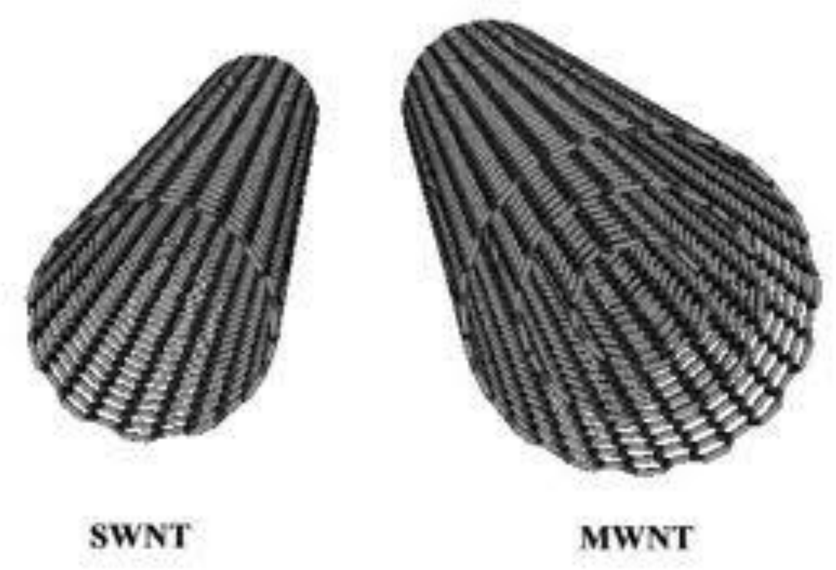

Figure 1.9. Schematic representation of single and multiwalled nanotubes.

CHAPTER 2:

SYNTHESIS AND CHARACTERIZATION OF ZnO FUNCTIONALYZED SINGLE WALLED CARBON NANOTUBES HYBRID GAS SENOSRS

Abstract

In this work we exploit ZnO nanostructures as a sensitizing material for SWNT network gas sensors. Electrochemical synthesis conditions were explored to tailor the structural properties of the ZnO nanoparticles and correlate these features with sensing performance. Room temperature conductometric detection of low molecular weight molecules of interest (i.e. CO, CO_2, NO_2, NH_3, SO_2, H_2S) with ZnO/SWNT hybrid structures exhibited enhanced sensitivity, selectivity, and response/recovery time contingent upon ZnO crystallinity. Optimal devices show a doubling in sensitivity over bare SWNT networks from 2.54 % per ppm to 4.96% per ppm with a maximum response of ~80% for 500 ppb H_2S, suggesting a lower detection limit well into the double digit ppb range. Additionally these hybrid sensors demonstrated uncharacteristic selectivity towards H_2S with little to no response for other analytes examined.

2.1 Introduction

Gas sensors are existing and emerging components in a spectrum of fields with longstanding utilization for the recognition of toxic substances, operational /process control, and monitoring of effluent streams. Recent research has focused on the maturity of a simple, robust sensor whose operation can be based on a measurable signal created from the interaction of an analyte with the sensing material and output in the form of a change in resistance, capacitance, temperature or luminescence. In particular, conductometric sensors are amenable to development for higher level analysis of gas mixtures and compact, portable platforms required for ubiquitous deployment. To overcome current challenges in sensitivity, power consumption and response/recovery times, 1-dimensional nanostructures, such as singe wall carbon nanotubes (SWNTs), have been rigorously investigated as transducing and sensing elements for gas sensors due to their promising electronic properties, thermal stability, and chemical inertness. Since SWNTs are composed entirely of surface atoms, interactions with adsorbing molecules can substantially alter their electronic properties, however highly specific and sensitive sensors are not readily attainable with stand alone SWNT devices.

Prior work has shown that the sensitivity and selectivity towards certain analytes can be significantly enhanced when the carbon nanotubes are covalently or non-covalently functionalized with appropriate materials [143-150]. Efforts include the surface decoration or occlusion of SWNTs with metals, metal oxides, polymers, and other active materials [143, 146, 148-161]. In particular, the incorporation of metal oxides on the periphery of nanotubes combines the advantages of well developed metal oxide sensors with nanoengineering providing a more sensitive and stable platform for sensing purposes, of which SnO_2 is the most habitually demonstrated. Investigation of other metal oxides/SWNT elements is limited with little knowledge of structure-property relationships demonstrated. A dearth of information also resides in the numerous metal oxide/dopant combinations available for hybrid sensing systems along with synthesis dependent variability in morphology, crystallinity, and particle size/density, creating significant opportunity.

Nanostructured metal oxides have been of technological interest in gas sensing for nearly two decades due to enhanced sensitivity from trapped surface states and carrier depletion within nanocrystallites [162]. Furthermore, the high degree of crystallinity achieved in some metal oxide nanostructures can also provide greater long term high temperature stability desired for commercial devices [163]. Among nanostructured metal oxides, ZnO is one of the most widely studied nanomaterials largely due to its low cost, tunable properties and ease of synthesis, which have been extended to various vacuum techniques, chemical routes, so-gel process, spray paralysis and electrochemical deposition [164-169]. This n-type direct, wide band-gap semiconductor, 3.35eV, has excellent chemical and thermal stability with optoelectronic properties and a strong piezoelectric effect. These features along with its sensitivity to several small molecules have motivated several studies on ZnO nanostructure gas sensors. While significant improvements in sensing performance utilizing ZnO nanowires have been demonstrated they preclude the transduction potential of a truly one-dimensional material, SWNTs. Furthermore, the only ZnO hybrid gas sensors studied to date utilized sol gel and chemical routes to coated multiwalled carbon nanotubes resulting in hybrid nanocomposites [153, 170].

Herein we investigate the synthesis and characterization of ZnO nanoparticle decorated SWNT networks. ZnO nanoparticles were electrochemically deposited on SWNT networks, a process that permits intimate contact of the nanoparticle with the SWNTs by site specific nanoparticle decoration, utilizing a simple electrolyte with charge and temperature variation to tune nanoparticle size/density and crystallinity. Electron transport properties were probed with low temperature measurements. Bare SWNT networks and hybrid ZnO-SWNT devices were also challenged with several small molecules at room temperature. The ZnO nanoparticles crystallinity was shown to have a large impact on selectivity and sensitivity towards H_2S. Highly crystalline (002) oriented ZnO nanoparticles on SWNT networks exhibited a response of ~80% to 500ppb H_2S, which to the best of our knowledge is the highest reported room temperature sensitivity, showing significant promise for advanced detection systems.

2.2 Experimental Details

2.2.1 Electrodeposition of ZnO and ZnO coated SWNTs

ZnO synthesis was studied in a conventional three electrode cell. The working electrodes were gold-silicon and SWNT-coated silicon with areas of $1cm^2$, a Zn sheet (99.99%) and a saturated Ag/AgCl electrode were used as the counter and reference electrode, respectively. The electrolytes were comprised of xM $Zn(NO_3)_2$ + (0.2-2x)M

$NaNO_3$ [where $0<x<0.1$] using analytical grade reagents. Experiments were performed in 50 mL of electrolyte in the absence of N_2 bubbling or agitation in order to preserve the pH gradient. Electrodeposition was carried out under potentiostatic mode at 25°C and 70°C using a CH Instruments Electrochemical Analyzer CHI604c. Material analysis of the electrodeposited thin films was performed by X-ray diffraction (Bruker AXS Baltic Scientific Instruments D8 Advance) with Cu K_α radiation over a scanning range of 20°-90° in 0.1° increments. Microstructure and surface morphology were imaged by scanning electron microscopy (Leo SUPRA 55, Model 1550).

A carbon nanotube suspension was prepared by addition of 0.2 mg of commercially available carboxylated SWNTs obtained from Carbon Solutions Inc., to 20 mL of N,N-dimethylmethanamide (DMF). The contents were sonicated in a glass vial for 90 minutes using a VWR model 50D sonicator. All 20 mL of the SWNT suspension were transferred to a 50 mL Teflon centrifuge tube and centrifuged for 90 minutes at 15000 RPM and 23°C using a Beckman J2-HS centrifuge. Immediately after centrifugation, 10 mL of the supernatant was carefully removed and placed in a glass vial. The supernatant was additionally sonicated for 60 minutes prior to use.

Lithographically patterned Si chips with 16 electrode pairs (Ti/Au 20/180 nm) were utilized as substrates and contacts for sensor assemblages. The electrodes contained a 3 μm gap and large contact pads that enabled individual addressability for electrochemical functionalization. SWNTs were aligned across the electrode gaps via alternating current dielectrophoretic alignment by adding a 1.5 μL drop of SWNT suspension, applying 1 V_{pp} and 4 MHz (Keithley 3390 AC generator, 50 MHz arbitrary waveform generator). The device resistance was controlled by the alignment time. After alignment, electrochemical functionalization of the SWNT network was performed by addition of a 2 μL drop of 0.1 M $Zn(NO_3)_2$ electrolyte, using the gold pads as the working electrode, a Pt wire as the counter electrode, and a Ag/AgCl wire as a pseudo reference electrode. Electrical characterization was performed in a two point probe configuration using Keithley 2636 System. Temperature dependent electrical resistance was measured between 10 and 300 K in intervals of 10 K using CTI-Cryogenics (Helix Technology Co.) system in combination with a Keithley 2636 measurement system.

2.2.2 FET and Gas sensing Measurements

For gas sensing studies, the functionalized chip was integrated onto a pin chip holder by wire bonding (West Bond Inc. Model 7443A) and was subsequently loaded on a custom made bread board designed for the sensing system [161]. Each sensor was subjected to 1.0 V DC potential and the current was continuously monitored, the electrical resistance was then determined by applying Ohm's Law. A base line was achieved with exposure of dry air as the carrier gas and different analyte concentrations were attained by subsequent dilutions with the carrier gas. Exposure times were limited to 15 minutes and recovery time to 20 minutes; total gas flow rate was kept constant at 200 sccm for all experiments. Analyte and carrier gas flow rates were regulated by mass flow controllers (Alicat Scientific Incorporated) [161, 171].

2.3 Results and Discussion

2.3.1 Material Synthesis and Characterization

Among the various metal oxides deposition approaches, electrochemical synthesis was selected for advantageous control over size of structures, site specificity, and material quality. There are three different electrochemical routes for the deposition of zinc oxide; in each of the reaction pathways a precursor, either O_2, NO_3^-, or H_2O_2, is needed as an oxygen source. The electro-precipitation of zinc oxide material occurs by two sequential steps. First, the precursor is electrochemically reduced to form OH^-. This process occurs at the cathode surface creating a localized increase in pH. The second step is chemical precipitation of ZnO. In this reaction Zn ions interact with the hydroxide ions forming a zinc hydroxide complex, which then precipitates as zinc oxide. Because the stability of the hydroxide complex is highly dependent upon the solution pH, where higher pH values make the complex less stable, precipitation of ZnO occurs preferentially at the surface of the cathode, possibly according to the mechanism [164, 165, 172]:

$$H_2O + NO_3^- + 2e^- \Leftrightarrow NO_2^- + 2OH^- \qquad (1)$$

$$Zn^{2+} + 2OH^- \Leftrightarrow Zn(OH)_2 \qquad (2)$$

$$Zn(OH)_2 \Leftrightarrow ZnO + H_2O \qquad (3)$$

In this work a nitrate bath was developed for ZnO deposition as previous studies have demonstrated facile crystallographic control by manipulation of the oxygen precursor (NO_3^- concentration), applied voltage, solution temperature and pH [164, 165, 173-175]. Furthermore, a NO_3^- electrolyte permits systematic variation of $[Zn^{2+}]$ while maintaining a constant oxygen source concentration. The bath in this work maintained a high concentration of the oxygen precursor in solution, 0.2 M NO_3^-, while varying the $[Zn^{2+}]$ from 0.0 to 0.1 M to investigate the solution behavior as a function of $[Zn^{2+}]$ and applied voltage. The linear sweep voltammograms (LSVs) of x M $Zn(NO_3)_2$ + (.2-2x) $NaNO_3$, represented in Figure 2.1, show the absolute current density increasing nearly monotonically as the applied potential increased for every electrolyte, with the exception of a OH^- reduction peak. Electrolytes with $[Zn^{2+}]$ exhibited a slight negative shift in reduction potential as well as an increased deposition rate with greater $[Zn^{2+}]$. More concentrated solutions were also tested however LSV behavior depicted current fluctuations due to the competition between the reduction of the nitrate ions and the direct deposition of zinc metal (Appendix 2), thus further characterization of electrolytes containing > 0.1 M $Zn(NO_3)_2$ were not pursued.

Material crystallinity was manipulated by changing the solution temperature from 25°C to 70°C. Figure 2.2 (A) shows an increase in cathodic current at an earlier potential of -0.54 V vs Ag/AgCl and an overall general increase in current for both the 0.1 M $Zn(NO_3)_2$ and 0.2 M NO_3 solutions when performed at 70°C. In the nitrate electrolytes, sans Zn^{2+}, current increases at a smaller cathodic potential indicate an escalated OH^- generation by the reduction of nitrate ions at 70°C compared to the rate at 25°C. The LSV curve of 0.1 M $Zn(NO_3)_2$ at 25°C, figure 2.2 (B), shows distinct regions correlating to the reduction of nitrate ions (1), the electrochemically induced precipitation of zinc hydroxide to ZnO (2), and deposition of metallic zinc (3). The LSV data consequently indicates a potential window for ZnO deposition from -1.0 to -1.4 V at 25°C shifting to -

0.6 to -0.8 V when operating at the elevated temperature due to the early onset of nitrate reduction.

Thin films were subsequently deposited at -1.2, -1.3 and -1.4 V on 1 cm^2 Au/SiO_2 substrates with a constant charge density of 6 C cm^{-2} at 25°C to confirm material quality at the prescribed potential window. The XRD patterns for films deposited at each potential and plane view SEM images corresponding to the diffractograms reveal structural and compositional information of the deposits (Appendix 2). Polycrystalline ZnO thin films were obtained at -1.2 V with average grain size of 16.8 nm (Appendix 2). At more cathodic deposition potentials metallic zinc was incorporated and the average grain size was increased. SEM images reveal degradation in film quality at higher potentials, with a rough, porous morphology containing a dendritic surface layer. Thus, from analysis of LSV curves in conjunction with XRD patterns, the optimal potential for ZnO deposition is -1.2 V with the aforementioned conditions.

While the Au substrates provided well defined working areas for clarity in cyclic voltammetry features observed for temperature and electrolyte variation, the intention of this work is development of a ZnO electrolyte for decorating SWNT networks. For a more accurate crystallographic picture of ZnO deposition on carbon nanotube networks, SWNT thin films were spray coated on Si wafers for subsequent ZnO electrochemical functionalization and characterization. When thin films were deposited onto SWNTs (figure 2.3), polycrystalline ZnO deposits were observed at -0.6 V, with effete peaks at (100), (002), and (101). Although the substrate was changed from gold to SWNTs, the films deposited at 25°C showed little difference in the crystalline coordination indicating that the ZnO thin films exhibit similar bulk growth mechanisms, independent of the substrate. Moreover the growth rate was maintained at ~ 1.6 μm/hr for both substrates. ZnO deposits synthesized at 70°C on SWNT displayed a preferred orientation in the (002) direction as well as weak reflections at (100), (101), (102), and (110) planes, corresponding to ZnO hexagonal wurtzite structure, (figure 2.3 (D)). The average grain size for deposits at 25°C was determined to be 64.3, 38.7, and 42.0 nm and decreased to 37.5, 15.05, and 34.1 nm for (100), (002), and (101) crystal orientations, respectively, for thin films deposited at 70°C. Although a higher synthesis temperature produced smaller grains, the substantially larger peak intensity with respect to the low temperature synthesis is indicative of greater crystallinity with less defects. From the X-ray diffractograms of the ZnO thin films, it is evident that a preferred crystalline direction can be imposed by simply tuning the deposition temperature while maintaining all other parameters constant, i.e. substrate, solution concentration, deposition voltage.

The substrate and process for fabrication of ZnO-SWNT sensors are illustrates in Figure 2.4. The sensor architecture consists of 16 individually addressable Au electrode pairs with 3 μm gaps along a 50 μm edge, as shown in Figure 2.4 (A). This chip design enabled multiple devices and synthesis conditions to be investigated in a single sensing trial. Further details have been provided elsewhere [160]. SWNTs alignment was performed through dielectrophoretic alignment by adding a 1.5 μL drop of SWNT suspension and applying 1 V_{pp} and 4 MHz. The device resistance was tuned by adjusting the alignment time, as described previously [176]. After SWNT alignment, electrochemical functionalization on the surface of the SWNT network was performed by addition of a 2 μL drop of 0.1 M Zn $(NO_3)_2$ electrolyte, using the gold pads as the working electrode, an inserted Pt wire as the counter electrode and a Ag/AgCl wire as a pseudo reference electrode, as depicted in figure 2.4 (B). All ZnO deposition were performed with a fixed applied potential of -0.6 V as determined from cyclic voltammograms on SWNT thin films. The final structure consisted of ZnO nanoparticles on a SWNT network bridging two gold electrodes (Figure 2.4 (C)).

Other groups have performed surface functionalization of single and multi walled carbon nanotubes (MWNTs) with ZnO by other approaches for example, Zhang et al generated ZnO beaded MWNTs by first sputtering Zn particles followed by oxidation in ambient air; their resultant structures were cylindrical ZnO particles with hollow interiors, the sputtered time predetermined the particle size [1-7 min produced ~19 to ~70 nm particle size] and quantum confinement effects were observed where the energy gap was enhanced with decreasing particle size [177]. Jiang et al coated sodium dodecyl sulfate (SDS) surface treated MWNTs with ZnO via a sol process and produced a composite with average particle size of 6 nm. The group attributed their ZnO-coated MWNT composite formation to an electrostatc interaction mechanism where the MWCNT restricted the size of the ZnO particles due to the controlled negative functional groups on the side of the graphitic walls brought about by the SDS surface treatment [154]. Yu et al synthesized ZnO/MWNT composites by dispersion of thermally evaporated ZnO nanowires on an ITO substrate which was later employed as the cathode in an electrophoresis deposition process. Grinded MWNTs were added to the suspension and deposited on the cathode containing adhered ZnO nanowires, various composites were formed by controlling the deposition conditions (i.e. current voltage and time) and their field emission properties were investigated [178]. Gonzalez-Campo et al reported the in situ synthesis of ZnO particle coating on MWNTs by using a diethyl zinc chemistry resulting in nanocomposite of ZnO MWCNTs [153] and finaly, Zhu et al covered MWCNTs with a dense layer of ZnO nanaparticles with average particle size of 20 nm by a sol process [170]. The advantage of an electrochemical method is the ability to rapidly deposit ZnO particle in-situ with good control over size and structural features on a device in which contact to the transducing SWNTs is already established.

As observed for many different deposition techniques, the size and density of ZnO particles is directly related to the quantity of material deposited. Therefore, control over ZnO particle size was achieved by regulating the charge passed during the deposit. Although charges ranging from 0.5 to 500 μC were investigated, charges below 40 μC imparted the greatest control over nanoparticle size and distribution, as shown by the SEM images in figure 2.5 (A-D). The specified deposition conditions produced ZnO particle size spanning ~10 nm to 55nm for applied charges from -0.614 to -33 μC (figure 2.5). Based on the SEM images, ZnO particles grow by instantaneous nucleation with few or no nucleation sites with the progression of time only continued growth of existing nuclei. Moreover particle nucleation is believed to initiate at Stone-Wales defect sites, as these locations have been shown to exhibit greater electrochemical activity [179, 180]. This is further substantiated by observation that the number of particles on the SWNTs decreases with increasing charge due to coalescence of adjacent small particles to form a larger particle, figure 2.5 (E-F). Thus the size and density of ZnO nanoparticles can be manipulated starting from particle formation to continuous coating along the SWNT networks by controlling the deposition conditions, i.e. applied charge. The extent of SWNT coverage by ZnO is one parameter that plays a significant role in sensor performance as it dictates electrical transport properties and the surfaces available for interaction with the analyte.

2.3.2 Electrical Characterization of ZnO-SWNT Structures

The impact of ZnO nanoparticle deposits on the electron transport behavior of the SWNT network devices were examined by current-voltage (I-V) scans and activation energies extracted from low temperature measurements for bare and functionalized SWNTs. Since the electrical behavior of SWNT networks can vary significantly depending on the SWNT density and alignment, samples were selected to have similar initial resistances for a more direct comparison [181]. To maintain comparable ZnO coverage for the two deposition temperatures a charge of 20 μC was used in both cases. In general, the resistance increased after ZnO functionalization with the higher deposition temperature (70°C) resulting in a greater resistance (figure 2.6.B). Low temperature I-Vs permitted the activation energy, which is a measure of thermal energy required for charge carrier transport, to be obtained from an Arrhenius temperature dependence of the resistance (figure 2.6.B). The temperature dependent variation in the slope of the activation energy implies that different conduction mechanisms take place due to the shallow donor levels of and defect sites of ZnO. The activation energy was determined by the linear portion (slope) of the natural log of the resistance versus the inverse temperature at the low temperature region (20-120 K) and was determined to be 5.26 ± 0.16, 9.13 ± 0.67, and 7.25 ± 1.05 meV for the bare, ZnO/SWNT (25°C), and ZnO/SWNT (70°C), respectively [n=3] (figure 2.6). These activation energies are comparable to previously reported carboxylated SWNT networks (6 meV) and ZnO thin films (8 meV) [182, 183]. A larger activation energy was measured for the ZnO particles deposited at 25°C relative to those deposited at 70°C, possibly due to the increase in donor density of the more crystalline material obtained at the higher deposition temperature.

2.3.3 Gas Sensing Studies

Room temperature sensing performance of individual sensors was investigated as a function of charge towards H_2S to determine charge dependence on the sensing response for an optimal ZnO/SWNT sensor, the above analyte were chosen based on previous reports [184-186]. The dynamic responses of the sensors synthesized at 25°C at various charges towards H_2S are shown in figure 2.7 (A), and histograms of compiled responses towards 20 ppm of H_2S are summarized in figure 2.8 (B) and shows that an optimal ZnO/SWNT sensor can be conceived at 20 μC; hence forward, all sensors were synthesized at 20 μC. Optimized sensors were tested towards low molecular weight compounds of interest (humidity, CO, CO_2, NO_2, NH_3, SO_2, and H_2S) at concentration ranges abutting OSHA's permissible exposure limit ($^1/_8$, ¼, ½, 1, 2X PEL). Figure 2.8 summarizes the ZnO/SWNT hybrid sensor's sensitivity, functionalized at 25°C, towards the analytes at OSHA's PEL level. The ZnO/SWNT hybrid sensors are more sensitive than the bare SWNTs across the board, with the exception of reduced sensitivity towards NO_2.

Khanderi et al synthesized ZnO-MWCNT nanocomposites by an in situ thermal decomposition single source precursor route. The resultant nanocomposites contained average agragates consisting of individual paricles of 3-5 nm in diameter. At higher Zn oximate concentrations, the surface of CNTs were more densely enveloped with ZnO nanoparticles, in addition at higher concentrations, particles agglomerated and grow as larger scattered particles. The group investigated the sensing application of their composite system towards CO, wherein the sensing was performed in the absence of atmospheric oxygen, and found the lowest detactable concentration to be 20 ppm (OSHA's PEL $50ppm_v$). Conjointly, the group showed that their ZnO/CNT system outperformed pristine multiwall CNTs and ZnO particles synthesized by the same route, attributing their enhanced performance to addition of receptor sites introduced by surface functionalization [156]. Thus the lack of response towwards CO with our hybrid system could arise from the use of dry air as the carrier gas and room temperature operation.

Clearly the ZnO/SWNTs hybrid sensors were most sensivite towards H_2S with sensitivity of 2.54 resistance change per ppm of H_2S, compared to the bare SWNT which has sensitivity of 0.33 resistance cahnge per ppm of H_2S (determined from the slope of linear section of the change in resistance over concentration). Zhang et al synthesized ZnO 3-dimensional dendrites composed of prottruding nanorods with diamet ers of 60 to 800 nm via a Cu catalytic vapor-liquid-solid growth process. The group addressed a single dendrite by physically contacting the macrostructure with conductive sylver paste and investigated the sensing performance of the dendrite towards various analytes (H_2S, NH_3, H_2, NO_2 and H_2O) and found that ZnO dendritic macrostructure had the highest selectivity towads H_2S and was also extremely sensitive to humidity. The H_2S specificity is attributed to a larger affinity of H_2S towards the adsorbed oxygen ions on the surface of the structures described by $H_2S + 3O^-_{(ads)} \rightarrow H_2S + SO_2 + 3e^-$. The sensing mechanism is heavily attributed to the energy barrier being the more dominant factor in effecting the sensitivity of the sensors as opposed to the depleation layer; higher concentrations of H_2S effect the transport of electrons more fervently thus further modulating the energy barrier [187].

Past groups have experimentally investigated the dependence of the sensing ability on the grain size (available surface area), surface states (electronic contribution) and test molecule chemical affinity. Rout et al. investigated the sensing response of individual nanowires of three metal oxides [ZnO, TiO_2 and $WO_{2.72}$] via CAFM and compared the performance of the metal oxides based on oxide type and diameter size. Although direct size comparison between the different oxides was not well performed, the group determined that a 40 nm diameter $WO_{2.72}$ nanowire had higher sensitivity than a 16 nm diameter $WO_{2.72}$ nanowire, speculating that the larger diameter seized a longer depletion layer path thus providing a broader available surface area [188]. Lin and Rodriguez et al both independently investigated the surface decomposition/surface poisoning of H_2S on ZnO (0001) film surfaces by variable-energy photoelectron spectroscopy and first principles density functional study, respectively, and determined that the exposed Zn metal centers on the single crystal material play a larger role in the interaction with H_2S, while the O vacancies dominate the H_2S interaction in polycrystalline ZnO [189, 190].

SWNT sensors decorated with ZnO nanoparticles synthesized at a higher temperature (70°C) displayed a drastic enhancement in sensitivity, a faster response/recovery time as well as a decrease in detection limit towards H_2S, figure 2.9. The sensitivity increased to 4.96 $\Delta R/R_o$ per ppm of H_2S and a response to 500 ppb H_2S of ~80 % $\Delta R/R_o$ compared to 12% ΔR/Ro for the polycrystalline ZnO particles. This difference is indicative of a significant increase in the lower detection limit, very likely the double digit ppb range, suggesting promise as a low cost, room temperature H_2S sensor. The enhancement is a consequence of the highly crystalline ZnO phase and grain refinement. The reduced defects allow for greater numbers of electrons to be trapped in surface states of the particle by adsorbed oxygen ions, reducing the charge density of the particle. This charge carrier drop is hypothesized to create a low resistance state in the SWNT as the gating effect at the ZnO-SWNT interface is reduced. During H_2S exposure, the ZnO nanoparticle is reduced by displacement of the adsorbed oxygen ions increasing the charge density and space charge region induced in the SWNT, ultimately decreasing hole mobility transport through the SWNT.

Sensing mechanism of H_2S on ZnO/SWNT networks was investigated by using a ChemFET configuration, with an applied back gate. Typical FET transfer characteristic are the sensors are shown in figure 2.10, there is only a slight gate dependency on the current behavior of the sensors after exposure to the carrier gas and different concentrations of H_2S and sensors show no clear on-off state. The drain source voltage drops with higher concentrations of H_2S, more significantly for ZnO functionalized sensors than the bare SWNTs at similar resistance range, consistent with the chemiresistive sensor response.

2.4 Conclusions

Synthesis and material characterization of ZnO/SWNT hybrid structures is performed by a facile electrochemical route, with precise control over particle formation, size and density. Gas sensing performance of the ZnO/SWNT hybrid structures was investigated and exhibited uncharacteristic selectivity towards H_2S, with enhanced sensitivity, response and recovery times contingent upon crystallinity. Optimal sensors show a sensitivity increase from 2.54 % per ppm to 4.96% per ppm by tailoring the ZnO deposition temperature with a ~80% response at 500 ppb. These ZnO/SWNT hybrid gas sensor demostrate a clear structure-property realationship indicating material crystalinity has a large impact on metal oxide/SWNT hybrid sensor performance.

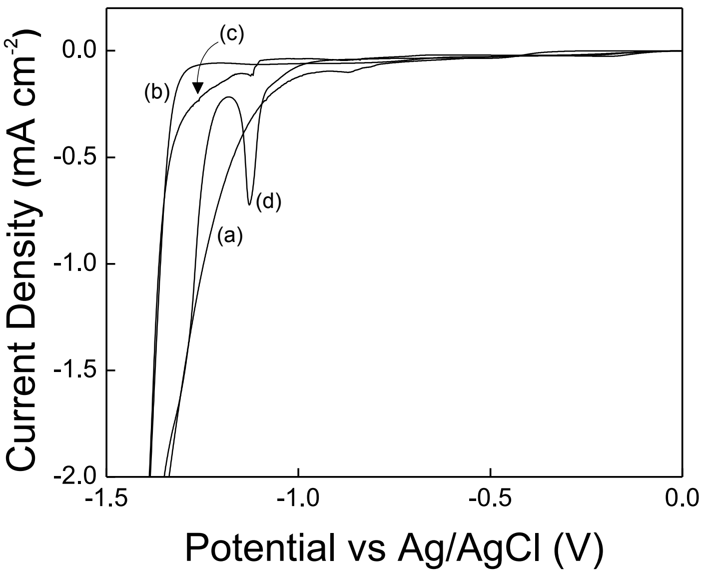

Figure 2.1. Linear sweep voltammetry of electrolytes at for SWNT thin film from open circuit potential to -2.0V vs Ag/AgCl at 10mV/s in electrolytes of (a) 0.0 M Zn(NO3)2 + 0.2 M NaNO3, (b) 0.02 M Zn(NO3)2 + 0.16 M NaNO3, (c) 0.05 M Zn(NO3)2 + 0.1 M NaNO3, (d) 0.1 M Zn(NO3)2 + 0.0 M NaNO3. All electrolytes are at 25°C and pH of 5.5.

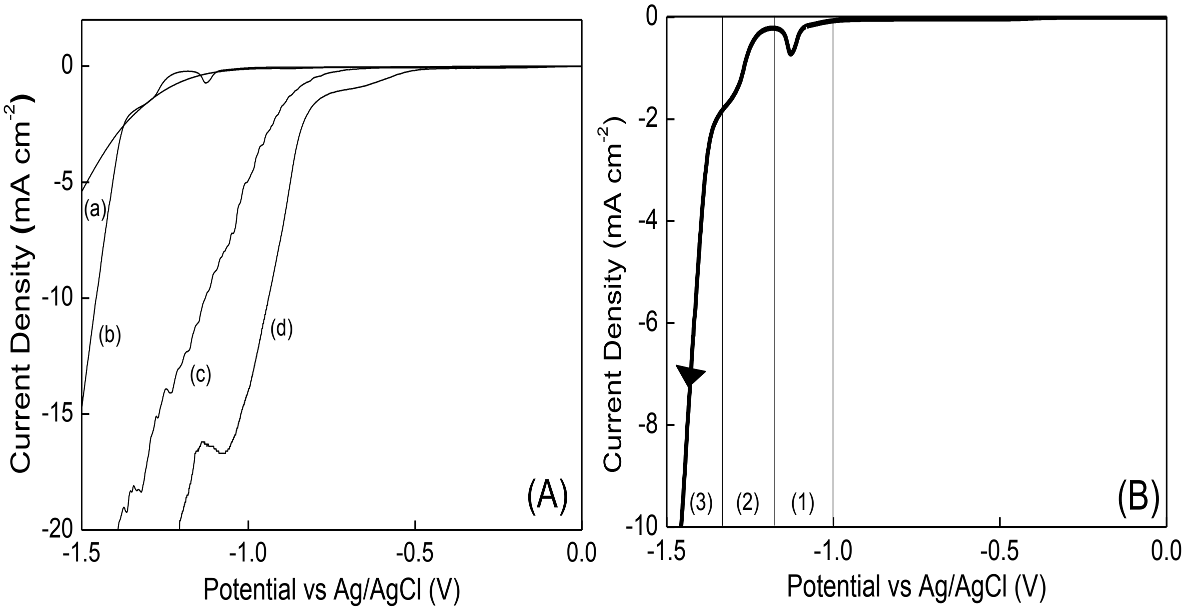

Figure 2.2. (A) Linear sweep voltammetry of (a) 0.0 M $Zn(NO_3)_2$ + 0.2 M $NaNO_3$ at 25^0C, (b) 0.1 M $Zn(NO_3)_2$ + 0.0 M $NaNO_3$ at 25^0C, (c) 0.0 M $Zn(NO_3)_2$ + 0.2 M $NaNO_3$ at 70^0C, (d) 0.1 M $Zn(NO_3)_2$ + 0.0 M $NaNO_3$ at70°C and (B) detailed LSV of 0.1 M $Zn(NO_3)_2$ at 25°C; all electrolytes were at pH 5.5. SWNT thin film substrates were swept from open circuit potential to -2.0V vs Ag/AgCl at 10mV/s.

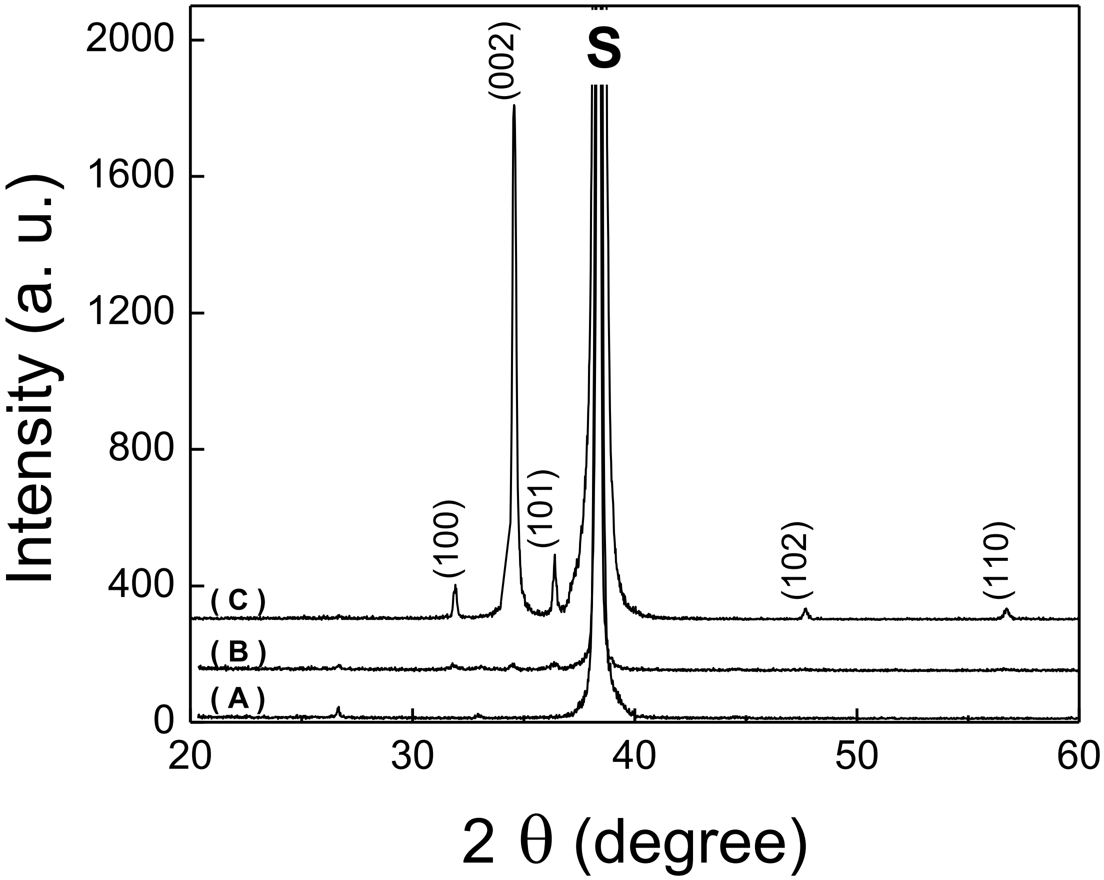

Figure 2.3. XRD diffraction pattern of (A) randomly oriented SWNTs, (B) as-synthesized ZnO thin film deposited at -0.6 volts and 25 °C and (C) ZnO thin film deposited at -0.6 volts 70 °C. ZnO crystal orientations are labeled and the substrate is indicated by “S”. Films were deposited from solution 0.1 M $Zn(NO_3)_2$, and pH 5.5.

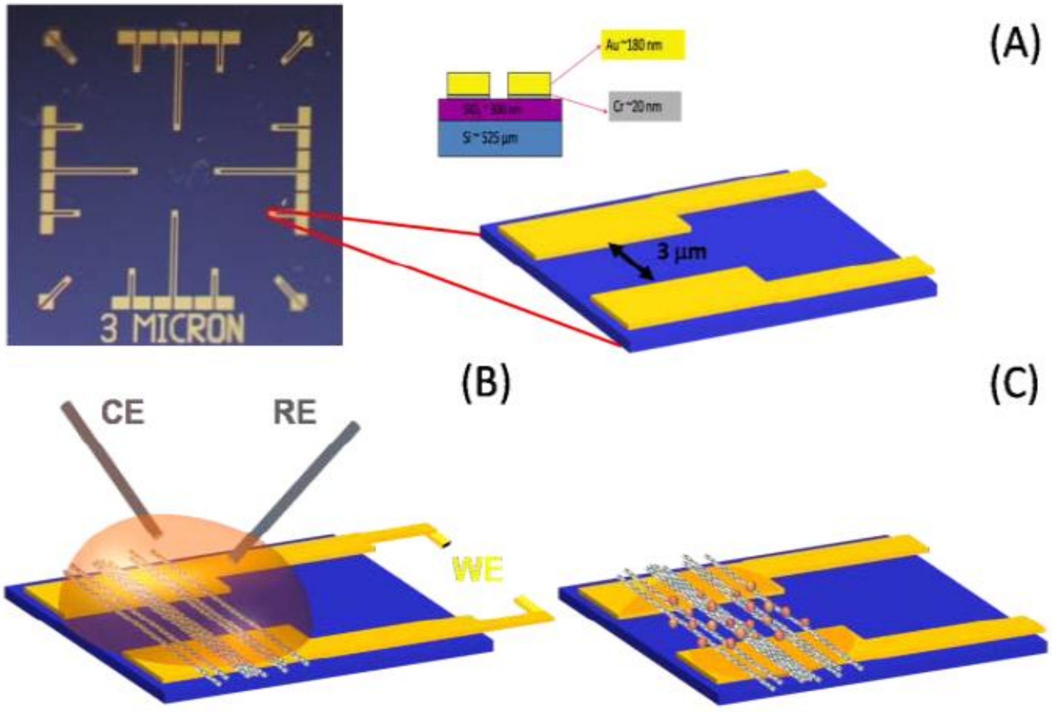

Figure 2.4. (A) Image of chip containing 16 prefabricated microelectrode pairs and cartoon representation of single electrode pair. The Cr/Au electrodes are 20/180 nm tall, deposited on Si/SiO$_2$ of 525/0.3 µm. (B) The electrochemical set up for ZnO functionalization consists of a 3µL 0.1 M Zn(NO$_3$)$_2$ droplet on a single electrode pair with aligned SWNTs as a working electrode (WE). A Pt wire counter electrode (CE) and Ag/AgCl wire pseudo reference electrode (RE) are submerged in the droplet to complete the cell. The completed ZnO functionalized SWNT hybrid network is depicted in (C).

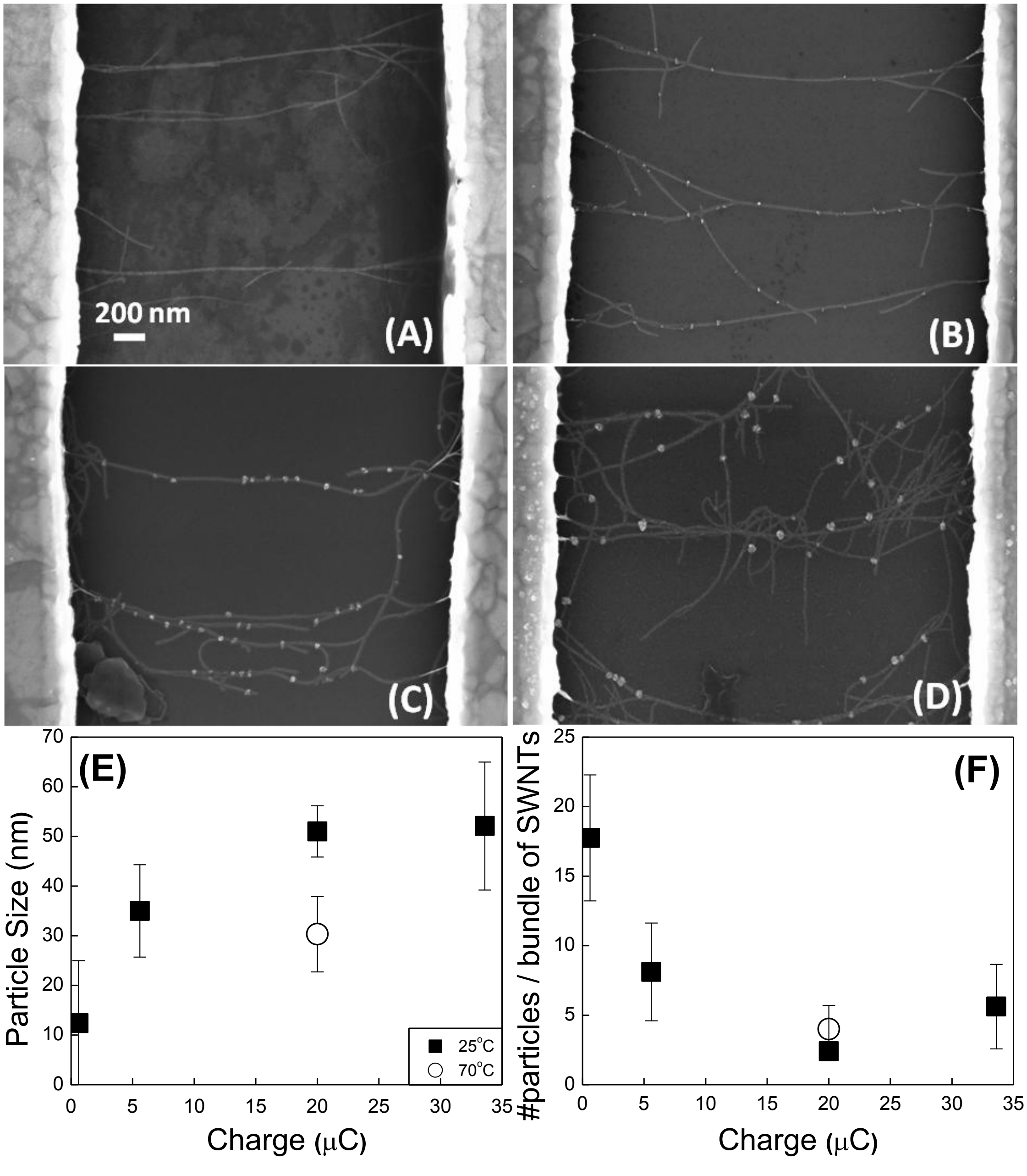

Figure 2.5. SEM images of aligned SWNT networks (A) unmodified and (B-D) functionalized with ZnO by electrodeposited at -1.1V vs Ag/AgCl and 25°C for applied charges of (B) -0.614, (C) -5.58 and (D) -33.6 μC. (E) The average particle size and (F) number of ZnO particles per bundle of SWNT is shown as a function of applied charge. The size and number distribution are represented by the error bars in (E-F). The error bars represent a set of 10.

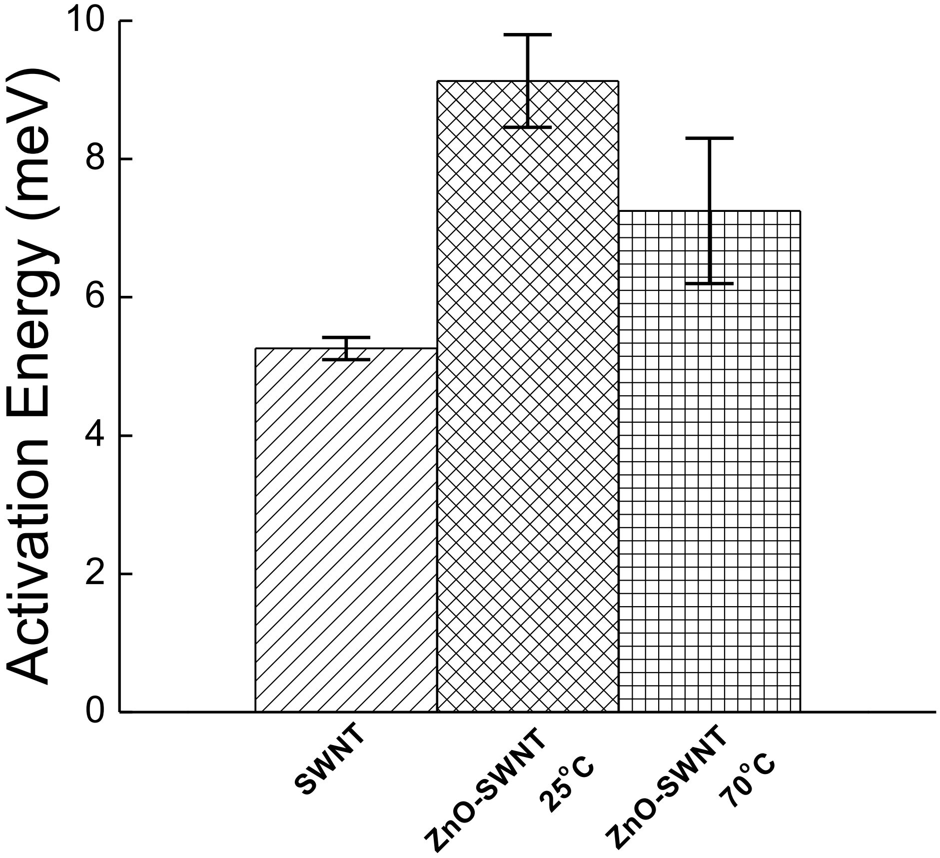

Figure 2.6. Activation energy determined from temperature dependent resistance behavior of bare SWNTs and ZnO-SWNTs functionalized at 25^{0}C and at 70^{0}C.

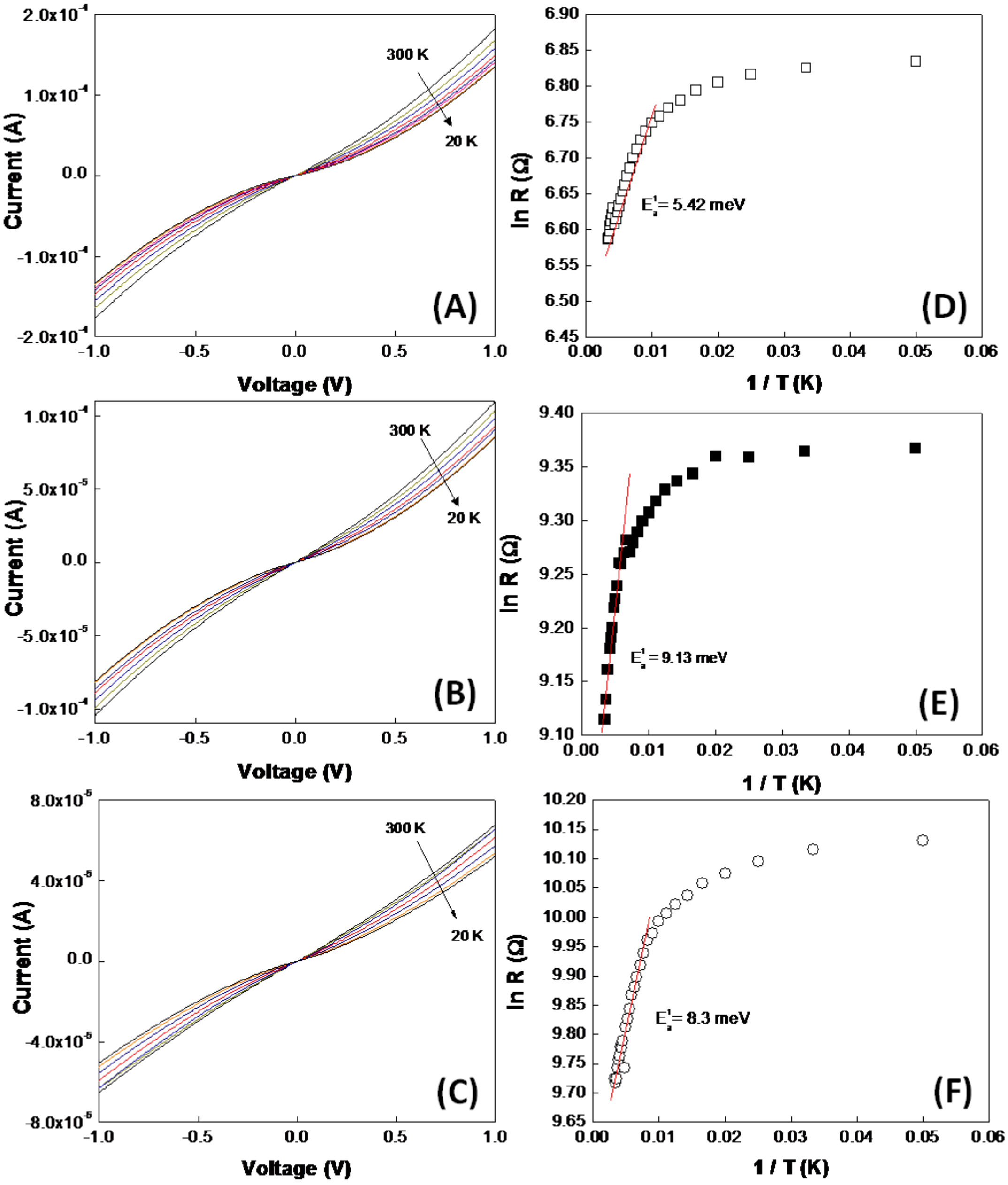

Figure 2.6.B. Typical temperature dependent resistance behavior of (A) & (D) aligned bare SWNTs, (B) & (E) ZnO/SWCNT at 20 μC and 20°C, (C) & (F) ZnO/SWNT at 20 μC and 70°C.

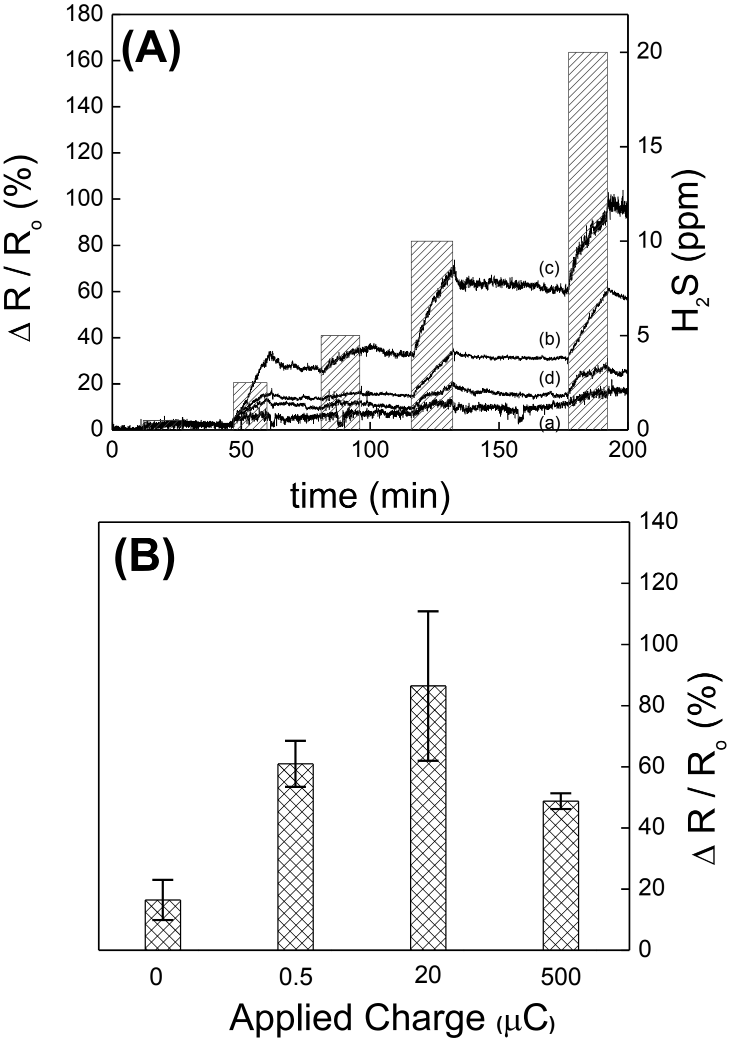

Figure 2.7. Sensor optimization (A) real time sensing behavior of (a) bare SWNTs, (b) ZnO-SWNT at 0.5 μC, (c) ZnO-SWNT at 20 μC, (d) ZnO-SWNT at 500 μC towards various exposures H_2S, (B) histogram of average sensor response towards 20 ppm of H_2S. All samples were synthesized at 25^{0}C.

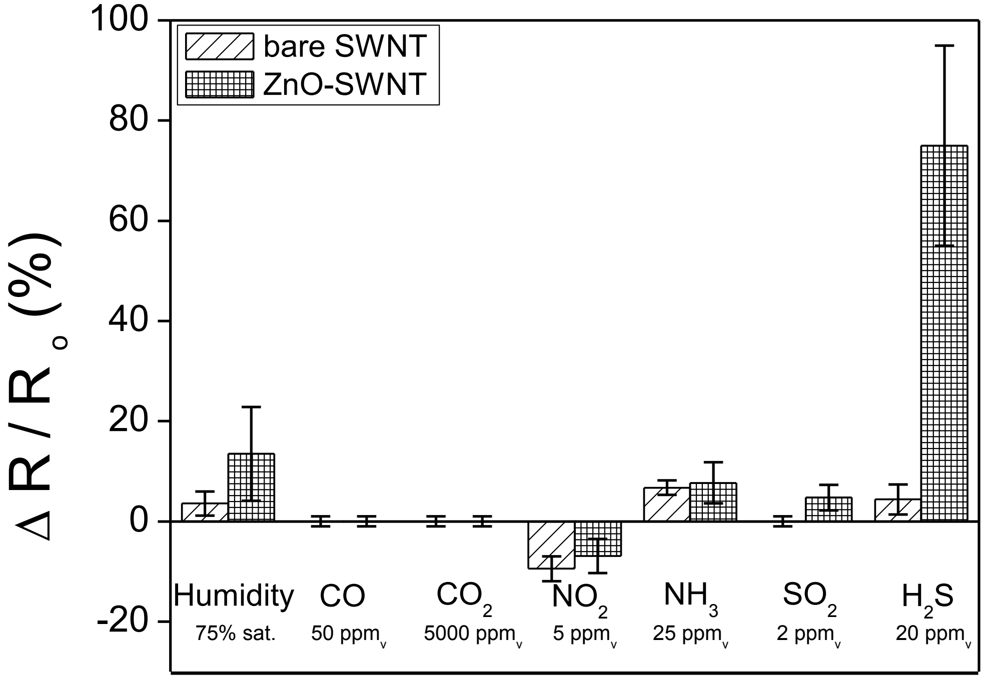

Figure 2.8. Mean response and standard deviations for bare SWNT and the ZnO/SWNT hybrid system to several light molecular weight molecules. The concentrations were determined by exposure limits set by OSHA. Standard deviations were taken from ten samples. The ZnO/SWNT hybrid system was synthesized at 25^0C and 20μC.

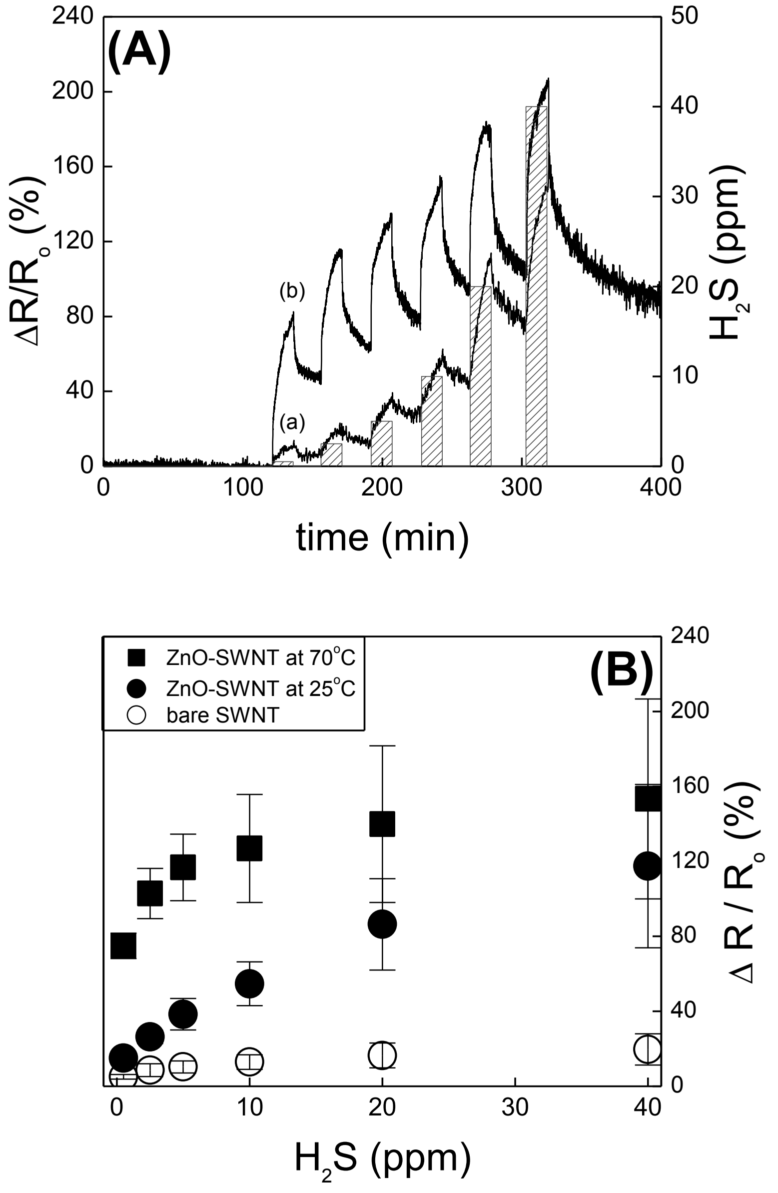

Figure 2.9. (A) Typical transient sensing response of ZnO-SWNT functionalized at 20 μC at (a)25^{0}C, (b) 70^{o}C. The normalized responses are all scaled to the left axis and the concentration level of the exposure profiles are indicated on the right axis. (B) Sensitivity of SWNT and ZnO-SWNTs systems towards H_2S. All ZnO/SWNT hybrid sensors are synthesized at 20 μC.

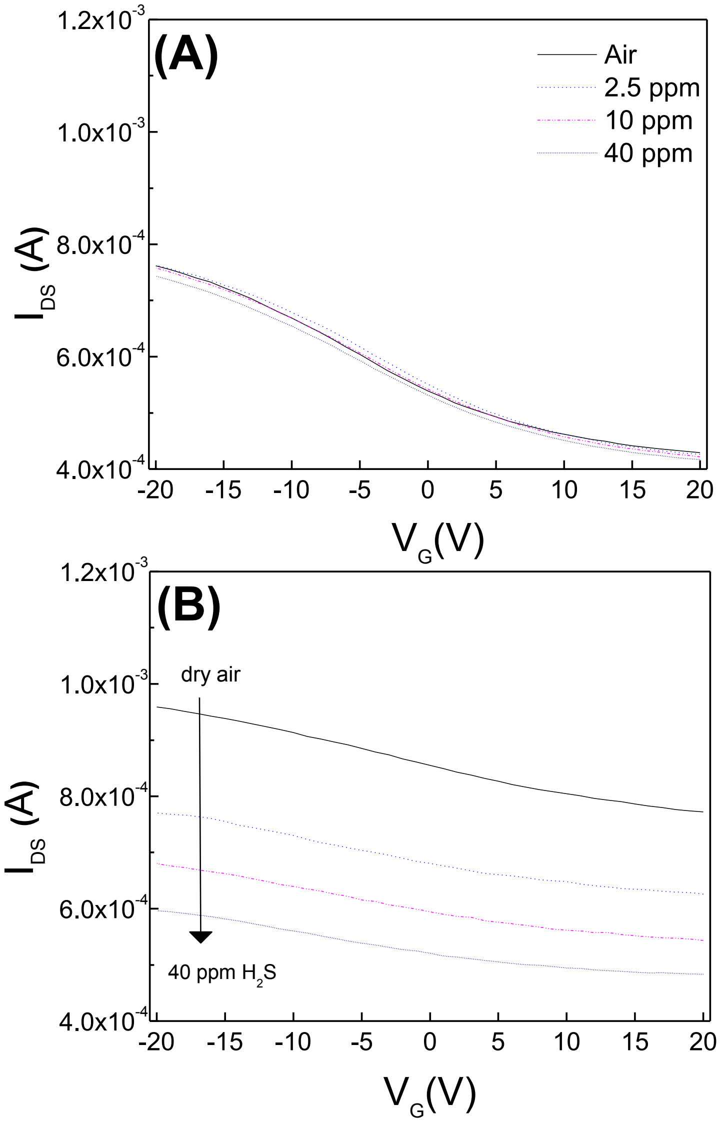

Figure 2.10. Back-gated FET I-V_G sensing responses to dry air, 0.5 ppm, 2.5 ppm, 5 ppm, 10 ppm, 20 ppm, and 40 ppm H_2S for V_{DS} = 1 V. (A) The bare SWNT network shows little sensitivity by comparison to the (B) ZnO decorated SWNT network. The ZnO/SWNT hybrid sensors is synthesized at 20 μC and 70^{0}C.

CHAPTER 3:

RECOGNITION OF XYLENE ISOMERS USING ZnO-SWNT HYBRID STRUCTURES

Abstract

In this work the sensing performance of ZnO-SWNTs hybrid structures was investigated. The devices consisted of ZnO nanoparticles electrodeposited on the surface of SWNT networks, and were challenged with a host of potential VOC biomarkers including benzene derivatives, ketones, alcohols, and alkanes. Conductometric responses for a range of gaseous analytes were established with room temperature operation, including the detection and distinction of xylene isomers (*ortho, para*, *meta*). The enhanced sensitivity towards *p*-xylene is the first demonstration of isomer selective gas sensing with a metal oxide based system. Further mechanistic investigation of the sensor behavior was performed by field effect chemiresistive measurements.

3.1 Introduction

Alveolar breath analysis of human patients has revealed the presence of alkanes, benzene derivatives, alcohols and keytones, whose presence and concentrations have been correlated to a host of diseases and physiological conditions such as asthma, diabetes, periodontal disease, as well as lung and breast cancer [191-196]. Volatile organic compound (VOC) breath signatures are consequently promising biomarkers for a non-invasive approach to earlier medical diagnostics in addition to a complementary method for current medical testing [197]. However, to avoid misdiagnosis, high specificity of a single biomarker is desirable and at the same time challenging due to the difficulty in differentiating structurally similar compounds. Specifically, the ability to distinguish between a single isomer of xylene could mean a difference in diagnosis between asthma, with high levels of *p*-xylene, versus lung cancer, which has been correlated to *o*-xylene [192, 193, 198, 199]. Although, gas chromatography-mass spectrometry (GC-MS) can be used to accurately detect and quantify isomeric VOCs in breath samples, a more rapid detection system based on a simple, cost effective, portable design is desirable for standardized screening tools.

One dimensional nanostructures are strong candidates for such a platform as the diminutive sizes of these materials have demonstrated enhanced sensor performance, including previously demonstrated utility for medical diagnosis, differentiating simulated gas mixtures of lung cancer patients from healthy subjects [150, 193, 200-210]. From a structure standpoint, SWNTs can be considered ideal nanosensor materials as they are composed entirely of surface atoms. Unfortunately, unmodified SWNT are quite stable, displaying limited interaction in most chemical environments. Nevertheless, they are promising nanomaterials as the transducing elements for gas sensors due to their exceptional electronic properties, mechanical rigor, and thermal stability. Moreover, their small sizes make them ideal conduits for interfacing arrays of nanoparticles, entities that maximize quantum confinement effects with characteristic lengths well below the Debye length. Prior work has shown that the sensitivity and selectivity towards certain analytes can be enhanced when the carbon nanotubes are covalently or non-covalently functionalized with desirable materials, especially metals and polymers [147, 149, 160, 161, 211-215].

On the other hand, SWNT gas sensors with integrated metal oxide materials have been limited, despite the well established stability, longevity, and library of metal oxide gas sensors. In particular, ZnO has gained favor as a nanosensor due to its low cost, ease of synthesis and sensitivity to some VOCs. Nanostructures of this n-type semiconductor (band gap of 3.35eV) have also been explored for room temperature gas sensing significantly reducing power consumption [185, 216]. Thus, the incorporation of zinc oxide nanoparticles on the periphery of carbon nanotubes offers the advantages of nanoengineering with a robust, marketable metal oxide [143-150]. Although several groups have studied the sensing performance of ZnO nanowires, to date, the performance of ZnO decorated SWNTs have not been scrutinized.

In this work the gas sensing performance of electrodeposited ZnO-SWNTs hybrid structures, consisting of ZnO nanoparticles on the surface of SWNTs, towards a pool of potential VOC biomarkers, including benzene derivatives, alcohols, ketones, and hydrocarbons, was investigated. Bare SWNT networks were similarly challenged with

VOCs to determine the effect of ZnO functionalization on sensor behavior. Chemiresistive responses revealed sensor cognizance of xylene isomers (*ortho, para, meta*), with strong selectivity towards p-xylene, displaying significant utility for advanced sensor systems such as electronic noses. Field effect transistor measurements were implemented to provide insight on the mechanism of isomer selectivity. To the best of our knowledge, this is the first demonstration of xylene isomer recognition with a simple metal oxide based chemiresistor [213].

3.2 Experimental Details

3.2.1 Synthesis and Characterization

Sensor arrays were prepared on dies containing sixteen lithographically fabricated Au microelectrode pairs with 3 μm gaps. The substrate architecture allowed for individual addressability and sensor assembly/synthesis without cross contamination between adjacent devices, the details of which have been described elsewhere [160]. Commercially available carboxylated single walled carbon nanotubes (SWNTs) were obtained from Carbon Solutions Inc. and dispersed in dimethylformamide (DMF). SWNTs were aligned across the electrode gaps via alternating current dielectrophoretic alignment by placement of a 1.5 μL drop of SWNT suspension across the electrodes, applying 1 V_{pp} and 4 MHz (Keithley 3390 AC generator, 50 MHz arbitrary waveform generator), and the device resistance was monitored by administering the alignment time. Following SWNT alignment, the sensors were rinsed with DI water twice to remove residual DMF and annealed at 300°C for 60 minutes under reducing environment (5% H_2 / 95% N_2) to reduce contact resistance.

A solution based electrochemical synthesis approach was used for the deposition of ZnO on SWNTs due to its operational simplicity and flexibility of process parameters. Electrochemical functionalization of the SWNT network was performed by addition of a 2 μL drop of 0.1 M $Zn(NO_3)_2$ electrolyte at pH of 5.5, using the gold pads as the working electrode, an inserted Pt wire as the counter electrode and a pseudo Ag/AgCl wire as the reference electrode. The deposition potential was kept constant at -0.6 volts versus pseudo Ag/AgCl reference electrode, and the applied charge was varied from 0 to 500 μC, optimized sensors were synthesized at 20 μC. Electrodeposition was carried out under potentiostatic mode at 25°C, and ambient pressure using CH Instruments Electrochemical Analyzer CHI604c. Following the deposition, sensors were lightly rinsed with DI water by placing a 10 μL drop over the deposited area and removal with N_2 gas. Verification of ZnO nanoparticle decoration on the surface of SWNTs was verified by scanning electron microscopy (SEM).

3.2.2 FET and Gas Sensing Studies

Room temperature gas sensing studies were performed on the functionalized sensor array by integration of the sensor chip with a pin IC adapter via wire bonding (West Bond Inc. Model 7443A) and subsequent electrical connection to a bread board in a custom made sensing system [161]. Each sensor was subjected to 1.0 V (DC) and the resistance was continuously recorded every 0.2 seconds simultaneously for the sixteen sensors by use of Keithley 236 source measurement unit controlled by a LabView program. A base line was achieved by continuous exposure to dry air and the various analytes were introduced by bubbling through high purity chemical grade liquid forms of the desired analyte with the carrier gas. Analyte concentrations were attained by subsequent dilutions with the carrier gas, flow rates were regulated by mass flow controllers (Alicat Scientific Incorporated) and total gas flow rate was kept constant at 200 sccm for all experiments [161, 171]. A field effect configuration was used with the current sensing set-up by applying a back gate potential sweep from -20 to 20 volts with 1 volt increments under the presence of the desired analytes and carrier gas.

3.3 Results and Discussion

3.3.1 Sensor Characterization

Figure 3.1 shows a schematic representation of the fabricated ZnO-SWNT hybrid sensor, in which SWNTs were first AC aligned across the 3μm gap of a gold electrode pair and then electrochemically functionalized with ZnO. A typical SEM micrograph shows that the resulting hybrid structures are nanoparticle surface decorated SWNTs with average particle size of 51.0 ± 5.16 nm and average particle density of 5.4 ± 0.5, where particle density is defined as number of particles per bundle of SWNTs and determined from 5 different sensors. The energy dispersive X-ray spectrum of the corresponding SEM image identifies the main elemental components to be ZnO, SiO_2 and Au where the latter two constitute the silicone chip and gold electrode pads. The resulting optimized charge for the sensor was determined from exposure to 75 % saturated vapor of methanol to sensors synthesized at charges varying from 0.5 to 500 μC. From which it was observed that the maximum sensor response was obtained from sensors synthesized at 20 μC, the average sensor response was determined from n=10 sensors (included in supplemental information).

Room temperature sensing performance of the SWNTs and ZnO-SWNT hybrid structures was investigated towards saturated vapors of water/humidity, BETX compounds (benzene, ethyl-benzene, toluene, xylenes), alcohols (methanol, ethanol isopropanol), ketones (acetone, methylethylketone), cyclohexane, n-hexane, n-octane and dichloromethane at exposure percent saturations ($p/p^{*} \times 100$) of 2.5, 5, 10, 20, 50, 75, and 100. Xylene encompasses *ortho*-, *meta*-, and *para*- isomers of dimethyl benzene (denoted by *o*-, *m*- and *p*-) and signify to which carbon atoms on the benzene ring the two methyl groups are attached to. The *o*- isomer has the IUPAC name of 1,2-dimethylbenzene, the *m*- isomer has the IUPAC name of 1,3-dimethylbenzene, and the *p*-isomer has the IUPAC name of 1,4-dimethylbenzene. Based on prior work within our group, sensor devices of both the SWNTs and hybrid structures were chosen to fall within a resistance range of 10-100 kΩ to maximize sensor response while minimizing the signal noise [160, 215]. Typical sensing responses towards structural isomers of xylene are shown in figure 3.2, with responses of the bare SWNTs depicted in figure 3.2 (A), (D), (G) and responses from ZnO-SWNT hybrid system depicted in (B), (E), and (H) towards *o*-xylene, *m*-xylene and *p*-xylene, respectively. Sensor response is determined by the resistance change and is defined as $100*(R_f-R_o)/R_o$; where R_f is final resistance at 95% of the peak height and R_o is initial resistance from the base line before any exposures. There was a slight change in device resistance of the bare SWNTs network in the presence of xylene isomers, where *p*-xylene had the most notable effect causing a resistance change of 9.6% when exposed to 75% saturated vapor (~30,000 ppm), shown in figure 3.2 G. While *o*- and *m*- isomers had a clear sensor response, the resistance change was less than 2.5% when exposed to 75% saturated vapors (~23,500 and ~29,300 ppm, respectively) figures 3.2 D and G. The ZnO-SWNT hybrid sensors had a stronger and distinct detection towards xylene isomers compared to the bare SWNTs. Most notably is the response of ZnO-SWNT hybrid structures towards *p*-xylene responding with 116.5% resistance increase towards 75% saturated vapor, an order of magnitude increase in sensor response from bare SWNTs (figure 3.2 H). ZnO-SWNT had a decrease in resistance of -6.3% at 75% of saturated vapor in the presence of *o*-xylene, however the hybrid sensors did not begin to respond until exposure to 75% saturation of the *o*- isomer. This change in conductance direction is believed to be contributed by the presence of ZnO nanoparticles since the same behavior was not observed in the bare SWNT sensors. In the presence of *m*-xylene the ZnO-SWNT hybrid structures had an increase in resistance change of 9.8 % at 75% saturated vapor, an enhancement compared to the SWNT response (figure 3.2 E). The corresponding calibration curves depict the overall sensor performance at the various exposed percent saturations and illustrates that the combination of ZnO-SWNT hybrid system increases the overall sensor response and change in resistance cognizance of xylene isomers (figure 3.2 C,F,I).

Sensor performance of the SWNTs and ZnO-SWNT hybrid structures towards 75% saturated vapor of water, BETX compounds, alcohols, ketones, alkanes and other hydrocarbon compounds are summarized in figure 3.3. Based on the response of the bare SWNT and ZnO-SWNT sensors towards the analyzed VOCs, it is evident that the sensitivity is introduced by incorporation of ZnO in the hybrid structures, more notably towards benzene derivatives [BETX group]. Within the benzene and benzene derivatives that were analyzed it was observed that ZnO-SWNTs structures had little detection towards benzene however additional methyl groups on the benzene ring increased the sensor activity. In addition it was observed that the sensitivity of the ZnO-SWNT hybrid structures was strongly dependent on the number of methyl side groups and can be summarized as benzene (C_6H_6) $\leq$ toluene (C_7H_8) < ethyl-benzene (C_8H_8) < xylene (C_8H_{10}). To better understand the discriminating sensor response of ZnO-SWNT hybrid structures towards p-xylene, the effect of polarity, chain length and compound shape were investigated.

The effect of polarity on sensing response cyclohexane was examined as a non-polar analyte and the sensing response was compared to benzene. Polarity is observed to play a small role in sensor detection for both bare SWNTs and ZnO-SWNT hybrid structure showing a response of ~3.3% for bare SWNT and ~3.97% $\Delta R/R_o$ for ZnO-SWNT under exposure of 75% saturated vapor of benzene and no response under exposure to cyclohexane. The effect of chain length, without contribution of an induced dipole, was explored by analysis of hexane (C_6H_{14}) and octane (C_8H_{18}) compounds. SWNT sensors had no response for either compounds while ZnO-SWNT hybrid sensors responded with -4.7% $\Delta R/R_o$ towards hexane and 19.5% $\Delta R/R_o$ for octane, indicating that longer chain length also influences the sensor behavior of the hybrid structures. Shape, on the other hand, has little effect on the sensing performance of ZnO-SWNTs as evident from the sensing behavior of cyclohexane compared to hexane. Based on the alcohol compounds that were analyzed, a decrease in hybrid sensor response from 22.7% to 4.7% $\Delta R/R_o$ was observed as the carbon chain increased from one carbon to three. Although the ZnO-SWNT sensors were more sensitive than bare SWNTs towards alcohols, the general trend of the hybrid sensor sensitivity was methanol (CH_3OH) > ethanol (C_2H_5OH) > isopropanol (C_3H_7OH), suggesting that ZnO-SWNTs hybrid structures may have a stronger chemical activity towards methyl groups over carbon chain length.

3.2.2 FET Studies

To further investigate the sensing mechanism of the xylene isomers towards bare SWNTs and ZnO-SWNT hybrid structures, a field effect configuration was adopted with an applied back gate. Typical FET transfer characteristics of the sensors under exposure to dry air and to *o*-, *m*- and *p*- xylene isomers at 10, 50 and 75% saturated vapors are shown in figure 3.4. The bare SWNT sensors demonstrated p-type behavior as expected with no clear on-off state and no gate dependency sensing current with only a slight change in I_{DS} when exposed to increasing xylene isomer concentrations (figure 3.4 A, C and E), which is consistent with the transient chemiresistive responses. The FET behavior of the ZnO-SWNT hybrid structures was characteristic to the specific xylene isomer that was tested. When exposed to dry air, the ZnO-SWNTs structures demonstrated an “on” state at gate voltages more negative than -5 V, as seen in figure 3.4 B, D, and F. Under exposure to *o*-xylene, the ZnO hybrid structures showed an increase in drain source current at higher concentrations of the isomer, with a more pronounced change at more negative gate voltages. The overall responses to all three xylene analytes is consistent with a gating or mobility mechanism, with the most notable transconductance change occurring with increasing *p*-xylene concentrations.

Despite the chemical diversity in the analytes probed and the FET results, the high selectivity for p-xylene is still difficult to reconcile. It is hypothesized that the enhanced transduction of *p*-xylene arises from a reduced dipole moment and increased displacement of adsorbed oxygen on the metal oxide nanoparticles. Since *p*-xylene is a symmetrical molecule it has no dipole moment, whereas *m*-xylene and *o*-xylene have dipole moments of 0.30 and 0.62 D, respectively, due to their structural configurations [217]. The dipole moment is believed to partially compensate for some of the free electrons generated by the displaced oxygen on the ZnO nanoparticle surface, which is further offset by an induce dipole moment or polarizability, resulting in a small overall resistance change for the *m*- and *o*- isomers. Additionally, the monolayer adsorption isotherms of these two xylene isomers on ZnO have been shown to be nearly half that of *p*-xylene. The difference in coverage has been attributed to repulsive forces introduced by the dipole moments when these molecules are oriented in the same direction and steric hindrance from the larger cross section [218]. Therefore, the large *p*-xylene response can be rationalized by the higher adsorption isotherm for *p*-xylene, and the lack of dipole moment and very low polarizability. The collective result of which displaces extra adsorbed oxygen with mitigated charge compensation, liberating more electrons into the ZnO nanoparticle bulk. The increased electron density creates a stronger depletion layer for an augmented gating effect that directly reduces hole transport and conductivity through the SWNTs.

3.4 Conclusions

In summary, we have developed a hybrid ZnO-SWNT based sensor capable of distinguishing between different xylene isomers. This sensor shows high selectively towards the *p*-xylene isomer and demonstrates the capability of discriminating structurally similar chemical compounds. Furthermore this investigation provides useful insight into the interaction of VOCs and ZnO based nano gas sensors, demonstrating promising applications for detection of volatile organic biomarkers for early medical diagnostics. The effectiveness of electrochemically synthesized ZnO-SWNTs hybrid sensors demonstrates the ability to fabricate stable and selective nano-gas sensors in a facile and cost effective route, a process that can be extended to other metal oxide materials.

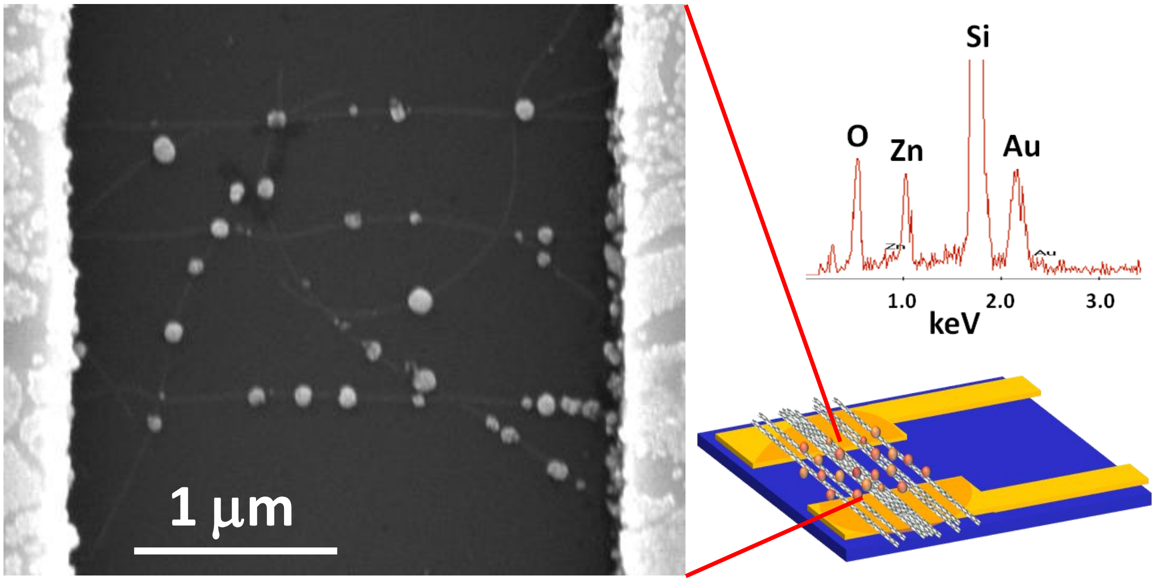

Figure 3.1. Schematic view of the ZnO-SWNT hybrid sensor containing aligned SWNTs across two gold electrodes with ZnO nanoparticles on the periphery of the SWNTs. SEM image depicting a typical sensor and corresponding EDAX graph showing the presence of ZnO.

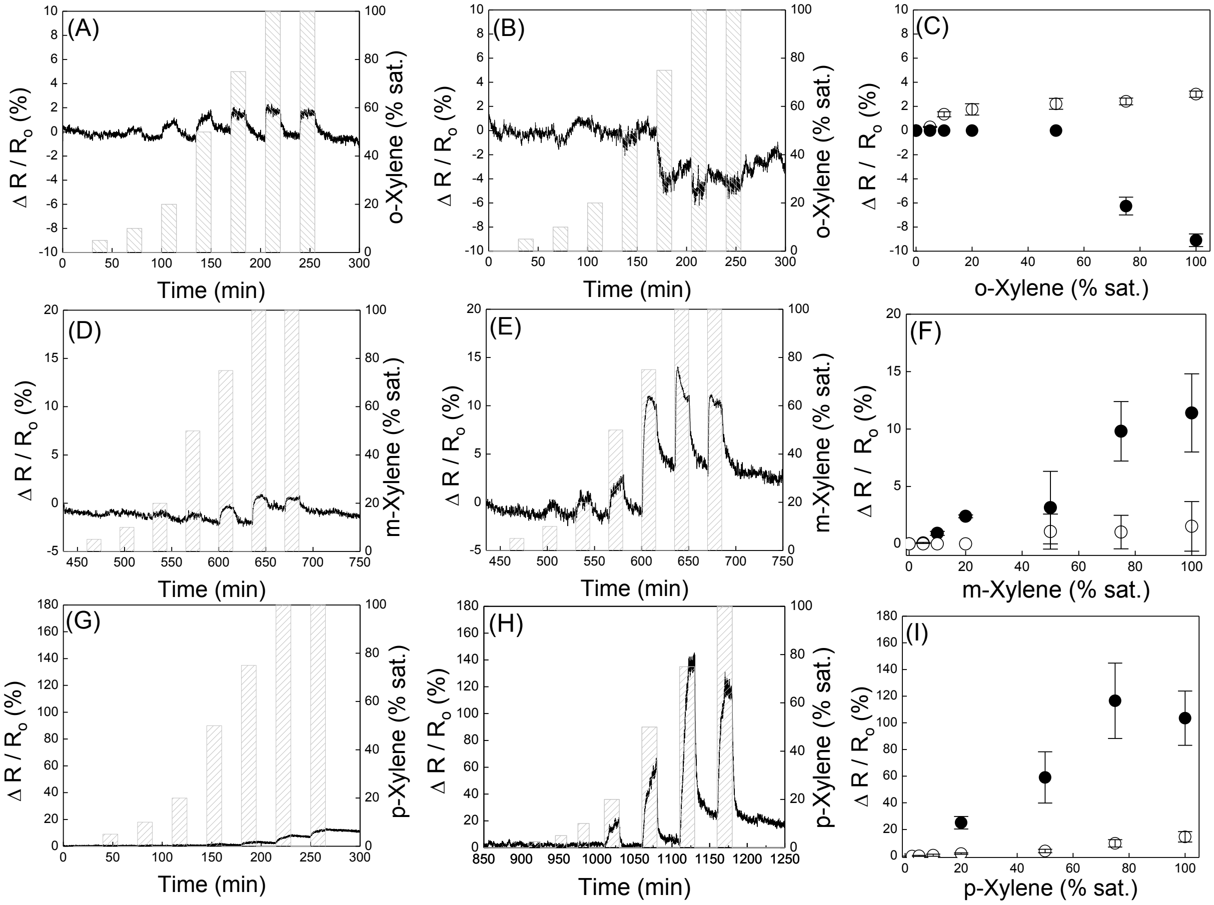

Figure 3.2. Typical real time responses of bare and ZnO/SWCNT systems towards o-xylene (A and B), m-xylene (D and E), p-xylene (G and H) and the corresponding calibration curves (C,F, and I). Open circles correspond to bare SWNTs and solid circles represent ZnO-SWNT hybrid system, error bars are determined form n=6 sensors.

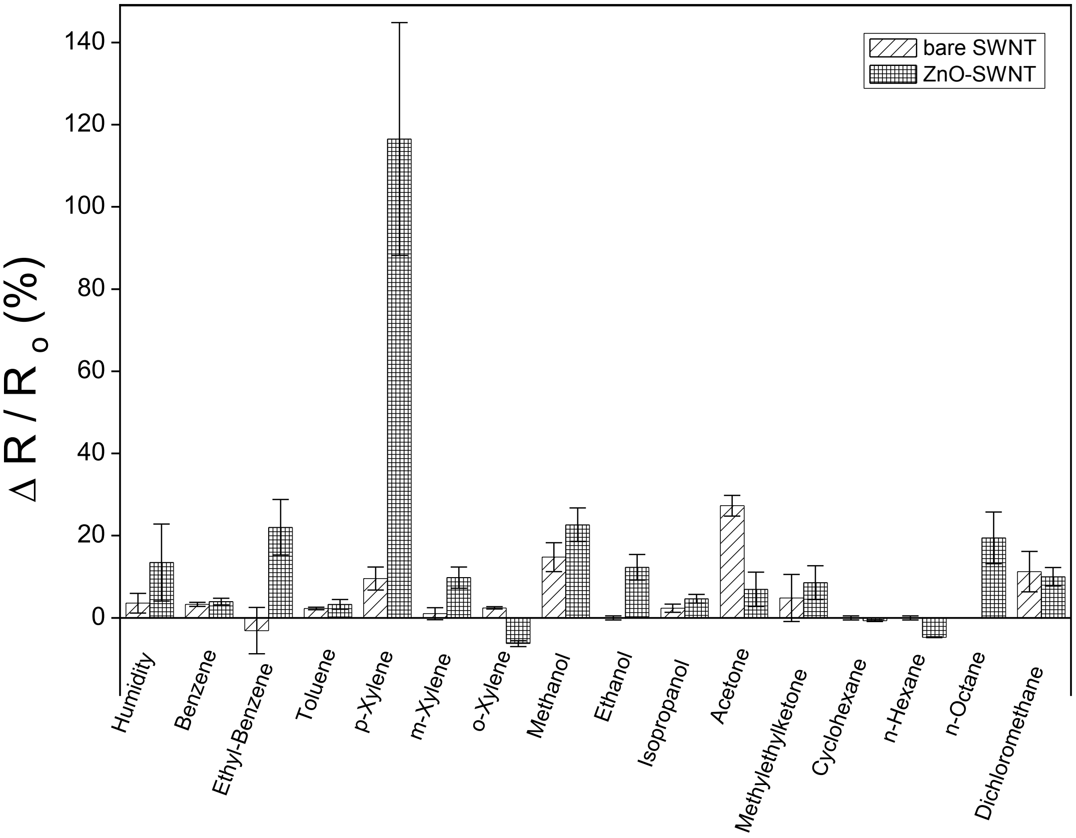

Figure 3.3. Response of bare SWNT and ZnO-SWNT hybrid system towards humidity, BETX, alcohol, ketone, and hydrocarbon compounds. Average responses are determined from n = 6-10 sensors.

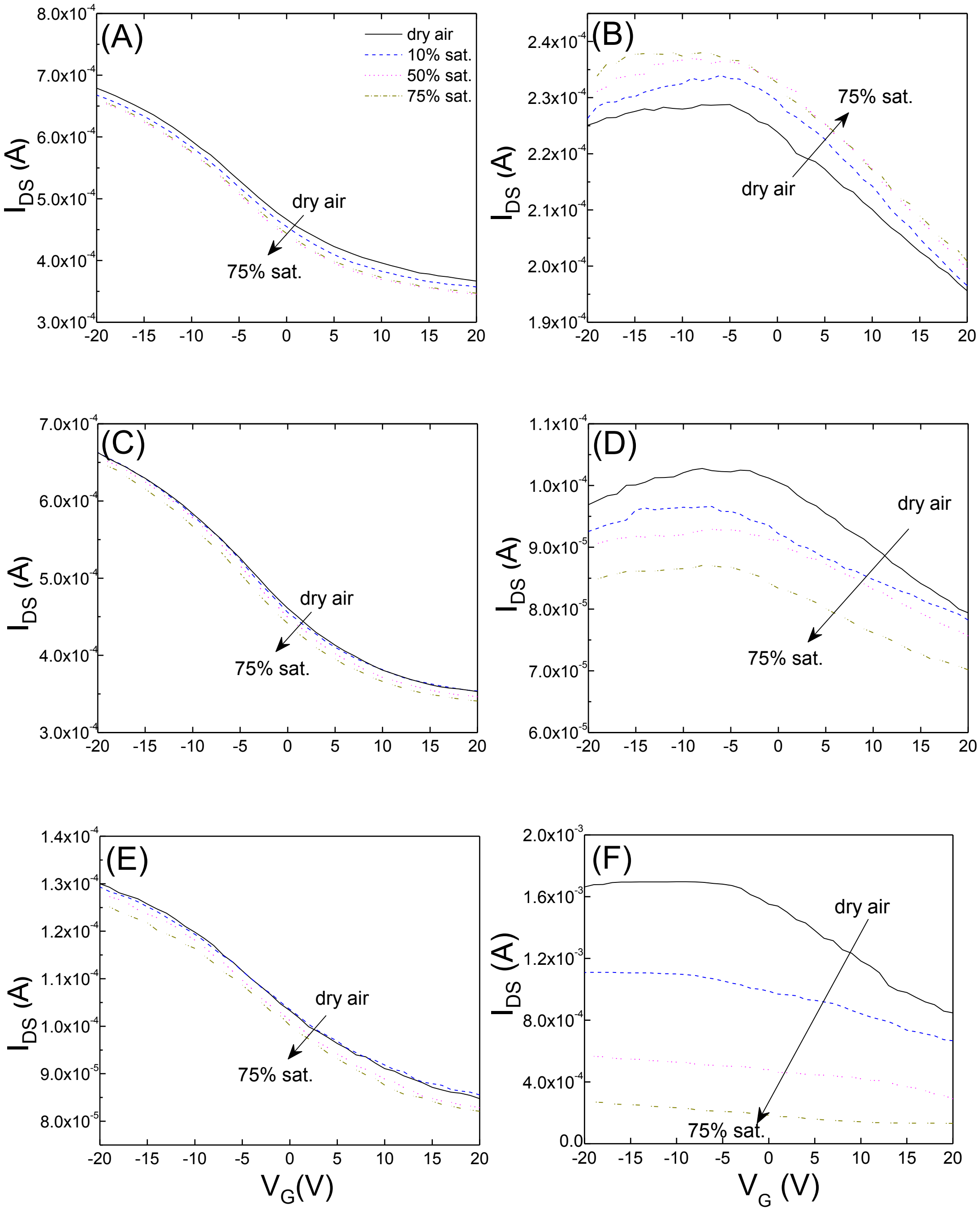

Figure 3.4. FET characterization of bare SWNTs (A, C, E) and ZnO-SWNT (B, D, F) sensors while exposed to xylene isomers. (A) and (B) towards o-xylene , (C) and (D) towards m-xylene, (E) and (F) towards p-xylene, at VDS of 1volt.

CHAPTER 4:

LIGHT INDUCED CHARGE TRANSFER IN ZnO-SWNTS HYBRID SYSTEMS

Abstract

Photocurrent responses of electrochemically synthesized ZnO-SWNT hybrid structures were demonstrated. The hybrid structures are composed of ZnO nanoparticles on the periphery of the SWNTs. The effects of particle size, particle density and material quality on photoconduction were also investigated. The photoconduction studies were performed in ambient conditions and the current behavior was monitored in the dark and under UV irradiation. Transient photocurrent responses reveal that the current change, $\Delta I/I_o$, was strongly dependent on material quality, with $\Delta I/I_o$ of 136.4±29.2% for devices synthesized at 20μC and 70°C, and less dependent on surface coverage of SWNTs, while the current of SWNTs was unaffected by the presence or absence of the UV light. The increase in conductivity indicated m-SWNTs dominated charge transport. Field effect measurements substantiate these results with flat gate sweeps and no measurable thresh-hold voltage.

4.1 Introduction

Hybrid fullerene-based organic/inorganic materials have been the focus of numerous studies for energy conversion and storage, from novel electrodes materials for batteries and fuel cells to active components of photovoltaic devices[219-221]. These efforts are largely motivated by the ideal mechanical properties, thermal stability, and chemical inertness of fullerenes, with particular focus on carbon nanotubes (CNTs) as their one-dimensional structures are excellent conduits for long range charge transfer. Moreover, CNTs are attractive as scaffolds for interfacing other nanostructures, particularly nanoparticles as they are more difficult to address, that exhibit confinement effects or size related enhanced performance. These features of CNTs may also enabling more complex optoelectronic designs such as those targeted to improve upon thin film technologies by operating in three dimensions to reduce charge recombination in particles. In the case of single wall nanotubes (SWNTs), which are comprised entirely of surface atoms, the potential for extremely high nanoparticle loadings have provoked several efforts for covalent and non-covalent attachment of nanoparticles to SWNTs. Recent work has also elucidated charge transfer mechanisms of SWNT/nanoparticle ensembles for several semiconducting materials upon illumination [222-229].

Although numerous II-VI semiconductor materials have been reported in CNT composites, ZnO has also attracted attention as a nontoxic, abundant material that can be easily synthesized and doped for tailored sensor, optoelectric, piezoelectric, magnetic and electric properties. Furthermore, the low cost, direct wide band gap (3.35eV) and large exciton binding energy (60 meV) of ZnO have roused interest in developing light emitting diodes, solar cells, and UV detectors [141]. These devices typically exploit nanostructured ZnO, including nanoparticles, nanowires, and hierarchical nanostructures [142]. The impetus for utilizing the ZnO nanostructures stems from their surface dominated behavior, augmented specific surface/interfacial area and well controlled crystallinity. For instance, the characteristic length of these nanoparticles is comparable to the Debye length resulting in surface interactions that fully penetrate the electronic structure of the particle [230]. This is important because a larger fraction of the atoms are involved in surface processes, whether it is adsorption or catalytic in nature, to enhance the overall device performance. Furthermore, the low number of defects generally observed in these nanocrystals permits longer carrier lifetimes and more efficient absorption and emission of photons, including significantly enhanced photoconductive gain in single nanowire devices [140, 231, 232].

Composite ZnO/CNT devices have consequently attracted attention as light harvesting assemblages by auspicious use of ZnO as the photosensitive constituent and CNTs as the electron acceptors [142, 233-236]. These demonstrations have identified ZnO/CNT hybrid architectures as promising components of next generation solar cells while opening a large parameter space meriting greater understanding of interfacial quality, structure-property relations and fabrication procedures. Herein we investigate the photocurrent dependence on surface coverage and semiconductor material quality by surface functionalizing single walled carbon nanotubes (SWNTs). ZnO nanoparticles were deposited on SWNT networks with a facile electrochemical technique based on a simple $Zn(NO_3)_2$ electrolyte. Charge and electrolyte temperature variation were utilized to tune ZnO nanoparticle size/density and crystallinity, respectively. This approach permitted intimate contact between the ZnO particle and SWNTs as opposed to non-covalently attachment by linker molecules. Charge transfer behavior was studied with current-voltage (I-V) scans and photocurrent transients of both bare SWNT networks and ZnO-SWNT hybrid structures in the dark and under UV illumination. These results suggest metallic SWNTs (m-SWNTs) dominated charge transport in these networks. This was further corroborated by back gated field effect transistor (FET) measurements.

4.2 Experimental

Lithographically fabricated arrays containing sixteen gold electrode pairs with 3 μm gaps were used as the substrate architecture, which permitted individual addressability of each device. The electrodes are arranged such that all sixteen devices fit within 1cm^2 area and can be subjected to the same conditions simultaneously [160]. Further details of the substrates has been described elsewhere [160]. Commercially available carboxylated single walled carbon nanotubes (SWNTs) were obtained from Carbon Solutions Inc. and dispersed in dimethylformamide (DMF). SWNTs were aligned across the electrode gaps via alternating current dielectrophoretic alignment by placement of a 1.5 μL drop of SWNT suspension across the electrodes, applying 1 V_{pp} and 4 MHz (Keithley 3390 AC generator, 50 MHz arbitrary waveform generator), and the device resistance was tuned by the alignment time [176]. Following SWNT alignment, the sensors were rinsed with DI water twice to remove residual DMF and annealed at 300°C for 60 minutes in a reducing environment (5% H_2 / 95% N_2) to lower contact resistance.

A solution based electrochemical synthesis approach was used for the deposition of ZnO on to SWNTs due to its operational simplicity and flexibility over process parameters. Electrochemical functionalization on the surface of the SWNT network was performed by addition of a 2 μL drop of 0.1 M $Zn(NO_3)_2$ electrolyte at pH of 5.5, using the gold pads as the working electrode, an inserted Pt wire as the counter electrode and a pseudo Ag/AgCl wire as the reference electrode. The deposition potential was kept constant at -0.6 volts versus pseudo Ag/AgCl reference electrode, and the applied charge was set to 20 or 100 μC. Electrodeposition was carried out under potentiostatic mode at 25°C and 70°C, at ambient pressure using CH Instruments Electrochemical Analyzer CHI604c. Following deposition, the devices were lightly rinsed with DI water by placing a 10 μL drop over the deposited area and removal with N_2 gas. Verification of ZnO nanoparticle decoration on the surface of SWNTs was verified by scanning electron microscopy (SEM).

Room temperature photocurrent studies were performed on the functionalized UV photodetector array by integrating the die onto a pin IC adapter via wire bonding (West Bond Inc. Model 7443A), which was then electronically connected to a bread board of our custom made system [161]. An ultraviolet (UV) mercury lamp source was utilized as the photo irradiation source (Mark 560, Martronics Co.). For the time resolved photocurrent studies, each sensor was subjected to 1.0V DC potential and the resistance was continuously recorded every 0.1 seconds simultaneously for the sixteen sensors by use of Keithley 236 source measurement unit controlled by a custom made LabView program. A field effect configuration was employed by applying a back gate potential sweep from -20 to 20 volts with 1 volt increments to each devices individually, under the presence and absence of UV light. Scanning electron microscopy (SEM) image were obtained with a Phillips XL30-FEG.

4.3 Results and Discussion

Electrochemical deposition parameters (applied potential, temperature, etc.) are known to strongly influence the deposit microstructure and morphology and were consequently studied for ZnO. From the X-ray diffractograms of the ZnO thin films, it is evident that improved crystallinity can be imposed by simply tuning the deposition temperature while maintaining all other parameters constant, i.e. substrate, solution concentration, deposition voltage, deposition charge (figure 2.3). Deposits synthesized at 70°C were highly crystalline and displayed a preferred orientation in the (002) direction corresponding to the ZnO hexagonal wurtzite structure, while polycrystalline deposits were produced at 25°C. As shown in Figure 4.1 (A), this temperature differences, as well as total charge passed, has little influence the device resistance. The resistance of the devices is shown to be nearly unaffected for samples decorated at 25°C (square symbol) and increased slightly for the samples decorated at 70°C (triangle symbol) and 20μC. After decoration at 70°C sand 100 μC the device displayed a weak decrease in resistance. The resistance decrease at higher temperature is consistent with the more crystalline ZnO behaving as stronger scattering sites that disrupt the flow of holes in the SWNTs and the decrease in resistance at higher charge may be due to nearly continuous ZnO coatings that permit concomitant charge transfer.

The extent of ZnO coverage is qualitatively shown for bare SWNTs and ZnO loadings of 20 μC and 100 μC at 70°C by SEM images in Figure 4.1(B-D). Nanoparticle formation is clearly visible with average ZnO nanoparticle sizes of 30.3±7.6 and 53.7±3.4 nm for 20 and 100 μC respectively. Although the two charges display drastic differences in coverage, from well isolated particle formation to near continuous coatings along the SWNT networks, the nanoparticle densities are very near to one another with particle densities generally decreasing slightly as more charge is passed due to coalescence of nanoparticles. ZnO particles are believed to grow by instantaneous nucleation in which original nuclei continue to grow with little to no new nucleation sites as time progresses. Moreover, particle nucleation is assumed preferentially initiate at the Stone-Wales defect sites due to higher electrochemical activity [179, 180].

Photocurrent measurements were performed in ambient conditions on bare SWNTs and hybrid ZnO-SWNT structures functionalized at 20μC, with solution temperature at 25°C and 70°C (Figure 4.2). These I-V characteristics show linear behavior around the zero applied bias which indicates that the bare SWNTs make good ohmic contact with the gold pads. Under UV illumination, the current of bare SWNTs is slightly altered by less than 6% while that for the hybrid system increases dramatically by ~147% $\Delta I/I_{o,}$ defined as the difference between the illuminated and dark current value divided by the dark current value. Thus, there is a 30 fold increase in the current behavior by the incorporation of ZnO nanoparticles on the surface of SWNTs upon UV illumination. However, these results are contradictory to similarly functionalized SWNT devices and implicate m-SWNT as the primary charge conducting elements in these networks [231]. This is not surprising considering the preferential m-SWNT alignment obtained for the solvent and dielectrophoretic conditions used and low resistance of the devices [237].

Upon exposure to UV light two processes have been reported to occur in ZnO: photons exceeding the band gap of ZnO photogenerate electron-hole pairs (Equation 1) and holes recombine with electrons to discharge adsorbed O_2 (Equation 2) [231, 238, 239]. This process has been demonstrated to yield significant internal photoconductance gains in ZnO nanowires. After turning off the UV light, both the recombination of the electron-holes and the adsorption of oxygen gases (Equation 4.3) from the ambient atmosphere reduce the carrier density leading to a decrease in current. In ZnO/SWNT ensembles electron transfer has been shown to occur from nanoparticle to SWNTs by both spectroscopy and electrical measurements. In the case of semiconducting SWNTS (s-SWNTs) the donated electrons decrease or scatter holes for an overall increase in resistance. In contrast, this system observes an increase in current upon UV illumination, indicating that m-SWNTs or electrons dominate charge transport, in which case photogenerated electrons donated by the ZnO nanoparticles would increase the conductivity of these networks [170]. After terminating UV the exposure free electrons are consumed by transfer to the m-SWNT and association with O_2 adsorbates on the ZnO surface for a decrease in conductivity of the ZnO/SWNT network.

$$h\upsilon \rightarrow e^- + h^+ \qquad \text{Equation 1}$$

$$O_2^-(ad) + h^+ \rightarrow O_2(g) \qquad \text{Equation 2}$$

$$O_2(g) + e^- \rightarrow O_2^-(ad) \qquad \text{Equation 3}$$

Further device interrogation was performed by measuring the transient current behavior of the ZnO-SWNT hybrid systems in the dark and under UV illumination with ambient conditions. An external bias of 1.0 volt was applied to all sensors with the gate voltage at $V_g = 0V$. Measurements were conducted simultaneously for 6-8 sensors per set of synthesis conditions with exposure and recovery times of 10 and 20 min, respectively. The spot size of the UV source was adjusted to completely cover the 1 cm^2 as to ensure that all devices were illuminated equally. Typical dynamic photocurrent responses of bare SWNTs (figure 4.3 A), and the ZnO/SWNTs hybrid structures are shown in figure 4.3 B-D. The current of the bare SWNT network was almost unaffected when exposed to UV light, increasing slightly. If the bare SWNT network charge transport characteristics were dominated by p-type semiconducting tubes with holes as the charge carriers, the device conductance might be anticipated to decrease in response to photodesorption of oxygen species; however, it is worth noting that the device configuration, consisting of SWNT on top of Au electrodes, would mitigate these effects [240] [241]. Here the opposite trend is observed, with slight reprieve in conduction upon UV illumination, which, if due to photodesorption of oxygen, supports electron charge transfer in m-SWNT. Also in accord with the observed I-Vs, the transients for ZnO-SWNT hybrid structures exhibited an increased in current upon UV illumination. The ZnO-SWNT hybrid structures synthesized at 25°C and 20 μC had average current change of 71.1±20.83% $\Delta I/I_o$. The ZnO-SWNTs synthesized at 70°C and charges of 20 μC and 100 μC showed a larger current increase under the UV irradiation with $\Delta I/I_o$ of

136.4±29.2% and 121.5±15.9%, respectively, suggesting good interfacial quality between ZnO and the nanotube surface [154].

These results also identify two main variables affecting the photocurrent behavior of the ZnO-SWNT hybrid structures, the first is the material quality of ZnO determined by the functionalization temperature, and the second is the extent of surface coverage on the perimeter of the SWNTs. Comparison of the photocurrent response for the hybrid structures synthesized at 20 μC and 20°C (figure 4.3 B) and the hybrid structures synthesized at 20 μC and 70°C (figure 4.3 C) reveals a threefold increase in $\Delta I/I_o$. This is attributed to the better crystallinity of ZnO which translates to less defect sites at the higher temperature since the particle size and density remain roughly the same. Secondly, the surface coverage of the SWNTs with ZnO did not improve the device performance as noted by evaluating the hybrid devices fabricated at 20 μC and 70°C (figure 4.3 C) to the one synthesized at 100μC and 70°C (figure 4.3 D). Instead the major difference arises from the recovery of the two structures illustrated in figure 4.4 A, with the one synthesized at 100μC reaching half of its original current value in the time allotted. Since the underlying conduction pathway is through the SWNTs there is a ceiling on the extent of effect of SWNT conductivity, thus more ZnO on the periphery of the nanotubes contributed no further enhancement in photoconduction [238].

The photoresponse dynamics show a rapid increase in current upon illumination with UV light and a slow decay when the UV source is turned off, summarized in figure 4.4. This trend is characteristic of a photogenerated response and an adsorption like recovery consistent with the low power density of the lamp, 16 $\mu W/cm^2$ [234]. Immediately after turning on the UV light rapidly generates electron-hole pairs for quick desorption of oxygen, which reduces electron scattering from the hole induced depletion layer. Free electrons may also contribute a small portion of charge carriers to the SWNT for an overall expedited increase in conductivity. After exposure free electrons remain in the ZnO particles permitting electrons in the conduction channel of the m-SWNT to continue to flow freely until oxygen re-adsorbs to the surface to consume them. This process is slower as it is an adsorption process as opposed to the photogeneration dependent desorption of oxygen. This also explains the lag in response for smaller ZnO nanoparticles and less coverages as smaller particles have larger surface to volume rations requiring more time for bulk generated electron-hole pairs to compensate surface bound electrons. Similarly, the prolonged recovery for larger ZnO nanoparticle or greater coverage is also expected as the larger volumes require more complete readsorption for complete consumption of free electrons [242]. The generally slow recovery of initial conductance has also been reported on ZnO NWs after exposure of UV light and was attributed to the effects of surface chemistry and or surface interactions of the holes to other negatively charged species in the ambient, such as humidity[239, 243].

The field effect transfer characteristics of ZnO-SWNT hybrid systems synthesized at 20μC and 70°Care demonstrated in figure 4.5. As was the case with the dynamic responses, there is a significantly enhanced current in the FET gate sweep when samples are illuminated with the UV light. However, both the dark and UV irradiated gate scan nearly horizontal on linear scale supporting the m-SWNT conduction. A very weak transconductance, $\Delta I/\Delta V$, defined as the changed in current divided by the change in voltage, increase from 266.2 nS to 509 nS in the dark and excited state, respectively, and lack of measureable threshold voltage also allude to metallic conduction. The carrier mobility (μ) doubled from 7.71 to 14.75 cm^2/Vs, while the carrier concentration decreased slightly from $4.80x10^{16}$ to $3.24x10^{16}$ cm^{-3} with exposure to UV light. Thus exposure to UV light had a greater influence on the rate of electron-hole recombination of the ZnO-SWNT hybrid system, since largest effect on electronic properties was on the mobility and transconductance. The bare SWNT network showed similar gate independent behavior and a negligible current response when exposed to UV light.

4.4 Conclusions

We report the synthesis and photoconduction behavior of electrochemically synthesized ZnO-SWNT hybrid structures. An increase in conductance upon UV irradiation supports m-SWNT dominated networks. The hybrid structures are composed of various degrees of surface coverage (i.e. particle size and particle density) and material quality. The photoconduction studies were performed in ambient conditions and the current behavior was monitored in the dark and presence of UV irritation. Dynamic photocurrent responses reveal that the current change of the hybrid system was $\Delta I/I_o$ was more strongly dependent on material quality and response/recovery rates were dependent on surface coverage of SWNTs, while the current of bare SWNTs was unaffected by the presence or absence of the UV light. Field effect measurements corroborate metallic conduction for SWNT networks and demonstrate that the UV source has the largest contribution to electron-hole recombination by showing increased changes in carrier mobility transconductance.

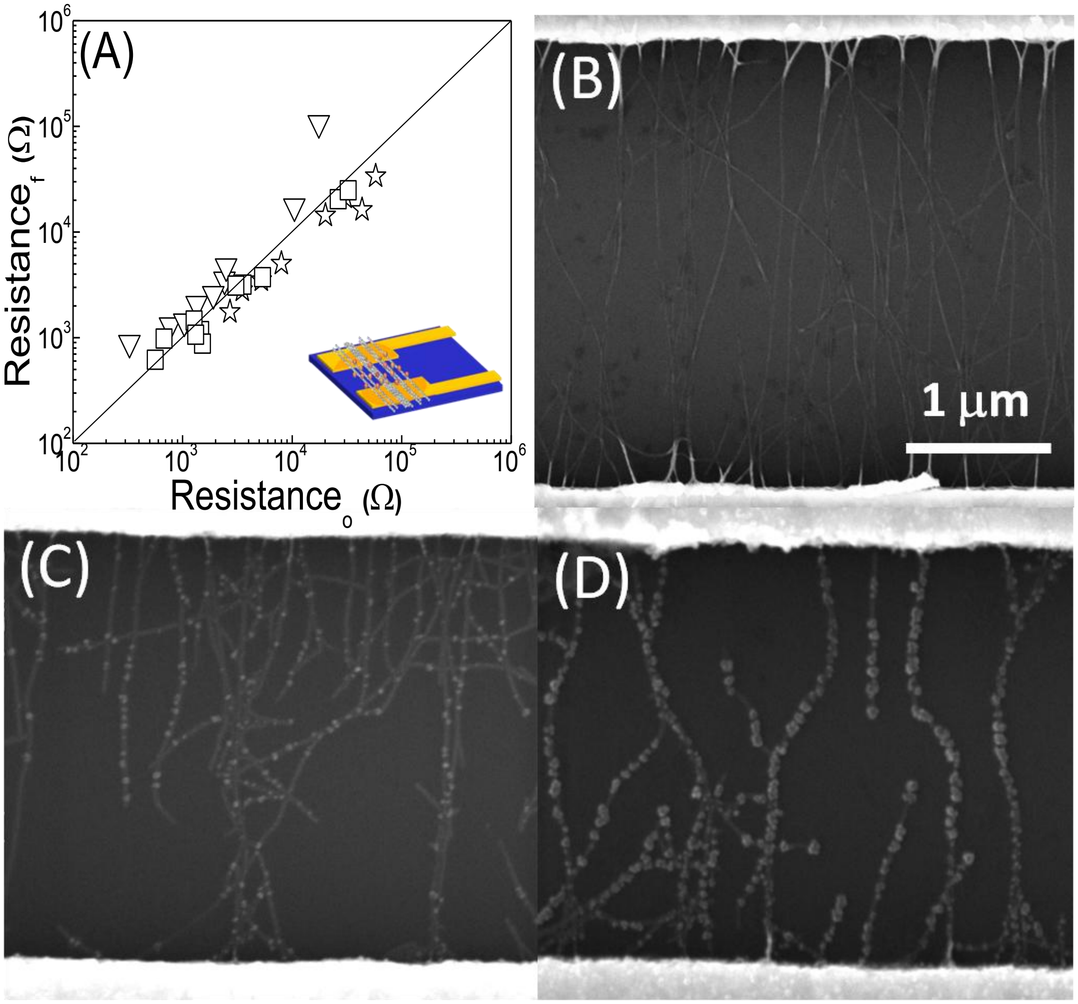

Figure 4.1. (A) Resistance change distribution after functionalization of SWNTs with ZnO at 25°C and 20μC (square symbol), 70°C and 20μC (triangle symbol), 70°C and 100 μC (star symbol). SEM images of (B) bare SWNTs, ZnO-SWNTs functionalized at 70°C and (C) 20 μC (D) 100 μC.

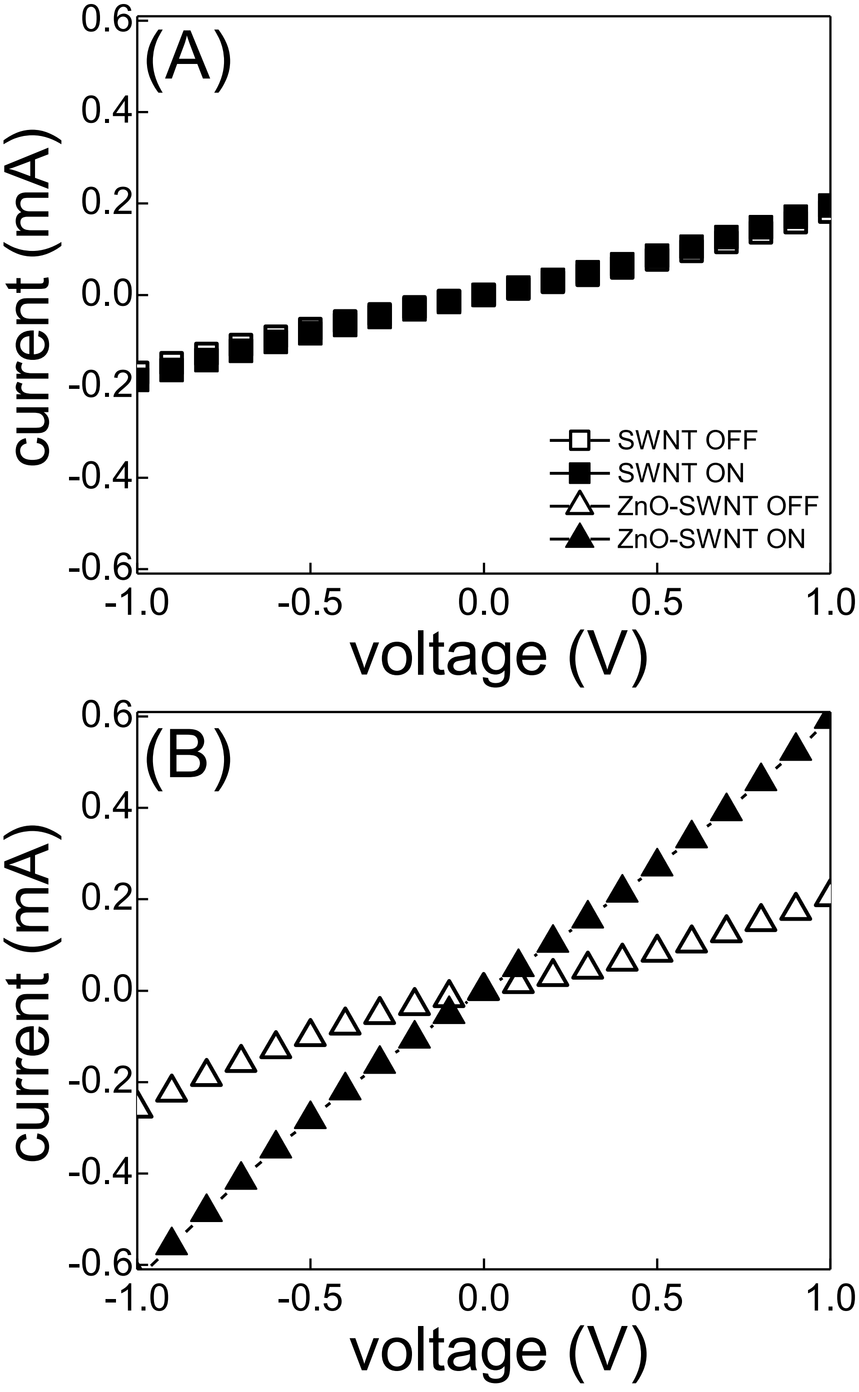

Figure 4.2. I-V characteristics of (A) bare SWNTs and (B) ZnO-SWNT hybrid system synthesized at 20μC and 70°C in the dark (open symbol) and upon UV illumination (close symbol).

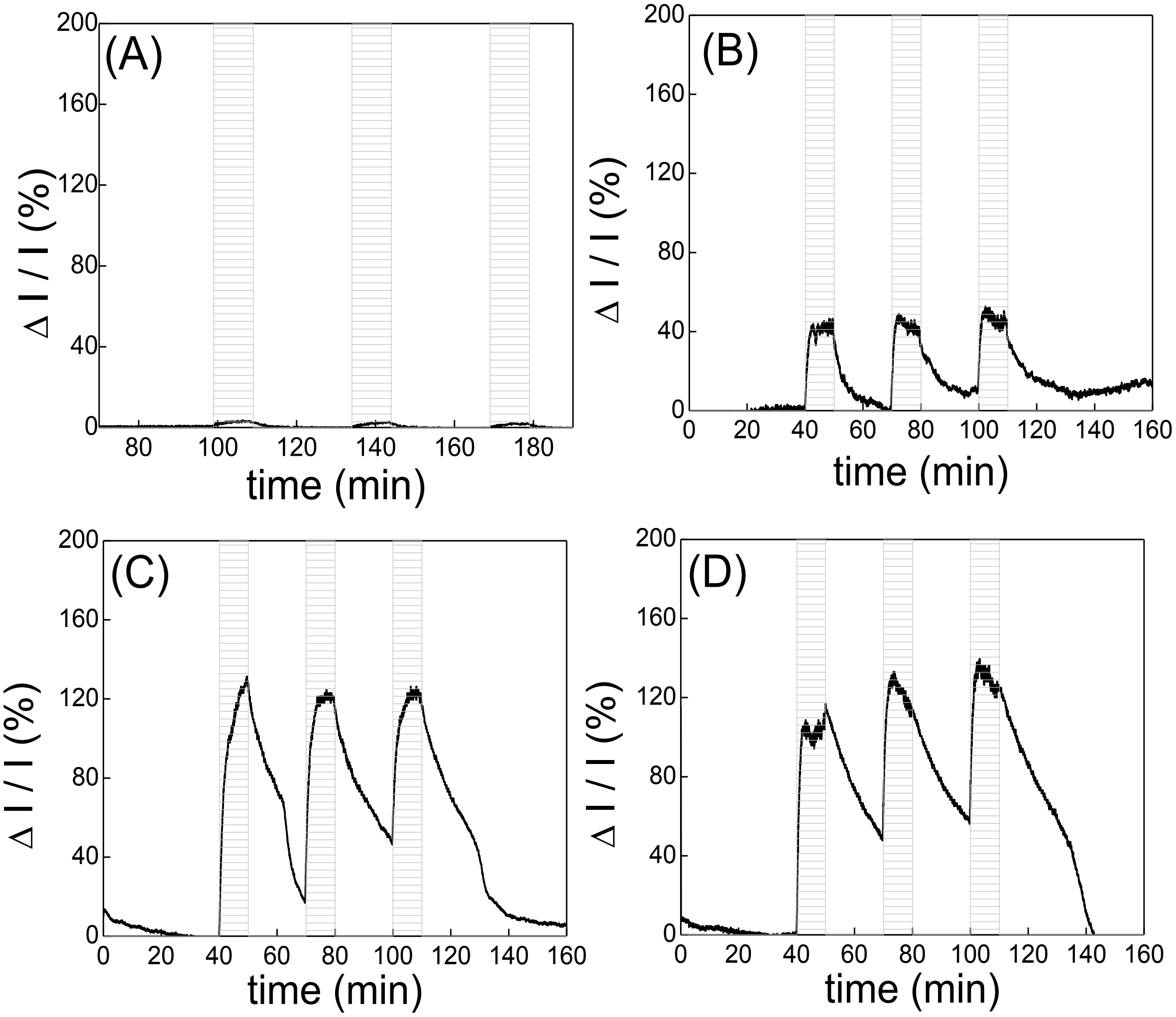

Figure 4.3. Typical transient photocurrent response of (A) bare SWNTs, ZnO-SWNT hybrid system synthesized at 20μC and (B) 25°C, (C) 70°C and (D) 100μC at 70°C. Exposure to UV light is indicated as the shaded area of the bar graph.

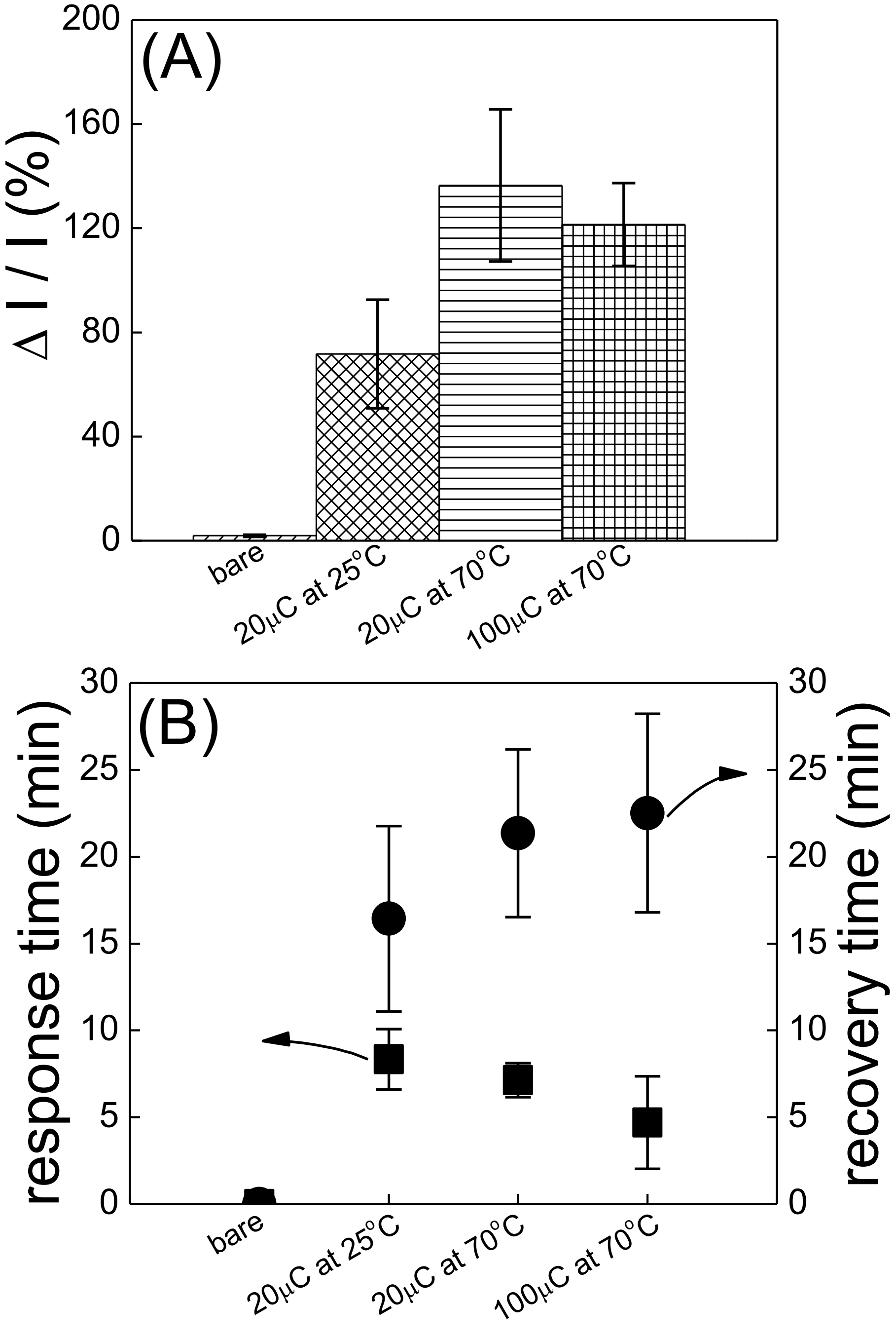

Figure 4.4. (A) Histogram of percent change in current and (B) response (square symbol) and recovery time (circle symbol) of nanostructures when exposed to UV light depending on material conditions.

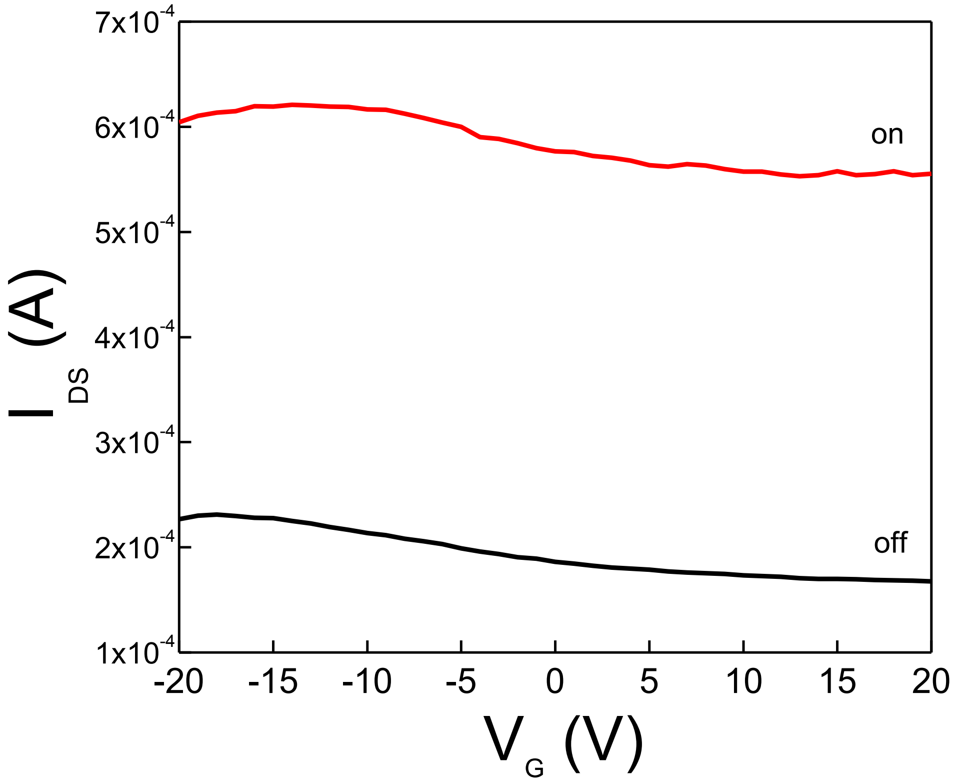

Figure 4.5. Field effect transfer characteristics of ZnO-SWCNT hybrid system synthesized at 20μC and 70°C upon the absence (off) and presence (on) of UV light with an applied V_{ds} of 1 volt.

CHAPTER 5:

SEQUENTIAL CATALYSTS INCORPORATION ON TO ZnO/SWNT HYBRID STRUCTURES

Abstract

Sequential incorporation of metal catalyst on to ZnO/SWNT hybrid was investigated. Metal catalysts of interest include Au, Pt, Ag and Pd and were deposited at charges ranging from -0.5μC to -500μC on the surfaces of ZnO/SWNT sensors. The surface morphology, growth mechanism and room temperature sensing performance were investigated as a function of charge, and presence or absence of seeded metal oxide. In the case of the Au and Ag catalyst, there was a charge dependent sensing behavior and specificity towards H_2S and NO_2. The metal-SWNT structures were most sensitive at smaller charges and the metal-ZnO/SWNT hybrid structures experiencing higher sensitivities when the metal is deposited at larger charges. With incorporation of the Pt catalyst, the sensing behavior was dramatically suppressed for H_2S, where Pt/SWNT structures outperformed the Pt/ZnO/SWNT sensors towards H_2S and NH_3. Interestingly the sensing performance was independent of the applied charge for both sets of hybrid structures.

5.1 Introduction

Single wall carbon nanotubes are promising nanomaterials as the transducing element building block for gas sensors due to their electronic properties, thermal stability, and chemical inertness. Since carbon nanotubes are composed entirely of surface atoms and have an exceptional high surface area available for interaction, molecular adsorbents can substantially alter their electronic properties making these entities increasingly sensitive to their chemical environment. Prior work has shown that the sensitivity and selectivity towards certain analytes can be further enhanced when the carbon nanotubes are covalently or non-covalently functionalized [143-150]. To this respect, I will functionalize single wall carbon nanotubes (CNTs) with zinc oxide nanoparticles to increase the sensitivity and selectivity towards selected volatile organic compounds and hazardous chemicals.

ZnO is naturally an n-type semiconductor due to the presence of intrinsic defects, oxygen vacancies and Zn interstitials, a slight alteration in the purity of the original material can produce dramatic changes in electrical and chemical properties. The motivation behind utilizing the ZnO nanostructured entities as conductometric sensors stems from the idea that one dimensional oxide nanostructures are expected to possess novel characteristics such as large surface-to-volume ratio and comparable Debye length to the radius of the wires, which translates to an exponential increase in the percentage of surface atoms available for surface reactions as we decrease the diameter of a wire into this nanoscale regime; together with a decrease in electron-hole recombination time and ability to modulate material properties along the axial direction of the wires [230]. This is important because we have a larger fraction of the atoms involved in surface processes whether it is adsorption or catalytic in nature and a decreased time for the entities to respond to the changes in their environment which combined can enhance the overall senor performance. Furthermore, the stability of sensors built upon better defined entities with greater level of crystallinity can be heighted, compared to their thin film counterparts, due to the reduction of instability associated with conduction hopping [140]. Appreciable amount of work describing the doping of ZnO with group III elements to enhance n-type conductivity, group V elements to generate p-type behavior, and magnetic elements (Fe, Co, Ni, Mn) to synthesize dilute magnetic materials is available [140]. Recently, detection of various chemicals has been reported with a variety of nanowire sensor configurations. To summarize, ZnO nanostructure networks (ribbons, rods, wires) synthesized by thermal evaporation, liquid-solid method, and epitaxy (MBE) have been analyzed towards CO, NO_2, NH_3, H_2, H_2S, ethanol, O_2 and O_3. However there has been no clear correlation between the synthesis method, material properties, quantity of nanostructures, and effect of dimensions towards the sensing performance of the ZnO NW networks, the reports mostly address the sensing efforts towards the different analytes [184, 185, 244-247]. In spite of the sensitivity, selectivity of the sensors remains a challenge, thus the strategic introduction of specific dopants or catalysts can potentially enhance selectivity and/or impart selectivity towards specific analytes.

5.2 Experimental

5.2.1 ZnO Nanoparticle Deposition

A carbon nanotube suspension was prepared by addition of 0.2 mg of commercially available carboxylated SWNTs obtained from Carbon Solutions Inc., to 20 mL of N,N-dimethylmethanamide (DMF). The contents were sonicated in a glass vial for 90 minutes using a VWR model 50D sonicator. All 20 mL of the SWNT suspension were transferred to a 50 mL Teflon centrifuge tube and centrifuged for 90 minutes at 15000 RPM and 23°C using a Beckman J2-HS centrifuge. Immediately after centrifugation, 10 mL of the supernatant was carefully removed and placed in a glass vial. The supernatant was additionally sonicated for 60 minutes prior to use.

Lithographically patterned Si chips with 16 electrode pairs (Ti/Au 20/180 nm) were utilized as substrates and contacts for sensor assemblages. The electrodes contained a 3 μm gap and large contact pads that enabled individual addressability for electrochemical functionalization. SWNTs were aligned across the electrode gaps via alternating current dielectrophoretic alignment by adding a 1.5 μL drop of SWNT suspension, applying 1 V_{pp} and 4 MHz (Keithley 3390 AC generator, 50 MHz arbitrary waveform generator). The device resistance was controlled by the alignment time. After alignment, electrochemical functionalization of the SWNT network was performed by addition of a 2 μL drop of 0.1 M $Zn(NO_3)_2$ electrolyte at pH of 5.5 and solution temperature of 70°C. Using the gold pads as the working electrode, a Pt wire as the counter electrode, and an Ag/AgCl wire as a pseudo reference electrode, chrono-coulometry controlled experiments were terminated at 20 or 100 μC of ZnO deposition. After functionalization, the sensor array was lightly rinsed with nanopure water and dried with purified nitrogen gas.

5.2.2 Catalyst Deposition

Electrodeposition of the catalyst metal nanoparticles was performed by *s*equential electrochemical functionalization in a three electrode system. Unitizing the sensor architecture as the functionalization cell, where the gold pads and ZnO/SWNTs networks were employed as the working electrodes, a Pt wire as the counter electrode and a chlorinated Ag/AgCl wire as the reference electrode. Deposition of gold nanocatalysts was performed by using a commercially available ready to use electroplating electrolyte from Technic Inc. (CA), with neutral ph. A 5 μL drop of the Au plating solution was placed across the two electrodes completely covering the Au pads and ZnO/SWNT networks, a potential of -1.0 volts vs. pseudo Ag/AgCl was applied and deposition was terminated by controlling the charge passed through the system from 0.5 to 500 μC. Deposition of platinum nanoparticles was performed by using a commercially available ready to use electroplating electrolyte from Technic Inc. (CA), with pH between 7.5 and 8. A 5 μL drop of the Pt plating solution was placed across the two electrodes completely covering the Au pads and ZnO/SWNT networks, a potential of -1.0 volts vs. pseudo Ag/AgCl was applied to the system and experiment was as terminated by controlling the charge from 0.5 to 500 μC. For deposition of palladium nanoparticles a 5 μL drop of electrolyte composed of 0.47 M $Pd(NH_3)_2Cl_2$ + 58 mM NH_4Cl at pH of 7 (US Patent number 4487665) was utilized as the Pd source, -0.5 volts versus the Ag/AgCl reference electrode was applied and the charge was varied from 0.5 to 500 μC. Silver nanoparticles were electrodeposited by use of ready to use electroplating electrolyte from Technic Inc. (CA), at a potential of -0.3 volts vs. pseudo Ag/AgCl, with applied charge of 0.5 to 500 μC. After functionalization, the sensor array was lightly rinsed with nanopure water and dried with purified nitrogen gas.

Scanning electron microscopy (SEM) and energy dispersive X-ray spectroscopy microanalysis (EDAX) was used for verification of catalyst deposition and nanoparticle visual quantification.

5.2.3 Gas Sensing Studies

Room temperature gas sensing studies were performed on the functionalized sensor array by integration of the sensor chip with a pin IC adapter via wire bonding (West Bond Inc. Model 7443A) and subsequent electrical connection to a bread board in a custom made sensing system [161]. Each sensor was subjected to 1.0 V (DC) and the resistance was continuously recorded every 0.2 seconds simultaneously for the sixteen sensors by use of Keithley 236 source measurement unit controlled by a LabView program. A base line was achieved with exposure of dry air as the carrier gas and different analyte concentrations were attained by subsequent dilutions with the carrier gas. Exposure times were limited to 15 minutes and recovery time to 20 minutes; total gas flow rate was kept constant at 200 sccm for all experiments. Analyte and carrier gas flow rates were regulated by mass flow controllers (Alicat Scientific Incorporated) [161, 171]. A field effect configuration was used with the current sensing set-up by applying a back gate potential sweep from -20 to 20 volts with 1 volt increments under the presence of the desired analytes and carrier gas.

5.3 Results

5.3.1 Metal Catalyst Verification

Since ZnO can easily dissolve in both acidic and basic conditions, it was imperative to determine whether the selected deposition electrolytes for the metal catalyst had a dissolution effect on the zinc oxide nanoparticles. For the purpose of deposition verification of the metal catalysts onto the ZnO/SWNT system, ZnO was deposited at 100 μC with average particle size of 53.7±3.4, and imaged under SEM prior to metal catalyst incorporation (figure 5.1 A, C, E, G). Due to de various deposition rates of the metal catalysts Au, Pt, Pd and Ag were subsequently deposited at 500μC, 100μC, 50μC and 100μC, respectively. The SEM images in figure 5.1 B, D, F and H verify the deposition of the metal catalyst initiating at the surface of the ZnO nanoparticle. Nucleation of the metal catalyst is preferential to the ZnO particle due to its higher surface energy; the images show a drastic increase in the initial particle size with different morphological appearances intrinsic of the deposited metal and little to no new nucleation sites along the SWNT wall. From these SEM images it can be concluded that the positioning of the catalyst is on the metal oxide surface, and that that the growth morphologies is predetermined by the ZnO material quality.

Most evident is in the gold catalyst system (figure 5.1B), where Au nanoparticles grew in star like structures, suggesting preferential growth of Au along ZnO crystalline (002) face. On the other hand Pt, Pd and Ag had more of a nodular peripheral growth around the ZnO nanoparticle. For Pt, the growth seemed governed by a smooth radial deposition along the initial particles, while Pd began to show nodular growth upon its palladium shell. Ag also had nodular deposition with very high surface roughness. In addition to revealing the deposition preference of the metal catalysts, the SEM images also verified the presence of initial ZnO nanoparticles shown in areas where the catalyst did not grow (figure 5.1 F), thus expelling the possibility of ZnO nanoparticle dissolution with the selected electrolytes.

5.3.2 Au Catalyst Effect on the ZnO/SWNT Hybrid System

Gold nanoparticles were electrodeposited on to SWNTs and ZnO/SWNT hybrid structures with ZnO deposited at 20μC. Figure 5.2 A shows the average deposition time of Au deposition on to ZnO/SWNT hybrid structures at various charges. As expected, the deposition time linearly increased with increasing charge, resulting in larger amounts of incorporated Au. Figure 5.2 B depicts the change in resistance when ZnO, Au, and Au/ZnO are functionalized on to SWNTs, illustrating that when Au is deposited on SWNTs the tendency is for the resistance to decrease, while when Au is deposited on to ZnO, the resistance generally increases. While it is reasonable for the of metal nanoparticles to decrease the resistance of the SWNTs, the increase in resistance when Au is sequentially added on the ZnO nanoparticles is indicative of intimate contact of the Au with ZnO thus altering the electronic pathway.

To analyze the morphological effects that Au has upon the incorporation to ZnO/SWNT, SEM images of Au/SWNTs and Au/ZnO/SWNTs at Au deposition charges of 1, 5, 50 and 500μC are shown in figure 3. When Au is deposited on bare SWNTs, there is an immense dense particle formation and with small particle size, as seen in figure 5.3 A-D. At all charges, Au deposition initiates on the SWNTs and progresses through nanoparticle growth, at 500 μC the morphology of the Au nanoparticles appears to be "popcorn" like in structure, bridging across the gold electrodes along the periphery of the SWNTs. In contrast to the deposition growth observed of Au on SWNTs, the growth mechanism was vastly different when Au was deposited on to ZnO/SWNTs. As demonstrated in figure 5.3E-H, at the same applied charges Au nanoparticles deposited less densely with larger particle sizes. On the ZnO/SWNT hybrid structures, Au particle nucleation initiates on the ZnO nanoparticles, with the progression of charge particle size is increased followed by nodular growth on the Au coated ZnO nanoparticles, eventually the budding nods turn into protruding limbs giving the final structures star-like appearances. Thus the presence of ZnO influences the growth of Au to be concentrated around the oxide surface and developing Au facets at energetically favored positions.

Particle size and distribution of Au on bare SWNT and ZnO/SWNTs are shown in figure 5.4. Extracted from various SEM images taken of multiple samples, the average particle size (for Au on SWNT) increased linearly from 18.3±6.2 nm to 139.2 ±38.7nm with increasing applied charges of 1 to 500μC, as demonstrated in figure 4 A. When Au is deposited on ZnO/SWNTs, there is an exponential increase in particle size from 67.02±19.06nm to 354.1±61.4 nm as the charge increased from 1 to 500μC substantiated by the explicit morphological differences in particle growth at the highest charge (figure 5.4 A). The particle density for Au deposited on SWNTs had a Gaussian distribution indicating progressive nucleation with new Au nuclei being formed with applied charge. Au on ZnO/SWNTs had a constant particle density throughout the whole applied charge rang suggesting instantaneous nucleation of the initial Au nanoparticles followed by progressive particle growth, illustrated in figure 5.4 B.

Room temperature sensing performance of the Au/SWNT and Au/ZnO/SWNT hybrid structures was performed against H_2S, SO_2, NO_2, NH_3, CO, CO_2 and water vapor. For comparison purposes, all charges were analyzed to determine optimal sensor performance and to obtain a finger print response towards all desired analytes. Demonstrated in figure 5.5 are the dynamic sensor responses towards NO_2 (figure 5.5 A & C), and their corresponding calibration curves, most notably, the Au had opposite charge dependent sensing behavior built upon on whether the catalyst was deposited on to bare SWNTs or ZnO/SWNTs. In the absence of ZnO, the sensor sensitivity towards NO_2 is diminished as the charge is increased, with the highest $\Delta R/R_o$ of -39.7±3.4 at 5 ppm of NO_2 arising from Au deposited at 1μC, consisting of average particle size and density of 18.02±6.2 nm and 28.3±2.6 particles/SWNT bundle, respectively. This could be the effect of particle size on sensing performance, mainly the smaller particles being more chemically active and high particle density which collectively provide larger number of available sites with high surface area available for analyte interaction. On the other hand, when the Au catalyst is incorporated on to ZnO/SWNTs hybrid structures, the increased charge of Au nanocatalysts enhances the overall senor performance with $\Delta R/R_o$ of -49.1±24.1 at 5 ppm of NO_2. Under these synthesis conditions, the average particle size and density of the Au/ZnO/SWNT hybrid structures is 163.49±49.8nm and 12±0.82, respectively, indicating that particle size and density are not the sole players responsible for the detection. The inverse sensing phenomena dependent on applied charge of the Au catalysts advocate geometrical differences between the two systems to be the stronger factor for the observed sensing performance. In the case of Au on SWNTs, the resultant sensor architecture consists of nanoparticles templated along the surface wall of the SWNTs, with neighboring particles coalescing to form larger units, resulting in a decreased sensitivity with progression of charge. Whereas for Au on ZnO/SWNTs, the resulting hybrid structures first creates a gold shell around the ZnO nanoparticles followed nanoparticle nodular formation with progression of charge, thus increased sensor performance with increased charge.

Of the gaseous species analyzed (H_2S, SO_2, NO_2, NH_3, CO, CO_2 and water vapor), Au/SWNTs and Au/ZnO/SWNTs hybrid systems had notable responses towards H_2S and NO_2, little response towards water vapor SO_2 and NH_3, and no response towards CO ad CO_2. Figure 5.6 summarizes the mean sensor response towards detectable analytes at concentrations set by OSHA’s permissible exposure limits. H_2S and NO_2 showed similar charge dependent trends where the single metal is more sensitive towards H_2S and NO_2 at increasing charges and reduced response at increasing charges when Au is incorporated on to ZnO/SWNTs. Interestingly the addition of Au catalyst to the ZnO/SWNTs hybrid system suppressed the response towards H_2S possibly due to the surface coverage of ZnO allowing less ZnO surfaces to interact with the H_2S molecules, as a result Au/ZnO/SWNTs hybrid structures behaved more like Au/SWNTs sensors. The sensor response towards SO_2 and NH_3, was unaffected by the addition of Au catalysts, and humidity had little to no effect on the sensing performance of the resulting hybrid structures.

FET mechanistic sensing towards NO_2 of Au/SWNTs with Au deposited at (A) 1μC, (C) 50μC and Au/ZnO/SWNT hybrid network with Au deposited at (B) 1μC and (D) 50μC is demonstrated in figure 5.7. ChemFET configuration was investigated by applying a back gate, sweeping the gate voltage from -20 to 20 volts in intervals of 1 volt under the presence of various NO_2 concentrations. The sensors show the drain source current increasing at higher concentrations of NO_2, more significantly for the Au/SWNT functionalized sensors as well as no clear on-off state, consistent with the chemiresistive sensor response. The sensing mechanism towards NO_2 was difficult to examine due to high metallic contribution and nature of the current behavior.

5.3.3 Pt Catalyst Effect on the ZnO/SWNT Hybrid System

Platinum nanoparticles were functionalized on the surfaces of bare SWNTs and sequentially on the surface of ZnO/SWNT hybrid structures at charges of 1, 5, 50, and 500 μC. Morphological images of the resulting hybrid structures are demonstrated in figure 5.8. When Pt is electrodeposited on the surface of bare SWNTs, small nanoparticles grow on the periphery of the SWNT networks; consistently the nanoparticles appear round and spherical in shape, shown in figure 5.8 (A) - (D). The Pt nanoparticle size decreased from 34.9±8.9nm to 6.0±2.6nm, while the particle density increased from 2±0.8 to 23.5±5.1 particles per SWNT bundle with the progression of the applied charge of 1 to 500μC, figure 5.9 (A). The simultaneous decrease in particle size and increase in particle density suggests that the Pt nanoparticles nuclease continuously throughout the functionalization process. With the incorporation of the Pt metal catalyst, the resulting Pt/ZnO/SWNT structures progressively developed from small nanoparticles to fully encapsulated ZnO core surrounded with a rough Pt shell, illustrated in figure 5.8 (E) – (H). On the other hand, for the Pt/ZnO/SWNTs structures both particle size and density of the incorporated Pt structures increase from 51.1±18.14 nm to 201.1±44.9 nm and 3.2±0.9 to 7.8±2.04 particles per bundle of SWNTs, respectively, with increasing applied charge of 1 to 500μC (figure5. 9 (B)). The SEM images indicate that the growth of the Pt structures is concentrated on the origins of ZnO nanoparticles, since there is a small increase in the density of Pt/ZnO nanoparticles and bare sections of SWNTs. In the absence of ZnO, Pt deposits ubiquitously on the surface of the SWNTs and with the progression of time particle growth is not observed, instead the additional energy provided to the system causes creation of new nucleation sites, resulting in high density of small nanoparticles.

Room temperature sensing performance of the Pt/SWNTs and Pt/ZnO/SWNTs hybrid structures was investigated towards low molecular weight molecules of interest as previously described above. For comparison purposes, all charges of the Pt/SWNT and

Pt on ZnO/SWNTs were analyzed to determine optimal sensor performance and to obtain a finger print response towards all desired analytes. The comprehensive sensing response towards OSHA's permissible exposure limits of H_2S, SO_2, NO_2, NH_3, and water vapor are demonstrated in figure 5.10. It should be noted that no response was observed towards vapors of CO and CO_2 and little sensitivity was detected towards $SO_{2,}$ with a positive resistance increase for the Pt/SWNT system and negative resistance decrease for the Pt/ZnO/SWNT structures. The sensing performance of the hybrid structures towards H_2S was generally improved compared to the bare SWNTs (4.4±3% $\Delta R/R_o$) with higher sensitivity originating from the Pt/SWNTs system possessing an average response of 38.9±3.6% $\Delta R/R_o$, independent of applied charge. Unexpectedly, when Pt is sequentially added to the ZnO/SWNT hybrid system the sensing response was suppressed to 12.2±1.5% $\Delta R/R_o$, over an order of magnitude decrease from that of ZnO/SWNT hybrid structures (139.9±41.9% $\Delta R/R_o$) and a 3-fold decrease from Pt/SWNT structures.

Interestingly, both Pt/SWNTs and Pt/ZnO/SWNT hybrid structures had an increased detection towards NO_2 vapors, compared to both bare SWNTs and ZnO/SWNTs. The Pt/SWNTs and Pt/ZnO/SWNT hybrid structures responded similarly both in magnitude of response and autonomous of applied charge with the Pt/SWNT structures having an average $\Delta R/R_o$ of -28.5±3.6% and Pt/ZnO/SWNTs an average resistance change of -32.7±2.3% $\Delta R/R_{o.}$ Suggesting that since ZnO/SWNT hybrid structures had little response towards NO_2, the sensing behavior could originate from the introduction of the Pt catalyst. The sensor sensitivity towards NH_3 was also increased with the introduction of Pt structures, however the effect was more pronounced in the absence of the native ZnO nanoparticles. All sensors had limited interference from humidity with response averaging below $\Delta R/R_o$ of 10%.

5.3.4 Ag Catalyst Effect on the ZnO/SWNT Hybrid System

Surface functionalization with Silver metal catalyst was performed at 0.5, 1, 5, 50, and 500μC on bare SWNTs and ZnO coated SWNTs, where ZnO was first deposited at 20μC. Silver depositions were fast, lasting less than 5 second for the largest charge, when deposited at charges from 0.5 to 5μC the resistances of the SWNT and ZnO/SWNT networks were relatively unchanged due to the small amount of material incorporated on the surface of the SWNTs, represented in figure 5.11. However, when Ag was deposited at charges of 50- 500μC, the final resistance of the device decreased due to the complete bridging of the metal across the gold electrodes. Figure 12 (A) - (H) displays SEM images showing the morphological differences and providing a snapshot portrayal of the growth progression of the Ag/SWNTs and Ag/ZnO/SWNT structures with increasing applied charge. When Ag is deposited on bare SWNTs, the growth begins with multiple particle formation, with increasing charge new nuclei are formed, and at even larger applied charges the existing particles rapidly grow coalescing together until bridging across the electrode gap, as demonstrated in figure 5.12 (A) – (D). Figure 12 (D) clearly shows the large Ag grains and multitude of particles adhering and interconnecting across the gold pads.

When Ag was sequentially deposited on to ZnO/SWNT structures, there was first small particle formation throughout followed by coalescence of neighboring particles until bridging occurred at the largest charge. By comparison of the SEM images, the growth rate of the Ag catalyst appeared slower with the existence of ZnO, and the surface morphology was drastically rougher with a flake-like nodular appearance and the particle size/grain size was dramatically smaller in size compared to the singular deposition of Ag, demonstrated in figure 5.12 (E) – (H). The average particle size for the Ag/SWNT system increased from 56.8±27.9nm to 1098.3±518.9nm while the particle density decreased from 20.3±2.9 to 1.7±0.6 particles per bundle of SWNTs with increasing applied charge from 1 to 500μC. When Ag was deposited on the surface of ZnO/SWNTs, the particle size had a similar effect as the singular metal with an increase from 73.9±1.3nm to 1297.8±461.5nm while the particle density decreased from 7.8±1.3 to 1.41±0.5 particles per SWNT bundle with increasing charge. In the case where Ag was sequentially added, initially the particle density was ~2.5 times lower than in the absence of ZnO, suggesting a variant growth mechanism due to the differing surface energy provided by the metal oxide.

Room temperature sensing performance of the Ag/SWNT and Ag/ZnO/SWNT hybrid structures was performed on low molecular weight molecules of interest. Typical sensor responses are demonstrated in figure 5.14 (A) and (C) for Ag/SWNT and Ag/ZnO/SWNT hybrid structures deposited at various charges, respectively. The corresponding calibration curves towards NO_2 are shown in figure (B) and (D). Most notably, there is charge dependant sensitivity towards H_2S and NO_2 from both the

Ag/SWNT and Ag/ZnO/SWNT hybrid structures. In the absence of ZnO, hybrid structures are more sensitive at smaller charges, while when incorporated with ZnO, the Ag/ZnO/SWNT hybrid structures are most sensitive when Ag is deposited at larger charges. Figure 5.15 portrays the compiled sensing performance of all the various hybrid structures towards H_2S, SO_2, NO_2, NH_3 and 75% humidity, where the concentrations of the low molecular analytes are displayed at OSHA's permissible exposure limits.

5.4 Conclusion

Sequential functionalization of ZnO/SWNT hybrid structures with metal catalyst (Au, Pt, Ag and Pd) was performed at charges ranging from -0.5μC to -500μC. The surface morphology, growth mechanism and room temperature sensing performance were investigated as a function of charge, and presence or absence of seeded metal oxide. In the case of the Au and Ag catalyst, there was a charge dependent sensing behavior and specificity towards H_2S and NO_2. The metal-SWNT structures were most sensitive at smaller charges and the metal-ZnO/SWNT hybrid structures experiencing higher sensitivities when the metal is deposited at larger charges. With incorporation of the Pt catalyst, the sensing behavior was dramatically suppressed for H_2S, where Pt/SWNT structures outperformed the Pt/ZnO/SWNT sensors towards H_2S and NH_3. Interestingly the sensing performance was independent of the applied charge for both sets of hybrid structures.

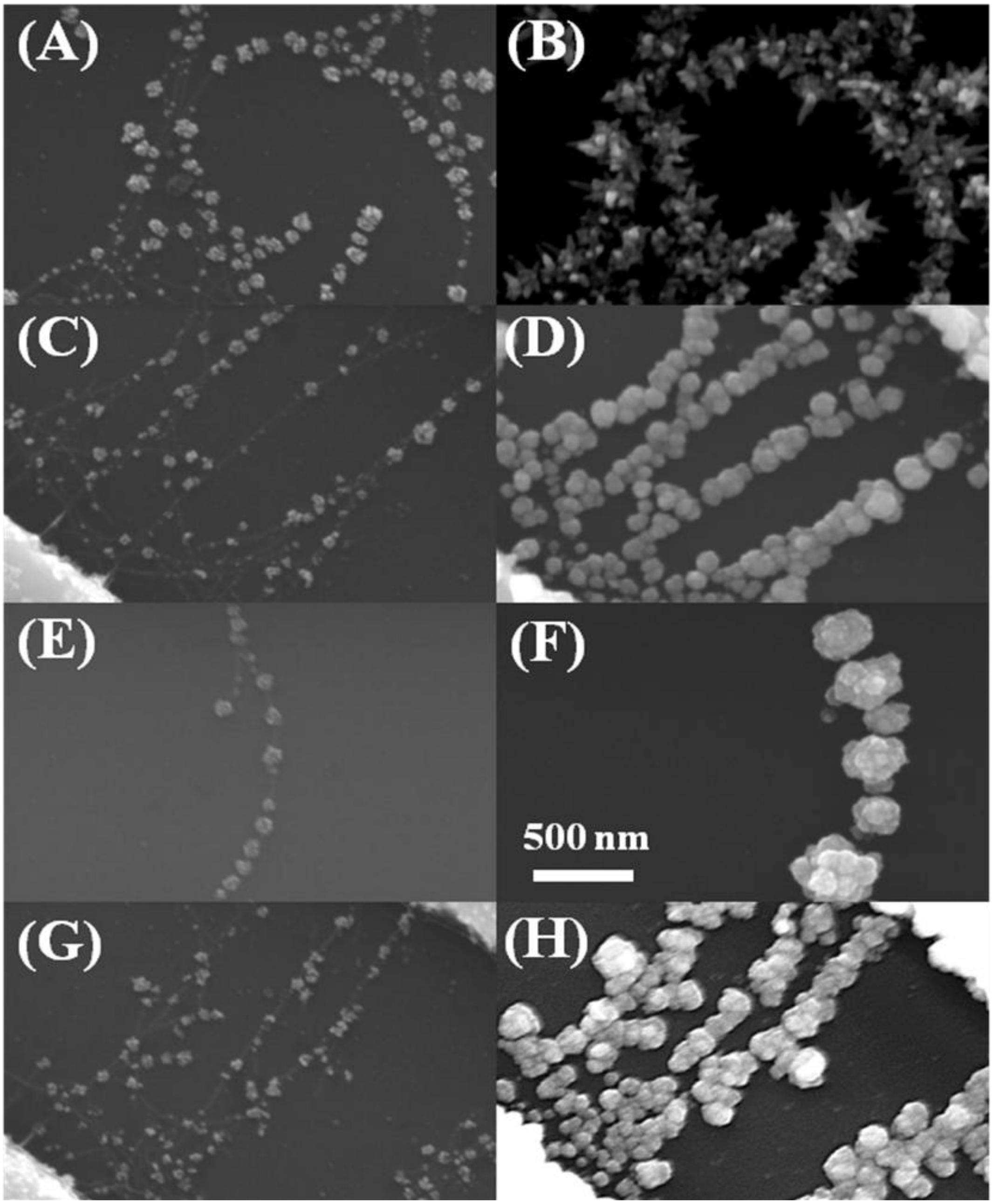

Figure 5.1. SEM micrographs of (A) Au/SWNT , (B) Au/ZnO/SWNT, (C) Pt/SWNT, (D) Pt/ZnO/SWNT, (E) Pd/SWNT, (F) Pd/ZnO/SWNT, (G) Ag/SWNT, and (H) Ag/ZNO/SWNT hybrid structures. The scale bar represents 500 nm.

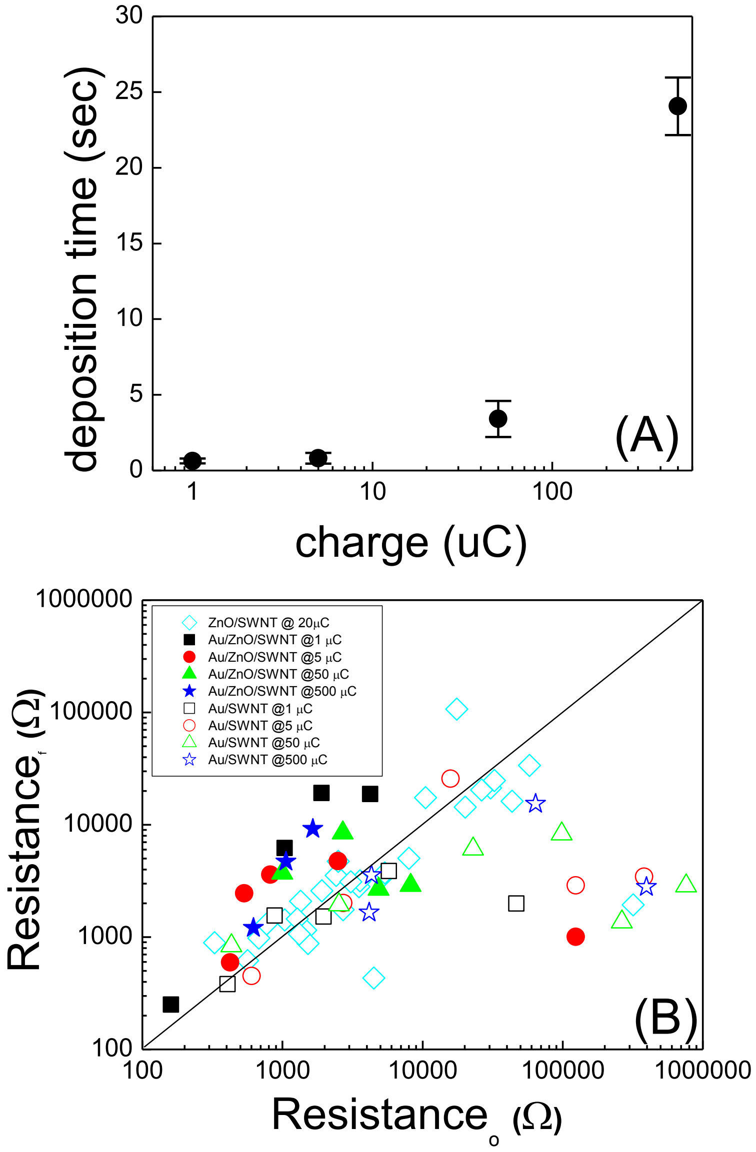

Figure 5.2. (A) Deposition time as a function of charge for Au deposition on ZnO/SWNTs. (B) Resistance distribution after functionalization of SWNTs with ZnO, Au and Au + ZnO at various Au charges.

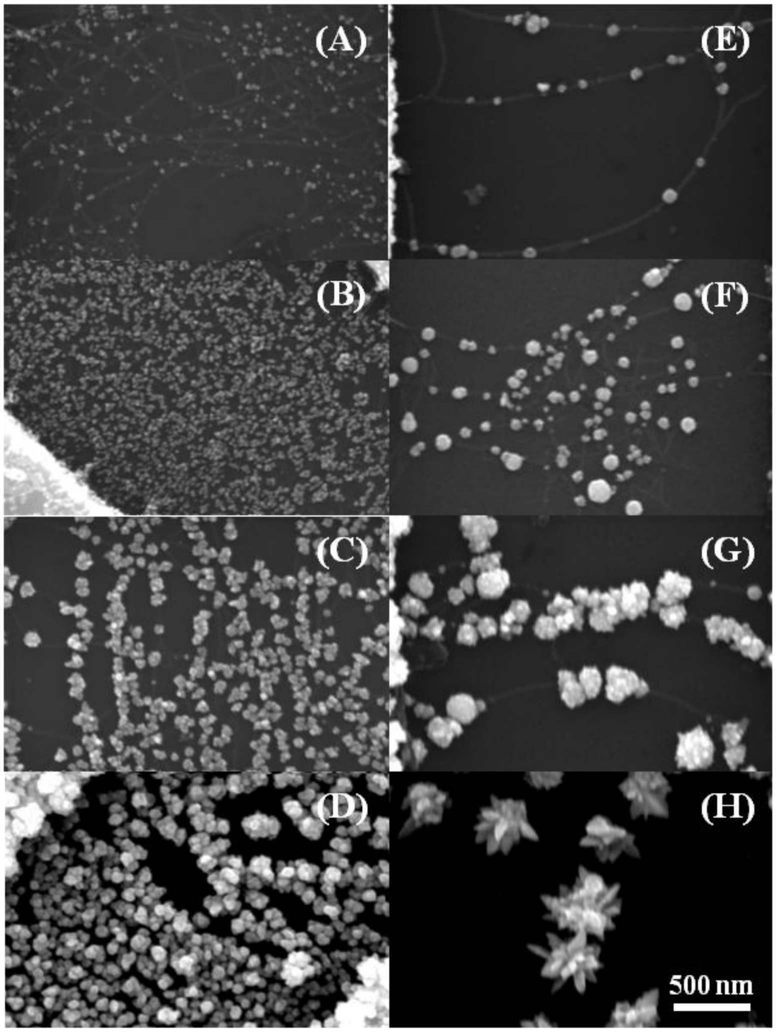

Figure 5.3. SEM micrographs of Au/SWNT hybrid system at (A) -1.0 μC, (B) -5.0 μC, (C) -50 μC, (D) -500 μC; and Au/ZnO/SWNT hybrid system at (E) -1.0 μC, (F) -5.0 μC, (G) -50 μC, (H) -500 μC. The scale bar represents 500 nm.

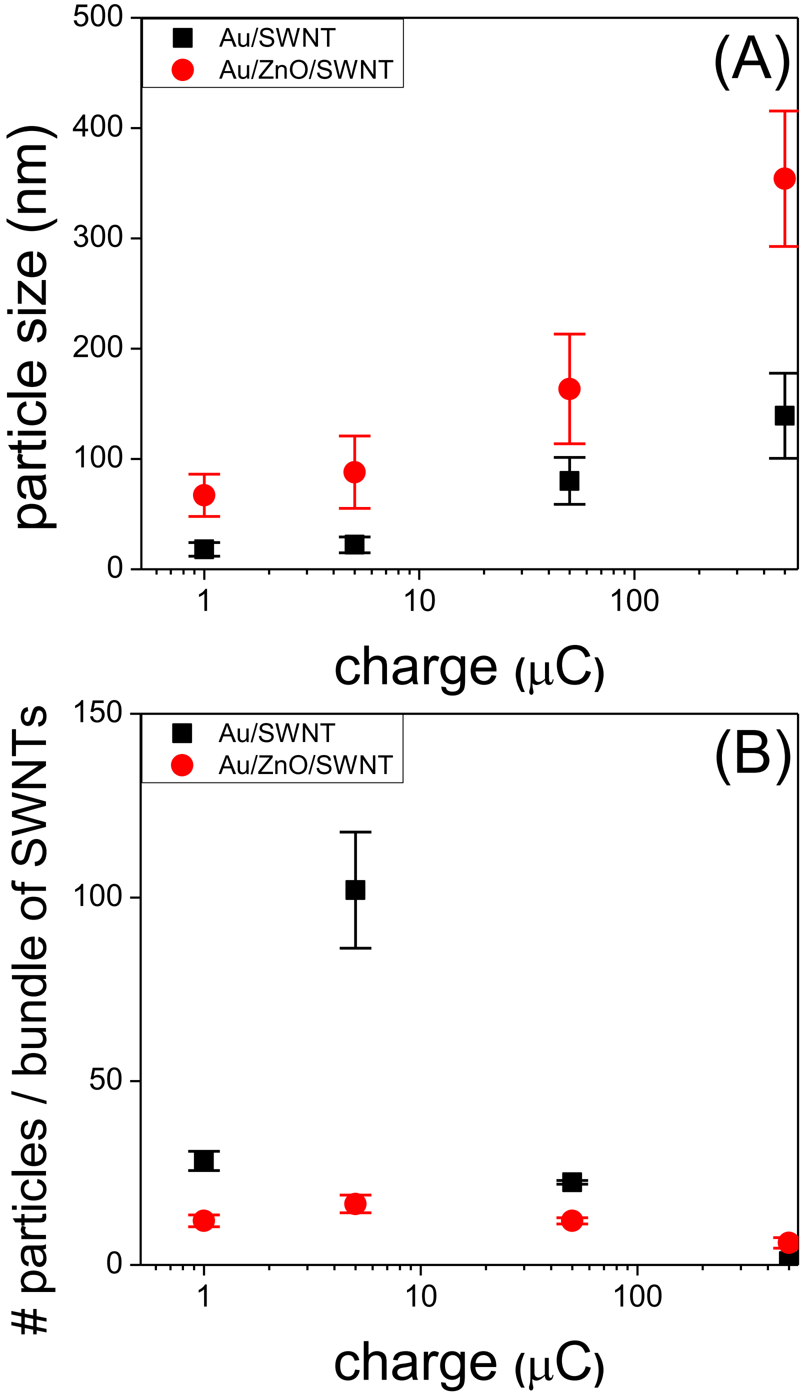

Figure 5.4. (A) Particle size and (B) particle density distribution of Au/SWNT (square symbol) and Au/ZnO/SWNT (circle symbol) hybrid structures as a function of applied charge.

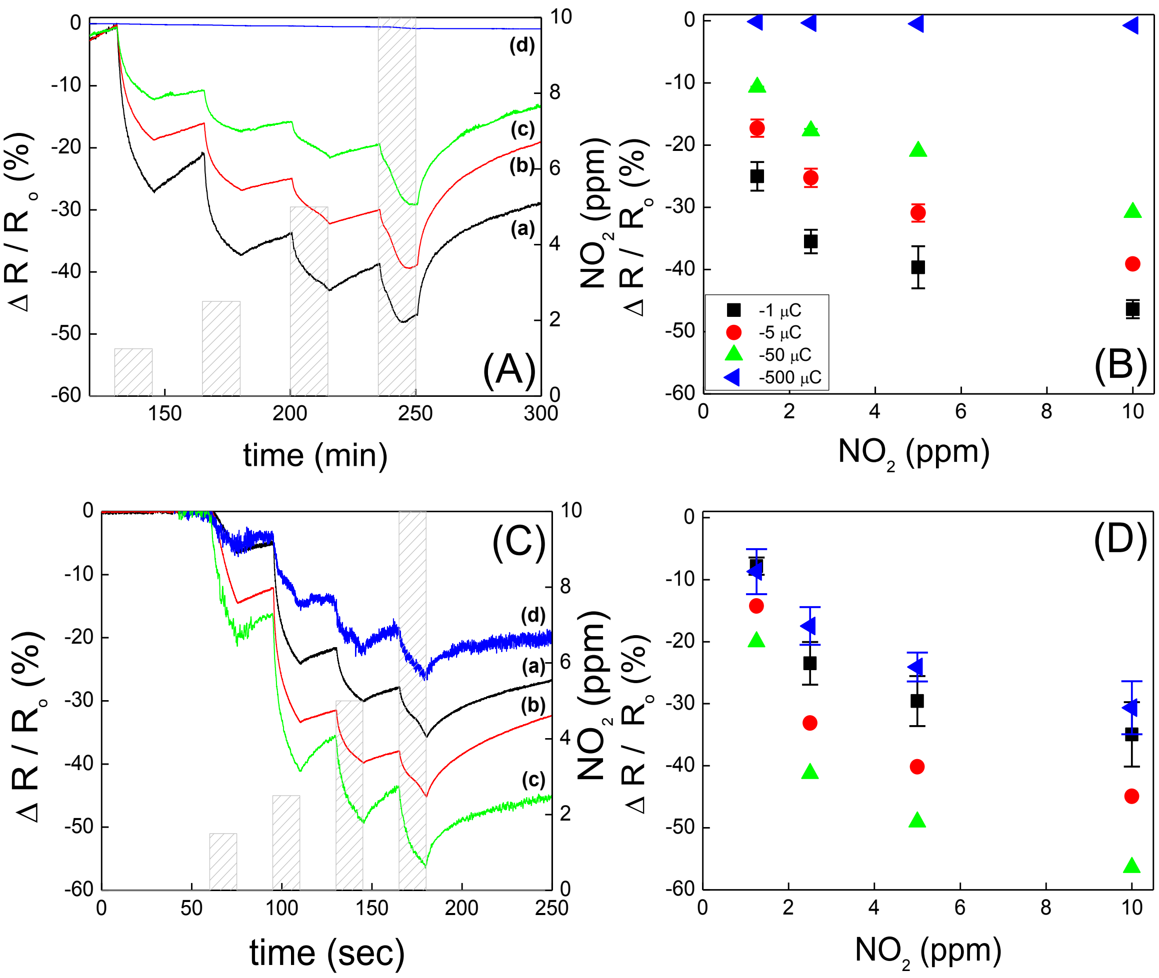

Figure 5.5. Typical sensor response of (A) Au/SWNT hybrid system and (C) Au/ZnO/SWNT hybrid system at (a) -1.0 µC, (b) -5.0 µC, (c) -50 µC and (d) -500 µC of Au deposition towards NO_2. Calibration curves of (B) Au/SWNT and (C) Au/ZnO/SWNT hybrid sensors towards various exposures of NO_2.

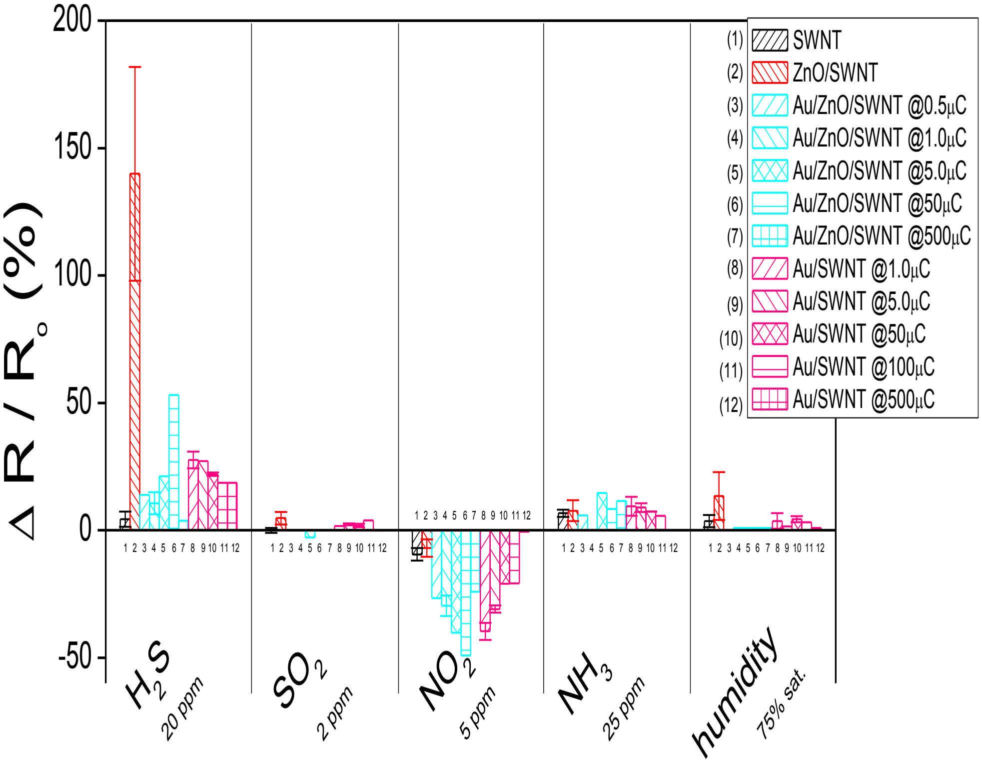

Figure 5.6. Mean response and standard deviation of bare SWCNT, Au/SWNTs, and Au/ZnO/SWNT hybrid systems to low molecular weight molecules. The concentrations were determined by exposure limits set by OSHA. Standard deviations were taken from four samples.

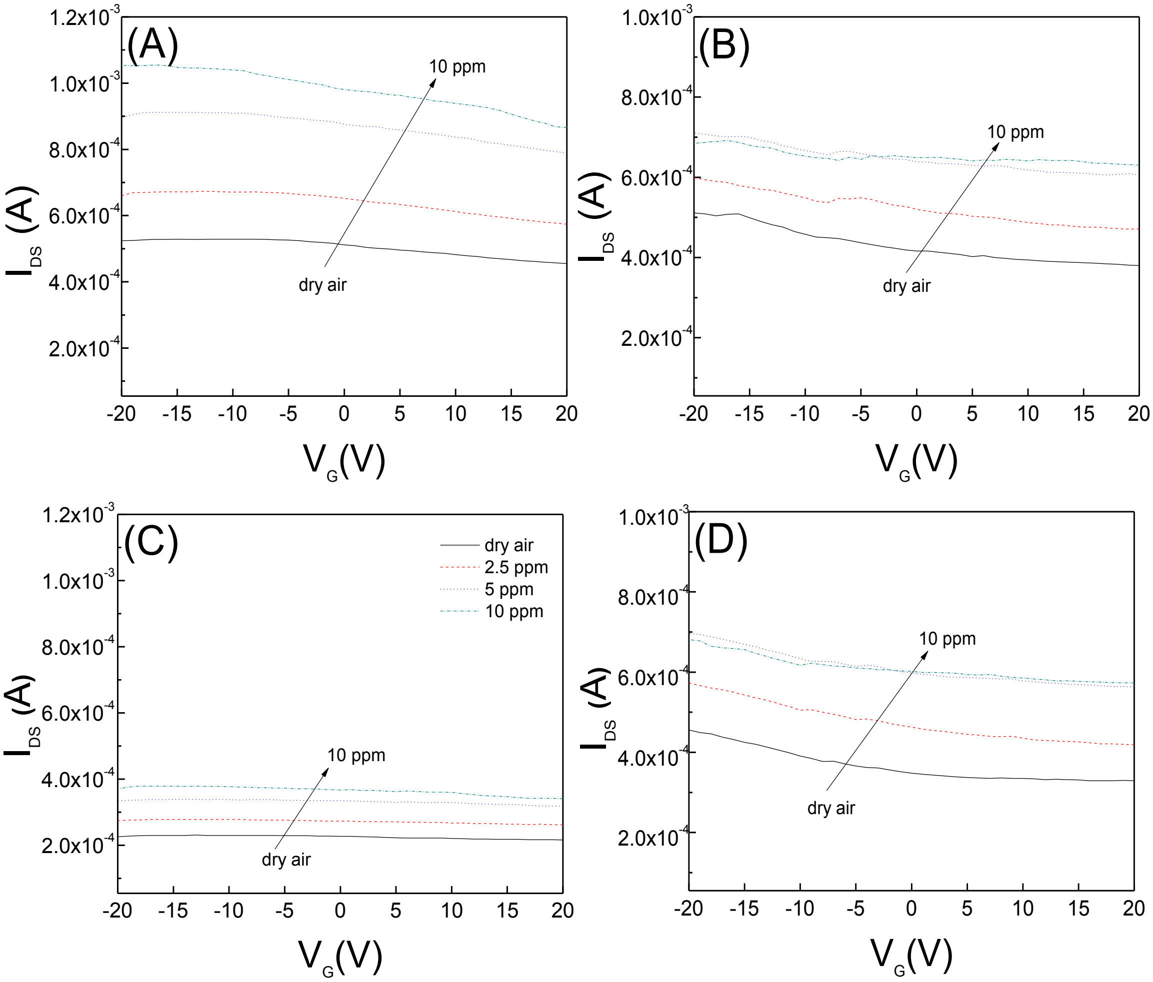

Figure 5.7. FET mechanistic sensing towards NO_2 of Au/SWNTs with Au deposited at (A) 1μC, (C) 50 μC and Au/ZnO/SWNT hybrid network with Au deposited at (B)1μC and (D) 50 μC. Experiments were performed at a V_{DS} of 1volt.

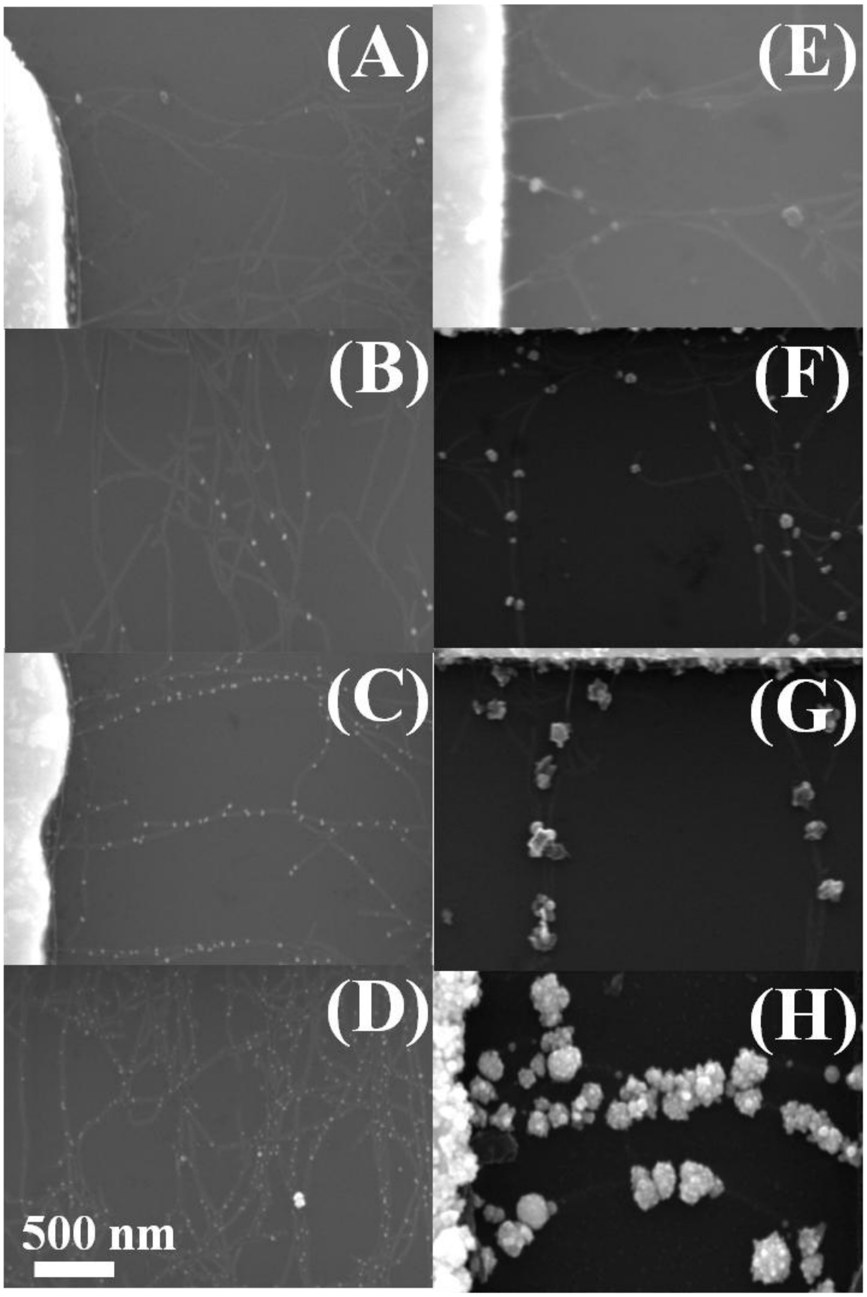

Figure 5.8. SEM micrographs of Pt/SWNT hybrid system at (A) 1.0 μC, (B) 5.0 μC, (C) 50 μC, (D) 500 μC; and Pt/ZnO/SWNT hybrid system at (E) 1.0 μC, (F) 5.0 μC, (G) 50 μC, (H) 500 μC. The scale bar represents 500 nm.

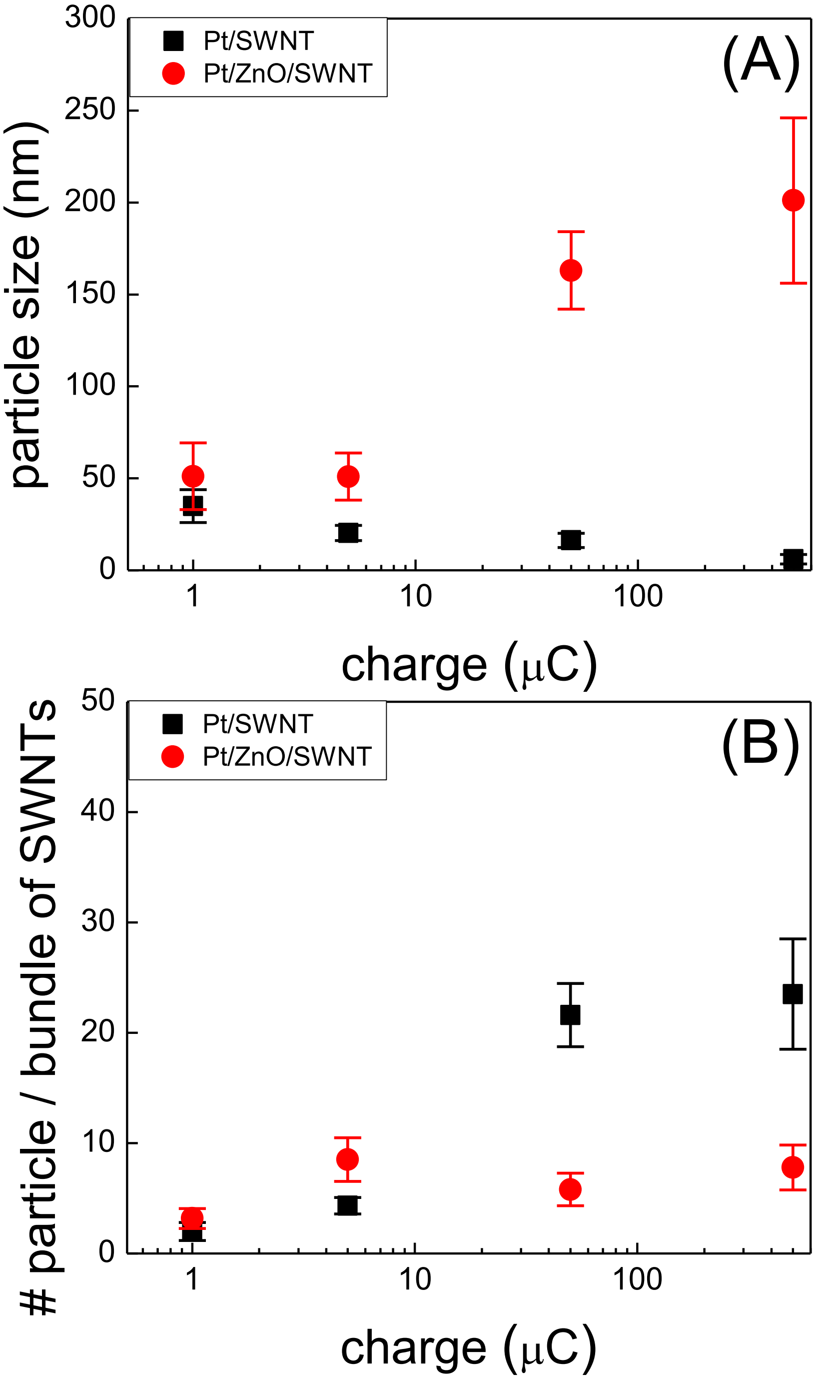

Figure 5.9. (A) Particle size and (B) particle density distribution of Pt/SWNT (square symbol) and Pt/ZnO/SWNT (circle symbol) hybrid structures as a function of applied charge.

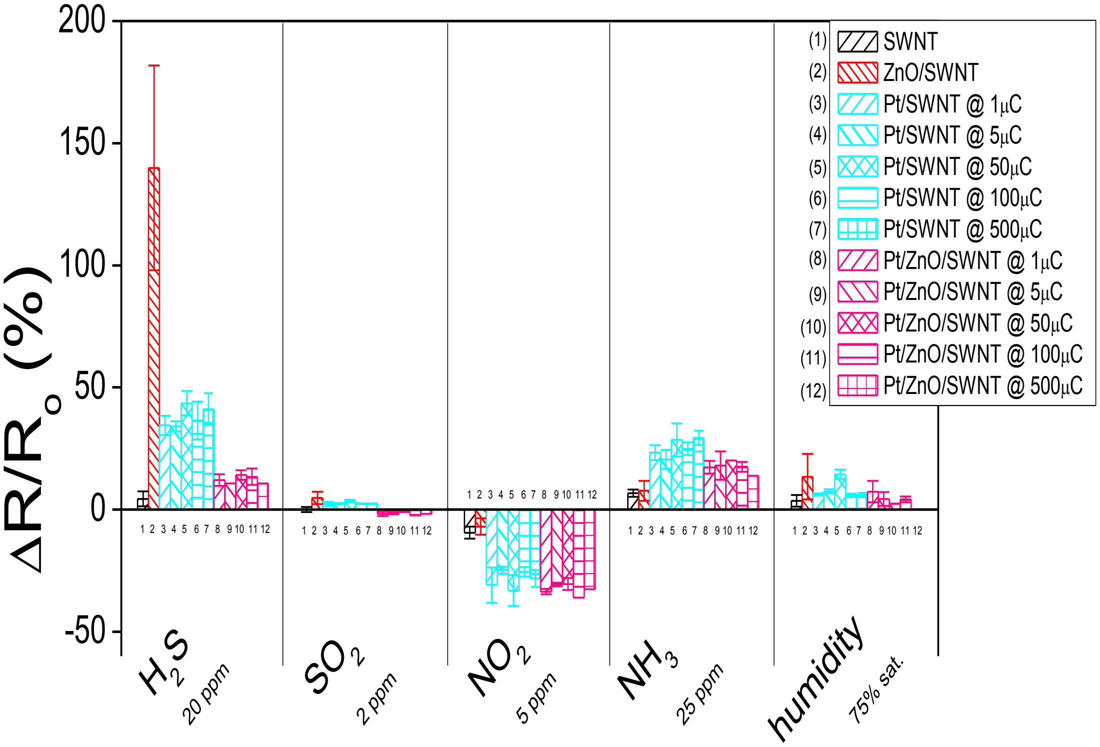

Figure 5.10. Mean response and standard deviation of bare SWNTs, Pt/SWNTs, and Pt/ZnO/SWNTs hybrid systems towards low molecular weight molecules. The concentrations were determined by exposure limits set by OSHA. Standard deviations were taken from four samples.

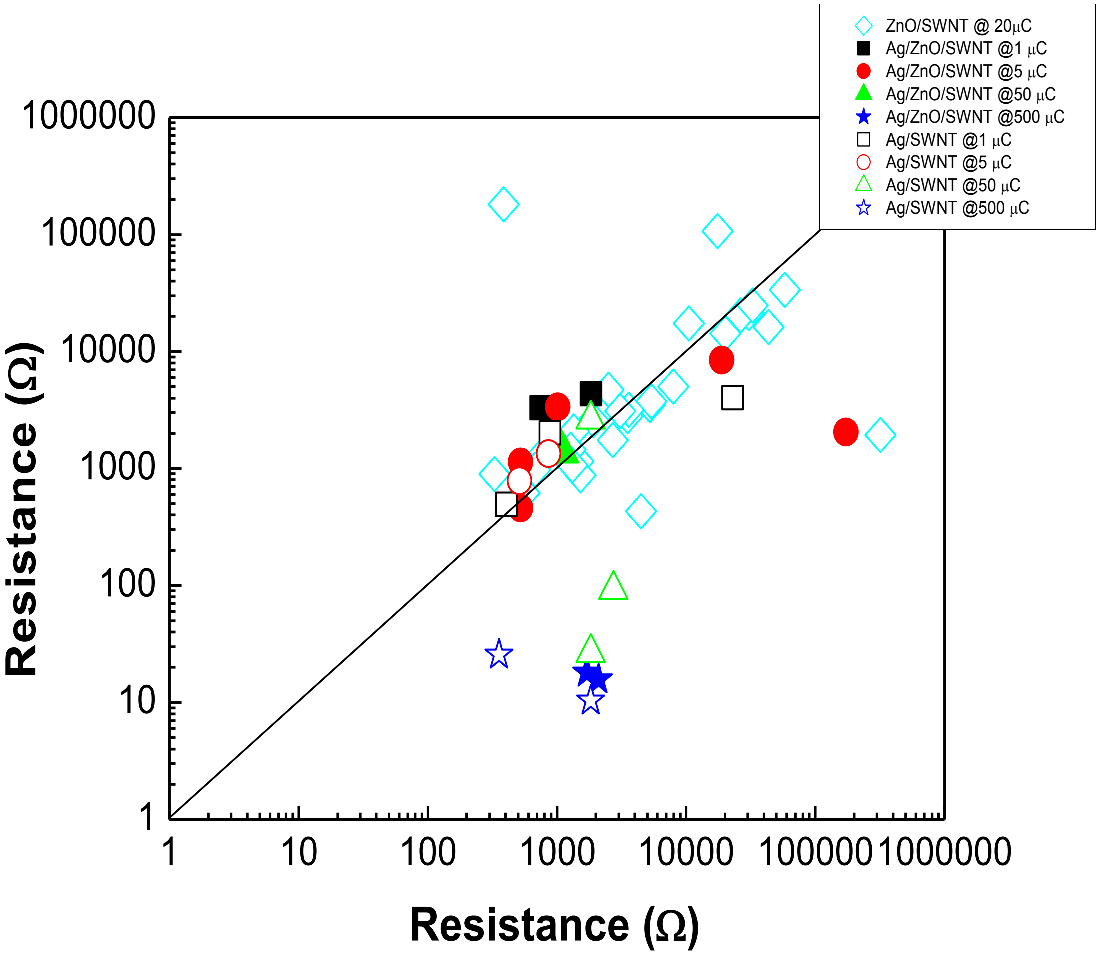

Figure 5.11. Resistance distribution after functionalization of SWNTs with ZnO, Ag and Ag + ZnO at various Ag charges.

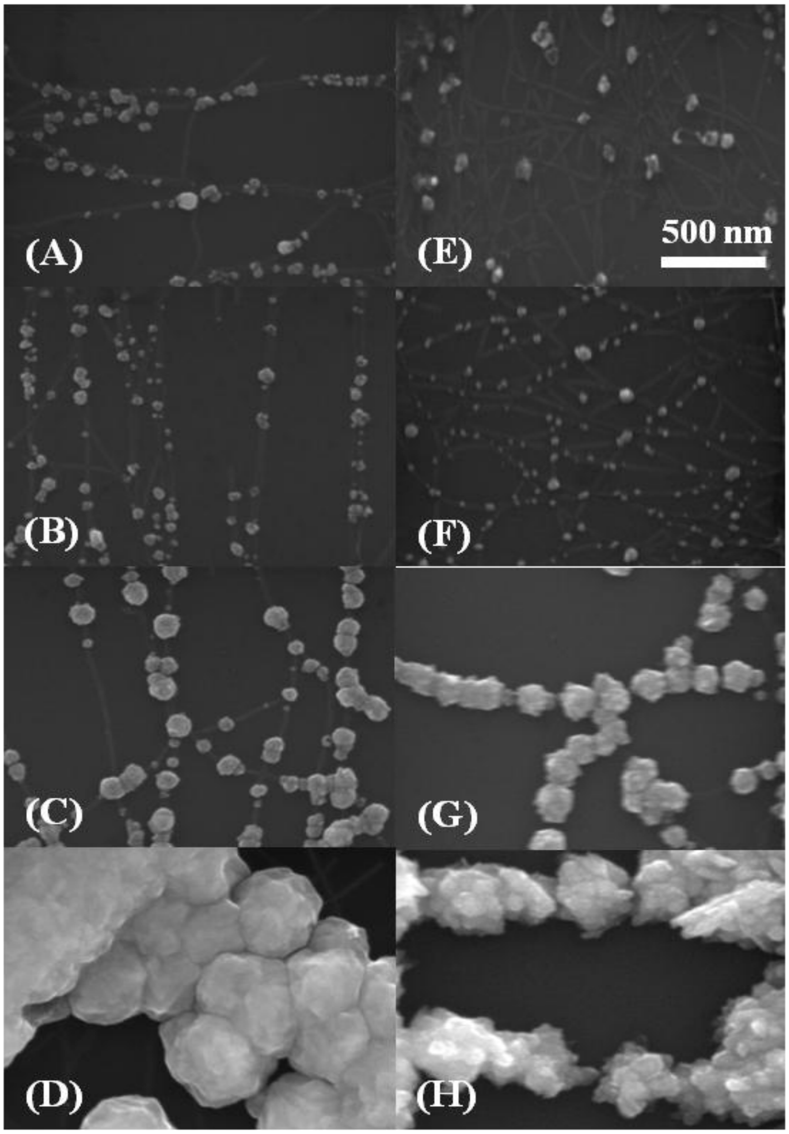

Figure 5.12. SEM micrographs of Ag/SWNT hybrid system at (A) -1.0 μC, (B) -5.0 μC, (C) -50 μC, (D) -500 μC; and Ag/ZnO/SWNT hybrid system at (E) -1.0 μC, (F) -5.0 μC, (G) -50 μC, (H) -500 μC. The scale bar represents 500 nm.

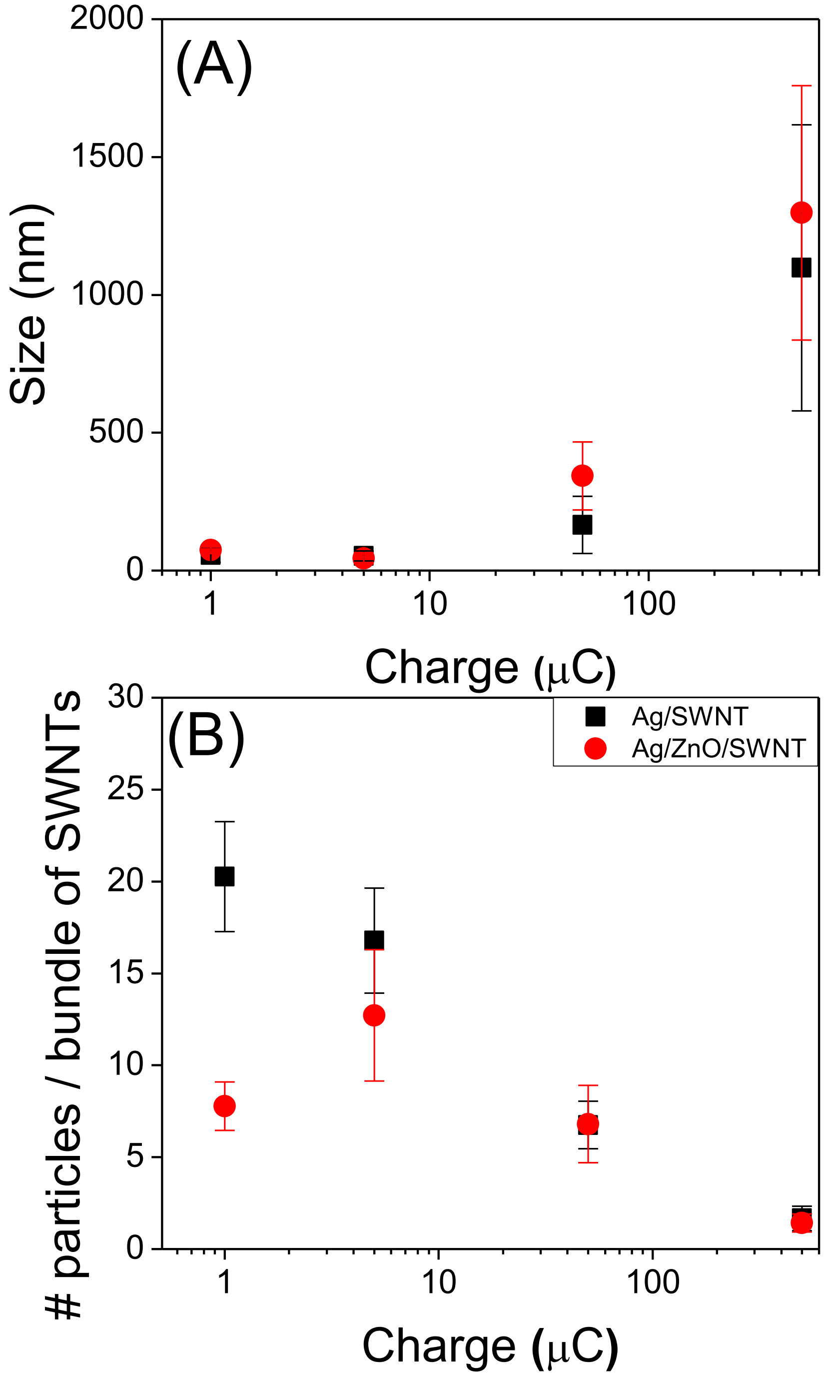

Figure 5.13. (A) Particle size and (B) particle density distribution of Ag/SWNT (square symbol) and Ag/ZnO/SWNT (circle symbol) hybrid structures as a function of applied charge.

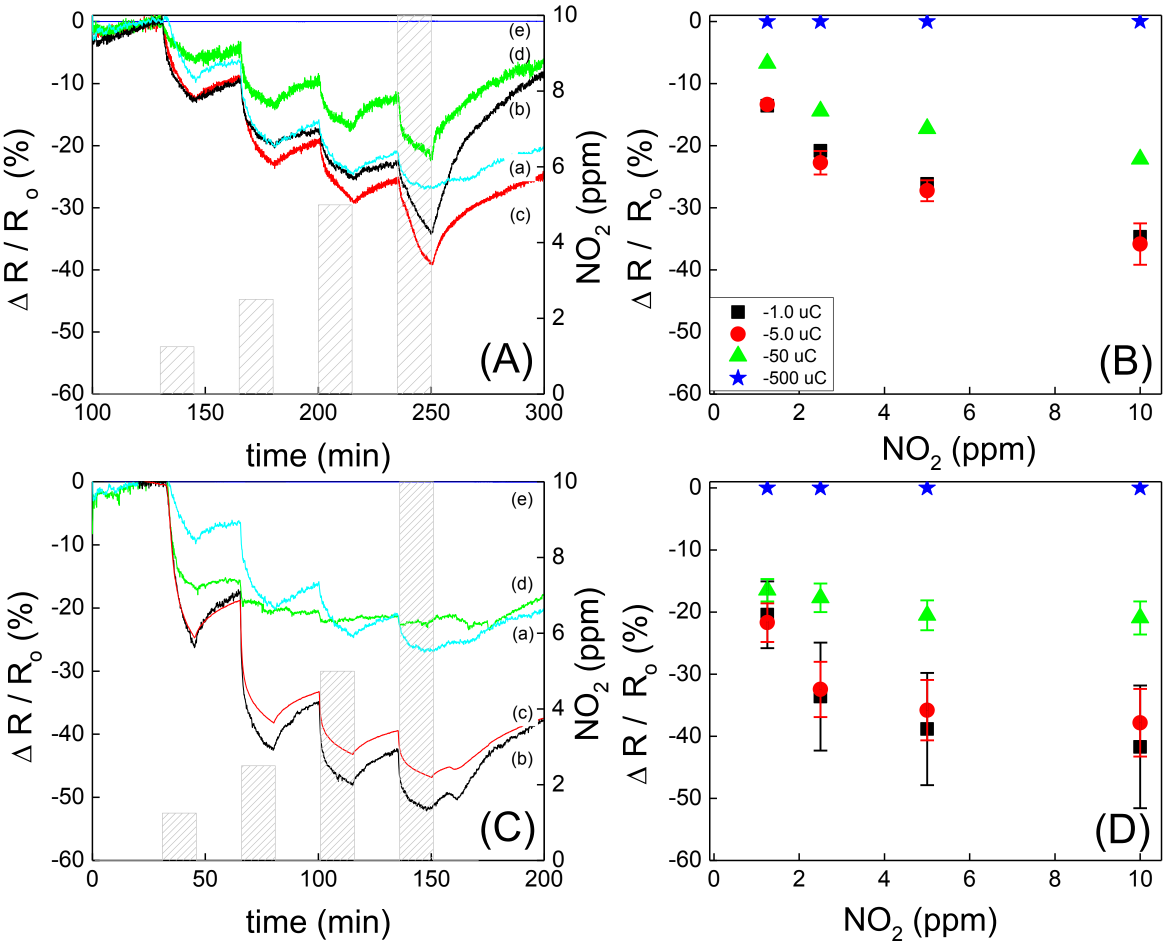

Figure 5.14. Typical sensor response of (A) Ag/SWNT system and (C) Ag/ZnO/SWNT hybrid system at (a) bare SWNT, (b) -1.0 μC, (c) -5.0 μC, (d) -50 μC and (e) -500 μC towards NO_2. Calibration curves of (B) Au/SWNT and (C) Au/ZnO/SWNT hybrid sensors towards various exposures of NO_2.

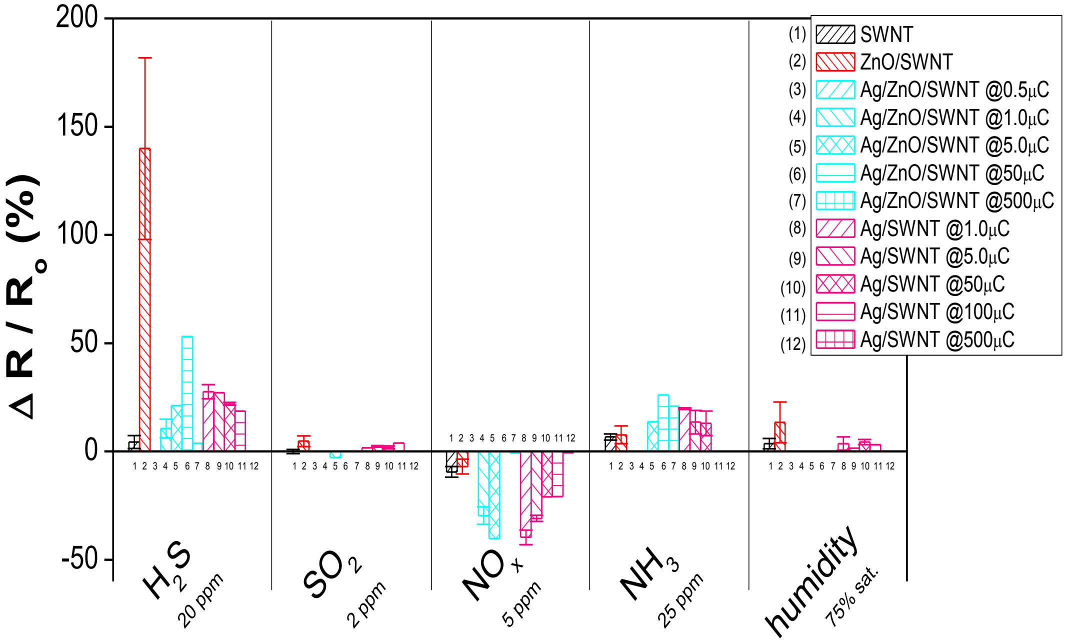

Figure 5.15. Mean response and standard deviation of bare SWNTs, Ag/SWNTs, and Ag/ZnO/SWNTs hybrid systems towards low molecular weight molecules. The concentrations were determined by exposure limits set by OSHA. Standard deviations were taken from four samples.

CHAPTER 6:

METAL-METAL SEQUENTIAL SURFACE FUNCTIONALIZATION OF SWNTS STRUCTURES

Abstract

Multiple metals were strategically deposited to understand the behavior of binary/dual metal catalyst and metal catalyst sequence on sensing performance. Sequential electrochemical functionalization of silver and palladium catalyst was performed on gold nanoparticle-decorated carbon nanotube networks in an attempt to improve sensitivity and impart selectivity towards analytes of interest. Chemical functionalization with mercaptohexanol was performed to passivate the native gold nanoparticles and thus allow side by side functionalization of the secondary metal catalyst. However it was observed that the MCH preferentially adhered on to the SWNTs instead of the gold nanoparticles and thus forcing sequential deposition to encapsulate the original gold nanoparticle creating Ag/Au/SWNTs and Pd/Au/SWNTs hybrid structures, in addition to suppressing new metal nuclei to form on the surface of bare SWNTs.

The sequence in electrochemical deposition of gold, silver and palladium revealed morphological differences and distinctive sensing behavior stemming from the order of

deposition and sequence pair. Furthermore, site specific electrodeposition was further exploited by controlling the applied potential of the second material to advantageously control the positioning of the sequential metal catalyst.

6.1 Experimental

6.1.1 Metal Nanoparticle Deposition and Material Characterization

Sensor arrays were prepared on dies containing sixteen lithographically fabricated Au microelectrode pairs with 3 μm gaps. The substrate architecture allowed for individual addressability and sensor assembly/synthesis without cross contamination between adjacent devices, the details of which have been described elsewhere [160]. Commercially available carboxylated single walled carbon nanotubes (SWNTs) were obtained from Carbon Solutions Inc. and dispersed in dimethylformamide (DMF). The SWNT suspension was prepared by addition of 0.2 mg of SWNTs to 20 mL of N,N-dimethylmethanamide (DMF). The contents were sonicated in a glass vial for 90 minutes using a VWR model 50D sonicator. All 20 mL of the SWNT suspension were transferred to a 50 mL Teflon centrifuge tube and centrifuged for 90 minutes at 15000 RPM and 23°C using a Beckman J2-HS centrifuge. Immediately after centrifugation, 10 mL of the supernatant was carefully removed and placed in a glass vial. The supernatant was additionally sonicated for 60 minutes prior to use.

SWNTs were aligned across the electrode gaps via alternating current dielectrophoretic alignment by placement of a 1.5 μL drop of SWNT suspension across the electrodes, applying 1 V_{pp} and 4 MHz (Keithley 3390 AC generator, 50 MHz arbitrary waveform generator), and the device resistance was monitored by administering the alignment time. Following SWNT alignment, the sensors were rinsed with DI water twice to remove residual DMF and annealed at 300^{o}C for 60 minutes under reducing environment (5% H_2 / 95% N_2) to reduce contact resistance.

Surface functionalization of the metal nanoparticles was performed by electrochemical functionalization in a three electrode configuration, unitizing the pair of gold pads as the working electrodes, a Pt wire as the counter electrode and a chlorinated Ag/AgCl wire as the reference electrode. Deposition of gold nanocatalysts was performed by using a commercially available ready to use electroplating electrolyte from Technic Inc. (CA), with neutral ph. A 5 μL drop of the Au plating solution was placed across the two electrodes completely covering the Au pads, a potential of -1.0 volts vs. pseudo Ag/AgCl was applied and deposition was terminated by controlling the charge passed through the system at 5μC For deposition of palladium nanoparticles a 5 μL drop of electrolyte composed of 0.47 M $Pd(NH_3)_2Cl_2$ + 58 mM NH_4Cl at pH of 7 (US Patent number 4487665) was utilized as the Pd source, -1.0 volts versus the Ag/AgCl reference electrode was applied and the charge was controlled at 5μC. Silver nanoparticles were electrodeposited by use of ready to use electroplating electrolyte from Technic Inc. (CA), at a potential of -0.3 volts vs. pseudo Ag/AgCl, with applied charge of 5μC. After functionalization of the first metal, the sensor array was lightly rinsed with nanopure water and dried with purified nitrogen gas. Sequential electrodeposition of a second metal was then performed using the same conditions and solutions described above. Mercaptohexanol (MCH) was prepared by adding of MCH in ethanol (EtOH) resulting to mixture concentration of 1mM MCH. In the experiments where chemical functionalization of the system was used, the Si chip was immersed in 10 mL of 1mM

MCH solution for 12 hours prior to the addition of the second metal deposition. Following the incubation and before sequential electrodeposition of the second metal, the Si chip was rinsed lightly with EtOH to remove residual MCH, and allowed to dry. Scanning electron microscopy (SEM) and energy dispersive X-ray spectroscopy microanalysis (EDAX) was used for verification of catalyst deposition and nanoparticle visual quantification.

6.1.2 Gas Sensing Studies

Room temperature gas sensing studies were performed on the functionalized sensor array by integration of the sensor chip with a pin IC adapter via wire bonding (West Bond Inc. Model 7443A) and subsequent electrical connection to a bread board in a custom made sensing system [161]. Each sensor was subjected to 1.0 V (DC) and the resistance was continuously recorded every 0.2 seconds simultaneously for the sixteen sensors by use of Keithley 236 source measurement unit controlled by a LabView program. A base line was achieved with exposure of dry air as the carrier gas and different analyte concentrations were attained by subsequent dilutions with the carrier gas. Exposure times were limited to 15 minutes and recovery time to 20 minutes; total gas flow rate was kept constant at 200 sccm for all experiments. Analyte and carrier gas flow rates were regulated by mass flow controllers (Alicat Scientific Incorporated) [161, 171].

6.2 Results and Discussion

Multiple metals were systematically investigated to understand the behavior of binary/dual metal catalyst and metal synthesis sequence on sensing performance. Furthermore, site specific electrodeposition was exploited as to advantageously control the position of the second metal catalyst.

6.2.1 Chemical Functionalization of SWNTs and Metal Catalysts: Silver as the Sequential Catalyst

Gold nanoparticles were functionalized on the surface of SWNTs at 5 μC, demonstrated in the SEM images of figure 1 A and C. Sequential electrodeposition of the second metal catalyst was performed on as-synthesized Au/SWNT structures and Au/SWNT structures incubated with mercaptohexanol (MCH). Au/SWNT structures were treated with MCH in an attempt passivate the Au nanoparticle and selectively deposit the second metal catalyst alongside the first. Upon sequential addition of Ag at 5 μC on the Au/SWNTs and in the absence of MCH, there is notable increase in particle size of the initial Au particle, demonstrated in figure 6.1 B. The SEM images taken before and after the addition of the second metal at the exact sample location show the sequential addition of Ag to occur preferentially on the surface of Au, indicative by the increase in particle size and the absence of new nucleation sites. Un-expletively, the same deposition behavior was observed when Au/SWNT structures were surface treated with MCH, where the second Ag nanoparticle deposited on the surface of Au and not on

SWNTs, demonstrated in figure 6.1 D. Suggesting either the complete removal of MCH during the post rinse with ethanol or adherence of MCH to the surface of the SWNTs instead of the Au nanoparticles.

The particle distribution of the Ag/Au/SWNTs was unaltered while the difference in particle size was slightly affected by the chemical treatment with MCH. Ag nanoparticles grown in the absence of MCH had an overall particle size increase of 32.43 ± 2.80 nm, while in the presence of MCH, the overall particle size increased by 37.79 ±0.28 nm, demonstrated in figure 6.2. The surface roughness and growth mode appeared independent of the chemical treatment. Although the chemical treatment with MCH did not preferentially passivate the Au nanoparticles to allow side by side nanoparticle decoration, it did interact with SWNTs forcing the Ag metal nanoparticle to selectively deposit on top of the Au. Additionally, MCH chemically functionalize SWNTs providing a different form of surface functionalization, most notably seen in the device sensing performance.

Figure 6.3 is a histogram depicting the average sensing performance of bare SWNTs, Au/SWNT, Ag/SWNT, and Ag/Au/SWNT hybrid structures with and without MCH. The responses displayed are towards OSHA's permissible exposure limits of H_2S, NO_2, NH_3, and SO_2, and the average sensor performance was determined from 4-8 simultaneously tested sensors. The two main variables affecting the sensing performance were the presence and absence of the sequential catalyst and the chemical treatment with MCH. Ag/SWNT and Au/SWNT structures showed increased sensitivity towards H_2S and NO_2 compared to bare SWNTs. In the absence of chemical treatment, the sensitivity of Ag/Au/SWNT hybrid structures was nearly doubled towards H_2S and slightly enhanced towards NO_2, while unaffected towards NH_3 and SO_2, when compared to Ag/SWNT and Au/SWNT hybrid structures. Thus the addition of the sequential catalyst had an additive sensing behavior towards H_2S, possibly due to the combine interaction of H_2S with Ag and Au particles since the individual metal-SWNT structures independently interact with the analyte.

In the presence of MCH, the sensing behavior of unfunctionalized SWNT changed dramatically when compared to untreated bare SWNTs. For instance, the sensitivity towards H_2S and SO_2 was suppressed while the sensitivity was tripled for NH_3 and increased six fold towards NO_2, indicating that the chemical surface modification of the SWNTs with MCH effects sensor behavior. Interestingly, with either gold or silver nanoparticles followed by MCH incubation, the sensing response towards H_2S is decreased by half compared to unmodified Ag/SWNTs or Au/SWNT systems. For NO_2, the response of MCH/Au/SWNT and MCH/Ag/SWNT structures is doubled while no response is observed towards NH_3 and SO_2, compared to the unmodified structures. When the silver catalyst was incorporated in the presence of MCH, the sensing performance of the Ag/MCH/Au/SWNT hybrid structures showed distinct selectivity and synergistic response towards H_2S with $\Delta R/R_o$ of 121.9±19.9 %, about a ten-fold increase from the single metal/SWNT networks and binary metal-metal/SWNT hybrid structures. In summary, the chemical modification of the SWNTs structures with MCH improved the sensitivity towards NO_2 independent of the metal or sequential catalyst. On the other hand, the combination of both MCH and the sequential catalyst dramatically improved the sensing sensitivity towards H_2S, a small response was observed for NH_3, while little to no response towards SO_2, demonstrated in figure 6.3.

6.2.2 Chemical Functionalization of SWNTs and Metal Catalysts: Palladium as the Sequential Catalyst

Beginning with gold nanoparticles deposited at 5 μC, palladium nanoparticles were subsequently sequentially deposited as the second catalyst at 5 μC in the presence and absence of mercaptohexanol (MCH), as previously described for the silver catalyst. Figure 6.4 shows SEM images are taken on the exact location before and after the second metal catalyst in the absence and presence of MCH. Figure 6.4 (A) shows the gold nanoparticles deposited on SWNTs and figure 6.4 (B) shows the sequential deposition of palladium catalysts in the absence of chemical treatment. In the absence of MCH the SEM images demonstrate the growth of new palladium nucleation sites as well as deposition over the pre-existing gold nanoparticles. Thus palladium does not preferentially deposit on either gold or on the bare portions of the SWNTs, and instead deposits continuously throughout. Similarly as before, when Au/SWNTs were incubated with MCH the deposition of the sequential catalyst preferentially grew on the previous gold nanoparticles with no new nucleation sites on the bare sections of the SWNTs. Indicative from an increased in particle size and nodular particle growth, substantiating the idea that MCH preferentially adsorbs on to SWNTs passivating the bare sections of the nanotubes, as demonstrated in figure 6.4 (C) and (D).

With addition of the second metal catalyst, the average particle size increased from 76.11±16.23nm to 116.67±26.87nm in the absence of MCH and from 64.86±11.98nm to 118.37±24.74nm in the presence of MCH, the large error bars are due to the increased surface roughness shown in figure 6.5. Sequential deposition of the palladium catalyst in the presence of MCH caused a larger particle increase by 53.51±12.45nm than in the absence of chemical treatment. We speculate that the rough nodular growth evident from the SEM images demonstrate a patchy evolution by palladium originating from multiple nucleation sites on a single gold nanoparticle.

Figure 6.6 is a histogram displaying the typical sensor response of SWNTs, MCH, Au, Pd, and the combination thereof towards H_2S, NO_2, NH_3, and SO_2 at OSHA's permissible exposure limits. When looking at the Au and Pd nanoparticle hybrid systems, the senor response of the single metals is mostly enhanced towards NO_2 and NH_3 compared the bare SWNT networks. Most notably, with the introduction of palladium as the sequential catalyst, there is an overall increase in sensor response towards NH_3 from $\Delta R/Ro$ of 6.71±1.4% by bare SWNT to 27.2±3.5% for Pd/SWNTs, followed by a synergistic sensor response increase of 42.2±7.6% for Pd/Au/SWNTs. In the presence of chemical treatment, the sensor response of Pd/MCH/Au/SWNT hybrid structures towards H_2S was enhanced possibly due to the nodular nanoparticle growth of the palladium catalyst in the presence of MCH which offers larger surface area available for analyte interaction. Since other hybrid structures show a suppression of sensitivity towards H_2S in the presence of MCH, the chemical treatment does not appear to play a role in the sensor behavior of Pd/MCH/Au/SWNT hybrid structures towards H_2S other than modifying the surface morphology of the catalyst. As previously observed, chemical modification with MCH resulted in enhanced sensor sensitivity towards NO_2, regardless of the metal or metal-catalyst combination.

In summary, sequential electrochemical functionalization of silver and palladium catalyst was performed on gold nanoparticle-decorated carbon nanotube networks in an attempt to improve sensitivity and impart selectivity towards analytes of interest. The Pd/Au/SWNT hybrid structures were most sensitive and selective towards NH_3. Chemical functionalization with mercaptohexanol was performed to passivate the native gold nanoparticles and thus allow side by side functionalization of the secondary metal catalyst. However it was observed that the MCH preferentially adhered on to the SWNTs instead of the gold nanoparticles and thus forcing sequential deposition to encapsulate the original gold nanoparticle creating Ag/Au/SWNTs and Pd/Au/SWNTs hybrid structures, in addition to suppressing new metal nuclei to form on the surface of bare SWNTs. The sensing performance of the chemical treated hybrid structures was investigated and compared to its un-treated counterparts, and revealed that MCH has preferential interaction with NO_2 regardless of the accompanying metal catalysts, while Ag/MCH/Au/SWNTs hybrid structures showed a synergistic effect towards H_2S vapors.

6.2.3 Sequence of Metal Catalysts

To further investigate the metal interaction with the chemical analytes, the sequence of deposition of the functional metals varied and the sensing behavior of the resultant hybrid structures was analyzed. Figure 6.7 (A) & (B) shows SEM images of

Au/SWNTs before and after sequential deposition of the Ag catalysts at the same location, resulting in encapsulated core-shell nanoparticles where the core is the Au particle and the shell is composed of the Ag catalyst. The Ag catalyst preferentially deposited on the surface of Au, with little to no nucleation sites on the exposed surfaces of the SWNTs. When Ag nanoparticles are deposited first, followed by the sequential deposition of Au, the growth primarily originates on the Ag surfaces and grows in a porous rough flower-like manner with few additional nucleation sites on exposed bare SWNTs, demonstrated in figure 6.7 (C) & (D).

The sensing performance of the Ag/Au/SWNTs and Au/Ag/SWNTs hybrid structures was tested towards H_2S, NO_2, and NH_3 at concentrations of $^1/_8$, ¼, ½, 2 times the recommended OSHA permissible exposure limit for that particular analyte. The Ag/Au/SWNTs and Au/Ag/SWNTs were analyzed to determine the dominating effect of the metal responsible for the sensor response towards certain analytes. Figure 6.8 shows the calibration curves obtained for the hybrid structures and demonstrate side by side response of the two systems response to (A) H_2S, (B) NO_2, and (C) NH_3. Both systems have similar sensitivity towards the electron donating analyte NO_2, and differing responses towards electron withdrawing analytes indicating distinct affinities to either H_2S or NH_3 dependent on the outermost catalyst or on the combination there of.

Figure 6.9 is a histogram depicting the compiled sensor responses of Ag/Au/SWNTs, Au/Ag/SWNTs hybrid structures and their single metal counter parts towards various analytes at OSHA's PEL limit. Looking at the Ag/Au/SWNTs hybrid sensors where the silver catalyst is on the exterior, the sensitivity of Ag/Au/SWNT hybrid structures was nearly doubled towards H_2S and slightly enhanced towards NO_2, while unaffected towards NH_3 and SO_2, when compared to Ag/SWNT, Au/SWNT hybrid structures and bare SWNTs. Therefore the addition of the sequential catalyst had an additive sensing behavior towards H_2S, possibly due to the combined interaction of H_2S with Ag and Au particles since the individual metal-SWNT structures independently interact with the analyte. Interestingly, the Au/Ag/SWNTs hybrid structures where Au is the outermost catalyst and Ag is the core nanoparticle, the sensing behavior towards H_2S is suppressed to $\Delta R/R_o$ of 7.45±4.1% while the hybrid response is dramatically increased to 84.47±15.5% $\Delta R/R_o$ towards $NH_{3,}$ sensitivity values are determined at OSHA's PEL. The reduction in sensitivity towards H_2S was unexpected since other works have demonstrated the a strong gold-sulfur interaction, however our sensing results demonstrate that the outer most layer is not the sole contributor to the sensing behavior, instead the sensor response originates from the combination of the dual metals.

The second combination of metal catalysts that was analyzed was the gold-palladium system, figure 6.10 (A) shows SEM images of Au/SWNTs system before and (B) after the sequential deposition of Pd, while figure 6.10 (C) has SEM images of Pd/SWNTs before and (D) after sequential deposition of Au catalyst. For the Pd/Au/SWNTs system the SEM images demonstrate the growth of new palladium nucleation sites as well as deposition over the pre-existing gold nanoparticles, demonstrating that palladium deposits without choice on either gold or on the bare portions of the SWNTs, instead depositing continuously throughout. On the other hand, when Au is sequentially added to Pd/SWNTs to form Au/Pd/SWNTs hybrid structures, gold preferentially nucleated on the preexisting palladium nanoparticles, demonstrated in figure 6.10 (D). Gold deposited on the surface of palladium by multiple nucleation points evident from the multiple small gold nodules on the palladium nanoparticles.

The sensing performance of the Au/Pd/SWNTs and Pd/Au/SWNT hybrid structures are summarized in figure 6.11 (A) - (C), it should be noted that there was little to no response towards SO_2, CO and CO_2 therefore the corresponding calibration curves were not shown. From the selected analytes, the Pd/Au/SWNT hybrid structures had the highest sensitivity towards NH_3 with a $\Delta R/R_o$ of 42.23±7.58% at the PEL compared to NO_2 or H_2S. When the sequence is reversed and gold is the outer most layer of the nanoparticle, the Au/Pd/SWNT hybrid structure's sensitivity towards NH_3 was dramatically enhanced to $\Delta R/R_o$ of 105.5±28.2% at the PEL. Similar to the Au/Ag/SWNT system, the sensor performance of Au/Pd/SWNTs sensors towards H_2S was suppressed to ~1.40±0.2% $\Delta R/R_o$ at the PEL, less than that of bare SWNTs, figure 6.12.

The sequence in electrochemical sequential deposition of gold, silver and palladium revealed morphological differences and distinctive sensing behavior stemming from the order of deposition and sequence pair. For example, in the gold-silver system, the second deposited metal, whether it is gold or silver, preferentially deposited on the first nanoparticle with little to no new nucleation sites along the bare portions of the bare nanotubes. On the other hand, for the gold-palladium system with palladium deposited second, Pd deposited both on the surface of the native gold nanoparticle and on the bare sections of the SWNTs. However when gold was deposited second, it preferentially nucleated on the surface of the palladium nanoparticles only. The sensing behavior towards H_2S, NO_2, NH_3, SO_2, CO and CO_2 was investigated for all of the sequence pairs. Generally, there was no response for CO and CO_2, and minimal response towards SO_2 for all pairs of hybrid structures. It was observed that when silver or palladium was on the outermost surface, the sensing behavior was enhanced compared to the single metal-SWNT structures however no selectivity was imparted. Interestingly, when gold was sequentially deposited on the outermost surface of either gold or silver native nanoparticles, the sensing behavior was synergistically improved towards NH_3 and dramatically suppressed towards H_2S.

6.2.4 Controlling the Position of the Second Metal Particle

Containment of the second metal catalyst was further investigated by controlling the applied deposition potential of the sequential catalyst. For the previous experiments, the deposition conditions for Au, Ag, Pd and Pt were determined from the LSV behaviors on the SWNT networks, however further exploration of smaller and larger applied potentials revealed the ability to consistently and reproductively selectively deposit the second metal. The two hybrid systems that were explored were the Ag/Au/SWNT and Pd/Au/SWNT hybrid structures where Ag and Pd were sequentially deposited at potentials bordering -0.3 V and -0.8 V, respectively.

Figure 6.13 shows SEM images of Ag/Au/SWNT before and after the sequential deposition of Ag deposited at -0.5 V, -0.3 V and -0.1 V versus a pseudo Ag/AgCl reference electrode, the SEM images are taken at the exact location before and after the subsequent Ag metal catalyst. When deposited at the larger voltage of -0.5 V, evident growth on the primary Au nanoparticle is observed as well as new near equal size Ag nanoparticles, whereas when Ag is deposited at -0.3 V deposition is observed only on the surface of the first metal particle with absence of new nucleation sites. The lower potential of -0.1 V indicated insufficient energy to promote growth since no deposition of Ag is observed. Similarly, when Pd is deposited at potentials larger than -1.0 volts, the density of new nucleation sites and the size of existing nanoparticles increases until complete bridging is observed, demonstrated in Figure 6.14. When palladium is deposited at -1.0 V, there is an increase in both the size of the existing particles and introduction of small Pd nanoparticles on the SWNTs, indicating non-preferential deposition of Pd on both the native Au nanoparticles and un-functionalized sections of the SWNTs. With increasing deposition potentials of -1.1 V and -1.2 V, the size and thickness of the Pd shell increased until beaded like structures bridged through the periphery of the SWNTs, with the larger particles consisting of encapsulated Au structures. When deposited at potentials smaller than -1.0 volts, the Pd deposition is confined to the native promoter Au nanoparticle. Evident from figure 6.14 (H) and (J), the deposition of Pd between -0.8 to -0.6 V results in an increase in particle size with nodular/flower like growth of Pd on the outer surface of Au nanoparticles. New particles are not observed under the highest SEM magnification at the described deposition range. At an even smaller applied potential of -0.4 V, there is no noticeable Pd deposition on the Au nanoparticles.

Elemental mapping of Pd/Au/SWNT structures where Pd is deposited at -1.2 V was performed to delineate the positioning of Au and Pd structures. Figure 6.15 (A) is an SEM image of the area of interest for elemental mapping, the corresponding secondary electron (SE) image is described in figure 6.15 (B). Elemental mapping of Pd (displayed in green) demonstrates Pd incorporation throughout the periphery of SWNTs and densifies over the larger particles, consistent with the growth development of Pd at incremental deposition potentials demonstrated in the SEM images of figure 6.14. Overlapped images of the elemental mapping with the SE image agree with the location of the palladium nanoparticles. The elemental mapping of gold is not shown due to the large amount of interference contributed from the gold electrode pads. Further in depth elemental analysis was achieved by performing EDAX along a thread of Pd-Au nanoparticles, the line scan is demonstrated in yellow in figure 6.16 (A). Tracing along small nanoparticles and three joint large particles, the line scan showed larger number of counts for gold (red line) than palladium (green line) along the large particle cluster, indicating a larger incorporation of gold while verifying the presence of a thin shell of palladium, figure 6.16 (B).

The sensing performance of the Ag/Au/SWNT and Pd/Au/SWNT structures, where the second metal was deposited at different voltages, was investigated towards H_2S, NO_2, NH_3, and SO_2. The compiled sensing behavior of the various hybrid structures is displayed in figure 6.17. Generally, the sensor response was improved towards NH_3 and NO_2 with addition of the second metal catalyst with little difference steaming form the applied voltage of the second metal catalyst. Compared to the single metal-SWNT networks, the response is enhanced two fold for NO_2, and 3 fold for NH_3. Both Ag and Pd dual metal systems responded similarly towards the analytes tested, with higher sensitivity than their single metal catalysts suggesting that the combination of the metal catalyst has larger affinity towards gaseous compound than the single metal structures.

6.3 Conclusion

Multiple metals were strategically deposited to understand the behavior of singular/dual metal catalyst and metal catalyst sequence on sensing performance. Sequential electrochemical functionalization of silver and palladium catalyst was performed on gold nanoparticle-decorated carbon nanotube networks in an attempt to improve sensitivity and impart selectivity towards analytes of interest. The Pd/Au/SWNT hybrid structures were most sensitive and selective towards NH_3. Chemical modification of the Au/SWNTs structures with mercaptohexanol (MCH) was performed in an attempt to passivate the Au nanoparticle to allow selective deposition of the second metal catalyst alongside the first. However it was observed that the MCH preferentially adhered on to the SWNTs instead of the gold nanoparticles and thus forcing sequential deposition to encapsulate the original gold nanoparticle creating Ag/Au/SWNTs and Pd/Au/SWNTs hybrid structures, in addition to suppressing new metal nuclei to form on the surface of bare SWNTs. The sensing performance of the chemical treated hybrid structures was investigated and compared to its un-treated counterparts, and revealed that MCH has preferential interaction with NO_2 regardless of the accompanying metal catalysts, while Ag/MCH/Au/SWNTs hybrid structures showed a synergistic effect towards H_2S vapors.

The sequence in electrochemical sequential deposition of gold, silver and palladium revealed morphological differences and distinctive sensing pattern stemming from the order of deposition and sequence pair. It was observed that when silver or palladium was on the outermost surface, the sensing behavior was enhanced compared to the single metal-SWNT structures however no selectivity was imparted. Interestingly, when gold was sequentially deposited on the outermost surface of either gold or silver native nanoparticles, the sensing behavior was synergistically improved towards NH_3 and dramatically suppressed towards H_2S.

Furthermore, site specific electrodeposition was further exploited by controlling the applied potential of the second material to advantageously control the positioning of the sequential metal catalyst. At potentials higher than -0.3 and -1.0 V for Ag and Pd respectively, there is deposition both on the native gold nanoparticle and on the bare sections of the SWNTs, evident by complete encapsulation of the gold nanoparticle and formation of new particles on the SWNTs. Whereas at smaller potentials, the deposition of Ag and Pd is confined to the pre-existing gold nanoparticle, here the coating-shell thickness of the second metal is monotonically decreasing with smaller potentials. The sensing behavior of the hybrid structures synthesized at different potentials of the second catalyst was similar in performance.

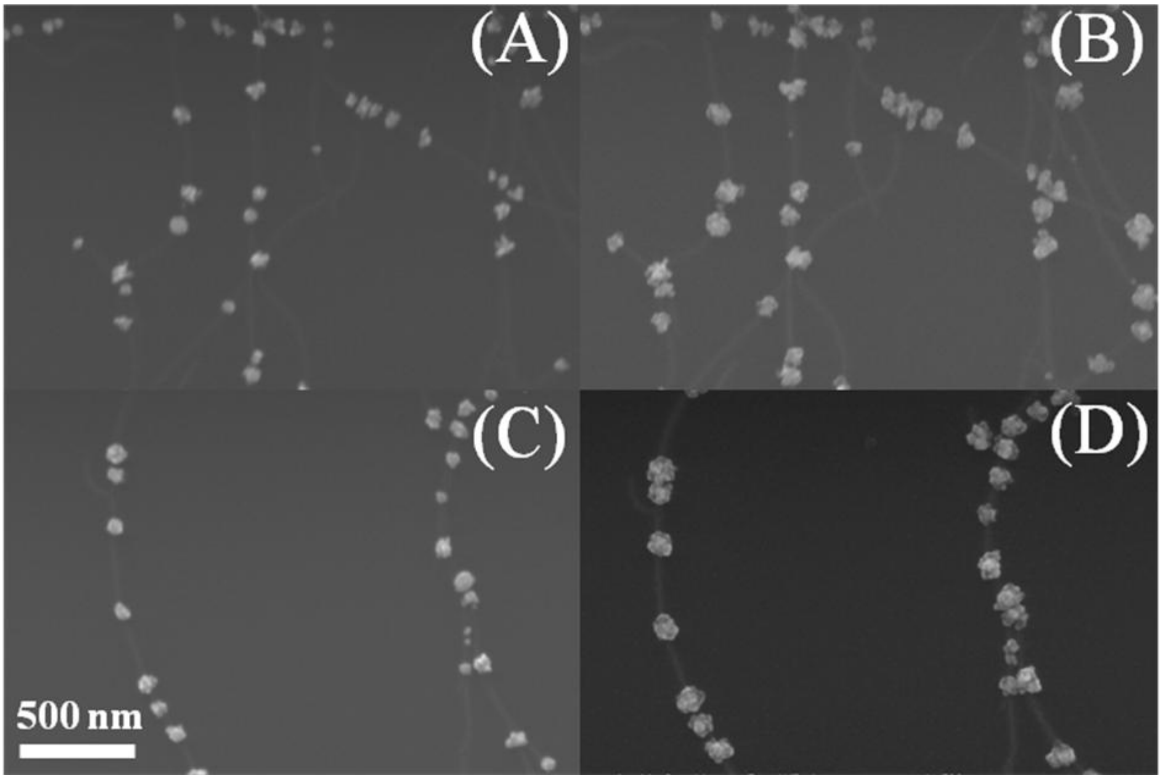

Figure 6.1. Typical SEM images of 5μC of Au on SWNTs (A) and (C). Sequential addition of 5μC of Ag (B) without chemical functionalization with MCH and (D) with chemical functionalization with MCH. SEM images are taken of the same sample and exact location before and after sequential deposition.

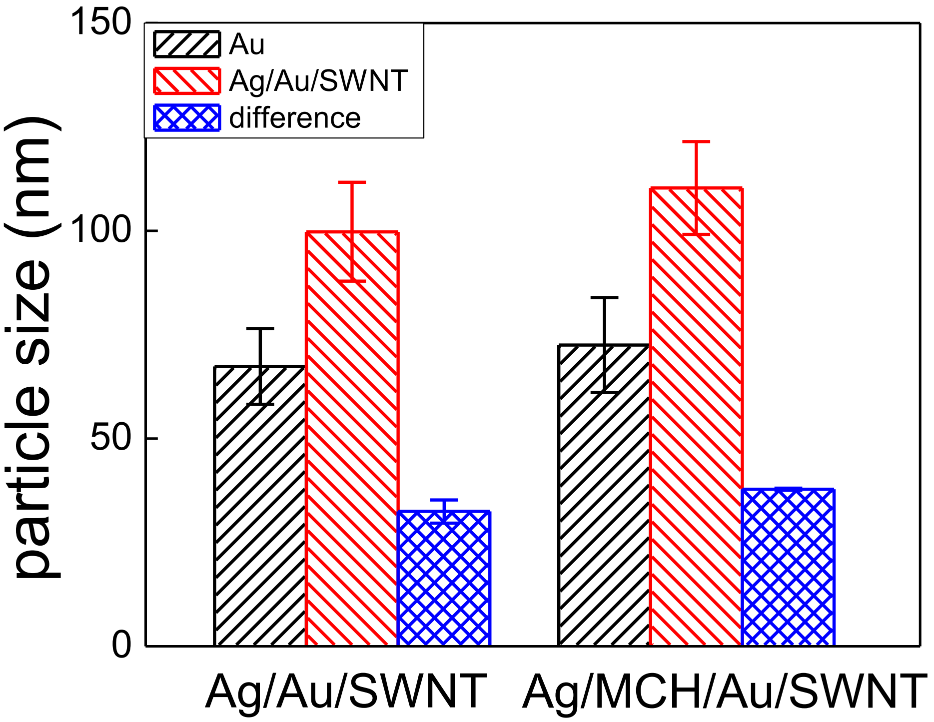

Figure 6.2. Particle size distribution of Au on SWNTs decorated at 5μC, and with sequential addition of 5μC of Ag in the presence and absence of chemical functionalization with MCH.

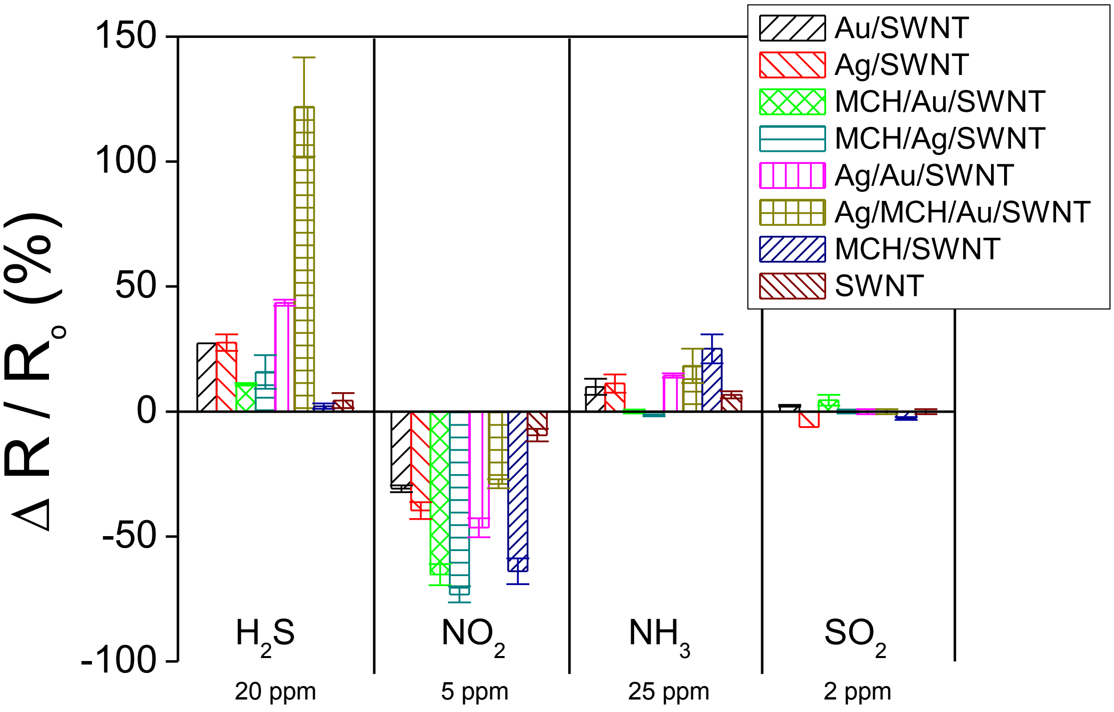

Figure 6.3. Histogram portraying typical sensor response of Ag and Au hybrid systems towards various analytes at OSHA's PEL limit, determined from n= 4 sensors.

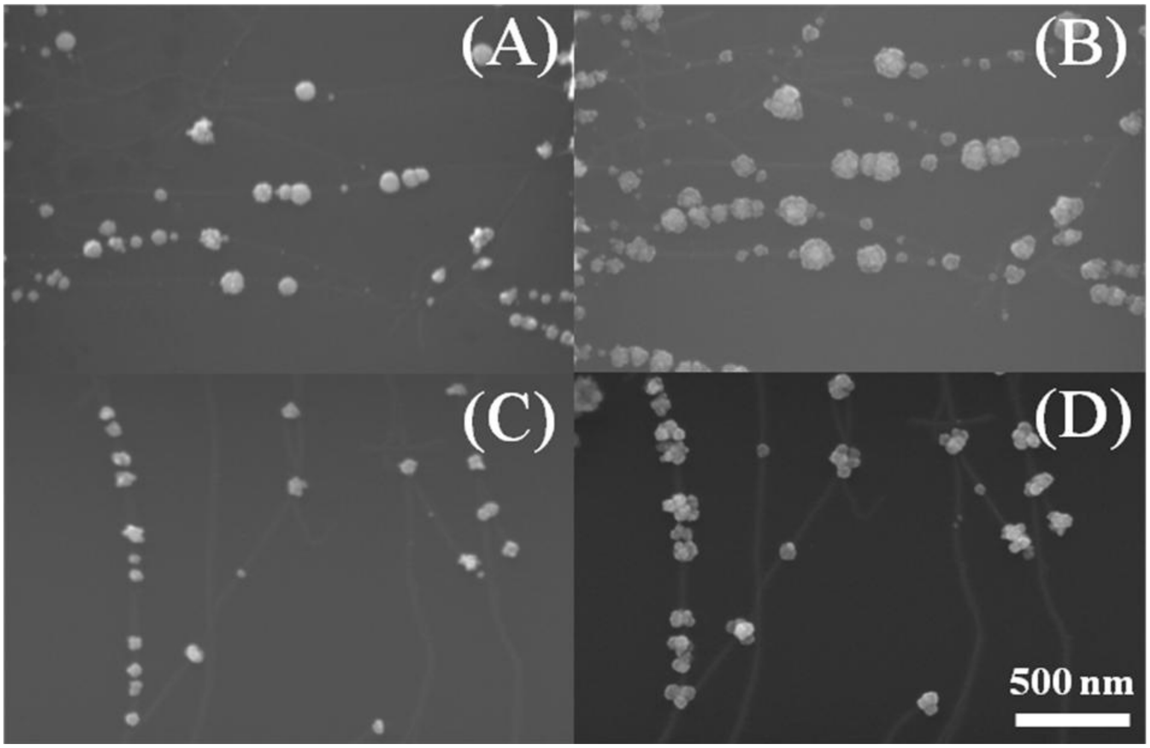

Figure 6.4. Typical SEM images of 5μC of Au on SWNTs (A) and (C). Sequential addition of 5μC of Pd (B) in the absence and (D) presence of MCH. SEM images are taken of the same sample and exact location before and after sequential deposition.

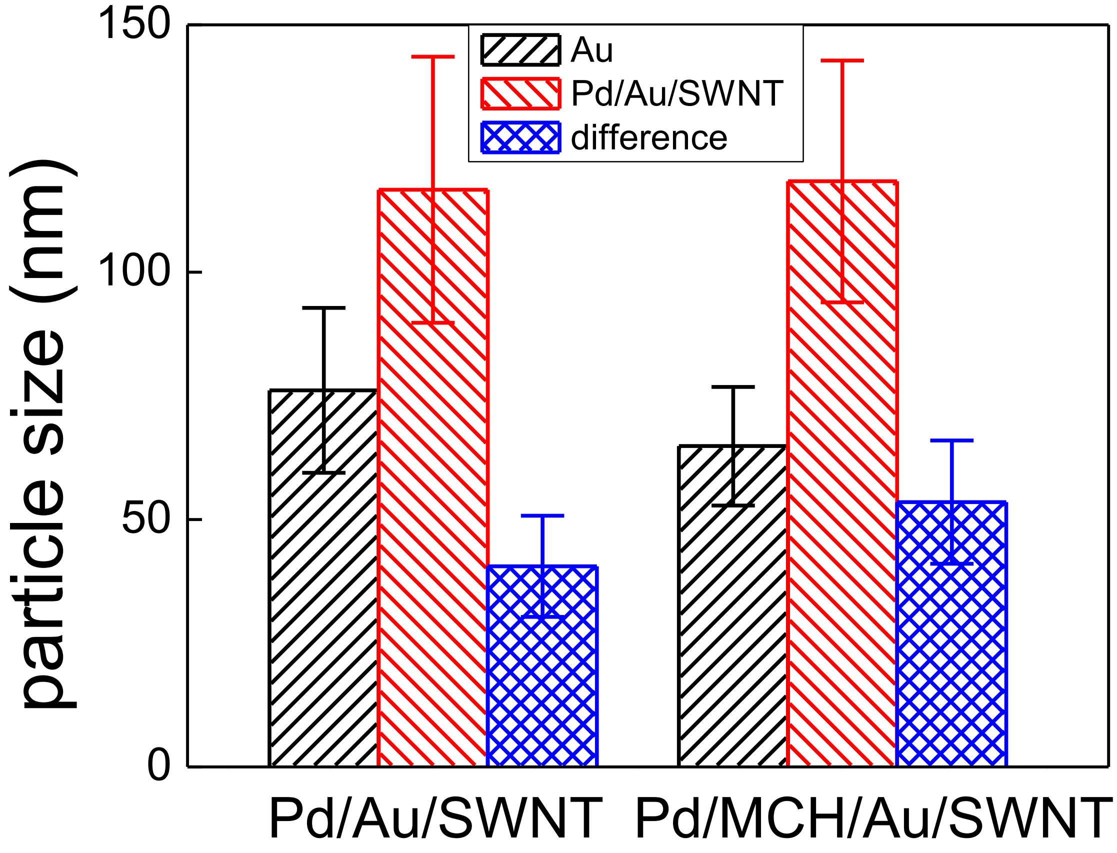

Figure 6.5. Particle size distribution of Au on SWNTs decorated at 5μC, and with sequential addition of 5μC of Pd in the presence and absence of chemical functionalization with MCH.

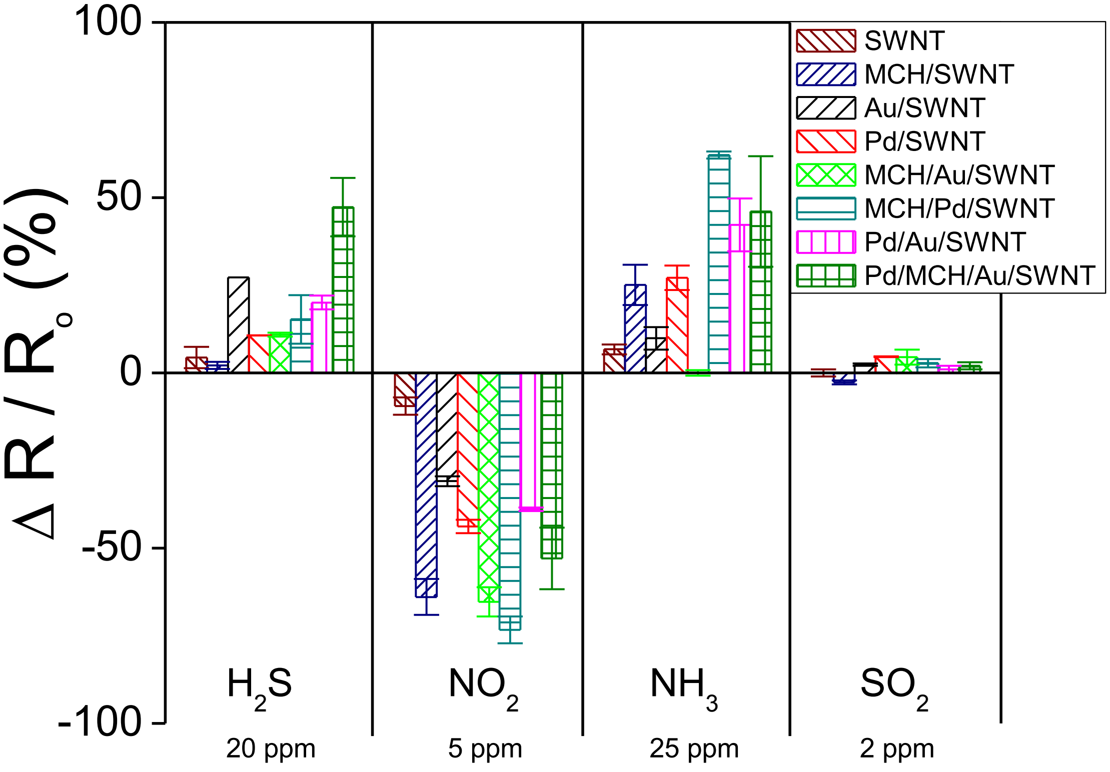

Figure 6.6. Histogram portraying typical sensor response of Au and Pd hybrid structures towards various analytes at OSHA's PEL limit, determined from n= 4 sensors.

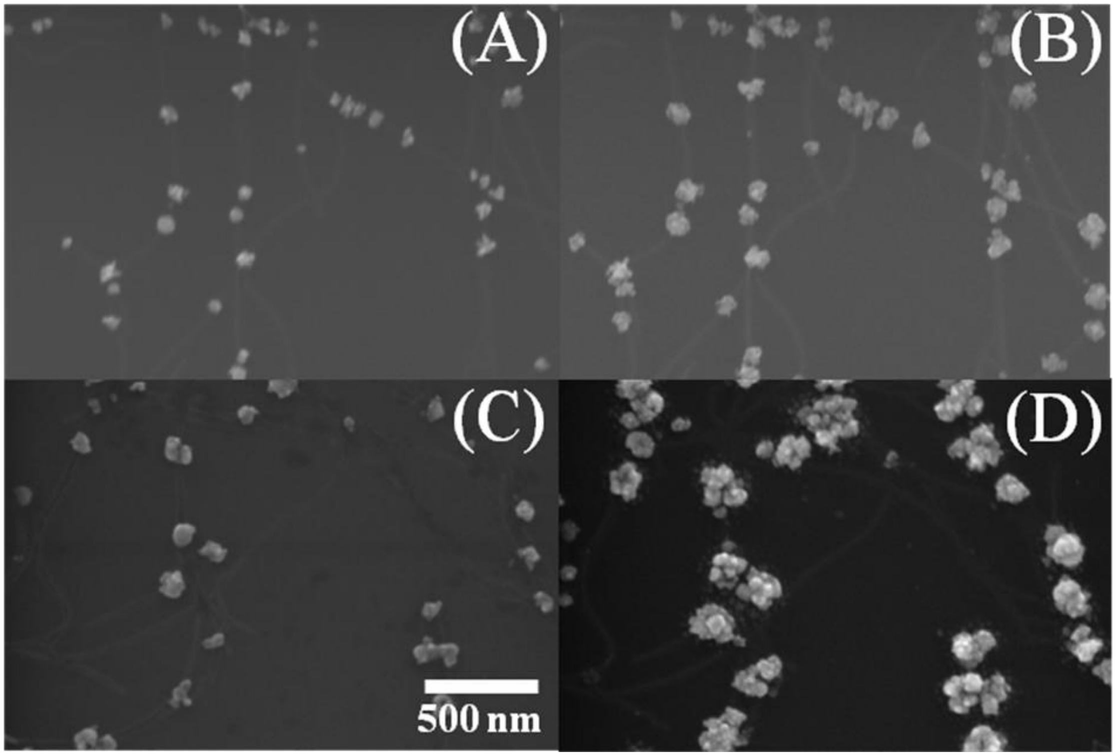

Figure 6.7. SEM images of (A) Au/SWNTs at 5 μC, (B) sequential deposition of Ag at 5 μC to create Ag/Au/SWNT hybrid system, (C) Ag/SWNT at 5μC and (D) sequential deposition f Au at 5 μC to create Au/Ag/SWNT hybrid structures.

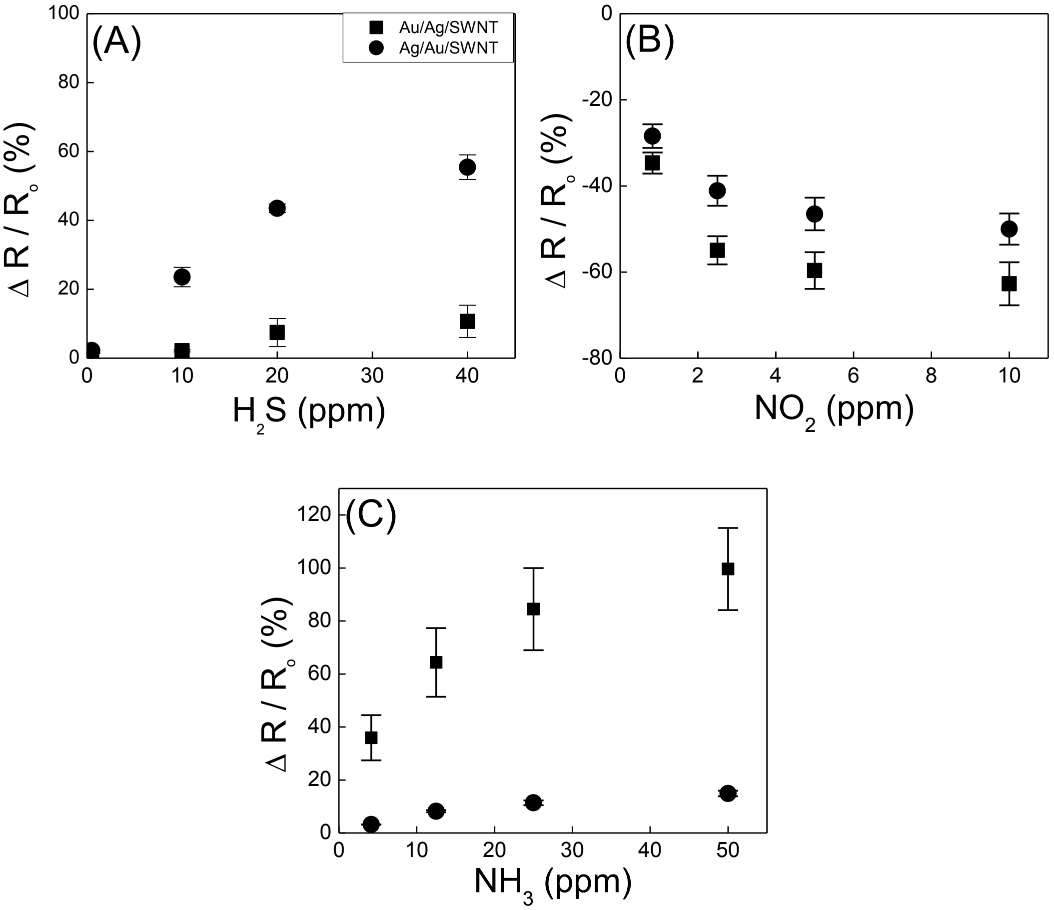

Figure 6.8. Calibration curves of the sensor performance of Ag/Au/SWNTs (circle symbols) and of Au/Ag/SWNTs (square symbols) hybrid structures towards (A) H_2S, (B) NO_2, and (C) NH_3.

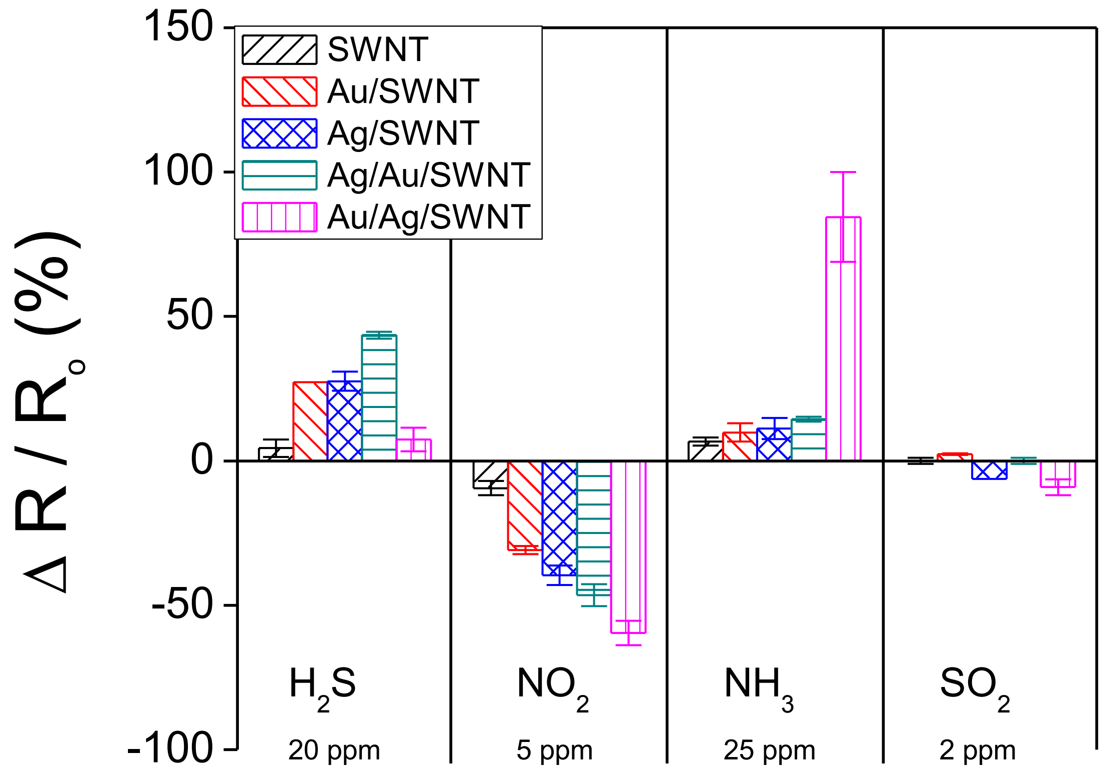

Figure 6.9. Histogram portraying typical sensor response towards various analytes at OSHA's PEL limit, determined from n= 4 sensors for Au/SWNTs at 5 μC, Ag/Au/SWNT hybrid Ag/SWNT and Au/Ag/SWNT hybrid structures.

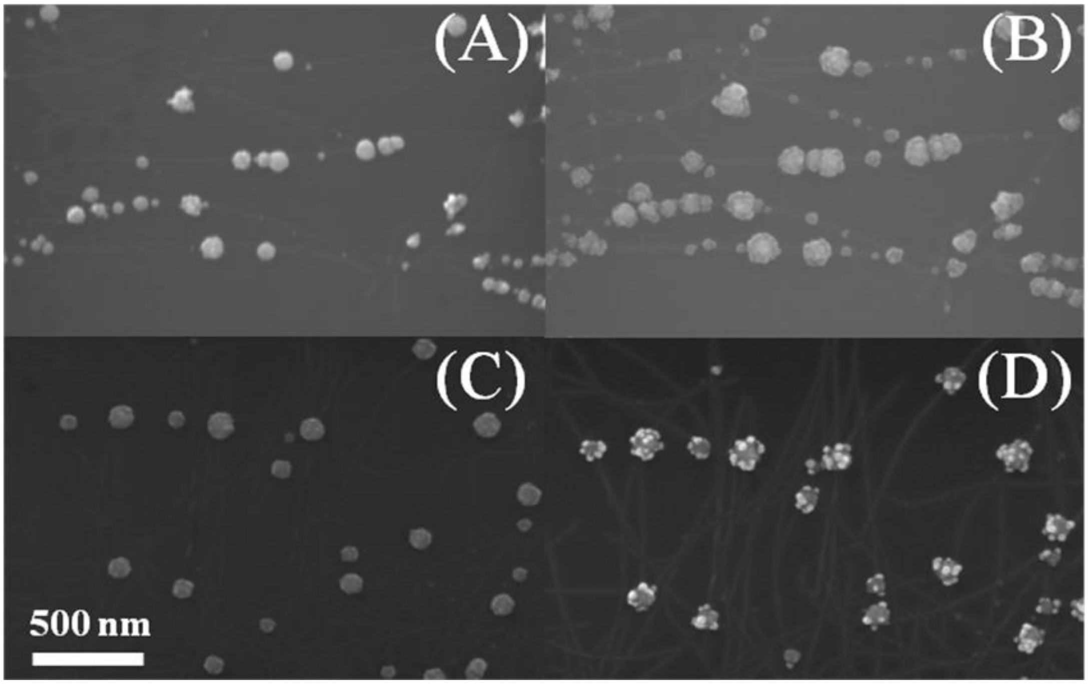

Figure 6.10. SEM images of (A) Au/SWNTs at 5 μC, (B) sequential deposition of Pd at 5 μC to create Pd/Au/SWNT hybrid system, (C) Pd/SWNT at 5μC and (D) sequential deposition of Au at 5 μC to create Au/Pd/SWNT hybrid structures.

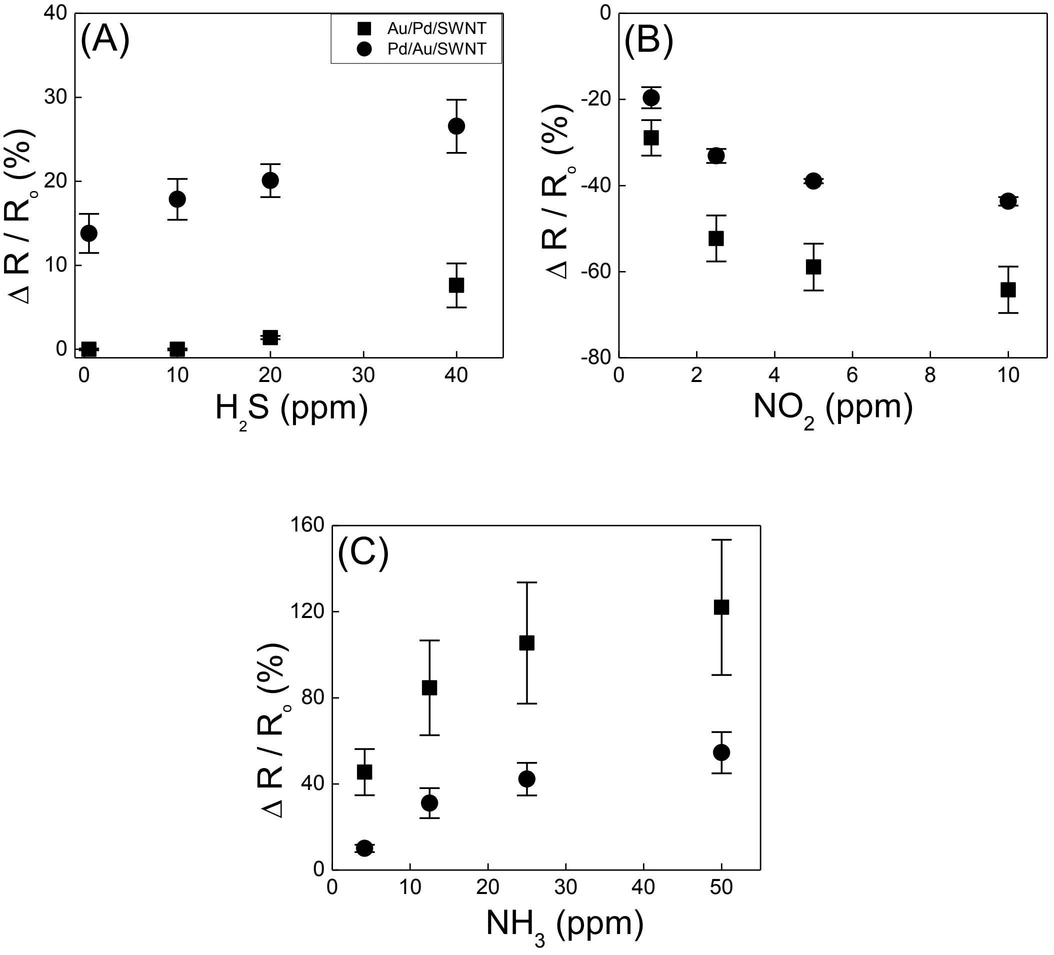

Figure 6.11. Calibration curves of the sensor performance of Pd/Au/SWNTs (circle symbols) and of Au/Pd/SWNTs (square symbols) hybrid structures towards (A) H_2S, (B) NO_2, and (C) NH_3.

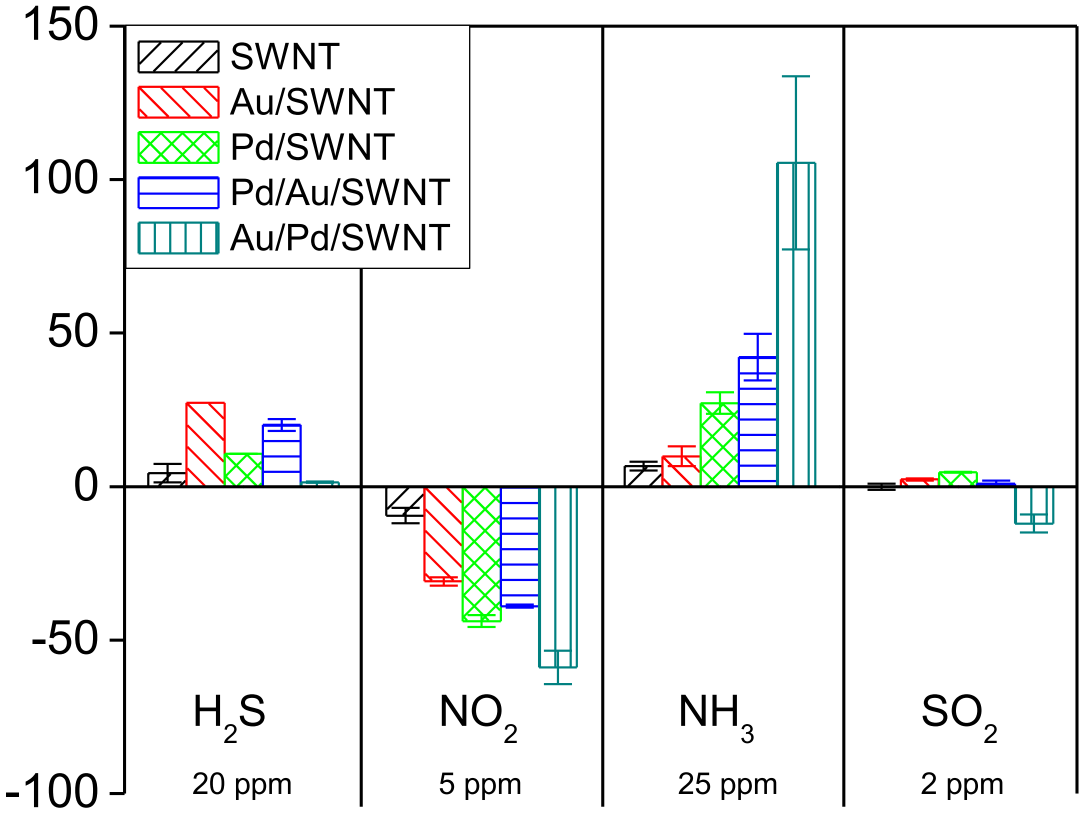

Figure 6.12. Histogram portraying typical sensor response towards various analytes at OSHA's PEL limit, determined from n= 4 sensors, for Au/SWNTs, Pd/SWNTs, Pd/Au/SWNTs, and Au/Pd/SWNTs hybrid structures.

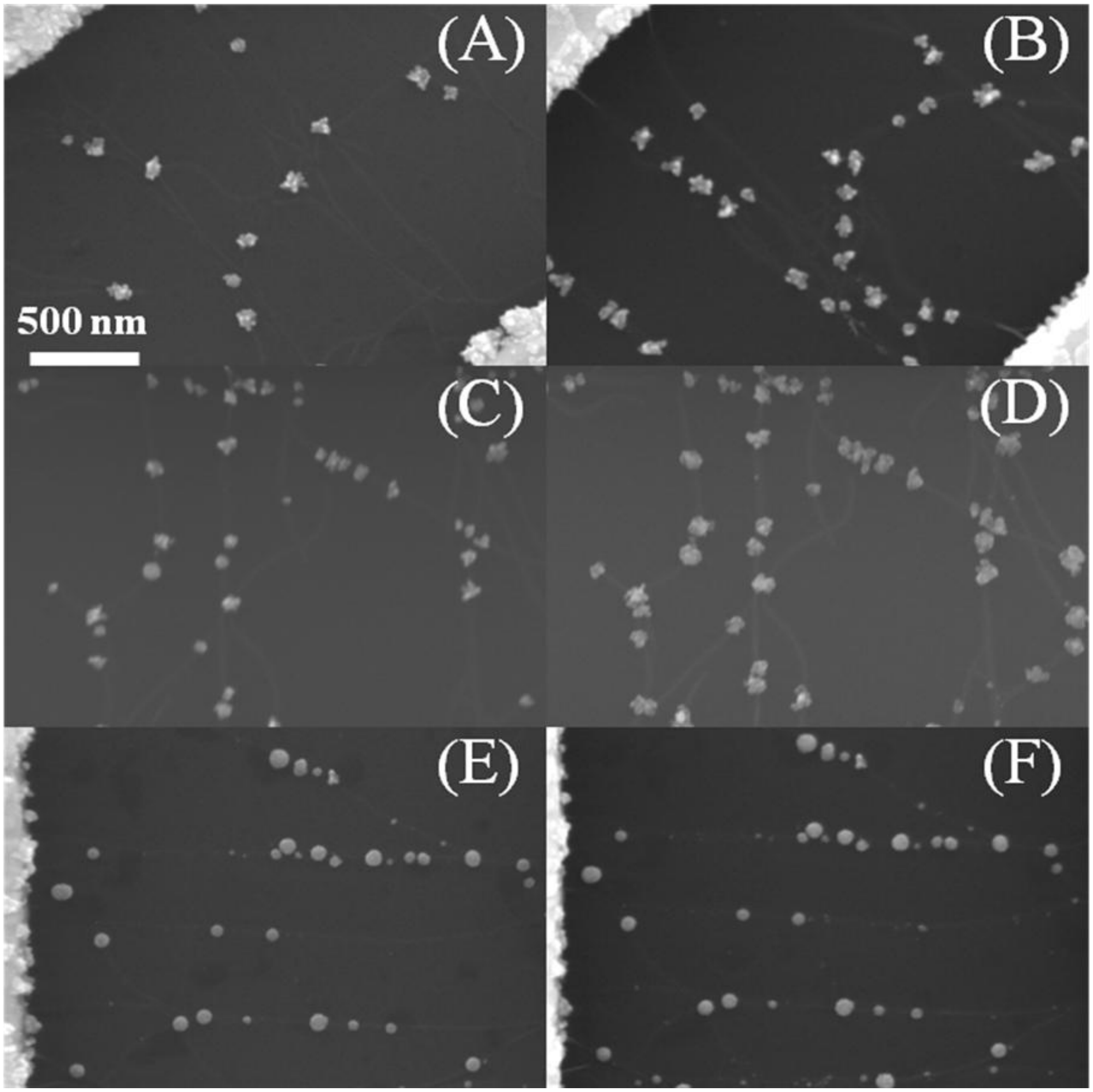

Figure 6.13. SEM images (A), (C) and (E) of Au/SWNTs at 5 μC, following sequential deposition of Ag at 5 μC deposited at (B) -0.5 V, (D) -0.3 V, and (F) at -0.1 V versus a pseudo Ag/AgCl.

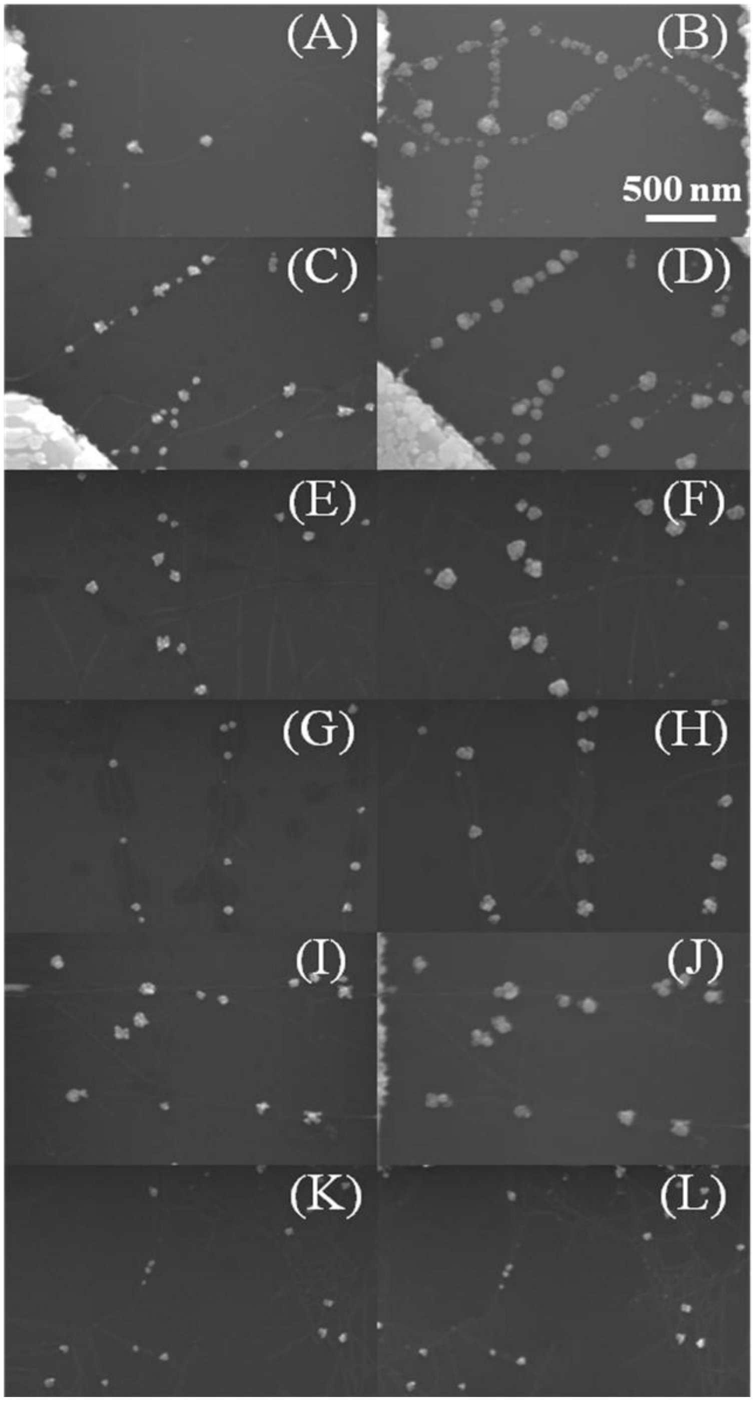

Figure 6.14. SEM images (A), (C), (E), (G), (I), and (K) of Au/SWNTs at 5 μC, and 5 μC of sequential deposition of Pd deposited at (B) -1.2 V, (D) -1.1V, (F) -1.0 V , (H) -0.8 V, (J) -0.6 V, and at (L) -0.4 V versus a pseudo Ag/AgCl.

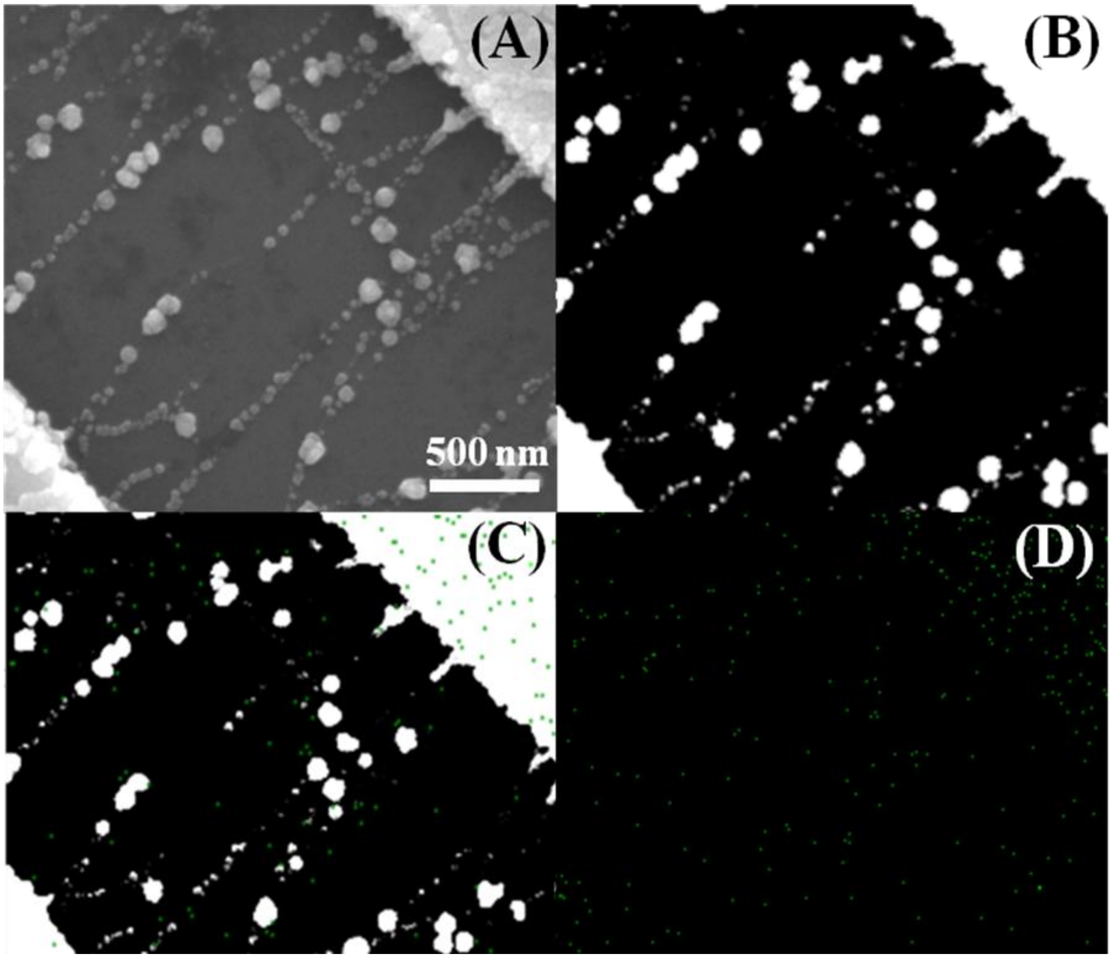

Figure 6.15. SEM image of (A) Pd/Au/SWNT hybrid structures where Pd is functionalized at -1.2 V versus a pseudo Ag/AgCl, (B) secondary electron image of area of interest, (C) overlapped elemental mapping of palladium (green) with SE image, and (D) individual elemental mapping of palladium.

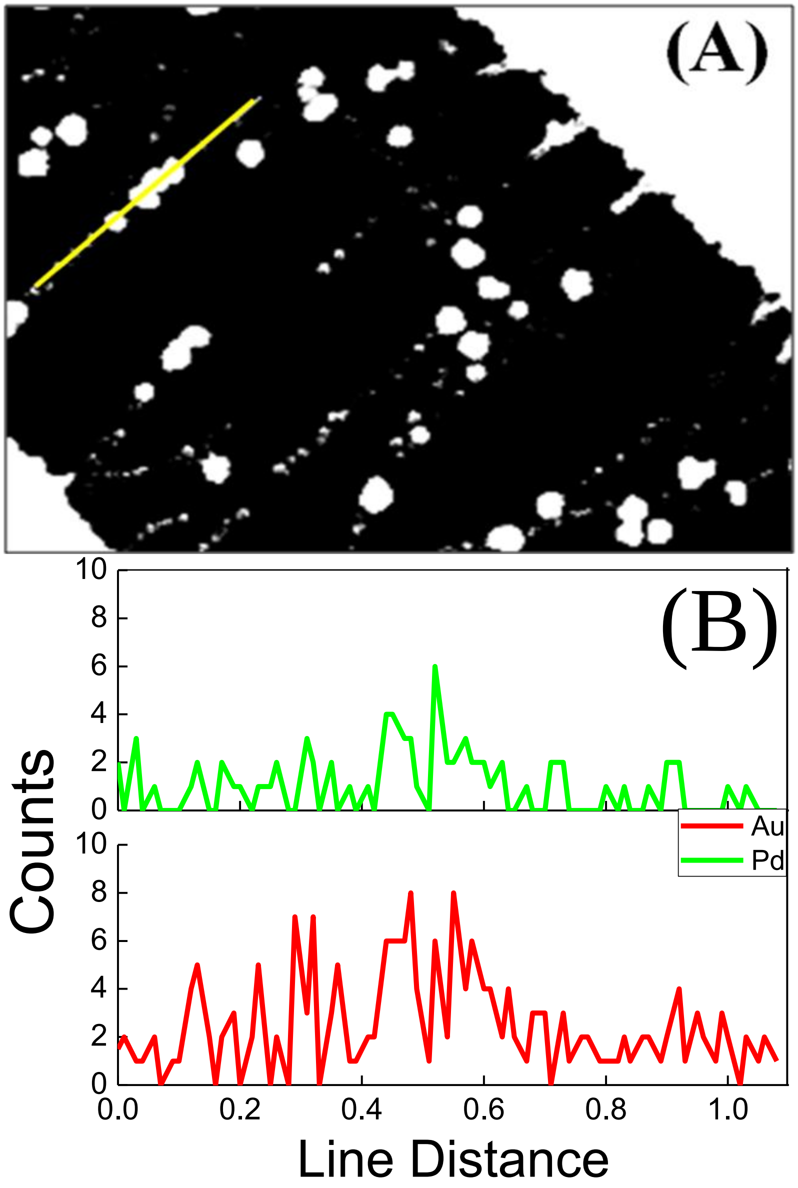

Figure 6.16. Secondary electron image of (A) Pd/Au/SWNT structures, with palladium sequentially deposited at -1.2 V versus pseudo Ag/AgCl reference electrode the yellow line indicates the location of the line scan, (B) EDAX along the line scan indicating the composition distribution of gold (red) and palladium (green) nanoparticles. The scale bar represents 500 nm.

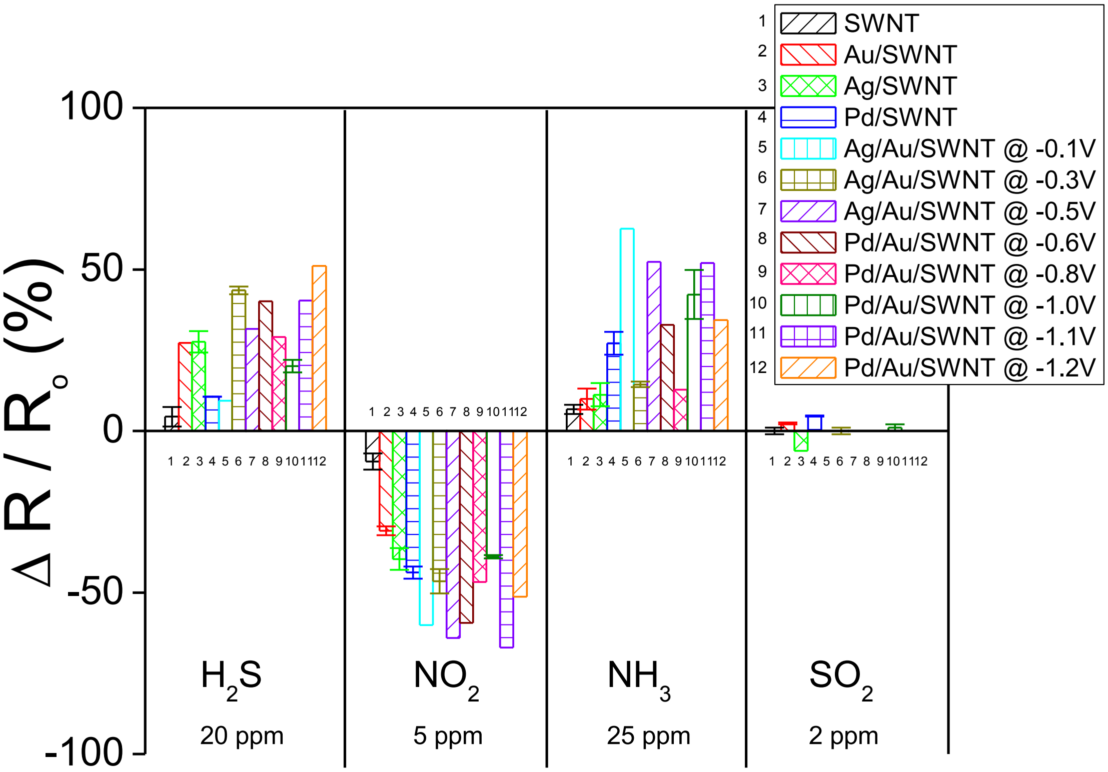

Figure 6.17. Histogram portraying typical sensor response towards various analytes at OSHA's PEL limit, for Ag and Pd systems deposited at various potentials.

Chapter 7:

Conclusion and Future Directions

Gas sensors are existing and emerging components in a spectrum of fields, ensuring emission compliance of greenhouse gases and worker safety in the industrial sector, providing early warning of toxins for homeland security, and monitoring the freshness of perishable foods and produce. Recent research has focused on the maturity of a simple, robust sensor whose operation can be based on a measurable signal created from the interaction of an analyte with the sensing material and output in the form of a change in resistance, capacitance, temperature or luminescence. In particular, conductometric sensors are amenable to development for higher level analysis of gas mixtures and compact, portable platforms required for ubiquitous deployment.

To overcome current challenges in sensitivity, power consumption and response/recovery times, 1-dimensional nanostructures, such as singe wall carbon nanotubes (SWNTs), have been rigorously investigated as transducing and sensing elements for gas sensors due to their promising electronic properties, thermal stability, and chemical inertness. Since SWNTs are composed entirely of surface atoms, interactions with adsorbing molecules can substantially alter their electronic properties, however highly specific and sensitive sensors are not readily attainable with standalone SWNT devices.

This dissertation tackles further application of the use of strategically engineered nanostructures towards the development of advanced sensors. By utilizing key metal oxides and catalytic metal nanoparticles, the effect of material quality, particle size and density, dopant kind, and material sequence were investigated both from a synthesis nano-engineering stand point but also from the resultant sensor performance point of view.

7.1. Summary:

The presentation of this thesis was first by Chapter 1 which provided a general introduction to sensors, applications of metal oxides and SWNTs, which lead to the objectives of this work. Chapter 2 then followed with the development of a bath and electrodeposition conditions to synthesize ZnO on the surface of SWNTs. Synthesis and material characterization of ZnO/SWNT hybrid structures was performed by a facile electrochemical route, with precise control over particle formation, size and density. Gas sensing performance of the ZnO/SWNT hybrid structures was investigated and exhibited uncharacteristic selectivity towards H_2S, with enhanced sensitivity, response and recovery time contingent upon crystallinity. These ZnO/SWNT hybrid gas sensor demostrate a clear structure-property realationship indicating material crystalinity has a large impact on metal oxide/SWNT hybrid sensor performance.

Chapter 3 followed with more detailed investigation of the ZnO/SWNT hybrid sensors towards a different pool of analytes. It was observed that the hybrid ZnO-SWNT based sensor was capable of distinguishing between different xylene isomers, showing high selectively towards the *p*-xylene isomer and demonstrating capability of discriminating structurally similar chemical compounds. Furthermore the investigation of ZnO/SWNTs provided useful insight into the interaction of VOCs and ZnO based nano gas sensors, demonstrating promising applications for detection of volatile organic biomarkers for early medical diagnostics.

In chapter 4, other material relevant properties were investigated such as the photoconduction behavior of electrochemically synthesized ZnO-SWNT hybrid structures. An increase in conductance upon UV irradiation supports m-SWNT dominated networks. The hybrid structures are composed of various degrees of surface coverage (i.e. particle size and particle density) and material quality. The photoconduction studies were performed in ambient conditions and the current behavior was monitored in the dark and presence of UV irritation. Dynamic photocurrent responses reveal that the current change of the hybrid system was $\Delta I/I_o$ was more strongly dependent on material quality and response/recovery rates were dependent on surface coverage of SWNTs, while the current of bare SWNTs was unaffected by the presence or absence of the UV light.

Sequential functionalization of ZnO/SWNT hybrid structures with metal catalyst (Au, Pt, Ag and Pd) was performed in chapter 5 in an attempt to impart selectivity. The surface morphology, growth mechanism and room temperature sensing performance were investigated as a function of charge, and presence or absence of seeded metal oxide. In the case of the Au and Ag catalyst, there was a charge dependent sensing behavior and specificity towards H_2S and NO_2. The metal-SWNT structures were most sensitive at smaller charges and the metal-ZnO/SWNT hybrid structures experiencing higher sensitivities when the metal is deposited at larger charges. With incorporation of the Pt catalyst, the sensing behavior was dramatically suppressed for H_2S, where Pt/SWNT structures outperformed the Pt/ZnO/SWNT sensors towards H_2S and NH_3. Interestingly the sensing performance was independent of the applied charge for both sets of hybrid structures. Thus a finger print pattern sensing behavior was obtained with the incorporation of metal catalysts towards the analytes of interest.

Chapter 6 dealt with the deposition of multiple metals to understand the behavior of binary/dual metal catalyst and metal catalyst sequence on sensing performance. Sequential electrochemical functionalization of silver and palladium catalyst was performed on gold nanoparticle-decorated carbon nanotube networks in an attempt to improve sensitivity and impart selectivity towards analytes of interest. The Pd/Au/SWNT hybrid structures were most sensitive and selective towards NH_3. Chemical modification of the Au/SWNTs structures with mercaptohexanol (MCH) was performed in an attempt to passivate the Au nanoparticle to allow selective deposition of the second metal catalyst alongside the first. However it was observed that the MCH preferentially adhered on to the SWNTs instead of the gold nanoparticles and thus forcing sequential deposition to encapsulate the original gold nanoparticle creating Ag/Au/SWNTs and Pd/Au/SWNTs hybrid structures, in addition to suppressing new metal nuclei to form on the surface of bare SWNTs. The sequence in electrochemical sequential deposition of gold, silver and palladium revealed morphological differences and distinctive sensing behavior stemming from the order of deposition and sequence pair. Furthermore, site specific electrodeposition was further exploited by controlling the applied potential of the second material to advantageously control the positioning of the sequential metal catalyst.

7.2 Future Directions

The effectiveness of electrochemically synthesized ZnO/SWNTs, M/ZnO/SWNTs, and M/M/SWNTs hybrid sensors demonstrates the ability to fabricate stable and selective nano-gas sensors in a facile and cost effective route, a process that can be extended to other metal oxide materials, metals and combination of materials.

With higher-level analytical capabilities, such as pattern recognitions, multiple analyte sensing, gas sensors could also be used as screening tools for medical conditions by detecting compounds whose presence can be correlated to a host of diseases and physiological conditions such as asthma, diabetes, periodontal disease, as well as lung and breast cancer.

Electrodeposition is a facile and cost effective route that allows for site specific deposition of desired materials however, to better control sensor synthesis reproducibility a different architectural design that allows for serial depositions should be implemented. Most of our efforts have focused on engineering the active material on the surface of SWNTs, however o enhance sensor stability and sensitivity, investigation of other transducing elements should be investigated. Currently carboxylated SWNTs have been heavily and thoroughly investigated within our group but even within the SWNT family, there are metallic, semiconducting and other surface functionalized nanotubes that have the potential to enhance the overall sensor performance. Furthermore, implementation of grapheme sheets as the transducing element could prove to be a strong sensing platform to investigate.

REFERENCES

1. J. G. Lu, P. C. Chang and Z. Y. Fan, *Materials Science & Engineering R-Reports*, 2006, **52**, 49-91.

2. Q. Wan, C. L. Lin, X. B. Yu and T. H. Wang, *Applied Physics Letters*, 2004, **84**, 124-126.

3. J. G. Ok, S. H. Tawfick, K. A. Juggernauth, K. Sun, Y. Zhang and A. J. Hart, *Advanced Functional Materials*, 2010, **20**, 2470–2480.

4. E. S. Snow, F. K. Perkins, E. J. Houser, S. C. Badescu and T. L. Reinecke, *Science*, 2005, **307**, 1942-1945.

5. E. S. Snow, F. K. Perkins and J. A. Robinson, *Chemical Society Reviews*, 2006, **35**, 790-798.

6. J. A. Robinson, E. S. Snow, S. C. Badescu, T. L. Reinecke and F. K. Perkins, *Nano Letters*, 2006, **6**, 1747-1751.

7. J. A. Robinson, E. S. Snow and F. K. Perkins, *Sensors and Actuators a-Physical*, 2007, **135**, 309-314.

8. T. Zhang, M. B. Nix, B. Y. Yoo, M. A. Deshusses and N. V. Myung, *Electroanalysis*, 2006, **18**, 1153-1158.

9. D. R. Kauffman and A. Star, *Journal of Physical Chemistry C*, 2008, **112**, 4430-4434.

10. A. Star, V. Joshi, S. Skarupo, D. Thomas and J. C. P. Gabriel, *Journal of Physical Chemistry B*, 2006, **110**, 21014-21020.

11. D. R. Kauffman and A. Star, *Angewandte Chemie-International Edition*, 2008, **47**, 6550-6570.

12. E. Bekyarova, I. Kalinina, M. E. Itkis, L. Beer, N. Cabrera and R. C. Haddon, *Journal of the American Chemical Society*, 2007, **129**, 10700-10706.

13. M. D. Ganji and A. Afsari, *Physica E-Low-Dimensional Systems & Nanostructures*, 2009, **41**, 1696-1700.

14. A. Gonzalez-Campo, K. L. Orchard, N. Sato, M. S. P. Shaffer and C. K. Williams, *Chemical Communications*, 2009, 4034-4036.

15. L. Q. Jiang and L. Gao, *Materials Chemistry and Physics*, 2005, **91**, 313-316.

16. T. G. Jiu, H. B. Liu, H. Y. Gan, Y. L. Li, S. Q. Xiao, H. M. Li, Y. Liu, F. S. Lu, L. Jiang and D. B. Zhu, *Synthetic Metals*, 2005, **148**, 313-319.

17. J. Khanderi, R. C. Hoffmann, A. Gurlo and J. J. Schneider, *Journal of Materials Chemistry*, 2009, **19**, 5039-5046.

18. H. Kim and W. Sigmund, *Applied Physics Letters*, 2002, **81**, 2085-2087.

19. Y. W. Koh, M. Lin, C. K. Tan, Y. L. Foo and K. P. Loh, *Journal of Physical Chemistry B*, 2004, **108**, 11419-11425.

20. J. Liu, M. J. Casavant, M. Cox, D. A. Walters, P. Boul, W. Lu, A. J. Rimberg, K. A. Smith, D. T. Colbert and R. E. Smalley, *Chemical Physics Letters*, 1999, **303**, 125-129.

21. S. Mubeen, T. Zhang, N. Chartuprayoon, Y. Rheem, A. Mulchandani, N. V. Myung and M. A. Deshusses, *Analytical Chemistry*, 2010, **82**, 250-257.

22. T. Zhang, S. Mubeen, B. Yoo, N. V. Myung and M. A. Deshusses, *Nanotechnology*, 2009, **20**, -.

23. N. Yamazoe, *Sensors and Actuators B-Chemical*, 1991, **5**, 7-19.

24. E. Comini, C. Baratto, G. Faglia, M. Ferroni, A. Vomiero and G. Sberveglieri, *Progress in Materials Science*, 2009, **54**, 1-67.

25. M. Izaki and T. Omi, *Applied Physics Letters*, 1996, **68**, 2439-2440.

26. M. Izaki and T. Omi, *Journal of the Electrochemical Society*, 1996, **143**, L53-L55.

27. S. J. Limmer, E. A. Kulp and J. A. Switzer, *Langmuir*, 2006, **22**, 10535-10539.

28. D. Lincot, *Thin Solid Films*, 2005, **487**, 40-48.

29. T. Yoshida, D. Komatsu, N. Shimokawa and H. Minoura, *Thin Solid Films*, 2004, **451-52**, 166-169.

30. L. S. Zhang, Z. G. Chen, Y. W. Tang and Z. J. Jia, *Thin Solid Films*, 2005, **492**, 24-29.

31. L. P. Zhu, G. H. Liao, W. Y. Huang, L. L. Ma, Y. Yang, Y. Yu and S. Y. Fu, *Materials Science and Engineering B-Advanced Functional Solid-State Materials*, 2009, **163**, 194-198.

32. S. C. Hernandez, D. Chaudhuri, W. Chen, N. V. Myung and A. Mulchandani, *Electroanalysis*, 2007, **19**, 2125-2130.

33. A. Brenner, *Electrodeposition of alloys: principles and practice*, Academic Press, New York,, 1963.

34. R. M. Nyffenegger, B. Craft, M. Shaaban, S. Gorer, G. Erley and R. M. Penner, *Chemistry of Materials*, 1998, **10**, 1120-1129.

35. S. Otani, J. Katayama, H. Umemoto and M. Matsuoka, *Journal of the Electrochemical Society*, 2006, **153**, C551-C556.

36. S. T. Jiang, M. Q. Wu, Y. Zhou, Y. Wen, C. T. Yang and S. R. Zhang, *Integrated Ferroelectrics*, 2007, **88**, 33-+.

37. J. H. Lim, N. Phiboolsirichit, S. Mubeen, Y. Rheem, M. A. Deshusses, A. Mulchandani and N. V. Myung, *Electroanalysis*, 2010, **22**, 99-105.

38. Y. W. Zhu, H. I. Elim, Y. L. Foo, T. Yu, Y. J. Liu, W. Ji, J. Y. Lee, Z. X. Shen, A. T. S. Wee, J. T. L. Thong and C. H. Sow, *Advanced Materials*, 2006, **18**, 587-+.

39. L. M. Yu and C. C. Zhu, *Applied Surface Science*, 2009, **255**, 8359-8362.

40. E. C. Walter, B. J. Murray, F. Favier, G. Kaltenpoth, M. Grunze and R. M. Penner, *Journal of Physical Chemistry B*, 2002, **106**, 11407-11411.

41. Y. W. Fan, B. R. Goldsmith and P. G. Collins, *Nature Materials*, 2005, **4**, 906-911.

42. L. Hu, D. S. Hecht and G. Gruner, *Nano Letters*, 2004, **4**, 2513-2517.

43. C. W. Zhou, J. Kong and H. J. Dai, *Applied Physics Letters*, 2000, **76**, 1597-1599.

44. M. Caglar, Y. Caglar, S. Aksoy and S. Ilican, *Applied Surface Science*, 2010, **256**, 4966-4971.

45. Q. Wan, Q. H. Li, Y. J. Chen, T. H. Wang, X. L. He, J. P. Li and C. L. Lin, *Applied Physics Letters*, 2004, **84**, 3654-3656.

46. C. H. Wang, X. F. Chu and M. W. Wu, *Sensors and Actuators B-Chemical*, 2006, **113**, 320-323.

47. N. Van Hicu and N. D. Chien, *Physica B-Condensed Matter*, 2008, **403**, 50-56.

48. N. Zhang, K. Yu, Q. Li, Z. Q. Zhu and Q. Wan, *Journal of Applied Physics*, 2008, **103**, -.

49. C. S. Rout, G. U. Kulkarni and C. N. R. Rao, *Journal of Physics D-Applied Physics*, 2007, **40**, 2777-2782.

50. J. Y. Lin, J. A. May, S. V. Didziulis and E. I. Solomon, *Journal of the American Chemical Society*, 1992, **114**, 4718-4727.

51. J. A. Rodriguez and A. Maiti, *Journal of Physical Chemistry B*, 2000, **104**, 3630-3638.

52. X. Chen, F. J. Xu, Y. Wang, Y. F. Pan, D. J. Lu, P. Wang, K. J. Ying, E. G. Chen and W. M. Zhang, *Cancer*, 2007, **110**, 835-844.

53. J. W. Dallinga, C. M. H. H. T. Robroeks, J. J. B. N. van Berkel, E. J. C. Moonen, R. W. L. Godschalk, Q. Jobsis, E. Dompeling, E. F. M. Wouters and F. J. van Schooten, *Clinical and Experimental Allergy*, 2010, **40**, 68-76.

54. G. Peng, U. Tisch, O. Adams, M. Hakim, N. Shehada, Y. Y. Broza, S. Billan, R. Abdah-Bortnyak, A. Kuten and H. Haick, *Nature Nanotechnology*, 2009, **4**, 669-673.

55. M. Phillips, R. N. Cataneo, R. Condos, G. A. R. Erickson, J. Greenberg, V. La Bombardi, M. I. Munawar and O. Tietje, *Tuberculosis*, 2007, **87**, 44-52.

56. M. Phillips, R. N. Cataneo, B. A. Ditkoff, P. Fisher, J. Greenberg, R. Gunawardena, C. S. Kwon, O. Tietje and C. Wong, *Breast Cancer Research and Treatment*, 2006, **99**, 19-21.

57. B. Zappacosta, A. Manni, S. Persichilli, A. Boari, D. Scribano, A. Minucci, L. Raffaelli, B. Giardina and P. De Sole, *Clinical Biochemistry*, 2007, **40**, 661-665.

58. B. Buszewski, M. Kesy, T. Ligor and A. Amann, *Biomedical Chromatography*, 2007, **21**, 553-566.

59. M. Phillips, K. Gleeson, J. M. B. Hughes, J. Greenberg, R. N. Cataneo, L. Baker and W. P. McVay, *Lancet*, 1999, **353**, 1930-1933.

60. D. Poli, P. Manini, R. Andreoli, I. Franchini and A. Mutti, *Journal of Chromatography B-Analytical Technologies in the Biomedical and Life Sciences*, 2005, **820**, 95-102.

61. M. Penza, G. Cassano, P. Aversa, F. Antolini, A. Cusano, M. Consales, M. Giordano and L. Nicolais, *Sensors and Actuators B-Chemical*, 2005, **111**, 171-180.

62. M. Penza, G. Cassano, P. Aversa, F. Antolini, A. Cusano, A. Cutolo, M. Giordano and L. Nicolais, *Applied Physics Letters*, 2004, **85**, 2379-2381.

63. M. Penza, G. Cassano, P. Aversa, A. Cusano, A. Cutolo, M. Giordano and L. Nicolais, *Nanotechnology*, 2005, **16**, 2536-2547.

64. M. Penza, R. Rossi, M. Alvisi, G. Cassano and E. Serra, *Sensors and Actuators B-Chemical*, 2009, **140**, 176-184.

65. M. Penza, R. Rossi, M. Alvisi, G. Cassano, M. A. Signore, E. Serra and R. Giorgi, *Sensors and Actuators B-Chemical*, 2008, **135**, 289-297.

66. M. Penza, R. Rossi, M. Alvisi, M. A. Signore, G. Cassano, D. Dimaio, R. Pentassuglia, E. Piscopiello, E. Serra and M. Falconieri, *Thin Solid Films*, 2009, **517**, 6211-6216.

67. M. Penza, M. A. Tagliente, P. Aversa and G. Cassano, *Chemical Physics Letters*, 2005, **409**, 349-354.

68. M. Penza, M. A. Tagliente, P. Aversa, G. Cassano and L. Capodieci, *Materials Science & Engineering C-Biomimetic and Supramolecular Systems*, 2006, **26**, 1165-1170.

69. X. F. Ma, X. B. Zhang, Y. Li, G. A. Li, M. Wang, H. Z. Chen and Y. H. Mi, *Macromolecular Materials and Engineering*, 2006, **291**, 75-82.

70. K. S. V. Santhanam, R. Sangoi and L. Fuller, *Sensors and Actuators B-Chemical*, 2005, **106**, 766-771.

71. C. Wei, L. M. Dai, A. Roy and T. B. Tolle, *Journal of the American Chemical Society*, 2006, **128**, 1412-1413.

72. Q. F. Pengfei, O. Vermesh, M. Grecu, A. Javey, O. Wang, H. J. Dai, S. Peng and K. J. Cho, *Nano Letters*, 2003, **3**, 347-351.

73. J. Kong, M. G. Chapline and H. J. Dai, *Advanced Materials*, 2001, **13**, 1384-1386.

74. F. Wang, Y. Yang and T. M. Swager, *Angewandte Chemie-International Edition*, 2008, **47**, 8394-8396.

75. F. Wang, H. W. Gu and T. M. Swager, *Journal of the American Chemical Society*, 2008, **130**, 5392-+.

76. S. Mubeen, T. Zhang, B. Yoo, M. A. Deshusses and N. V. Myung, *Journal of Physical Chemistry C*, 2007, **111**, 6321-6327.

77. O. Lupan, V. V. Ursaki, G. Chai, L. Chow, G. A. Emelchenko, I. M. Tiginyanu, A. N. Gruzintsev and A. N. Redkin, *Sensors and Actuators B-Chemical*, 2010, **144**, 56-66.

78. C. L. Yaws, *Chemical properties handbook : physical, thermodynamic, environmental, transport, safety, and health related properties for organic and inorganic chemicals*, McGraw-Hill, New York, 1999.

79. H. Malamud, R. Geisman and S. Lowell, *Analytical Chemistry*, 1967, **39**, 1468-&.

80. V. L. Pushparaj, M. M. Shaijumon, A. Kumar, S. Murugesan, L. Ci, R. Vajtai, R. J. Linhardt, O. Nalamasu and P. M. Ajayan, *Proceedings of the National Academy of Sciences of the United States of America*, 2007, **104**, 13574-13577.

81. T. M. Barnes, X. Wu, J. Zhou, A. Duda, J. van de Lagemaat, T. J. Coutts, C. L. Weeks, D. A. Britz and P. Glatkowski, *Applied Physics Letters*, 2007, **90**, -.

82. D. R. Kauffman, Y. F. Tang, P. D. Kichambare, J. F. Jackovitz and A. Star, *Energy & Fuels*, 2010, **24**, 1877-1881.

83. D. M. Guldi, G. M. A. Rahman, V. Sgobba, N. A. Kotov, D. Bonifazi and M. Prato, *Journal of the American Chemical Society*, 2006, **128**, 2315-2323.

84. S.-H.-I. Laila, B. Bernhard and W. Itamar, *Angewandte Chemie International Edition*, 2005, **44**, 78-83.

85. L. Hu, Y. L. Zhao, K. Ryu, C. Zhou, J. F. Stoddart and G. Grüner, *Advanced Materials*, 2008, **20**, 939-946.

86. B. Zebli, H. A. Vieyra, I. Carmeli, A. Hartschuh, J. P. Kotthaus and A. W. Holleitner, *Physical Review B*, 2009, **79**, -.

87. S. Banerjee and S. S. Wong, *Nano Letters*, 2002, **2**, 195-200.

88. B. H. Juarez, C. Klinke, A. Kornowski and H. Weller, *Nano Letters*, 2007, **7**, 3564-3568.

89. J. M. Haremza, M. A. Hahn and T. D. Krauss, *Nano Letters*, 2002, **2**, 1253-1258.

90. S. Banerjee and S. S. Wong, *Advanced Materials*, 2004, **16**, 34-+.

91. A. Kolmakov and M. Moskovits, *Annual Review of Materials Research*, 2004, **34**, 151-180.

92. C. Soci, A. Zhang, B. Xiang, S. A. Dayeh, D. P. R. Aplin, J. Park, X. Y. Bao, Y. H. Lo and D. Wang, *Nano Letters*, 2007, **7**, 1003-1009.

93. Z. X. Zhang, L. F. Sun, Y. C. Zhao, Z. Liu, D. F. Liu, L. Cao, B. S. Zou, W. Y. Zhou, C. Z. Gu and S. S. Xie, *Nano Letters*, 2008, **8**, 652-655.

94. F. S. Li, S. H. Cho, D. I. Son, T. W. Kim, S. K. Lee, Y. H. Cho and S. H. Jin, *Applied Physics Letters*, 2009, **94**, -.

95. S. Liu, J. F. Ye, Y. Cao, Q. Shen, Z. F. Liu, L. M. Qi and X. F. Guo, *Small*, 2009, **5**, 2371-2376.

96. H. E. Unalan, P. Hiralal, D. Kuo, B. Parekh, G. Amaratunga and M. Chhowalla, *Journal of Materials Chemistry*, 2008, **18**, 5909-5912.

97. F. Vietmeyer, B. Seger and P. V. Kamat, *Advanced Materials*, 2007, **19**, 2935-+.

98. R. Krupke, F. Hennrich, H. B. Weber, M. M. Kappes and H. von Lohneysen, *Nano Letters*, 2003, **3**, 1019-1023.

99. S. H. T. Jong G. Ok, K. Anne Juggernauth, Kai Sun, Yongyi Zhang, A. John Hart, *Advanced Functional Materials*, 2010, **Volume 20**, pages 2470–2480.

100. Y. B. Li, F. Della Valle, M. Simonnet, I. Yamada and J. J. Delaunay, *Applied Physics Letters*, 2009, **94**, -.

101. M. Shim, J. H. Back, T. Ozel and K. W. Kwon, *Physical Review B*, 2005, **71**, -.

102. R. J. Chen, N. R. Franklin, J. Kong, J. Cao, T. W. Tombler, Y. G. Zhang and H. J. Dai, *Applied Physics Letters*, 2001, **79**, 2258-2260.

103. Q. H. Li, Y. X. Liang, Q. Wan and T. H. Wang, *Applied Physics Letters*, 2004, **85**, 6389-6391.

104. Q. H. Li, Q. Wan, Y. X. Liang and T. H. Wang, *Applied Physics Letters*, 2004, **84**, 4556-4558.

105. O. Lupan, G. Chai and L. Chow, *Microelectronics Journal*, 2007, **38**, 1211-1216.

106. L. Valentini, I. Armentano, J. M. Kenny, C. Cantalini, L. Lozzi and S. Santucci, *Applied Physics Letters*, 2003, **82**, 961-963.

107. H. T. Wang, B. S. Kang, F. Ren, L. C. Tien, P. W. Sadik, D. P. Norton, S. J. Pearton and J. Lin, *Applied Physics Letters*, 2005, **86**, -.

108. Z. L. Wang, *Journal of Physics-Condensed Matter*, 2004, **16**, R829-R858.

109. C. Schonenberger, B. M. I. vanderZande, L. G. J. Fokkink, M. Henny, C. Schmid, M. Kruger, A. Bachtold, R. Huber, H. Birk and U. Staufer, *Journal of Physical Chemistry B*, 1997, **101**, 5497-5505.

110. J. W. Gardner and P. N. Bartlett, *Sensors and Actuators B-Chemical*, 1994, **18**, 211-220.

111. J. Janata and M. Josowicz, *Nature Materials*, 2003, **2**, 19-24.

112. K. Ramanathan, M. A. Bangar, M. H. Yun, W. F. Chen, A. Mulchandani and N. V. Myung, *Nano Letters*, 2004, **4**, 1237-1239.

113. H. Sangodkar, S. Sukeerthi, R. S. Srinivasa, R. Lal and A. Q. Contractor, *Analytical Chemistry*, 1996, **68**, 779-783.

114. M. Penza, E. Milella and V. I. Anisimkin, *Sensors and Actuators B-Chemical*, 1998, **47**, 218-224.

115. M. Penza, E. Milella, F. Musio, M. B. Alba, G. Cassano and A. Quirini, *Materials Science & Engineering C-Biomimetic Materials Sensors and Systems*, 1998, **5**, 255-258.

116. G. E. Collins and L. J. Buckley, *Synthetic Metals*, 1996, **78**, 93-101.

117. V. C. Nguyen and K. Potje-Kamloth, *Thin Solid Films*, 1999, **338**, 142-148.

118. S. Bouchtalla, L. Auret, J. M. Janot, A. Deronzier, J. C. Moutet and P. Seta, *Materials Science & Engineering C-Biomimetic and Supramolecular Systems*, 2002, **21**, 125-129.

119. K. Henkel, A. Oprea, I. Paloumpa, G. Appel, D. Schmeisser and P. Kamieth, *Sensors and Actuators B-Chemical*, 2001, **76**, 124-129.

120. C. N. Van and K. Potje-Kamloth, *Thin Solid Films*, 2001, **392**, 113-121.

121. S. Hamilton, M. Hepher and J. Sommerville, *Sensors and Actuators B-Chemical*, 2005, **107**, 424-432.

122. P. A. Wright and C. M. Wood, *Journal of Experimental Biology*, 1985, **114**, 329-353.

123. J. F. M. Huijsmans, J. M. G. Hol and G. D. Vermeulen, *Atmospheric Environment*, 2003, **37**, 3669-3680.

124. E. D. Rogdakis and G. K. Alexis, *Applied Thermal Engineering*, 2000, **20**, 213-226.

125. A. M. Glasgow, R. B. Cotton and Dhiensir.K, *American Journal of Diseases of Children*, 1972, **124**, 827-833.

126. P. W. G. G. Koerkamp, J. H. M. Metz, G. H. Uenk, V. R. Phillips, M. R. Holden, R. W. Sneath, J. L. Short, R. P. White, J. Hartung, J. Seedorf, M. Schroder, K. H. Linkert, S. Pedersen, H. Takai, J. O. Johnsen and C. M. Wathes, *Journal of Agricultural Engineering Research*, 1998, **70**, 79-95.

127. Y. D. Jiang, T. Wang, Z. M. Wu, D. Li, X. D. Chen and D. Xie, *Sensors and Actuators B-Chemical*, 2000, **66**, 280-282.

128. V. Vrkoslav, I. Jelinek, G. Broncova, V. Kral and J. Dian, *Materials Science & Engineering C-Biomimetic and Supramolecular Systems*, 2006, **26**, 1072-1076.

129. J. Huang, S. Virji, B. H. Weiller and R. B. Kaner, *Chemistry-a European Journal*, 2004, **10**, 1315-1319.

130. Q. Ameer and S. B. Adeloju, *Sensors and Actuators B-Chemical*, 2005, **106**, 541-552.

131. K. Ramanathan, M. A. Bangar, M. Yun, W. Chen, N. V. Myung and A. Mulchandani, *Journal of the American Chemical Society*, 2005, **127**, 496-497.

132. J. M. Mativetsky and W. R. Datars, *Solid State Communications*, 2002, **122**, 151-154.

133. H. L. Yan, L. Zhang, J. Y. Shen, Z. J. Chen, G. Q. Shi and B. L. Zhang, *Nanotechnology*, 2006, **17**, 3446-3450.

134. A. Bhattacharya, A. De, S. N. Bhattacharya and S. Das, *Journal of Physics-Condensed Matter*, 1994, **6**, 10499-10507.

135. J. Y. Shen, Z. J. Chen, N. L. Wang, H. L. Yan, G. Q. Shi, A. Z. Jin and C. Z. Gu, *Applied Physics Letters*, 2006, **88**, -.

136. M. Reghu, Y. Cao, D. Moses and A. J. Heeger, *Physical Review B*, 1993, **47**, 1758-1764.

137. G. Gustafsson, I. Lundstrom, B. Liedberg, C. R. Wu, O. Inganas and O. Wennerstrom, *Synthetic Metals*, 1989, **31**, 163-179.

138. H. Q. Liu, J. Kameoka, D. A. Czaplewski and H. G. Craighead, *Nano Letters*, 2004, **4**, 671-675.

139. J. H. Cho, J. B. Yu, J. S. Kim, S. O. Sohn, D. D. Lee and J. S. Huh, *Sensors and Actuators B-Chemical*, 2005, **108**, 389-392.

140. J. G. Lu, P. C. Chang and Z. Y. Fan, *Materials Science & Engineering R-Reports*, 2006, **52**, 49-91.

141. Q. Wan, C. L. Lin, X. B. Yu and T. H. Wang, *Applied Physics Letters*, 2004, **84**, 124-126.

142. J. G. Ok, S. H. Tawfick, K. A. Juggernauth, K. Sun, Y. Zhang and A. J. Hart, *Advanced Functional Materials*, 2010, **20**, 2470–2480.

143. E. S. Snow, F. K. Perkins, E. J. Houser, S. C. Badescu and T. L. Reinecke, *Science*, 2005, **307**, 1942-1945.

144. E. S. Snow, F. K. Perkins and J. A. Robinson, *Chemical Society Reviews*, 2006, **35**, 790-798.

145. J. A. Robinson, E. S. Snow, S. C. Badescu, T. L. Reinecke and F. K. Perkins, *Nano Letters*, 2006, **6**, 1747-1751.

146. J. A. Robinson, E. S. Snow and F. K. Perkins, *Sensors and Actuators a-Physical*, 2007, **135**, 309-314.

147. T. Zhang, M. B. Nix, B. Y. Yoo, M. A. Deshusses and N. V. Myung, *Electroanalysis*, 2006, **18**, 1153-1158.

148. D. R. Kauffman and A. Star, *Journal of Physical Chemistry C*, 2008, **112**, 4430-4434.

149. A. Star, V. Joshi, S. Skarupo, D. Thomas and J. C. P. Gabriel, *Journal of Physical Chemistry B*, 2006, **110**, 21014-21020.

150. D. R. Kauffman and A. Star, *Angewandte Chemie-International Edition*, 2008, **47**, 6550-6570.

151. E. Bekyarova, I. Kalinina, M. E. Itkis, L. Beer, N. Cabrera and R. C. Haddon, *Journal of the American Chemical Society*, 2007, **129**, 10700-10706.

152. M. D. Ganji and A. Afsari, *Physica E-Low-Dimensional Systems & Nanostructures*, 2009, **41**, 1696-1700.

153. A. Gonzalez-Campo, K. L. Orchard, N. Sato, M. S. P. Shaffer and C. K. Williams, *Chemical Communications*, 2009, 4034-4036.

154. L. Q. Jiang and L. Gao, *Materials Chemistry and Physics*, 2005, **91**, 313-316.

155. T. G. Jiu, H. B. Liu, H. Y. Gan, Y. L. Li, S. Q. Xiao, H. M. Li, Y. Liu, F. S. Lu, L. Jiang and D. B. Zhu, *Synthetic Metals*, 2005, **148**, 313-319.

156. J. Khanderi, R. C. Hoffmann, A. Gurlo and J. J. Schneider, *Journal of Materials Chemistry*, 2009, **19**, 5039-5046.

157. H. Kim and W. Sigmund, *Applied Physics Letters*, 2002, **81**, 2085-2087.

158. Y. W. Koh, M. Lin, C. K. Tan, Y. L. Foo and K. P. Loh, *Journal of Physical Chemistry B*, 2004, **108**, 11419-11425.

159. J. Liu, M. J. Casavant, M. Cox, D. A. Walters, P. Boul, W. Lu, A. J. Rimberg, K. A. Smith, D. T. Colbert and R. E. Smalley, *Chemical Physics Letters*, 1999, **303**, 125-129.

160. S. Mubeen, T. Zhang, N. Chartuprayoon, Y. Rheem, A. Mulchandani, N. V. Myung and M. A. Deshusses, *Analytical Chemistry*, 2010, **82**, 250-257.

161. T. Zhang, S. Mubeen, B. Yoo, N. V. Myung and M. A. Deshusses, *Nanotechnology*, 2009, **20**, -.

162. N. Yamazoe, *Sensors and Actuators B-Chemical*, 1991, **5**, 7-19.

163. E. Comini, C. Baratto, G. Faglia, M. Ferroni, A. Vomiero and G. Sberveglieri, *Progress in Materials Science*, 2009, **54**, 1-67.

164. M. Izaki and T. Omi, *Applied Physics Letters*, 1996, **68**, 2439-2440.

165. M. Izaki and T. Omi, *Journal of the Electrochemical Society*, 1996, **143**, L53-L55.

166. S. J. Limmer, E. A. Kulp and J. A. Switzer, *Langmuir*, 2006, **22**, 10535-10539.

167. D. Lincot, *Thin Solid Films*, 2005, **487**, 40-48.

168. T. Yoshida, D. Komatsu, N. Shimokawa and H. Minoura, *Thin Solid Films*, 2004, **451-52**, 166-169.

169. L. S. Zhang, Z. G. Chen, Y. W. Tang and Z. J. Jia, *Thin Solid Films*, 2005, **492**, 24-29.

170. L. P. Zhu, G. H. Liao, W. Y. Huang, L. L. Ma, Y. Yang, Y. Yu and S. Y. Fu, *Materials Science and Engineering B-Advanced Functional Solid-State Materials*, 2009, **163**, 194-198.

171. S. C. Hernandez, D. Chaudhuri, W. Chen, N. V. Myung and A. Mulchandani, *Electroanalysis*, 2007, **19**, 2125-2130.

172. A. Brenner, *Electrodeposition of alloys: principles and practice*, Academic Press, New York,, 1963.

173. R. M. Nyffenegger, B. Craft, M. Shaaban, S. Gorer, G. Erley and R. M. Penner, *Chemistry of Materials*, 1998, **10**, 1120-1129.

174. S. Otani, J. Katayama, H. Umemoto and M. Matsuoka, *Journal of the Electrochemical Society*, 2006, **153**, C551-C556.

175. S. T. Jiang, M. Q. Wu, Y. Zhou, Y. Wen, C. T. Yang and S. R. Zhang, *Integrated Ferroelectrics*, 2007, **88**, 33-+.

176. J. H. Lim, N. Phiboolsirichit, S. Mubeen, Y. Rheem, M. A. Deshusses, A. Mulchandani and N. V. Myung, *Electroanalysis*, 2010, **22**, 99-105.

177. Y. W. Zhu, H. I. Elim, Y. L. Foo, T. Yu, Y. J. Liu, W. Ji, J. Y. Lee, Z. X. Shen, A. T. S. Wee, J. T. L. Thong and C. H. Sow, *Advanced Materials*, 2006, **18**, 587-+.

178. L. M. Yu and C. C. Zhu, *Applied Surface Science*, 2009, **255**, 8359-8362.

179. E. C. Walter, B. J. Murray, F. Favier, G. Kaltenpoth, M. Grunze and R. M. Penner, *Journal of Physical Chemistry B*, 2002, **106**, 11407-11411.

180. Y. W. Fan, B. R. Goldsmith and P. G. Collins, *Nature Materials*, 2005, **4**, 906-911.

181. L. Hu, D. S. Hecht and G. Gruner, *Nano Letters*, 2004, **4**, 2513-2517.

182. C. W. Zhou, J. Kong and H. J. Dai, *Applied Physics Letters*, 2000, **76**, 1597-1599.

183. M. Caglar, Y. Caglar, S. Aksoy and S. Ilican, *Applied Surface Science*, 2010, **256**, 4966-4971.

184. Q. Wan, Q. H. Li, Y. J. Chen, T. H. Wang, X. L. He, J. P. Li and C. L. Lin, *Applied Physics Letters*, 2004, **84**, 3654-3656.

185. C. H. Wang, X. F. Chu and M. W. Wu, *Sensors and Actuators B-Chemical*, 2006, **113**, 320-323.

186. N. Van Hicu and N. D. Chien, *Physica B-Condensed Matter*, 2008, **403**, 50-56.

187. N. Zhang, K. Yu, Q. Li, Z. Q. Zhu and Q. Wan, *Journal of Applied Physics*, 2008, **103**, -.

188. C. S. Rout, G. U. Kulkarni and C. N. R. Rao, *Journal of Physics D-Applied Physics*, 2007, **40**, 2777-2782.

189. J. Y. Lin, J. A. May, S. V. Didziulis and E. I. Solomon, *Journal of the American Chemical Society*, 1992, **114**, 4718-4727.

190. J. A. Rodriguez and A. Maiti, *Journal of Physical Chemistry B*, 2000, **104**, 3630-3638.

191. X. Chen, F. J. Xu, Y. Wang, Y. F. Pan, D. J. Lu, P. Wang, K. J. Ying, E. G. Chen and W. M. Zhang, *Cancer*, 2007, **110**, 835-844.

192. J. W. Dallinga, C. M. H. H. T. Robroeks, J. J. B. N. van Berkel, E. J. C. Moonen, R. W. L. Godschalk, Q. Jobsis, E. Dompeling, E. F. M. Wouters and F. J. van Schooten, *Clinical and Experimental Allergy*, 2010, **40**, 68-76.

193. G. Peng, U. Tisch, O. Adams, M. Hakim, N. Shehada, Y. Y. Broza, S. Billan, R. Abdah-Bortnyak, A. Kuten and H. Haick, *Nature Nanotechnology*, 2009, **4**, 669-673.

194. M. Phillips, R. N. Cataneo, R. Condos, G. A. R. Erickson, J. Greenberg, V. La Bombardi, M. I. Munawar and O. Tietje, *Tuberculosis*, 2007, **87**, 44-52.

195. M. Phillips, R. N. Cataneo, B. A. Ditkoff, P. Fisher, J. Greenberg, R. Gunawardena, C. S. Kwon, O. Tietje and C. Wong, *Breast Cancer Research and Treatment*, 2006, **99**, 19-21.

196. B. Zappacosta, A. Manni, S. Persichilli, A. Boari, D. Scribano, A. Minucci, L. Raffaelli, B. Giardina and P. De Sole, *Clinical Biochemistry*, 2007, **40**, 661-665.

197. B. Buszewski, M. Kesy, T. Ligor and A. Amann, *Biomedical Chromatography*, 2007, **21**, 553-566.

198. M. Phillips, K. Gleeson, J. M. B. Hughes, J. Greenberg, R. N. Cataneo, L. Baker and W. P. McVay, *Lancet*, 1999, **353**, 1930-1933.

199. D. Poli, P. Manini, R. Andreoli, I. Franchini and A. Mutti, *Journal of Chromatography B-Analytical Technologies in the Biomedical and Life Sciences*, 2005, **820**, 95-102.

200. M. Penza, G. Cassano, P. Aversa, F. Antolini, A. Cusano, M. Consales, M. Giordano and L. Nicolais, *Sensors and Actuators B-Chemical*, 2005, **111**, 171-180.

201. M. Penza, G. Cassano, P. Aversa, F. Antolini, A. Cusano, A. Cutolo, M. Giordano and L. Nicolais, *Applied Physics Letters*, 2004, **85**, 2379-2381.

202. M. Penza, G. Cassano, P. Aversa, A. Cusano, A. Cutolo, M. Giordano and L. Nicolais, *Nanotechnology*, 2005, **16**, 2536-2547.

203. M. Penza, R. Rossi, M. Alvisi, G. Cassano and E. Serra, *Sensors and Actuators B-Chemical*, 2009, **140**, 176-184.

204. M. Penza, R. Rossi, M. Alvisi, G. Cassano, M. A. Signore, E. Serra and R. Giorgi, *Sensors and Actuators B-Chemical*, 2008, **135**, 289-297.

205. M. Penza, R. Rossi, M. Alvisi, M. A. Signore, G. Cassano, D. Dimaio, R. Pentassuglia, E. Piscopiello, E. Serra and M. Falconieri, *Thin Solid Films*, 2009, **517**, 6211-6216.

206. M. Penza, M. A. Tagliente, P. Aversa and G. Cassano, *Chemical Physics Letters*, 2005, **409**, 349-354.

207. M. Penza, M. A. Tagliente, P. Aversa, G. Cassano and L. Capodieci, *Materials Science & Engineering C-Biomimetic and Supramolecular Systems*, 2006, **26**, 1165-1170.

208. X. F. Ma, X. B. Zhang, Y. Li, G. A. Li, M. Wang, H. Z. Chen and Y. H. Mi, *Macromolecular Materials and Engineering*, 2006, **291**, 75-82.

209. K. S. V. Santhanam, R. Sangoi and L. Fuller, *Sensors and Actuators B-Chemical*, 2005, **106**, 766-771.

210. C. Wei, L. M. Dai, A. Roy and T. B. Tolle, *Journal of the American Chemical Society*, 2006, **128**, 1412-1413.

211. Q. F. Pengfei, O. Vermesh, M. Grecu, A. Javey, O. Wang, H. J. Dai, S. Peng and K. J. Cho, *Nano Letters*, 2003, **3**, 347-351.

212. J. Kong, M. G. Chapline and H. J. Dai, *Advanced Materials*, 2001, **13**, 1384-1386.

213. F. Wang, Y. Yang and T. M. Swager, *Angewandte Chemie-International Edition*, 2008, **47**, 8394-8396.

214. F. Wang, H. W. Gu and T. M. Swager, *Journal of the American Chemical Society*, 2008, **130**, 5392-+.

215. S. Mubeen, T. Zhang, B. Yoo, M. A. Deshusses and N. V. Myung, *Journal of Physical Chemistry C*, 2007, **111**, 6321-6327.

216. O. Lupan, V. V. Ursaki, G. Chai, L. Chow, G. A. Emelchenko, I. M. Tiginyanu, A. N. Gruzintsev and A. N. Redkin, *Sensors and Actuators B-Chemical*, 2010, **144**, 56-66.

217. C. L. Yaws, *Chemical properties handbook : physical, thermodynamic, environmental, transport, safety, and health related properties for organic and inorganic chemicals*, McGraw-Hill, New York, 1999.

218. H. Malamud, R. Geisman and S. Lowell, *Analytical Chemistry*, 1967, **39**, 1468-&.

219. V. L. Pushparaj, M. M. Shaijumon, A. Kumar, S. Murugesan, L. Ci, R. Vajtai, R. J. Linhardt, O. Nalamasu and P. M. Ajayan, *Proceedings of the National Academy of Sciences of the United States of America*, 2007, **104**, 13574-13577.

220. T. M. Barnes, X. Wu, J. Zhou, A. Duda, J. van de Lagemaat, T. J. Coutts, C. L. Weeks, D. A. Britz and P. Glatkowski, *Applied Physics Letters*, 2007, **90**, -.

221. D. R. Kauffman, Y. F. Tang, P. D. Kichambare, J. F. Jackovitz and A. Star, *Energy & Fuels*, 2010, **24**, 1877-1881.

222. D. M. Guldi, G. M. A. Rahman, V. Sgobba, N. A. Kotov, D. Bonifazi and M. Prato, *Journal of the American Chemical Society*, 2006, **128**, 2315-2323.

223. S.-H.-I. Laila, B. Bernhard and W. Itamar, *Angewandte Chemie International Edition*, 2005, **44**, 78-83.

224. L. Hu, Y. L. Zhao, K. Ryu, C. Zhou, J. F. Stoddart and G. Grüner, *Advanced Materials*, 2008, **20**, 939-946.

225. B. Zebli, H. A. Vieyra, I. Carmeli, A. Hartschuh, J. P. Kotthaus and A. W. Holleitner, *Physical Review B*, 2009, **79**, -.

226. S. Banerjee and S. S. Wong, *Nano Letters*, 2002, **2**, 195-200.

227. B. H. Juarez, C. Klinke, A. Kornowski and H. Weller, *Nano Letters*, 2007, **7**, 3564-3568.

228. J. M. Haremza, M. A. Hahn and T. D. Krauss, *Nano Letters*, 2002, **2**, 1253-1258.

229. S. Banerjee and S. S. Wong, *Advanced Materials*, 2004, **16**, 34-+.

230. A. Kolmakov and M. Moskovits, *Annual Review of Materials Research*, 2004, **34**, 151-180.

231. C. Soci, A. Zhang, B. Xiang, S. A. Dayeh, D. P. R. Aplin, J. Park, X. Y. Bao, Y. H. Lo and D. Wang, *Nano Letters*, 2007, **7**, 1003-1009.

232. Z. X. Zhang, L. F. Sun, Y. C. Zhao, Z. Liu, D. F. Liu, L. Cao, B. S. Zou, W. Y. Zhou, C. Z. Gu and S. S. Xie, *Nano Letters*, 2008, **8**, 652-655.

233. F. S. Li, S. H. Cho, D. I. Son, T. W. Kim, S. K. Lee, Y. H. Cho and S. H. Jin, *Applied Physics Letters*, 2009, **94**, -.

234. S. Liu, J. F. Ye, Y. Cao, Q. Shen, Z. F. Liu, L. M. Qi and X. F. Guo, *Small*, 2009, **5**, 2371-2376.

235. H. E. Unalan, P. Hiralal, D. Kuo, B. Parekh, G. Amaratunga and M. Chhowalla, *Journal of Materials Chemistry*, 2008, **18**, 5909-5912.

236. F. Vietmeyer, B. Seger and P. V. Kamat, *Advanced Materials*, 2007, **19**, 2935-+.

237. R. Krupke, F. Hennrich, H. B. Weber, M. M. Kappes and H. von Lohneysen, *Nano Letters*, 2003, **3**, 1019-1023.

238. S. H. T. Jong G. Ok, K. Anne Juggernauth, Kai Sun, Yongyi Zhang, A. John Hart, *Advanced Functional Materials*, 2010, **Volume 20**, pages 2470–2480.

239. Y. B. Li, F. Della Valle, M. Simonnet, I. Yamada and J. J. Delaunay, *Applied Physics Letters*, 2009, **94**, -.

240. M. Shim, J. H. Back, T. Ozel and K. W. Kwon, *Physical Review B*, 2005, **71**, -.

241. R. J. Chen, N. R. Franklin, J. Kong, J. Cao, T. W. Tombler, Y. G. Zhang and H. J. Dai, *Applied Physics Letters*, 2001, **79**, 2258-2260.

242. Q. H. Li, Y. X. Liang, Q. Wan and T. H. Wang, *Applied Physics Letters*, 2004, **85**, 6389-6391.

243. Q. H. Li, Q. Wan, Y. X. Liang and T. H. Wang, *Applied Physics Letters*, 2004, **84**, 4556-4558.

244. O. Lupan, G. Chai and L. Chow, *Microelectronics Journal*, 2007, **38**, 1211-1216.

245. L. Valentini, I. Armentano, J. M. Kenny, C. Cantalini, L. Lozzi and S. Santucci, *Applied Physics Letters*, 2003, **82**, 961-963.

246. H. T. Wang, B. S. Kang, F. Ren, L. C. Tien, P. W. Sadik, D. P. Norton, S. J. Pearton and J. Lin, *Applied Physics Letters*, 2005, **86**, -.

247. Z. L. Wang, *Journal of Physics-Condensed Matter*, 2004, **16**, R829-R858.

248. C. Schonenberger, B. M. I. vanderZande, L. G. J. Fokkink, M. Henny, C. Schmid, M. Kruger, A. Bachtold, R. Huber, H. Birk and U. Staufer, *Journal of Physical Chemistry B*, 1997, **101**, 5497-5505.

249. J. W. Gardner and P. N. Bartlett, *Sensors and Actuators B-Chemical*, 1994, **18**, 211-220.

250. J. Janata and M. Josowicz, *Nature Materials*, 2003, **2**, 19-24.

251. K. Ramanathan, M. A. Bangar, M. H. Yun, W. F. Chen, A. Mulchandani and N. V. Myung, *Nano Letters*, 2004, **4**, 1237-1239.

252. H. Sangodkar, S. Sukeerthi, R. S. Srinivasa, R. Lal and A. Q. Contractor, *Analytical Chemistry*, 1996, **68**, 779-783.

253. M. Penza, E. Milella and V. I. Anisimkin, *Sensors and Actuators B-Chemical*, 1998, **47**, 218-224.

254. M. Penza, E. Milella, F. Musio, M. B. Alba, G. Cassano and A. Quirini, *Materials Science & Engineering C-Biomimetic Materials Sensors and Systems*, 1998, **5**, 255-258.

255. G. E. Collins and L. J. Buckley, *Synthetic Metals*, 1996, **78**, 93-101.

256. V. C. Nguyen and K. Potje-Kamloth, *Thin Solid Films*, 1999, **338**, 142-148.

257. S. Bouchtalla, L. Auret, J. M. Janot, A. Deronzier, J. C. Moutet and P. Seta, *Materials Science & Engineering C-Biomimetic and Supramolecular Systems*, 2002, **21**, 125-129.

258. K. Henkel, A. Oprea, I. Paloumpa, G. Appel, D. Schmeisser and P. Kamieth, *Sensors and Actuators B-Chemical*, 2001, **76**, 124-129.

259. C. N. Van and K. Potje-Kamloth, *Thin Solid Films*, 2001, **392**, 113-121.

260. S. Hamilton, M. Hepher and J. Sommerville, *Sensors and Actuators B-Chemical*, 2005, **107**, 424-432.

261. P. A. Wright and C. M. Wood, *Journal of Experimental Biology*, 1985, **114**, 329-353.

262. J. F. M. Huijsmans, J. M. G. Hol and G. D. Vermeulen, *Atmospheric Environment*, 2003, **37**, 3669-3680.

263. E. D. Rogdakis and G. K. Alexis, *Applied Thermal Engineering*, 2000, **20**, 213-226.

264. A. M. Glasgow, R. B. Cotton and Dhiensir.K, *American Journal of Diseases of Children*, 1972, **124**, 827-833.

265. P. W. G. G. Koerkamp, J. H. M. Metz, G. H. Uenk, V. R. Phillips, M. R. Holden, R. W. Sneath, J. L. Short, R. P. White, J. Hartung, J. Seedorf, M. Schroder, K. H. Linkert, S. Pedersen, H. Takai, J. O. Johnsen and C. M. Wathes, *Journal of Agricultural Engineering Research*, 1998, **70**, 79-95.

266. Y. D. Jiang, T. Wang, Z. M. Wu, D. Li, X. D. Chen and D. Xie, *Sensors and Actuators B-Chemical*, 2000, **66**, 280-282.

267. V. Vrkoslav, I. Jelinek, G. Broncova, V. Kral and J. Dian, *Materials Science & Engineering C-Biomimetic and Supramolecular Systems*, 2006, **26**, 1072-1076.

268. J. Huang, S. Virji, B. H. Weiller and R. B. Kaner, *Chemistry-a European Journal*, 2004, **10**, 1315-1319.

269. Q. Ameer and S. B. Adeloju, *Sensors and Actuators B-Chemical*, 2005, **106**, 541-552.

270. K. Ramanathan, M. A. Bangar, M. Yun, W. Chen, N. V. Myung and A. Mulchandani, *Journal of the American Chemical Society*, 2005, **127**, 496-497.

271. J. M. Mativetsky and W. R. Datars, *Solid State Communications*, 2002, **122**, 151-154.

272. H. L. Yan, L. Zhang, J. Y. Shen, Z. J. Chen, G. Q. Shi and B. L. Zhang, *Nanotechnology*, 2006, **17**, 3446-3450.

273. A. Bhattacharya, A. De, S. N. Bhattacharya and S. Das, *Journal of Physics-Condensed Matter*, 1994, **6**, 10499-10507.

274. J. Y. Shen, Z. J. Chen, N. L. Wang, H. L. Yan, G. Q. Shi, A. Z. Jin and C. Z. Gu, *Applied Physics Letters*, 2006, **88**, -.

275. M. Reghu, Y. Cao, D. Moses and A. J. Heeger, *Physical Review B*, 1993, **47**, 1758-1764.

276. G. Gustafsson, I. Lundstrom, B. Liedberg, C. R. Wu, O. Inganas and O. Wennerstrom, *Synthetic Metals*, 1989, **31**, 163-179.

277. H. Q. Liu, J. Kameoka, D. A. Czaplewski and H. G. Craighead, *Nano Letters*, 2004, **4**, 671-675.

278. J. H. Cho, J. B. Yu, J. S. Kim, S. O. Sohn, D. D. Lee and J. S. Huh, *Sensors and Actuators B-Chemical*, 2005, **108**, 389-392.

Appendix 1:

Template Free Synthesis of ZnO Nanowires

A1.1 Introduction

There are three different electrochemical routes that allow for electrochemical synthesis of zinc oxide. In this work O_2 was used as the source for the hydroxide ion, where the formation of zinc oxide material occurs by two sequential steps. First is the electrochemical reduction of the precursor to form hydroxide ions, in this scenario O_2 is continuously bubbled through the solution e creating a localized increase in pH at the forefront of the cathode. The second step consists of the chemical precipitation of ZnO as the Zn ions interact with the hydroxide ions. The general process is described by the equation 1, and the overall process is summarized in equation 2.

$$\begin{aligned}&\frac{1}{2}O_2 + H_2O + 2e^- \rightarrow\ 2OH^- \\ &Zn^{2+} + 2OH^- \leftrightarrow Zn(OH)_2 \\ &Zn(OH)_2 \leftrightarrow ZnO + H_2O\end{aligned} \qquad \text{Equation 1}$$

$$Zn^{2+} + \frac{1}{2}O_2 + H_2O + 2e^- \rightarrow Zn(OH)_2 \leftrightarrow ZnO + H_2O \qquad \text{Equation 2}$$

A.1.2 Experimental

Glass covered with Indium Tin Oxide (ITO) was used as the substrates for ZnO nano-coulomb growth. ITO surfaces with approximate areas of 1 cm^2 were cleaned by washing with nanopure water followed by acetone prior to use. Once clean and dry, the ITO substrates were placed on a hot plate with the ITO surface face up and heated to 160°C. A zinc acetate seed later was added to the surfaces of ITO while heating at 160°C, by evenly placing a single drop (~50 μL) of 5 mM $Zn(CH_3COO)_2 \bullet 2H_2O$. Additional drops were placed after the prior one had completely evaporated, this was repeated ten times to ensure complete coating f the ITO substrate with the Zn seed later. The ITO substrate with the Zn seed later was then annealed at 350°C for 15 minutes by using conventional tube furnace under ambient conditions. ZnO nanocoulombs were electrodeposited on the surface of the Zn seed later by using a three electrode electrochemical system where the ITO/Zn substrate was used as the working electrode, a Pt sheet as the counter electrode, and a commercially available Ag/AgCl reference electrode. The deposition electrolyte consisted of 30 mM $ZnCl_2$ + 0.1 M KCl + 10μM $AlCl_3$ and saturated with O_2 by continuous bubbling of dry air to the electrolyte. The solution temperature was held at 80°C throughout the deposition process, a voltage of was -0.95 volts versus the reference electrode was applied, and experiment duration was 3600 seconds. After deposition, the ITO substrates containing the ZnO nanocoulombs were further annealed at 160°C for 15 minutes in a tube furnace under ambient conditions.

Material characterization was performed by use of X-ray diffraction (XRD), and Scanning Electron Microscopy (SEM). Room temperature gas sensing studies were performed on the ZnO nanocoulombs array by integrating the ITO substrate and establishing electrical contact by use of conductive silver paste to our custom made sensing system [161]. Each sensor was subjected to 1.0 V (DC) and the resistance was continuously recorded every 0.2 seconds simultaneously for three ITO/ZnO arrays by use of Keithley 236 source measurement unit controlled by a LabView program. A base line was achieved by continuous exposure to dry air and the methanol analyte was introduced by bubbling through high purity chemical grade liquid with the carrier gas. Analyte concentrations were attained by subsequent dilutions with the carrier gas, flow rates were regulated by mass flow controllers (Alicat Scientific Incorporated) and total gas flow rate was kept constant at 200 sccm for all experiments [161, 171].

A.1.3 Results and Discussion

Figure A.1.1 illustrates the process for the growth of template free ZnO nanocoulombs (ZnO NCs), demonstrating that the ZnO NCs grow perpendicular to the surface of the ITO substrate, beginning at the Zn seed layer which acts as a growth initiator. From the SEM images shown in figureA.1. 2, it is evident that there is a high yield of densely packed ZnO NCs produced by the hydrothermal-electrodeposition process and further confirms that the NCs growth originates at the base of the Zn seed later. The NCs have hexagonal cross section with average diameters of 51.79 ± 13.4 nm, and ZnO NC length less than 1 μm. The non-planer uniformity visible on the SEM images, indicated by the patchy growth, could be contributing to various NCs length and is speculated to be overcome by spin coating of the zinc acetate solution instead of drop casting.

The XRD patterns of ITO glass with the Zn seed later, ZnO NCs attached to the ITO grown for one hour [indicated by ZnO 1], and ZnO NCs attached to the ITO grown for 4 hours [indicated by ZnO 1] are shown in figure A.1.3. Interestingly, the Zn seed layer has peaks indicative of ZnO formation even though there has been no electrodeposition of ZnO NCs on the surface. Following the electrodeposition, the ZnO peaks become slightly stronger in intensity, and introduction of hydroxide peaks are clearly visible for the sample deposited for one hour. A longer deposition time of four hours eliminated the zinc-hydroxide peaks; however the ZnO peaks remained unaffected, in both intensity and position. Since the SEM images indicate that the lengths of the NCs are less than 1 μm, it also suggest that stronger XRD peaks are not attainable due to the lack of sample. Thus the substrate peak could contribute the most to the XRD pattern.

Sonicating the ITO containing ZnO NCs samples was initially anticipated as a way to detach the nanostructures fromm the ITO substrate however, since the length of the ZnO NCs was far smaller than electrically addressable by lithographic approaches, the full array of ZnO NCs was used as a devise for preliminary sensing studies and for proof of concept. Figure A.1.4 illustrates how the ITO substrates were utilizes as the sensing architecture for methanol sensing. The perimeter and top edges of the ITO containing ZnO NCs was insulated by applying non-conductive electrical tape and securing it with dielectric liquid adhesive (Microstop, Pyramind Plastics, Inc.). Electrical contact to the surface of ZnO NCs was established by applying conductive silver paste on the top surface of the substrates and extending it to the gold pads of the sensor architecture.

Gas sensing performance of the ZnO NCs was investigated by exposing the nanostructures to various concentrations of methanol. The initial resistance of the ZnO NC structures was stable at 26.6 kΩ, upon exposure to methanol vapors, the resistance increased linearly to the alcohol concentrations. Figure A.1.5 A demonstrates a typical sensing behavior, and figure A.1.5 B shows the corresponding calibration curve for the sensor performance.

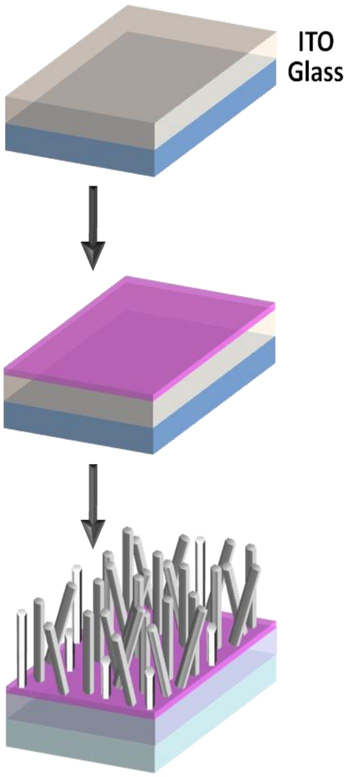

Figure A1.1. Illustration of the growth procedure for the template free ZnO nanocoulombs.

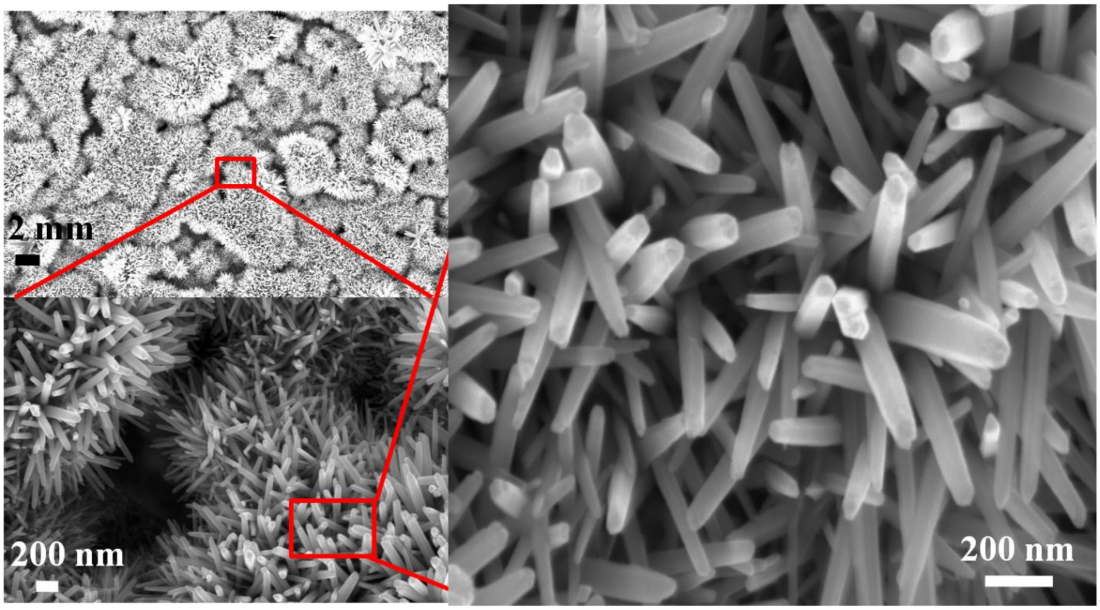

Figure A1.2. SEM micrographs of ZnO nanocoulombs demonstrating the high thorough put of the process and the resulting average diameter of the ZnO NCs.

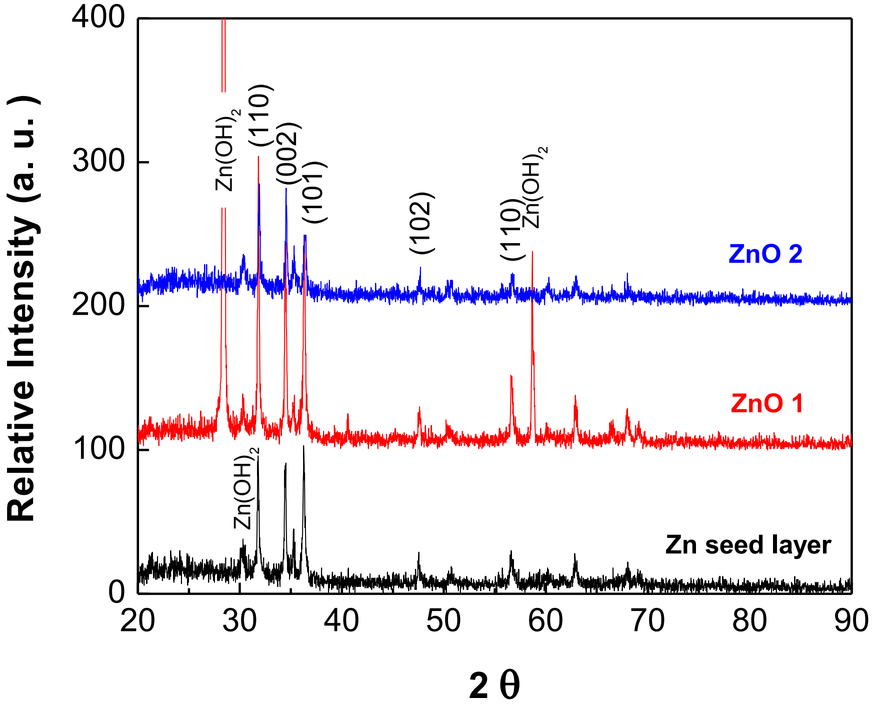

Figure A1.3. XRD pattern of ITO containing a seed layer, ZnO 1 represents ZnO NCs grown for one hour, and ZnO 2 represents ZnO NCs grown for 4 hours.

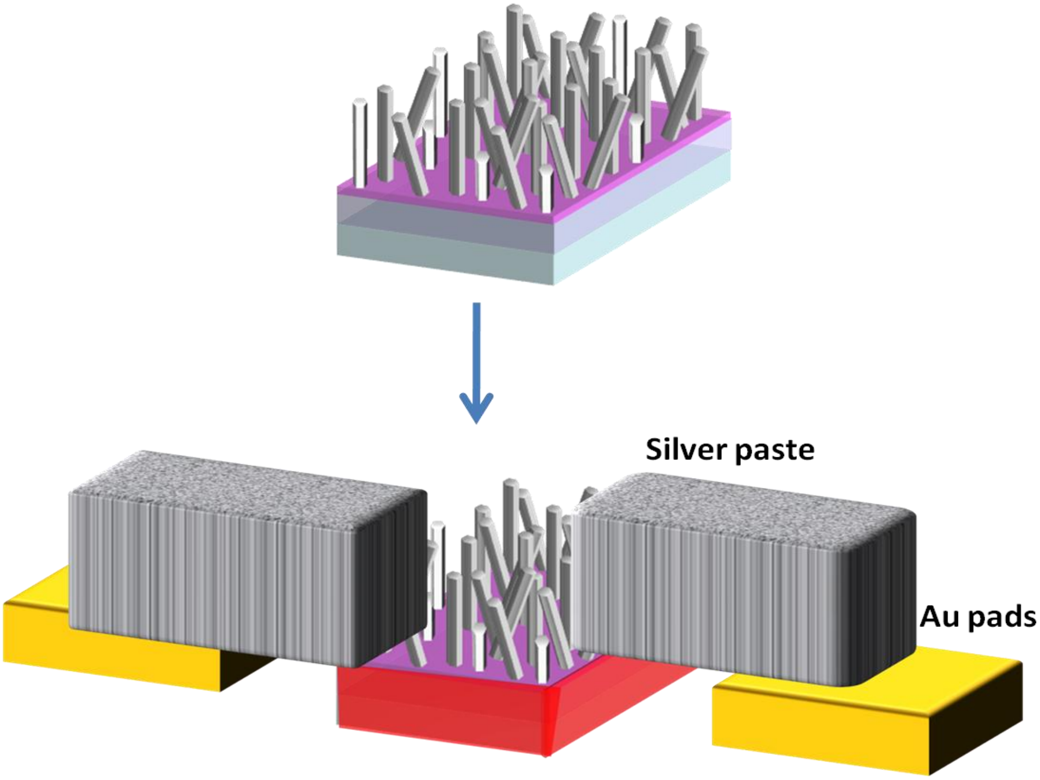

Figure A1.4. Illustration depicting electrical contact to ZnO NCs for gas sensing.

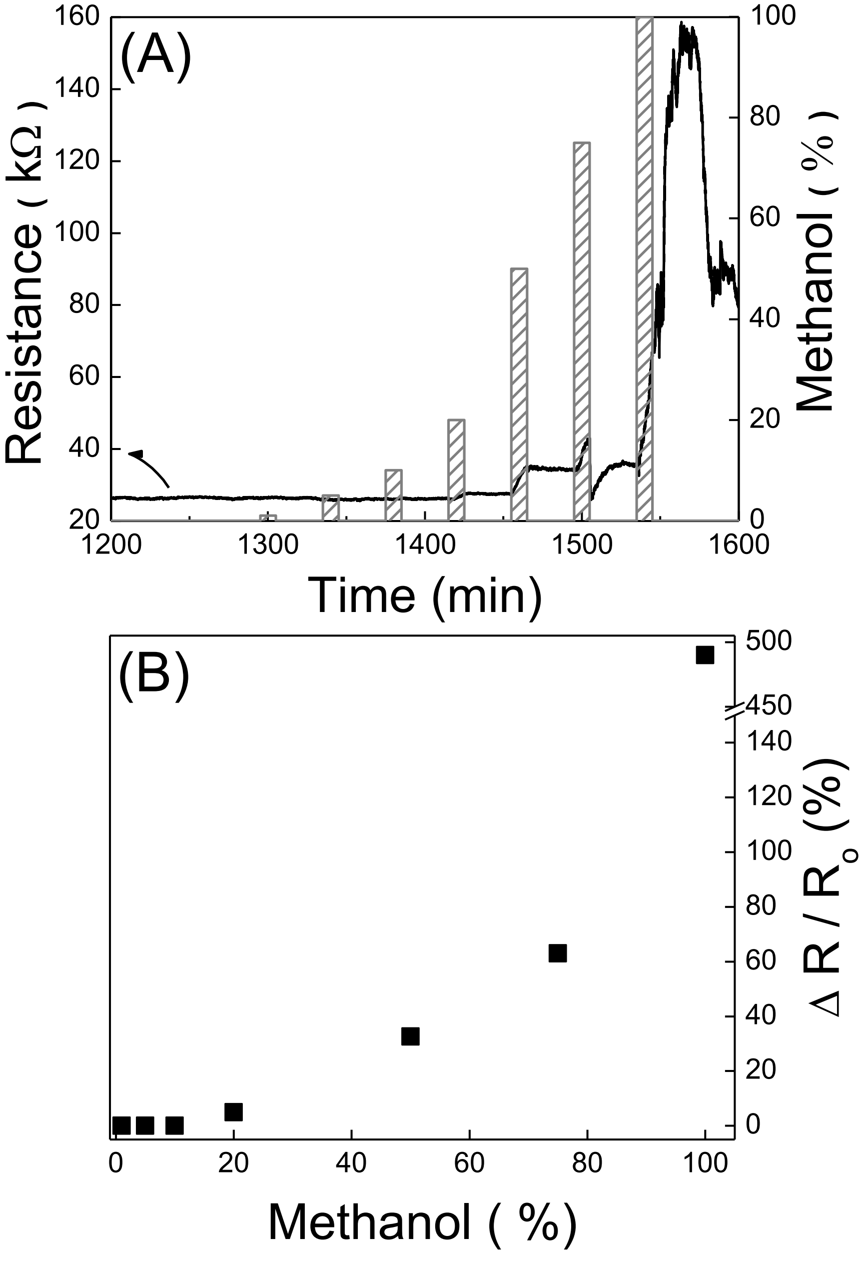

Figure A1.5. Gas sensing behavior of ZnO NCs annealed at 4 hours, towards methanol vapors.

Appendix 2:

Synthesis of ZnO nanowires with tailored material properties

A2.1 Introduction

The objective of this work was to develop a high density sensor array using ZnO nanowires (NWs) as the platform material for the realization of highly sensitive, selective and discriminative gas sensors. To conceive such desired sensor characteristics, ZnO nanowires with optimized material and electrical properties were utilized. Different electrochemical routes were investigated for the synthesis of ZnO nanowires in order to find an avenue that allows for manipulation of the structure dimensions and properties.

ZnO nanowires were be fabricated by conventional template directed electrodeposition where optimal deposition parameters such as solution composition, applied voltage, applied charge and operating temperature were investigated. Manipulation of the deposition parameters were employed to regulate material properties such as nanowire length, crystalline quality and dopant concentration. Furthermore, the diameter of the nanowires was adjusted by controlling the pore size of the polycarbonate membranes used as the deposition templates.

A2.2 Experimental

In an attempt to optimize the electrolyte composition, two solutions regions where investigated. In the first, the NO_3^+ was kept constant at 0.2M while varying the Zn^{2+} from 0.0 to 0.1 M. In the second, the NO_3^+ was kept constant at 2.0 M while the Zn^{2+} was varied from 0.2 to 1.0 M all solutions were kept at constant pH of 5.5. Experiments were performed using the conventional three electrode system, using a Zn sheet was as the soluble anode, and Au/Si wafers with working areas of $1cm^2$ as the cathodes and a standard Ag/AgCl reference electrode at room temperature in the absence of N_2 bubbling or agitation in order to preserve the pH gradient.

Nanowire synthesis was performed using the same solution based route by a bottom up approach. Using an electrolyte with composition of 0.1 M $Zn(NO_3)_2$, at 25°C and pH of 5.5, ZnO nanowires were synthesized within the pores of the polycarbonate templates, the electrochemically induced chemical precipitation mechanism is described by equation 2. Commercially available (Whatman Anodisc Nuclepore Track-Etch Membrane) polycarbonate membranes with average pore diameters of 15, 30, 50, and 100 nm were used as the templates for nanowire fabrication. A gold seed layer was sputtered on one side of the template using an Emitech K550 sputtering machine. The template was then fixed on to a glass support using double sided conductive copper tape, by attaching the face of the template with the seed layer on to the copper tape. In addition, single sided conductive copper tape was used as a lead to the glass slide. Finally, dielectric liquid adhesive (Microstop, Pyramind Plastics, Inc.) was applied over the copper tape and the whole glass support (front, back and edges), ensuring that everything but the desired deposition area and copper lead were insulated. Embedded nanowires were released from the polycarbonate template by introduction of 1mL of 1-methyl-2-pyrroinode in a 1.5 mL microcentrifuge tube. The contents were manually mixed and then allowed to sit for 15 minutes followed by centrifugation for 25 min at 5000rpm. The supernatant is then removed and more solvent is introduced, this washing procedure was performed four times or until template residue was eliminated.

Material characterization was performed by use of X-ray diffraction (XRD), scanning electron microscopy (SEM) and High Resolution Transmission Electron Microscopy (HR-TEM) in order to determine the morphology and crystal orientation of the structures.

A2.3 Results and Discussion

A2.3.1 Synthesis of ZnO Thin Films

Conventional production of metal oxides films can be divided by their synthesis environment, mainly vacuum based or solution based. A solution based synthesis approach was taken due to its operational simplicity and flexibility over process parameters. There are three different electrochemical routes described by the following equations that allow for electrochemical synthesis of zinc oxide.

$$\begin{gathered}\frac{1}{2}O_2 + H_2O + 2e^- \rightarrow 2OH^- \\ Zn^{2+} + 2OH^- \leftrightarrow Zn(OH)_2 \\ Zn(OH)_2 \leftrightarrow ZnO + H_2O\end{gathered} \tag*{Equation 1}$$

$$\begin{gathered}NO_3^- + H_2O + 2e^- \rightarrow NO_2^- + 2OH^- \\ Zn^{2+} + 2OH^- \leftrightarrow Zn(OH)_2 \\ Zn(OH)_2 \leftrightarrow ZnO + H_2O\end{gathered} \tag*{Equation 2}$$

$$\begin{aligned}&H_2O_2 + 2e^- \rightarrow 2OH^- \\ &Zn^{2+} + 2OH^- \leftrightarrow Zn(OH)_2 \\ &Zn(OH)_2 \leftrightarrow ZnO + H_2O\end{aligned} \qquad \textit{Equation 3}$$

In each of the above reaction pathways, a precursor either O_2, NO_3^-, H_2O_2, is needed as the source for the hydroxide ion. The formation of zinc oxide material occurs by two sequential steps. First is the electrochemical reduction of the precursor to form hydroxide ions. This process locally occurs at the forefront of the cathode creating a localized increase in pH, illustrated in figure A.2.1. The second step consists of the chemical precipitation of ZnO. Here Zn ions interact with the hydroxide ions forming a zinc hydroxide complex which then precipitates to zinc oxide. Because the stability of the hydroxide complex is highly dependent upon the solution pH, where higher pH values make the complex less stable, precipitation of ZnO occurs preferentially at the surface of the cathode [172]. The beauty of this process is that the rate of ZnO growth can be manipulated by controlling:

1. Precursor ion concentration (limiting reactant)
2. Applied voltage
3. Solution temperature

As demonstrated in figure A.2.2, the behavior of the linear sweep voltagrams (LSVs) for the two solution regions were very different. For the solution set of x M $Zn(NO_3)_2$ + (.2-2x) $NaNO_3$ (figure A.2.2 A), the absolute current density increased monotonically as the applied potential increased for every electrolyte. The rate of current density as a function of potential increased for electrolytes with higher Zn^{2+} concentration and exhibited a slight shift in reduction potential towards less negative values. For the solution set of x M $Zn(NO_3)_2$ + (2-2x) $NaNO_3$ (figure A.2.2 B), absolute current densities also increased with larger potentials, however there were more fluctuations indicating deposition instability. Since both nitrate and Zn^{2+} are present in larger amounts, the observed fluctuations were probably due to the competition between the reduction of the nitrate ion and the direct deposition of zinc metal. From these experiments it was deducted that a nitrate solution with Zn^{2+} concentration in the range of x M $Zn(NO_3)_2$ + (.2-2x) $NaNO_3$ was optimal.

A nitrate based electrolyte was analyzed with solution composition of 0.1 M $Zn(NO_3)_2$, pH of 5.5 adjusted with HCl or $NaNO_3$ using the same electrodeposition conditions as described above. Cyclic voltagrams were performed on the solution at room temperature and 70 °C in order to determine the potential window for ZnO given the prescribed conditions. As shown in figure A.2.3, there are differences in key characteristics of the deposition process when comparing the room temperature cycle to the one performed at higher temperature (arrow corresponds to the direction of the potential sweep) mainly a shift in deposition potential. For the system at 25 °C, there is no current with increasing potentials until voltages reach -1V and material can be deposited from -1. At 70 °C a small current is measured at -0.54 V and material can be deposited from thereafter. In both cases there is a nucleation potential difference, meaning that the forward sweep and reverse sweep don’t match up, and at this potential difference there is a simultaneous deposition and dissolution of the material. From the CV results we were able to determine a deposition potential window for the two operating temperatures (-1.3 to -1.4V for 25 °C and -1 to -1.4 V for 70 °C).

Films were deposited at -1.2, -1.3 and -1.4 volts versus a Ag/AgCl reference electrode at a constant charge density of 6 C cm^{-2} in 0.1 M $Zn(NO_3)_2$, 25°C and pH of 5.5. Although the potential window was determined to begin at -1.0 volt, the nucleation potential difference spans form -1.0 to -1.19 volts and consequently no films were obtained within that potential range. Illustrated in figure A.2.4 are XRD patterns that correspond to the films deposited at different voltages. At potentials between -1.2 to less than -1.3 V, only ZnO was deposited while at higher potentials Zn metal was incorporated in the films. From the XRD pattern it is evident that at 25°C we obtain polycrystalline ZnO films (-1.2V). The SEM images show the porous quality of the films obtained at the described deposition conditions. The purpose of the thin film depositions was to obtain knowledge of the deposition characteristics of the system and determine electrolyte concentration, proper anode (Zn vs. Pt), deposition potential window, and finally to obtain confirmation that ZnO was deposited at selected potentials.

A2.3.2 ZnO Template Directed Nanowires

Although the thin film studies showed a potential window of -1.2 to -1.3V versus Ag/AgCl at 25 °C, nanowires were obtained within the potential window of -0.6 to -1.0 V vs. Ag/AgCl, due to the differing mass transfer effects. In order to determine the growth rate of ZnO within the pores of the membranes, depositions were systematically investigated in the 30nm nominal pore diameter templates at 25°C and the suspended nanowires were imaged and measured by SEM (figure A.2.5). Nanowires were deposited at constant charge and time to determine the most effective and reproducible deposition route, and found that constant charge gave better control over the nanowire length. As depicted in figure A.2.6, regardless of the deposition voltage, the average NW length was dependent on the applied charge density with an average growth rate of 0.013 µm hr^{-1}. For example, ZnO nanowires were ~1 µm when deposited at 1 C cm^{-2}, and ~4.5 µm when deposited at 2 C cm^{-2}. The inset in figure A.2.6 shows a typical image of a high density network of nanowires deposited at -1.0 volts, and 2 C cm^{-2}.

As suggested by the SEM image in figure A.2.6, even though the nominal pore size of the polycarbonate templates was reported to be 30 nm, the nanowires adopted a larger diameter size due to pore swelling effects of the polycarbonate template during deposition. It has previously been reported that nanowires deposited from polycarbonate templates assume the inner structure of the pore, generally resulting in a more “cigarlike” with tapered ends and increased diameter at the middle section of the wire [248]. The swelling of the pores is even more pronounced when depositing at elevated temperatures, such as 70°C. As illustrated in figure A.2.7 A, the actual nanowire diameters were observed to be larger than the template nominal pore diameters with about a 20 nm increase in nanowire diameter when deposited at 70°C. The SEM images (figure A.2.7 B and C) correspond to ZnO nanowires deposited at -1.0 V at 25C and using a 30 nm template with the resulting NW diameter of ~ 70 nm and when using a 100nm template, the resulting NW diameter was ~ 230 nm. This work shows that the nanowire diameter can be manipulated both by varying the template pore diameter and deposition temperature allowing for size range of 70 to 240nm.

In addition to using the deposition temperature to modulate the dimensions of the nanostructures, temperature can be used to control the material crystallinity. Represented in figure A.2.8 are the effects of deposition temperature on the ZnO nanowire crystalline quality. The TEM images show that while polycrystalline ZnO nanowires were obtained at 25°C, single crystal nanowires with (002) orientation can be obtained at 70°C. Although more thorough work needs to be performed to fully understand the mechanism and the extent to which crystallinity can be manipulated, these preliminary results demonstrate the ability to tailor the crystallinity of ZnO nanowires by controlling the solution temperature.

A2.4 Conclusions and Future Directions

ZnO is naturally an n-type semiconductor due to the presence of intrinsic defects, oxygen vacancies and Zn interstitials, a slight alteration in the purity of the original material can produce dramatic changes in electrical and chemical properties. Appreciable amount of work describing the doping of ZnO with group III elements to enhance n-type conductivity, group V elements to generate p-type behavior, and magnetic elements (Fe, Co, Ni, Mn) to synthesize dilute magnetic materials is available [140]. Recently, detection of various chemicals has been reported with a variety of nanowire sensor configurations. To summarize, ZnO nanostructure networks (ribbons, rods, wires) synthesized by thermal evaporation, liquid-solid method, and epitaxy (MBE) have been analyzed towards CO, NO_2, NH_3, H_2, H_2S, ethanol, O_2 and O_3. However there has been no clear correlation between the synthesis method, material properties, quantity of nanostructures, and effect of dimensions towards the sensing performance of the ZnO NW networks, the reports mostly address the sensing efforts towards the different analytes [184, 185, 244-247]. In spite of the sensitivity, selectivity of the sensors remains the challenge, thus strategic introduction dopants of interest that have been associated with the enhanced selectivity towards specific analytes can be beneficial.

The synthesis of ZnO nanowires by a combination of electrochemically induced chemical precipitation route with template assisted synthesis has been investigated in this work. The growth characteristics of undoped ZnO NWs and the parameters dominating over the NW geometry and material crystallinity were analyzed. It was established that the diameters of the NWs can be adjusted by the nominal pore diameter of the template, and that the crystallinity can be tailored by the deposition temperature. The following step would be the optimization of material properties to enhance sensitivity, institute selectivity, and ameliorate sensor reproducibility.

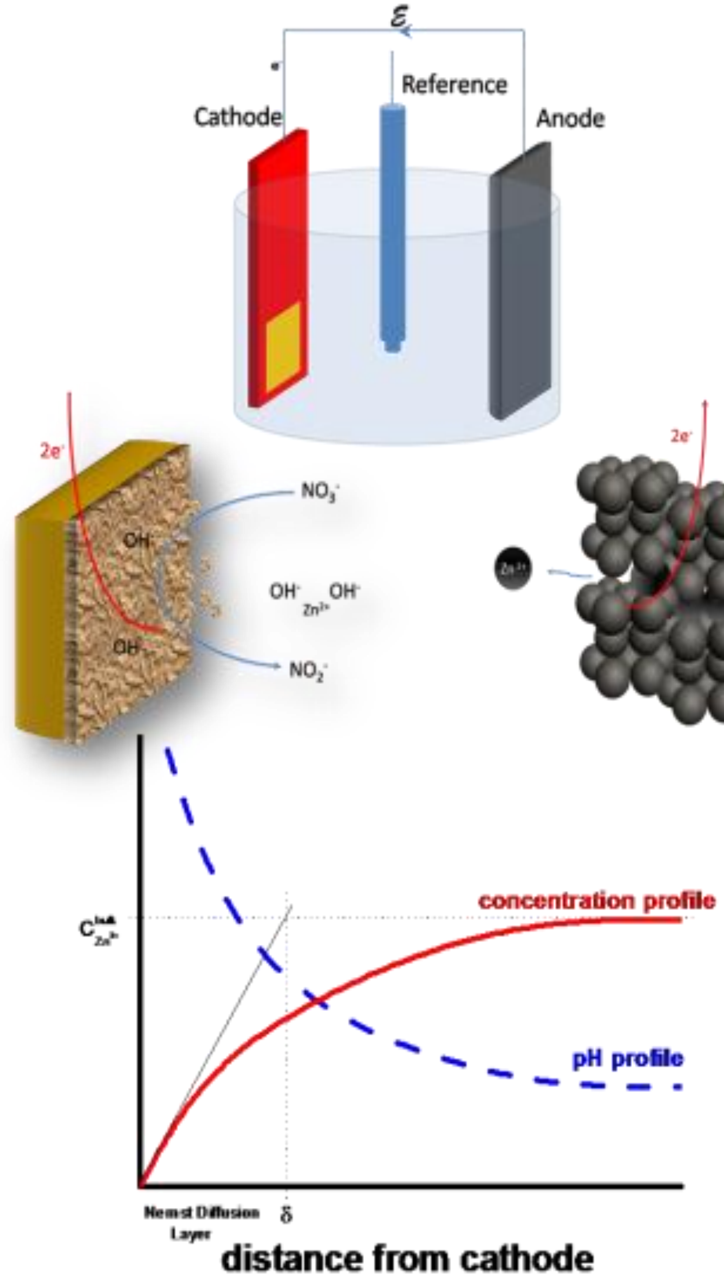

Figure A2.1. Schematic of electrochemical cell, representation of the process at the surface of the electrodes, and the corresponding concentration profiles.

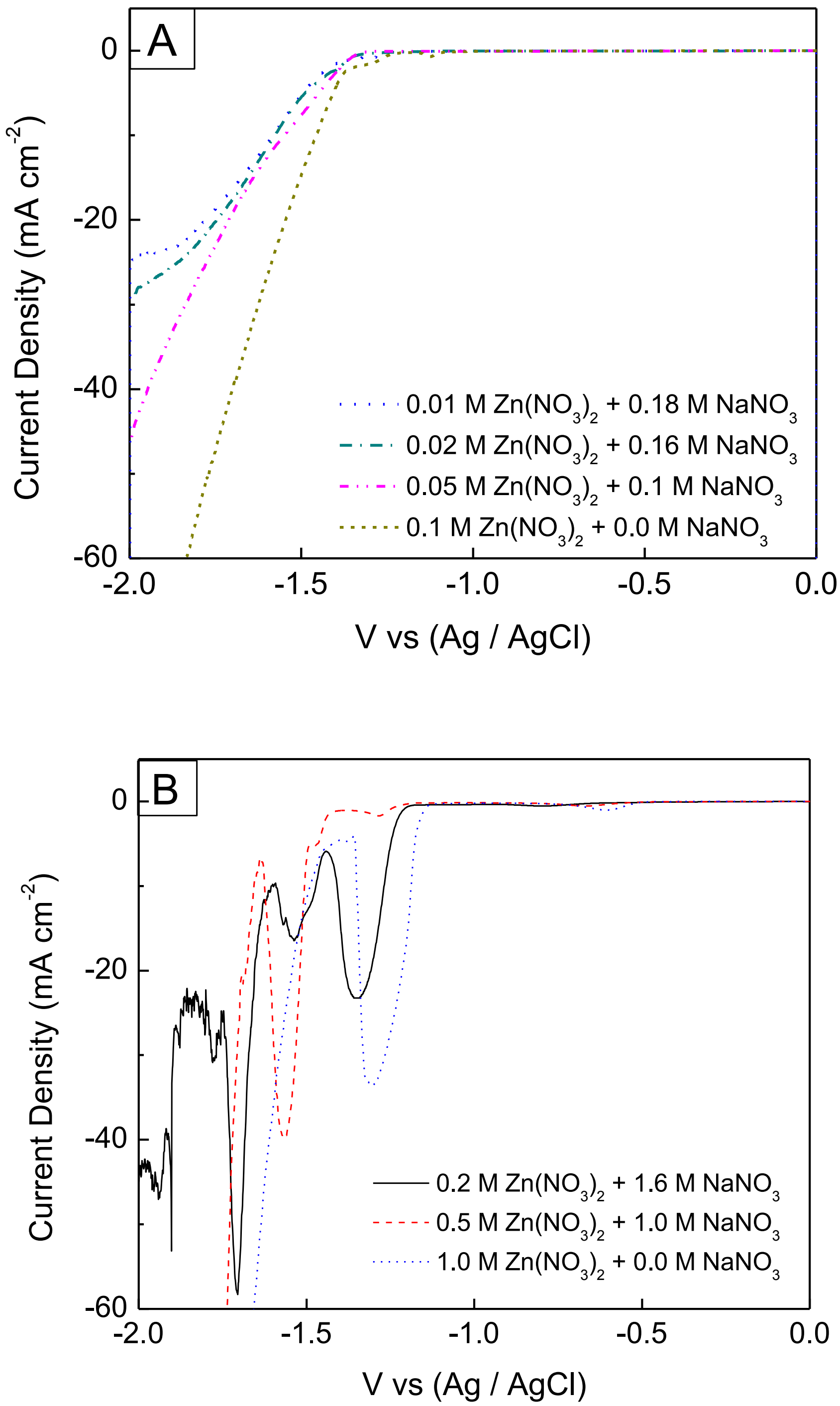

Figure A2.2. Linear sweep voltagrams of A) x M $Zn(NO_3)_2$ + (.2-2x) $NaNO_3$ and B) x M $Zn(NO_3)_2$ + (2-2x) $NaNO_3$ at pH of 5.5.

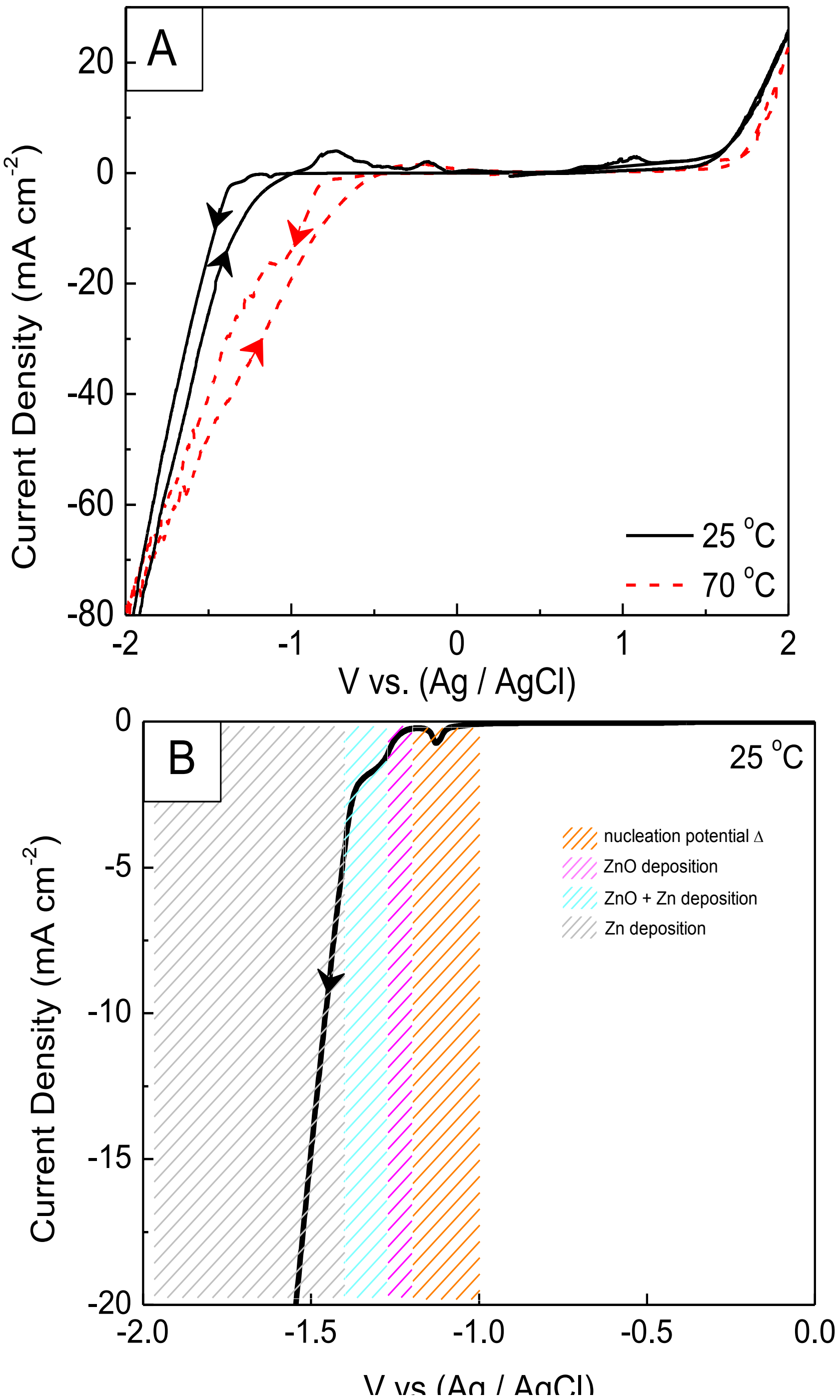

Figure A2.3. Cyclic voltametry of (A) 0.1 M $Zn(NO_3)_2$ at 25°C and 70°C at pH 5.5, and (B) linear sweep voltametry of same electrolyte at 25°C.

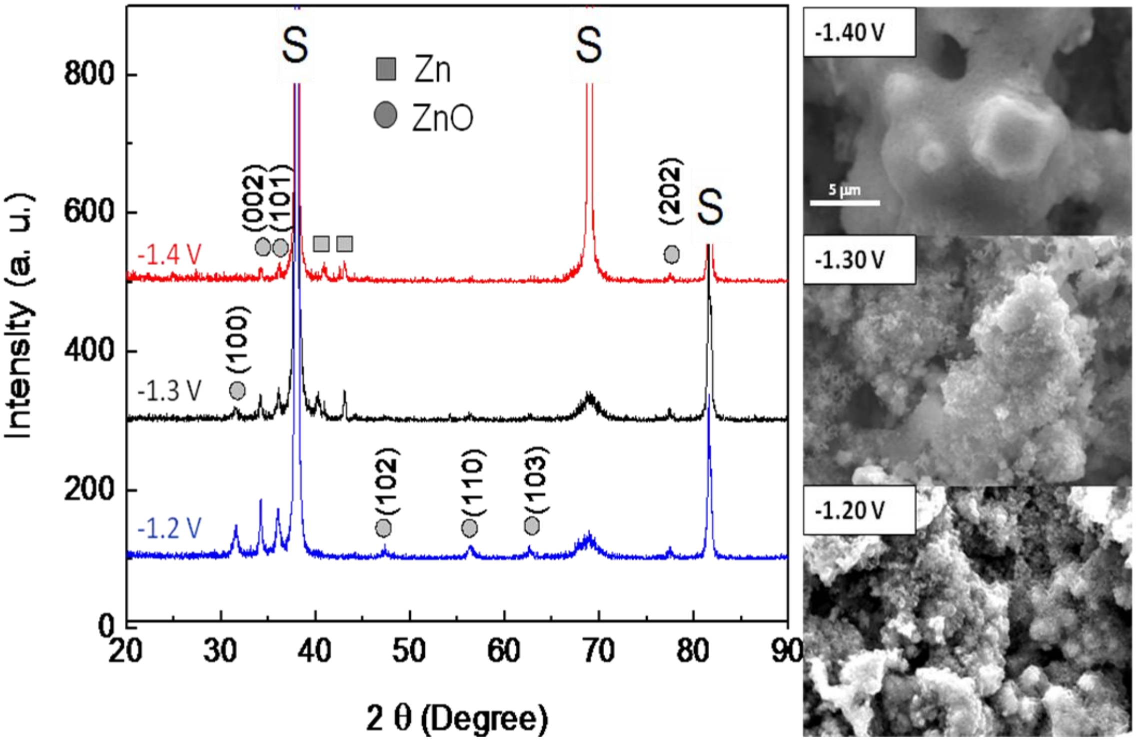

Figure A2.4. XRD and SEM films deposited at -1.2, -1.3, -1.4 V vs. Ag/AgCl from 0.1 M $Zn(NO_3)_2$ electrolyte at 25°C on Au substrates.

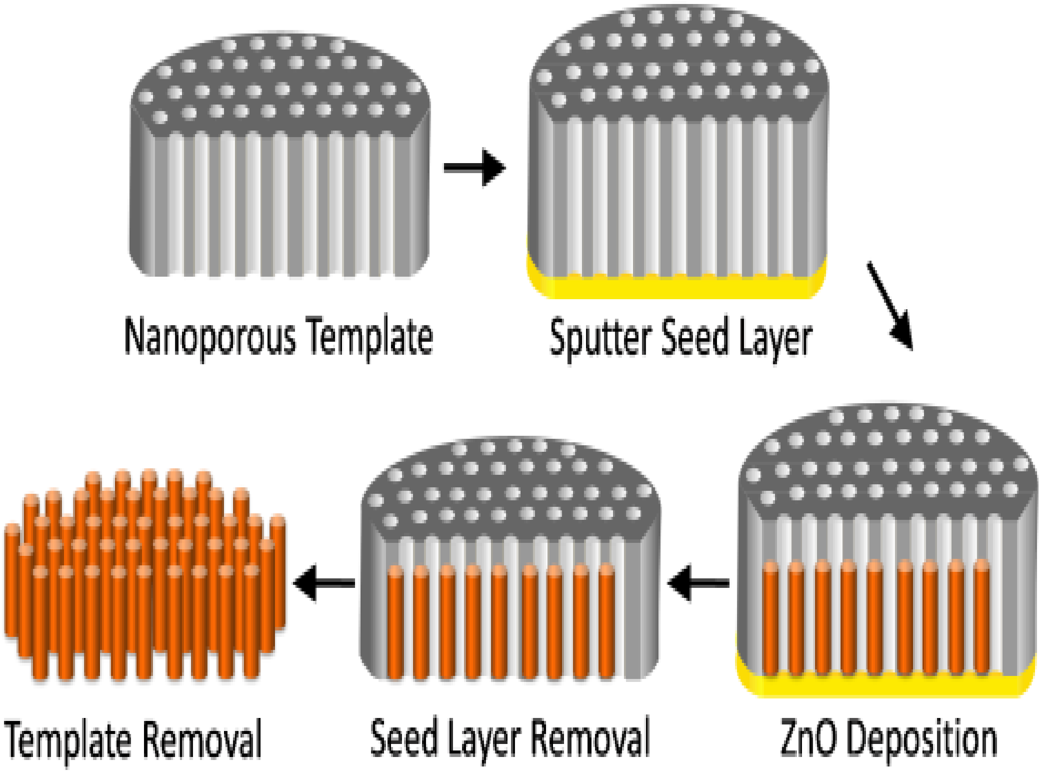

Figure A2.5. Illustration of template directed synthesis of nanowires.

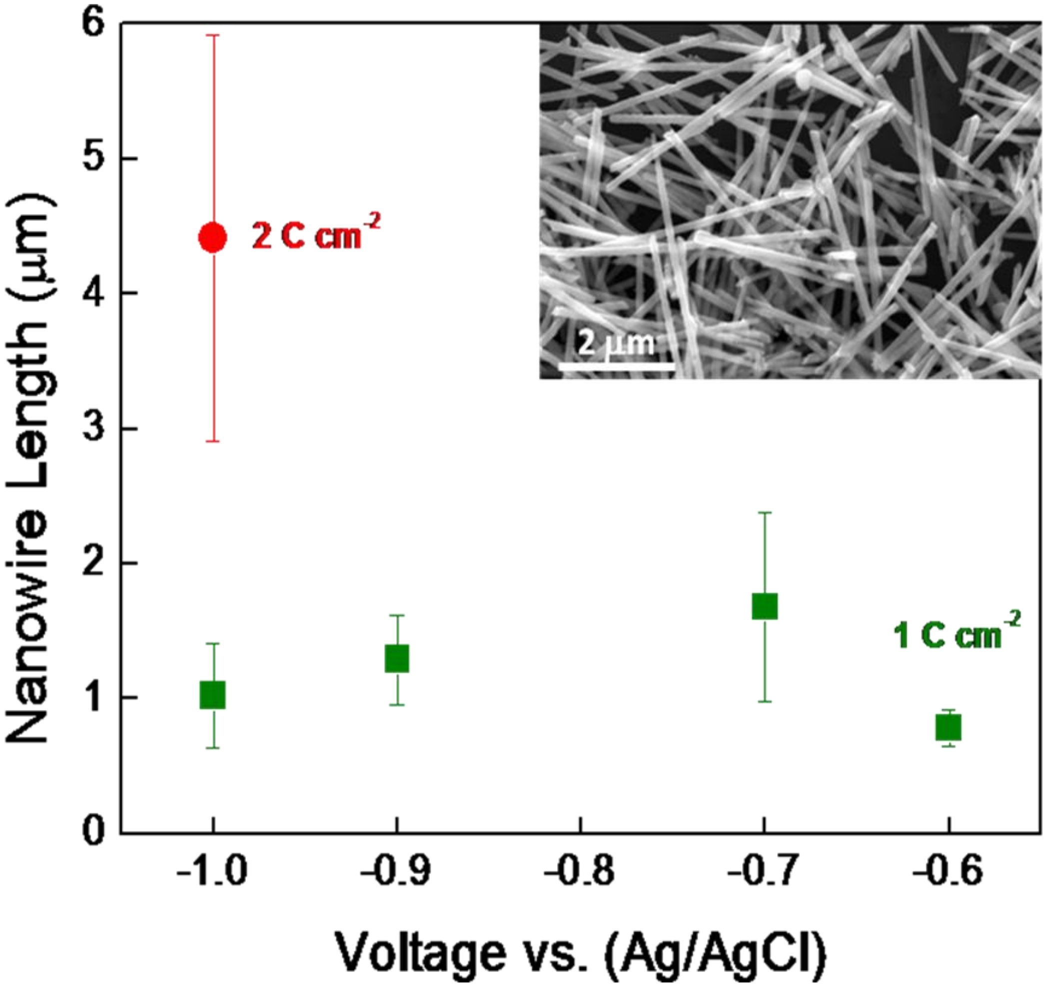

Figure A2.6. Effect of applied charge on nanowire length at 25°C; inset shows an SEM image of resulting ZnO nanowires. All experiments were performed using 0.1 M $Zn(NO_3)_2$ at 25°C and pH 5.5.

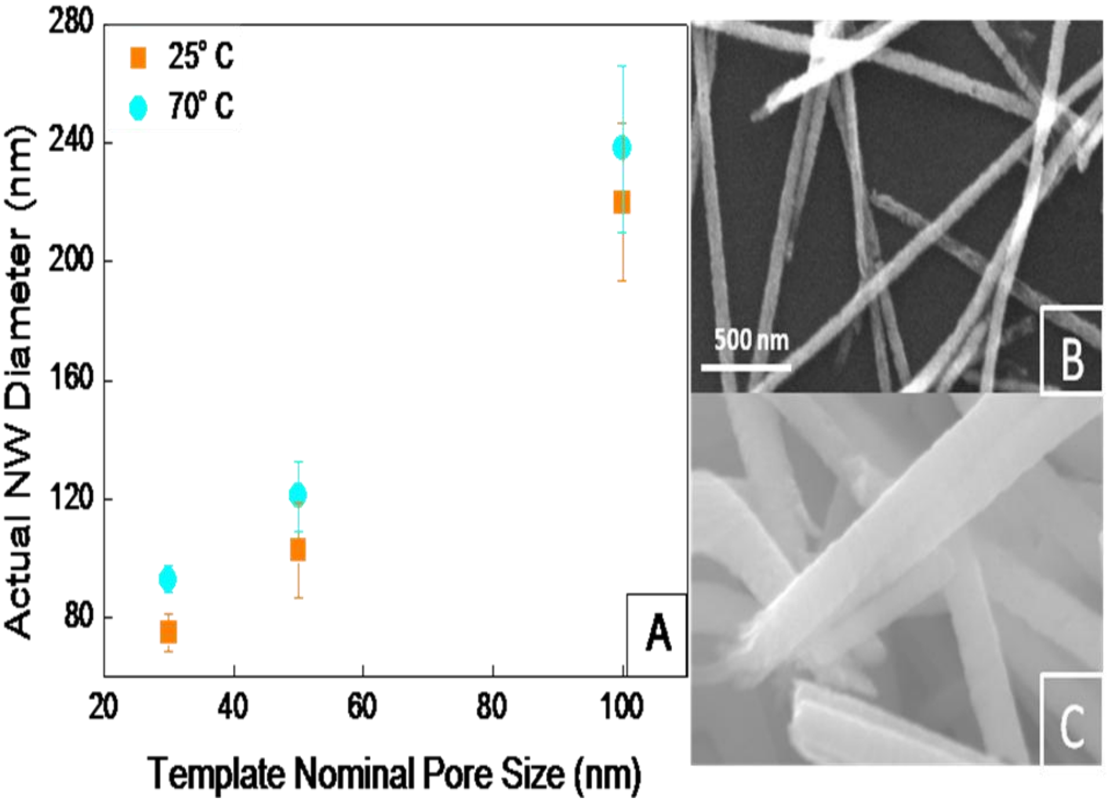

Figure A2.7. (A) Effect of template nominal pore diameter on actual diameter at different temperatures. SEM images of ZnO nanowires deposited at (B) 25 °C using a 30 nm pore diameter polycarbonate template and (C) at 70C using a 100 nm pore diameter polycarbonate template. All experiments were performed using 0.1 M $Zn(NO_3)_2$ at pH 5.5

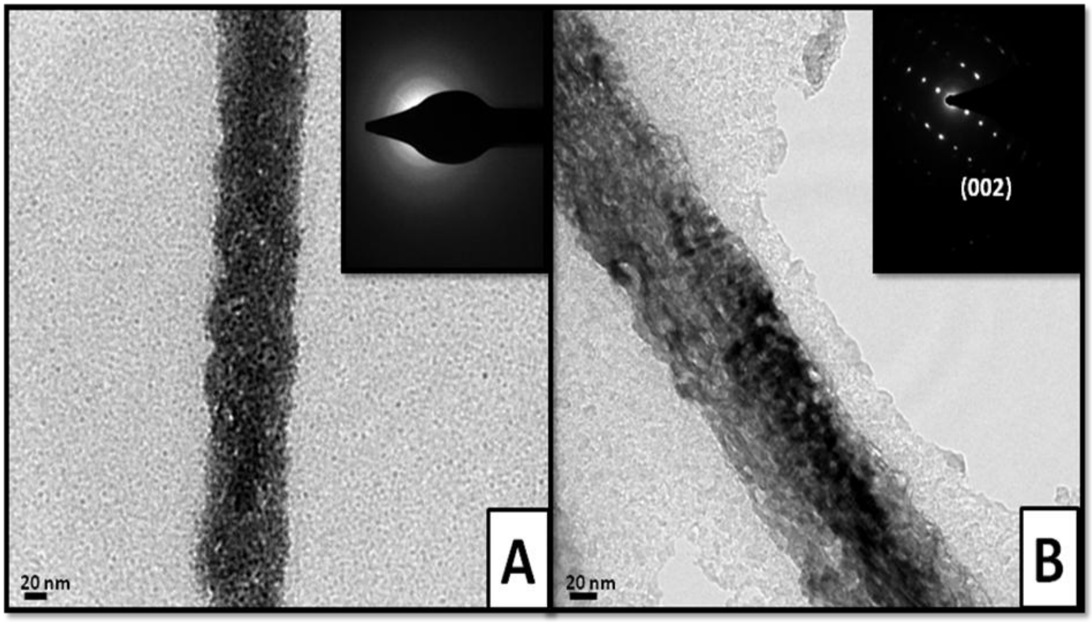

Figure A2.8. TEM and SAED images of ZnO nanowires deposited at (A) 25 °C and 70 °C using 0.1 M $Zn(NO_3)_2$ at 25°C and pH 5.5.

Appendix 3:

Single Polypyrrole Nanowire Ammonia Gas Sensor

This is the pre-peer reviewed version of the following article: *"Single Polypyrrole Nanowire Ammonia Gas Sensor" Electroanalysis*, Volume 19, Issue 19-20, pages 2125-2130, October 2007.

Abstract

We report the synthesis, electrical characterization and ammonia gas sensing with single nanowire of conducting polypyrrole. Three hundred nanometer in diameter and 50 to 60 μm long polypyrrole nanowires were synthesized by chemical polymerization inside SiO_2 coated alumina membranes. Temperature dependent electrical resistance studies established that the chemically synthesized nanowires were more ordered compared to electrochemically synthesized nanowires. We further demonstrated that gas sensors based on single polypyrrole nanowire exhibited good sensitivity towards ammonia, and provided a reliable detection at concentration as low as approximately 40 ppm.

A3.1 Introduction

Over the last few decades, conducting polymers have come a long way from being a new class of materials with interesting electron-transport behavior to a material with immense potential in technological applications. Their ease of processing together with their chemically tunable properties makes them especially useful in electronic, optoelectronic and electromechanical devices. One such area where the conducting polymers have shown great promise is in sensory applications [249-252]. Delocalized electronic states combined with the restriction on the extent of delocalization leads to the formation of a large energy gap making most conductive polymers behave like p-type semiconductors. The fact that these polymers are redox-active, allows one to alter its conductivity by altering the electron count on the backbone by means of doping/dedoping, interactions of ions, functional groups, lone pairs, or charge transfer between polar molecules. A great deal of sensing applications is designed by exploiting the very nature of conducting polymers. The interaction of volatile components, gases, and liquids with conductive polymer films have shown to produce changes in color, mass, work function or electrical conductivity of the polymer, analyzable by photoluminescence, photocurrent, surface acoustic wave, quartz microbalance, conductometric, voltammetric, potentiometric measurements [253-259]. Past research work has focused on using conducting polymer, polypyrrole in particular, thin film based conductometric sensors for detection of volatile organic components (VOC), where it was shown that the polypyrrole thin film sensors were sensitive with good response to VOC showing larger responses to polar than nonpolar compounds [260].

Reliable sensing of ammonia (NH_3) is required in several situations like detecting leaks in air for environmental analysis [261], explosives and fertilizer industries [262], compressor of air-conditioners [263], breath analysis for medical diagnoses [264], and animal housing [265]. Further, its high toxicity also warrants a rapid detection at very low concentrations. However, one of the serious bottlenecks in using conducting polymers for sensing lies with the poor diffusion of the analyte molecules to the bulk of the polymer, thereby reducing the entire response to a surface effect. To alleviate this problem and increase the sensitivity of the device, several approaches have been taken to increase the effective surface area of the polymer. These involve using monolayer thin films, [266] coating polymers on porous substrates, [267] and synthesis of nanostructured conducting polymers [268]. However, to further improve the sensitivity, there is an obvious need to develop sensors based on single polymer nanowires. While several groups have demonstrated the enhanced sensitivity of conducting polymer nanowires [269], there have been very few reports on developing single nanowire sensors [270]. In this work we report an ammonia sensor based on single nanowire of highly conducting polypyrrole. Being one of the most stable conducting polymers under ambient conditions, we selected polypyrrole for our studies.

A3.2 Experimental

A3.2.1 Materials

Alumina membranes of 200 nm nominal pore size and 60 μm thickness were purchased from Whatman International Ltd (Maidstone, England). Pyrrole was obtained from

Sigma-Aldrich (St. Louis, MO, USA) and tetraethylorthosilicate was purchased from Gelest Inc. (Mossisville, PA, USA). Hydrofluoric acid, ferric chloride, hydrochloric acid, ethanol and sodium acetate were purchased from Fisher Scientific (Fair Lawn, New Jersey, USA). All reagents were analytical grade and solutions were prepared in double distilled deionized water.

A3.2.2 Apparatus and Procedure

A3.2.2.1 Polypyrrole Nanowire Fabrication

Alumina membranes, used as template for nanowires growth, were heated overnight at 150 °C (the polymer ring on the circumference of the membranes were removed prior to heating) in an oven (Model 281A, Fisher Scientific, Tustin, CA) to avoid swelling of templates and thus maintaining pore diameter throughout the process. 5 mL of tetraethylorthosilicate (TEOS), 50 mL of ethyl alcohol (EtOH), and 1mL of 1 M hydrochloric acid (HCl) were mixed for 5 min and left to sit for 1 hr to stabilize. Alumina membranes were individually placed in the TEOS solution for 1 min and then sonicated for an additional min. Following sonication, the templates were pat dried with tissue paper (Kimwipes, Kimberly-Clark, Roswell, GA), washed with EtOH, air dried for 2 hrs and incubated in an oven overnight at 150 °C. The templates were then immersed in a freshly prepared and cooled (on ice for 30 min prior to use) 0.2 M pyrrole solution in 0.2 M sodium acetate followed by addition of an equal volume of cold 0.2 M ferric chloride solution in deionized water. The resulting mixture was placed on ice for 1 hr followed by 24 hrs of incubation at 4 °C. Subsequently, the content was sonicated to release membranes from the container walls followed by rinsing with deionized water aided with sonication for five times. Polypyrrole embedded alumina membranes were then placed in a 10% (v/v) hydrofluoric acid (HF) over night to dissolve the template to release the nanowires. HF was removed by washing with nanopure water until pH showed non acidic conditions as indication removal of residual HF and then nanowires were rinsed with EtOH. The EtOH was then evaporated under vacuum to obtain dried nanowires.

A.3.2.2.2 Characterization of Nanowires

Morphology and Crystal Structure

X-ray diffraction patterns were obtained by using the dried post-ethanol rinsed polypyrrole nanowires on an evaporated gold substrate with Cu K_α radiation and a scanning range of 10 to 80° with 0.1° increments (Bruker AXS Baltic Scientific Instruments D8 Advance). Nanowires were then imaged by scanning electron microscopy (SEM, Leo SUPRA 55, Model 1550).

Electrical Properties

A dilute solution of dispersed polypyrrole nanowires was made by suspending ~0.1 mg of dry nanowires in 1 mL of ethanol and sonicating the mixture until contents were fully dispersed. A 5 μL drop of well suspended nanowires was dispersed across microfabricated gold electrodes on SiO_2/Si substrate and a flow of nitrogen gas was passed over the electrode (parallel to the chip) until the ethanol evaporated. The nitrogen gas provided a preferred orientation for nanowire alignment. Optical microscopy (Hirox HI-Scope Advanced KH-3000, River Edge, NJ, USA) was used for visual verification of single nanowire bridging two gold electrodes. A two point probes method was used to measure I-V characteristics for the nanowires bridging the two electrodes via sweeping the potential between -1 V to +1 V D.C.. Temperature dependent electrical resistance of nanowires was measured between 8 and 300 K with a physical property measurement system (PPMS) from Quantum Design (San Diego, CA, USA) in combination with the semiconductor parameter analyzer (Hewlett Packard Model 4155A, Austin, TX, USA) to obtain the I-V characteristics at each set temperature.

A3.2.2.3 Gas Sensing

For gas sensing studies, electrodes with an aligned PPy nanowire were connected to a chip holder by wire bonding (West Bond Inc. Model 7443A, Anaheim, CA, USA). Subsequently, single nanowire PPy sensor was connected in series with a load resistance of comparable value to the resistance of the nanowire sensor in order to optimize resolution [270]. The sensor arrangement was subjected to 0.5V D.C. potential and the current was continuously monitored with sample rate of one sample per second. Electrical resistance of the sensor was determined by continuous monitoring the voltage over the load resistor and applying Ohm’s Law. A 1.3 cm^3 glass chamber with inlet and outlet ports was positioned over the microfabricated chip with a sandwiched O-ring and sealed by using a clamp. Gas at 150 std. cm^3 min^{-1} flowed through the glass chamber. Argon (purity: 99.998%) and ammonia (purity: 99.99%) were used as the carrier and analyte gases, respectively (Airgas Inc., Riverside, CA, USA). The carrier gas was diluted with the analyte gas to obtain different ammonia concentrations. Analyte and carrier gas flow rates were regulated by mass flow controllers (Alicat Scientific Incorporated, Tucson, AZ). A custom LabView computer program was developed to control a Field Point circuit system from National Instruments which combined were used to monitor the voltage of the nanowire circuit (Austin, TX, USA) [147].

A3.3 Results and Discussion

A3.3.1 Synthesis and Characterization

Figure 4.3.1 shows the schematic of the strategy employed for synthesizing polypyrrole nanowires. The technique employed in this work is slightly modified from that reported previously using porous alumina templates [271]. In the present work, instead of growing the nanowires inside as-is alumina membrane pores a thin layer of SiO_2 was first deposited on the inner walls of the alumina pores. This was followed by the chemical polymerization of pyrrole using $FeCl_3$ as the oxidizing agent. The average diameter of the polypyrrole nanowires was ~300 nm (Fig. A.3.2B), which was larger than the manufacturer reported average pore diameter (200 nm) for the membrane. As evident in SEM images (Fig. A.3.2), the surface of nanowires made using SiO_2 modified pores were smoother compared to unmodified pores. The smoother surface morphology in the SiO_2 coated pores can be attributed to the anionic sites on silica that act as molecular anchor to nascent cationic providing preferential nucleation for polypyrrole along the pore walls and producing a continuous coating. The rough and irregular blob morphology obtained from unmodified pore was in accordance with the literature report and is hypothesized to the absence of molecular anchors on the alumina pores causing nucleation to happen at random positions within the pores as opposed to along the walls in case of silica coated pores [271].

The XRD pattern reveals that the resulting polypyrrole nanowires were amorphous (Fig. A.3.3) showing a broad band in the region of 15° < 2θ < 30 ° indicating that short-range chain arrangement dominates as has been similarly observed for electrochemically synthesized polypyrrole nanowires [272]**.**

A3.3.2 Electrical Characteristics

To be used as a conductometric gas sensor, the nanowire should be semiconducting and have good quality, i.e. low degree of disorder. Figure A.3.4a shows the I-V characteristic of a single polypyrrole nanowire as a function of temperature. The inset shows the corresponding SEM micrograph of the nanowire bridging the gold electrodes. The current-voltage plot is fairly linear about the 0 V bias, revealing an ohmic contact between nanowire and electrodes. A decreasing current response upon lowering the temperature is indicative of the inherent semiconducting nature of these nanowires. The room temperature conductivity estimated from the ohmic part of the I-V curve (between -0.1 to 0.1 V) was determined to be 5.1 S cm^{-1}. This is in good agreement with previously reported value for chemically synthesized polypyrrole [273].

To further corroborate the fact that the polypyrrole nanowires are of superior quality, effect of temperature on the single nanowire resistance was analyzed between 8 and 300 K. As shown in Fig. A.3.4B, over this temperature range the resistance of the nanowires increased with decreasing temperature. This is a typical behavior for doped semiconducting materials and is in accordance with the observations for electrochemically and chemically synthesized polypyrrole nanowires within pores of alumina and polycarbonate membranes [271, 274]. The degree of disorder in a sample is another parameter for the evaluation of the nanowires quality. It is well known that the rate of increase in resistivity at lower temperatures is higher in the case of disordered samples [275]. Therefore, by monitoring the ratio of low temperature to room temperature resistivity, it is possible to obtain an indication of the degree of disorder in the sample. The ratio of the conductivity between 75 and 300 K for single nanowire synthesized in this work was found to be ~7. In comparison, the electrochemically synthesized chloride doped single polypyrrole nanowire exhibited a conductivity ratio of ~15, suggesting that the nanowires synthesized in the present work are much ordered. The difference in the degree of disorder is also reflected in the corresponding activation energies calculated by fitting the high temperature (100-300 K) resistivity data of the two samples to Arrhenius behavior, as per the following equation,

$$\rho = \rho_0 \exp[E_a / kT]$$

The activation energies (E_a) for single polypyrrole nanowire synthesized by chemical (present study), and electrochemical [275] polymerization were 19.4 and 25.9 eV, respectively.

A3.3.3 Gas Sensing

Conductometric sensing of ammonia was carried out with a single polypyrrole nanowire and the results are presented in Fig. A.3.5. Argon was chosen as the carrier gas in order to achieve a faster stabilization of the background signal. Ammonia concentration was varied from 40-300 ppm by diluting ammonia gas with argon. After each exposure, the sensor resistance was recovered by purging with argon. The time required for a stable base line to be obtained upon the first imposition of the bias potential was 30 minutes (data not shown). The recovery time, defined as time required for the resistance to return to the original value upon switching to 100% carrier gas, was ~15 min. It is important to note that although the recovery was near-complete for lower concentrations, it was not the case at higher concentrations, thereby suggesting some irreversible binding between polypyrrole and NH_3. This observation is consistent with previous studies on polypyrrole-based ammonia sensors [269], and the mechanism has been explained in terms of an irreversible electron transfer from ammonia to the doped polymer [276]. The response time, defined as the time to reach 90% of the total resistance change, of the sensor was found to be 15 min and 10 min, for the lower and higher ammonia concentrations, respectively. The slower response and recovery times in our samples could be due to the fact that the nanowire has very smooth surface morphology. Smoother surface morphology translates to less surface area for ammonia to diffuse into.

The sensitivity, determined from the slope of the linear range, was determined to be 0.06% per ppm of ammonia in the concentration range of 40-300 ppm (correlation coefficient, $r^2 = 0.9827$). The lower detection limit of the single polypyrrole nanowires sensor was 40 ppm, which is close to the recommended threshold limit value for human exposure (25 ppm) [277]. The sensitivity and lower detection limit of the sensor can be improved by operating the sensor in a field effect transistor mode with a back gate and changing the dopant to one that can promote enhanced changes in current due to the dual interaction of the dopant with the hydrocarbon chain and charged analyte.

The sensor exhibited an excellent selectivity towards ammonia with no detectable response to nitric dioxide (NO_2) even at concentration as high as 100 ppm. The absence of response to NO_2 is attributed to the highly doped state of the polypyrrole and therefore the inability for an electron acceptor like NO_2 to extract further electrons from the backbone. Polypyrrole-based gas sensors are reported to be sensitive to humidity with as much as 75% decrease in response resulting from a 5% increase in relative humidity [278]. The problem of humidity can be resolved by passing the sample through a desiccant before analyzing or replacing the chloride with a more hydrophobic dopant such as *p*-toluene sulfonate.

A3.4 Conclusion

To conclude, high quality polypyrrole nanowires were prepared by template directed chemical synthesis. Temperature dependent electrical transport measurements showed the sample to be semiconducting with low degree of disorder. Single nanowires-based sensors showed good limit of detection and sensitivity and excellent selectivity for gaseous ammonia.

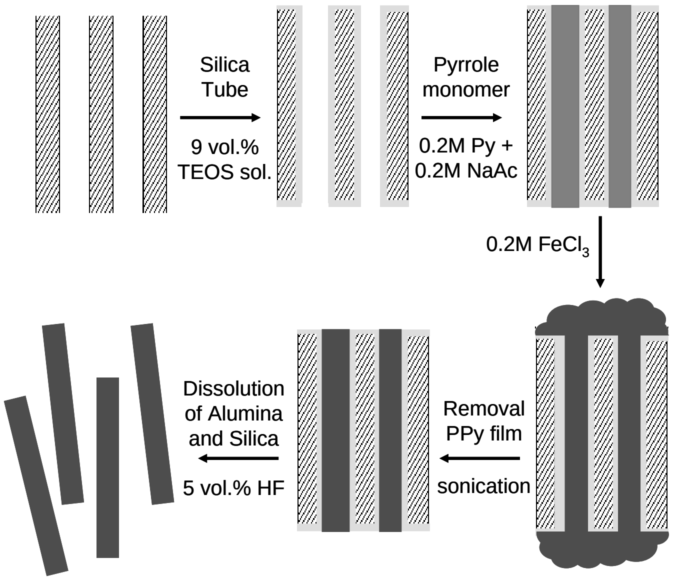

Figure A3.1. Schematic of polypyrrole nanowire synthesis.

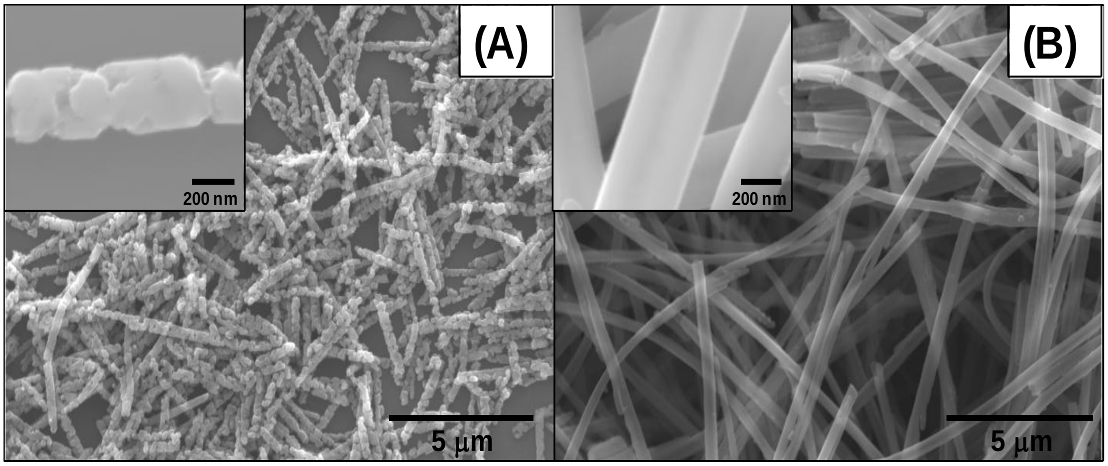

Figure A3.2. Scanning electron micrographs of polypyrrole nanowires synthesized (A) inside as obtained, unmodified alumina templates and (B) inside alumina templates modified with an inner layer of silica.

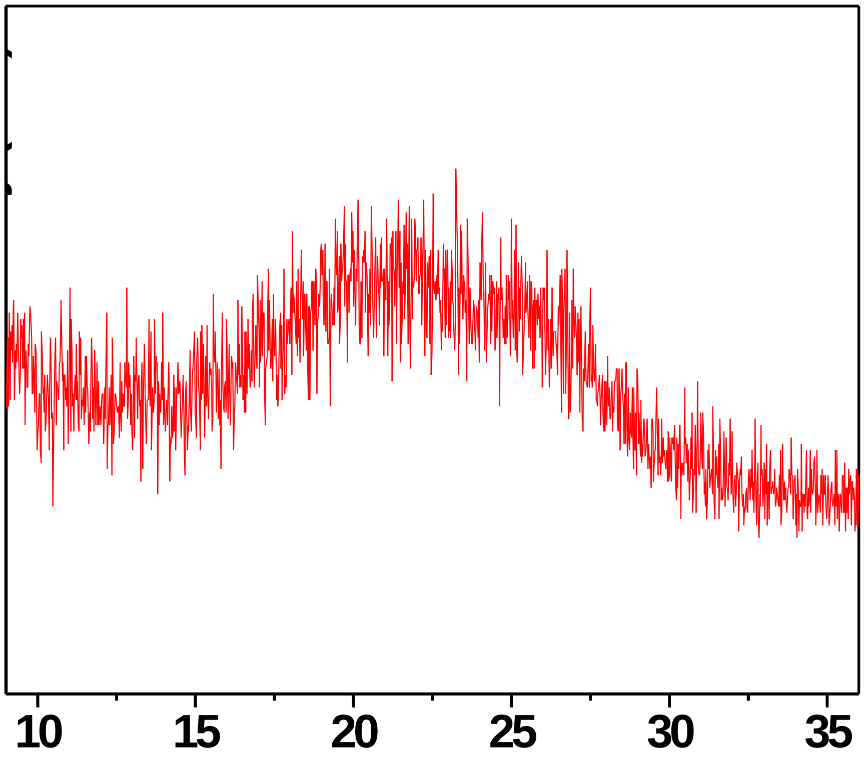

Figure A3.3. X-ray diffraction pattern of polypyrrole nanowires.

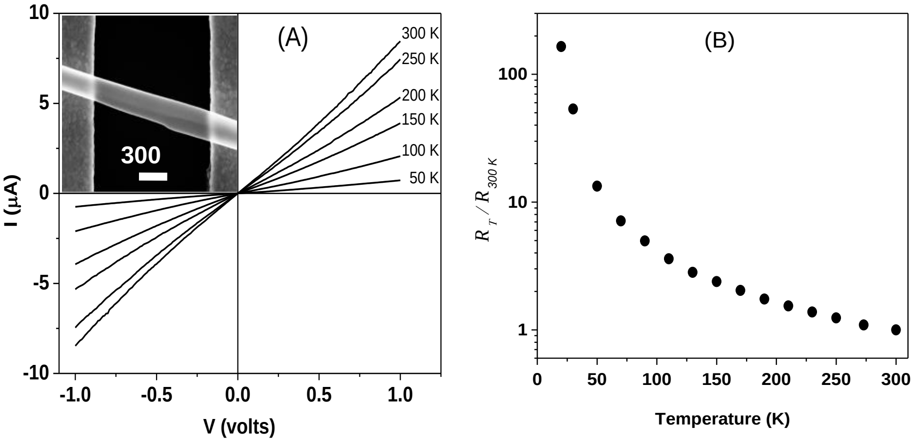

Figure A3.4. (A) Temperature dependent I-V characteristics of a single polypyrrole nanowire. The inset shows the SEM image of a single nanowire bridging across the gold microelectrodes. (B) Low temperature to room temperature resistance ratio *R(T)/R(300K)*, as a function of temperature.

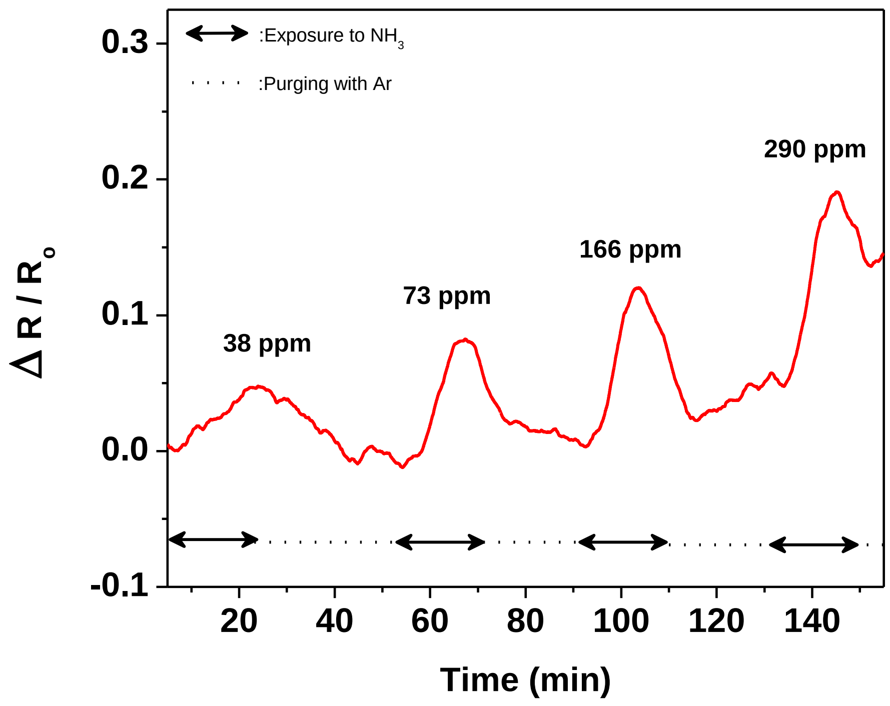

Figure A3.5. Conductometric response of a single polypyrrole nanowire to ammonia at an applied D.C. bias of 0.5 V. Arrows indicate a 15 minute exposure time.

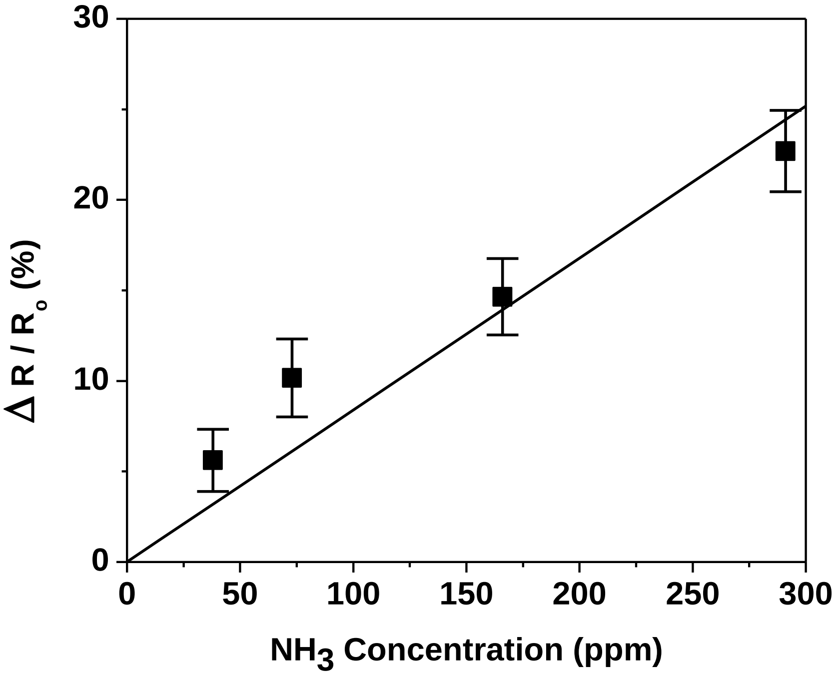

Figure A3.6. Calibration for ammonia of a single polypyrrole nanowire at an applied D. C. bias of 0.5V. The error bars show the standard deviation from the average values (n=5).

Apppendix 4:

Molecularly Imprinted Polymers

Abstract

Polymer nanowires synthesized by chemical polymerization of pyrrole into alumina templates were investigated for applications in biosensing. The nanowires were imprinted with various bio-molecules via a novel approach. Preliminary biosensing is demonstrated in steady state and transient modes. In addition, several contact routes were addressed to establish good electrical conduction while simultaneously anchoring the nanowires.

A4.1 Experimental

A4.1.1 Template Preparation

Commercially available Whatman and in-house fabricated alumina membranes with 200 nm and 80nm pore diameters, respectively, be were used as templates for nanowire growth. Alumina membranes were heated in a Fisher Scientific Isotemp Vacuum Oven (Model 281A) overnight at a temperature of 150 °C (if membranes have a polymer ring on the circumference, then the ring should be removed prior to heating).

A4.1.2 Silica Tube Deposition on Alumina Membranes

A TEOS solution was made by mixing 50mL of ethyl alcohol (EtOH), 5mL of tetraethylorthosilicate (TEOS) and 1mL of 1 M hydrocloric acid (HCl). The contents were stirred for 5 minutes and solution was left to sit for 1 hour to allow it to stabilize. Alumina membranes were individually placed in the TEOS solution for 1 minute and then sonicated for an additional minute. Following sonication, the templates were pat dried with Kimwipes, washed with EtOH, air dried for 2 hours and then placed in an oven overnight at 150 °C.

A4.1.3 Addition of Aldehyde Groups

The addition of aldehyde groups was performed via surface modification of the silica tubes by immersion of alumina membranes (containing SiO_2 tubes) into an alcohol based aldehyde solution. The solution consisted of 5% of 0.1M acetate buffer, 5% triethoxysilbutyraldehyde, 5% TEOS and remaining ethyl alcohol, the solution was then deoxygenated prior to use by bubbling of nitrogen for 10 minutes. Alumina membranes with SiO_2 tubes were submerged in to the solution for 10 minutes under vacuum followed by 20 minutes in nitrogen environment. The resulting surface modified aldehyde membranes were rinsed with ethyl alcohol and placed in nitrogen environment over night.

A4.1.4 Binding of Protein (BSA) on the Aldehyde Modified Silica Tubes

The aldehyde-modified membranes were placed in a solution of 4 mg/mL of BSA in PBS buffer. The membranes were incubated in the BSA solution under vacuum for 1 hour, followed by 12 hours at 4 °C, and an additional 24 hours at room temperature. The resulting BSA modified membranes were then rinsed with PBS buffer several times and placed under nitrogen environment for 24 hours.

A4.1.5 Fabrication of Polypyrole Nanowires

A 0.2 M pyrrole solution containing 0.2 M sodium acetate was prepared from a freshly distilled pyrrole solution, in addition, equal volume of 0.2 M iron chloride solution was made, both solutions were placed in ice for 30 minutes prior to use. The pyrrole solution was placed in a 50 mL centrifuge tube and the BSA modified membranes were then immersed into the solution. Steps 3 and 4 are omitted for Non-Imprinted nanowires. Finally, the iron chloride oxidant solution was then added, the solutions were mixed and the resulting mixture was placed in ice for 1 hour followed by 24 hours of incubation at 4 °C.

A4.1.6 Removal of Alumina Membrane and Silica Tubes

After 24 hour incubation period, the 50 mL centrifuge tube containing the alumina membranes with embedded polypyrole nanowires was sonicated to remove membranes from the container walls. The membranes were filtered out and rinsed five times with de-ionized water aided with sonication. Following the washing procedure, polypyrole embedded membranes were placed in a 50 mL centrifuge tube containing 10% vol. hydrofluoric acid (HF) over night. Special precaution should be taken when working with HF since it is a highly toxic and corrosive acid and it is notoriously known to dissolve glass by reacting with SiO_2.

A4.1.7 Removal of Imprinting Protein (BSA)

BSA surface imprinted nanowires were washed three times with 5 mL of 10% vol. Sodium Dodecyl Sulfate (SDS) and 10% vol. Acetic Acid (HAc). Following the SDS & HAc washings, the nanowires were then washed with nano-pure water at least 5 times, and finally rinsed with ethanol. To evaporate ethanol out of the wires, the ethanol containing nanowires were placed under vacuum overnight.

A4.2 Results

Figure A.4.1 shows the schematic representation for the synthesis of MIP PPY NWs. The multiple step process results in a high yield of surface imprinted (MIP) and non-imprinted (NIP) nanowires. The surface of the nanowires can be modified with different biomolecules such as cytochrome-C, horse radish peroxidase, human bovine serum, and BSA. Demonstrated in figure A.4.2 are SEM images depicting the high yield of the nanowires and typical geometries. Despite differences in their synthesis methods, the surface of both the MIP and NIP nanowires are smooth, average lengths are ~ 60 μm and average diameters are 250 nm.

Biosensing was performed by various routes. The first was steady state binding which was performed by traditional Bradford Protein Assay Procedure (Micro assay procedure for <50μm/mL protein), illustrated in figure A.4.3. NWs (MIP and NIP) were suspended and sonicated with PBS buffer + TWEEN 20 (as the control sample) and PBS buffer + TWEEN 20 + desired protein in 1.5 mL microcentrifuge tubes, in triplicates. Incubation was performed for three hours, under continuous rotation, after the allotted incubation time, the microcentrifuge tubes and its contents were centrifuged at 15rpm for 10 minutes. 0.2 mL of the supernatant was removed and an equal volume of Bio-Rad Protein Assay die was added, the contents were mixed in a clean microcentrifuge tube and mixed for 5 minutes. UV-Vis measurements were performed at a fixed wave length of 595 nm, first of standards to establish a calibration curve, followed by the control samples, and samples, all measurements were performed in triplicates to obtain appropriate error bars. Based on the OD reading and the calibration curve, the concentration of the protein left behind in the supernatant was correlated to the amount of protein that interacted with the pockets on the surface of the nanowires. Unfortunately, this method gave inconclusive results suggesting that non-specific binding had a large contribution to the interaction of the proteins to the surface of the wires, in addition to the inability to precisely measure the exact amount of NWs for each trial, and the quality of NWS (bundle vs. single) that were introduced to the protein.

The second route of sensing was performed by electrical probing of NIP and MIP PPY NWs. PPY nanowires were assembled across gold electrodes by drop casting a 10 μL drop of suspended NWs in ethanol. After complete evaporation of the ethanol solution, optical imaging was performed to verify presence of NWs bridging across the electrodes, followed by the measurement of electrical resistance via two probe method. After addition of water, a base line was achieved and subsequently 2 μL of 1.50 μM BSA were added until saturation. At each addition of solution the solution was allotted to interact with the NW, then removed followed by a resistance measurement. The voltage was swept from -1 volt to 1 volt using conventional 2 probe method. I-V characteristics are of a single NW is demonstrated in figure 4 as water and BSA are introduced to the system. The I-V sweep was performed after the liquid solution (water or BSA) was removed. The initial resistance of the dry NW was R = 4.7 kΩ, and decreased to 3.9 kΩ after addition of water. After addition of 1.50 μM of BSA, the resistance increased to R = 5.8 kΩ, a 20.51 change in resistance.

FET measurements were performed on a single 200 nm PPY nanowire that was aligned on Au electrode pads that were used as the source and drain and Ag/AgCl electrode wire was used as the gate. 2μL of 0.01 M NaCl solution with a pH of 5.8 was placed on the electrode (isoelectric pH of BSA is ~ 4.6). The gate voltage was varied from -0.8 to +1.0 volts. The I-V curves at various gate voltages are demonstrated in figure 5 A, and the calculated FET behavior is demonstrated in Figure A.4.5B.

Transient biosensing was performed by the same route as mentioned earlier, where non-imprinted and MIP PPY NWs were aligned and tested for BSA sensing. A bias potential of 100mV was applied while the resistance of the nanowire was continuously monitored. Once a base line was achieved, 2μL of water were added to the NIP or MIP wire and subsequently 2 μL of 1.50 μM BSA were added until the sensor showed saturation, as demonstrated in figure A.4.6. Encouragingly enough, there was a continuous increase in resistance with subsequent addition of BSA aliquots for the MIP single nanowire. The NIP nanowire, on the other hand showed an inconsistent response to BSA aliquots (shown in the insert of figure A.4.6).

In an attempt to further transient biosensing and eliminating NW movement with the addition of protein solutions, various approaches to establish good electrical contact to the NWS were investigated. Among the few include focused ion beam (FIB) to anchor NW at specific locations, shadow masking by use of a TEM grid and evaporation of Cu and Au metals to establish top contact on the nanowires, and maskelss electrodeposition. FIB locally added metal contacts on the surface of the NW, however as evident from figure A.4.7, the NW deformed during the writing process and was later confirmed by optical imaging that there was local heating/melting of the polymer nanowires. The FIB process destroy the nanowire, also confirmed by diminished electrical resistance and thus the method proved detrimental to our process since the purpose was to advantageously use the nano imprints on the surface of the nanowires.

The use of TEM grids as masks for shadow masking was investigated. In this process TEM grids are placed on the surface of randomly drop-casted NWs on glass slides, and metal contacts are evaporated on the surface, thus making top contact to the NW and anchoring it simultaneously. The custom tailored set up is illustrated in figure A.4.8, and the resultant optical images show the gap distance dependence on sample location with respect to the evaporation source. There were two main problems with this method; the first is that the TEM grids could not make physical contact to the NWs, and thus allowing for metal evaporation throughout the whole surface of the NWs. Secondly, the inability to evaporate an adhesion layer prior to the metal evaporation made the top contacts useless as they effortlessly were removed when trying to electrically address NWs bridging the electrodes.

Parallel to the contact efforts, an approach for microfluidics was explored. The idea was to use an ink jet printer to print out patterns that would serve as a mold for microfluidic channels. The designs demonstrated in figure A.4.9, were printed on to plastic transparencies where the ink would offer a different height. The patterns were cut out, placed on petri dishes, the inlet and outlet channels were secured in place by adding small diameter fishing wire, and PDMS was poured over the transparencies. The resulting disposable microfluidic channels could then be cut out and placed over the silicone chips contacting NWs providing a well-defined area for biosensing, shown in picture in figure A.4.10. Again since the NWs were unable to be anchored via the routes that were investigated, the microfluidic configuration was not furthered past the described initial stages.

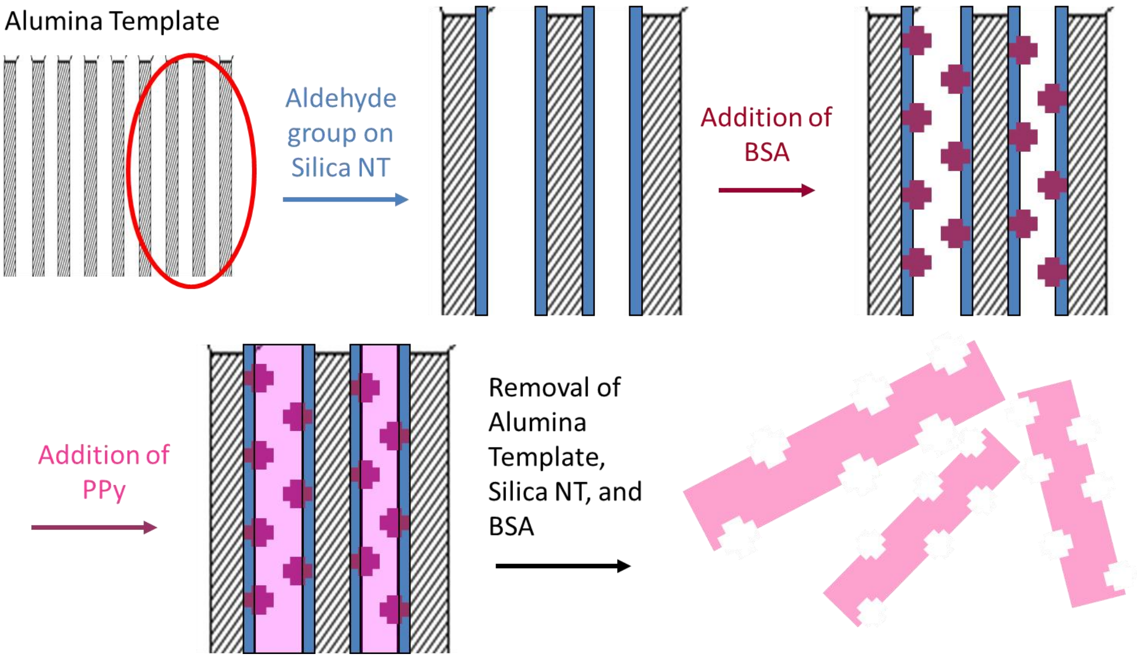

Figure A4.1. Schematic of molecular imprinting process for polypyrrole nanowires within alumina templates.

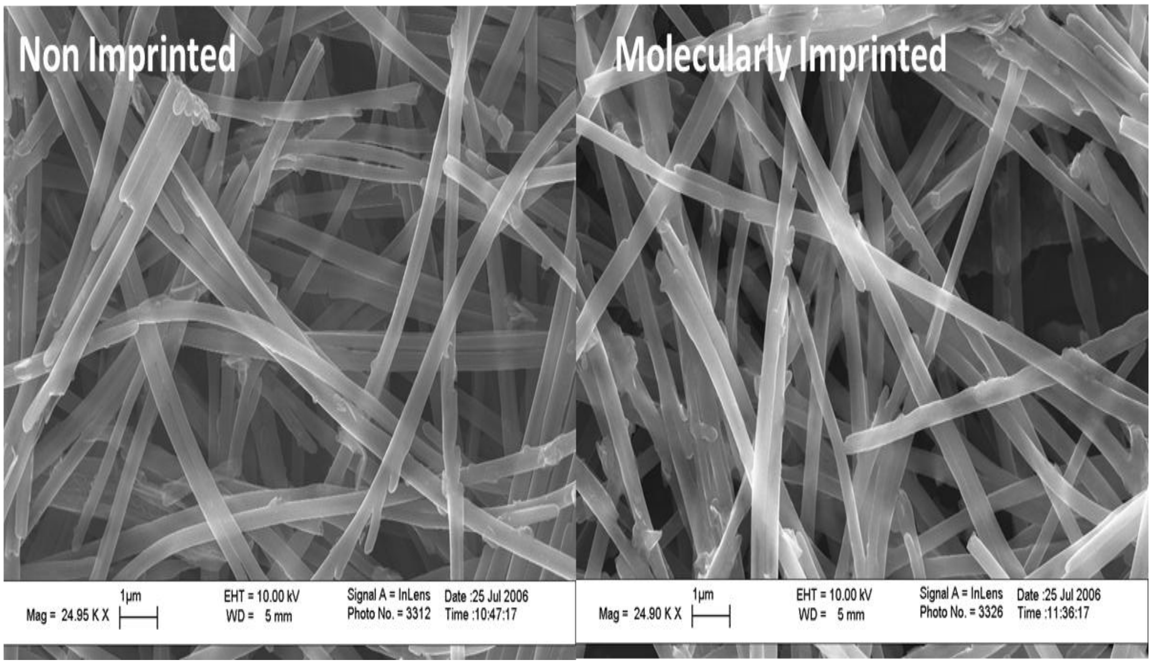

Figure A4.2. Scanning electron micrographs of non-imprinted and imprinted polpyrrole nanowires.

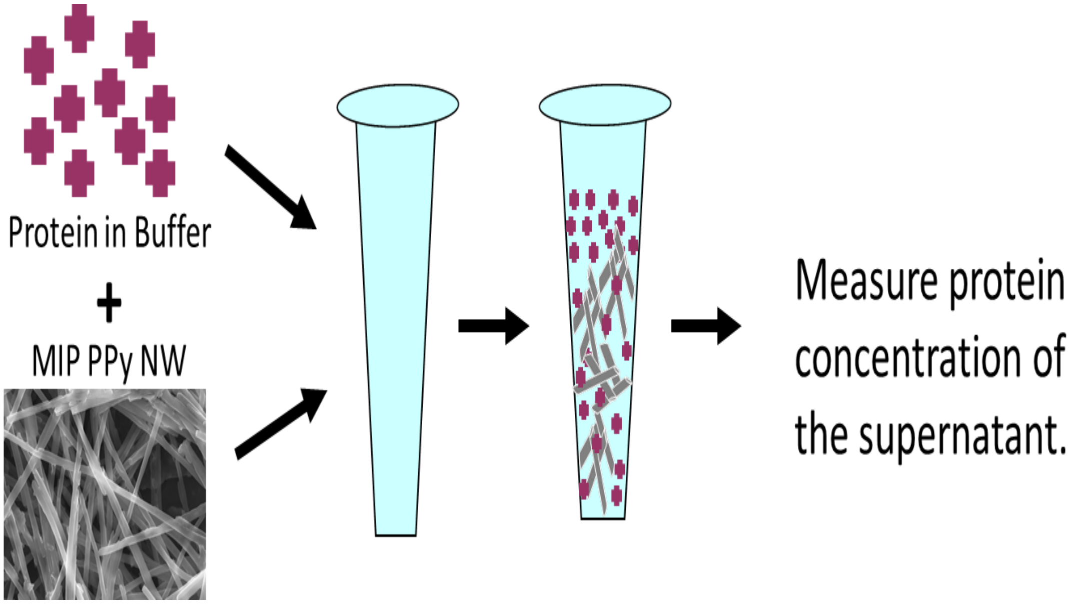

Figure A4.3. Schematic of steady state binding process of imprinted and non-imprinted polypyrrole nanowires.

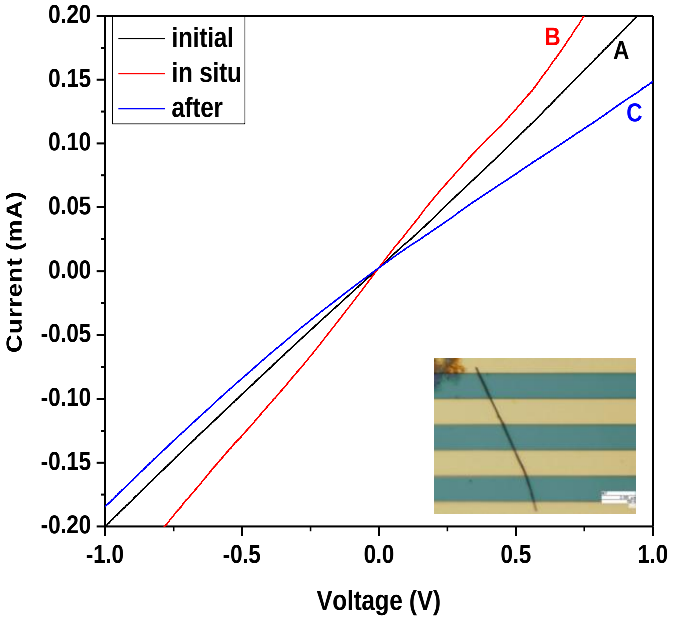

Figure A4.4. I-V characteristics of imprinted nanowires taken (A) before addition of BSA, (B) Addition of 2 uL of 100 ug/mL (BSA dissolved in DI water) and (C) After drying of BSA.

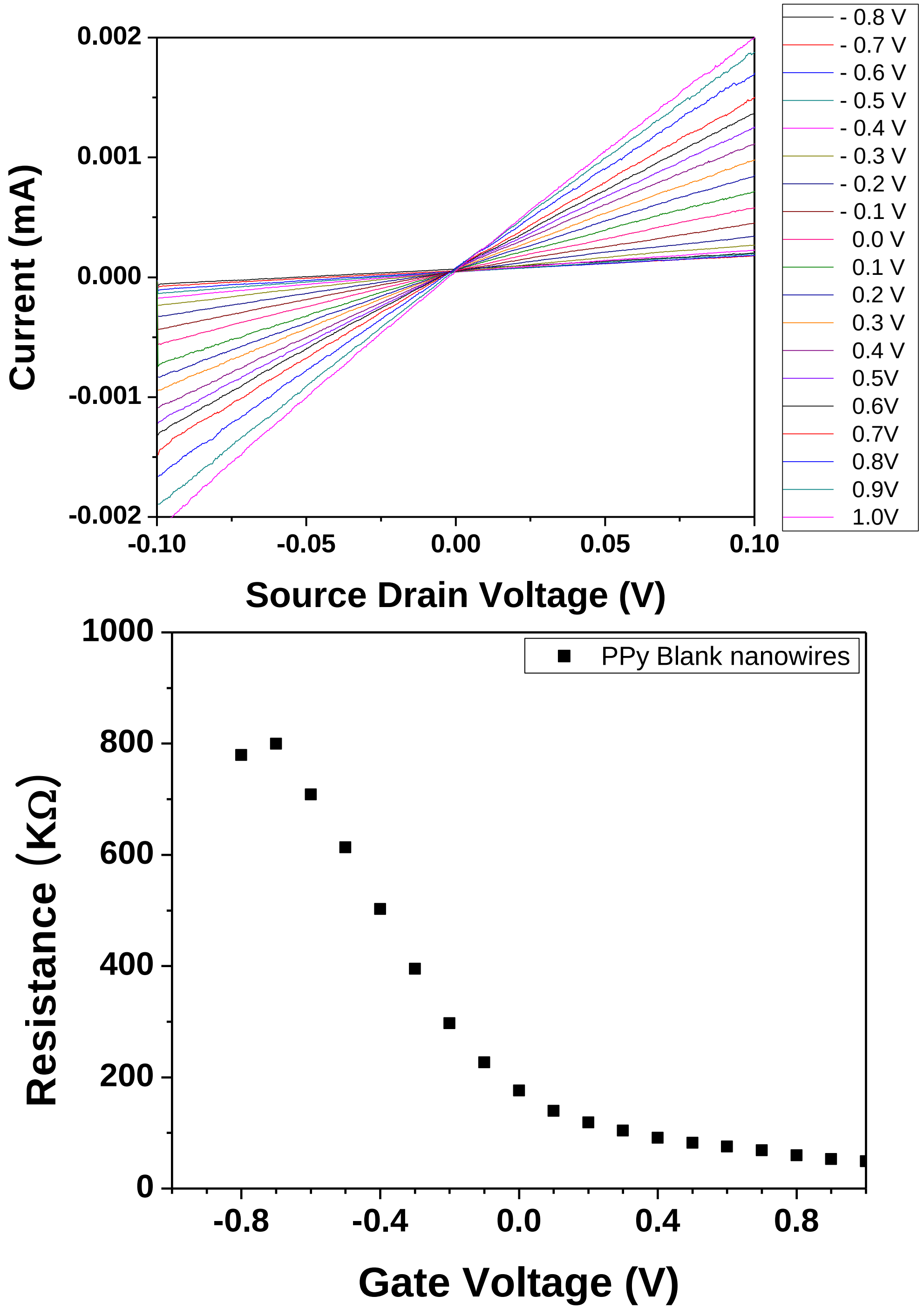

Figure A4.5. (A) Current Voltage response of the source and drain at the different gate potentials and (B) calculated resistance as the gate voltage was varied for the blank PPY NW.

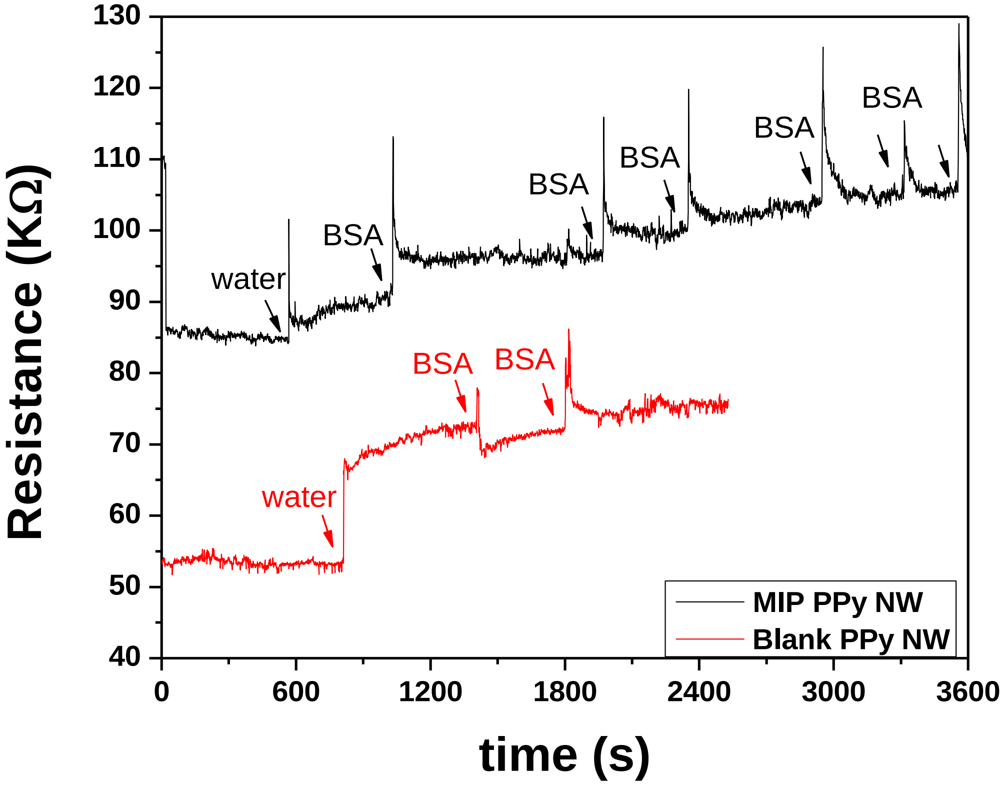

Figure A4.6. Real time response of a single BSA molecularly imprinted polypyrrole nanowire to addition of 2 uL of 100 ug/mL BSA. The inset corresponds to the response of the non-imprinted nano wire towards the same BSA concentrations. The addition point is indicated by the arrow.

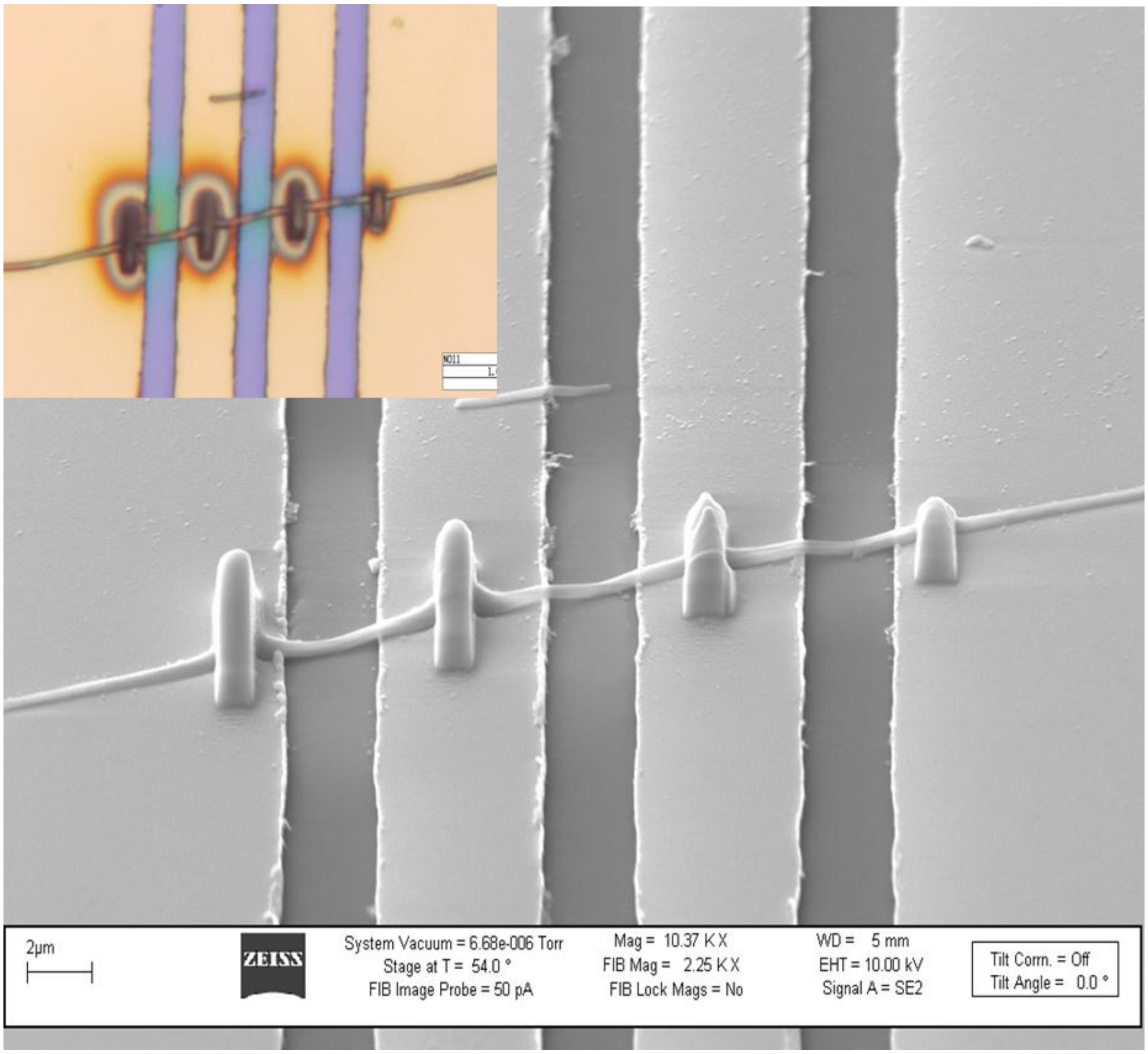

Figure A4.7. SEM image of molecularly imprinted NW after anchoring with focused ion beam, the inset is an optical image of the same sample showing local burning at the contacts after the FIB anchoring.

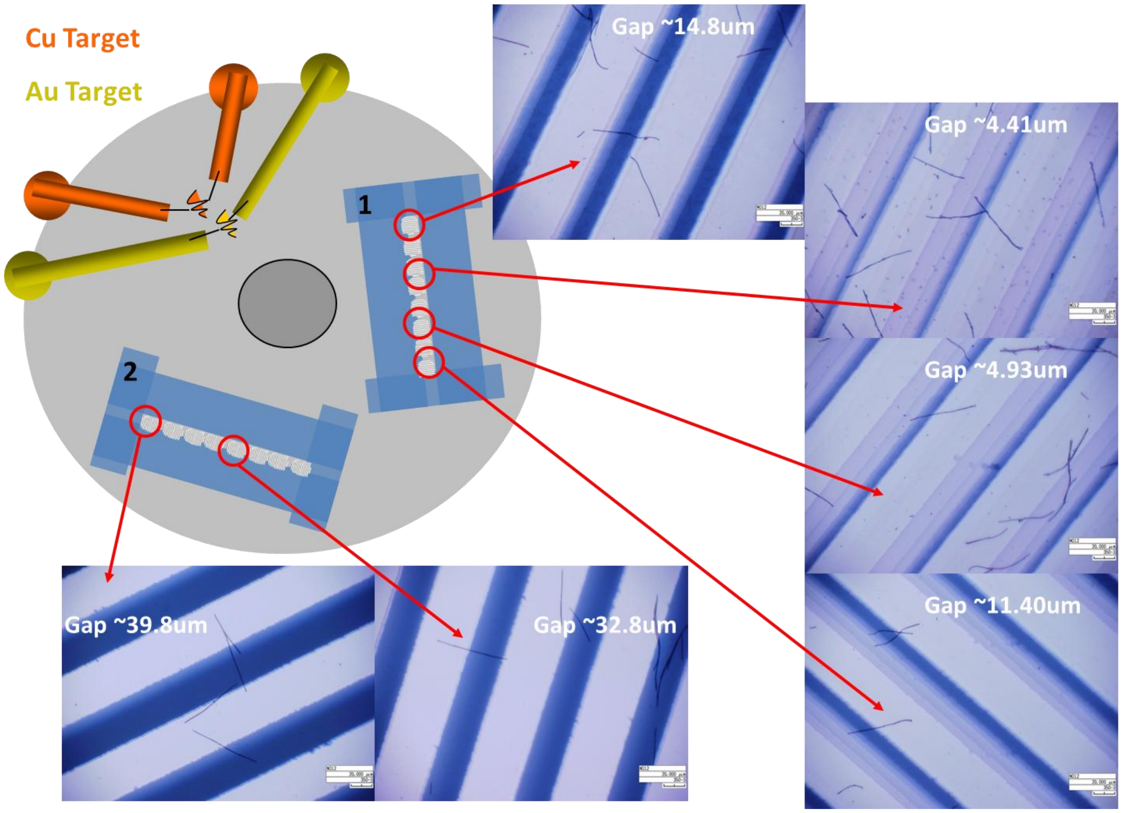

Figure A4.8. Illustration of evaporation shadow mask set up and optical images of the resulting Cu/Au electrodes.

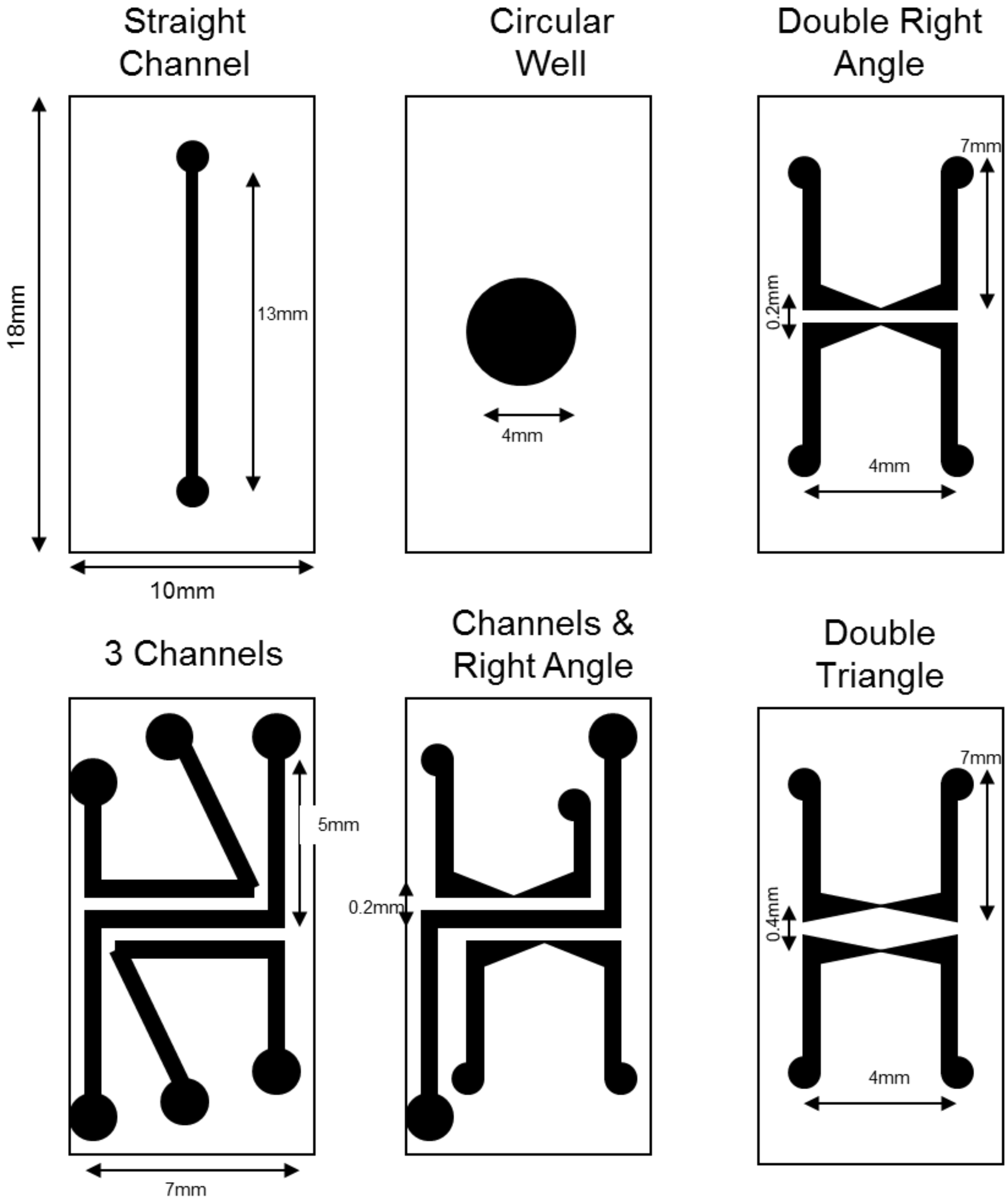

Figure A4.9. Designs of microfluidic designs for PDMS molds prepared by ink jet printing.

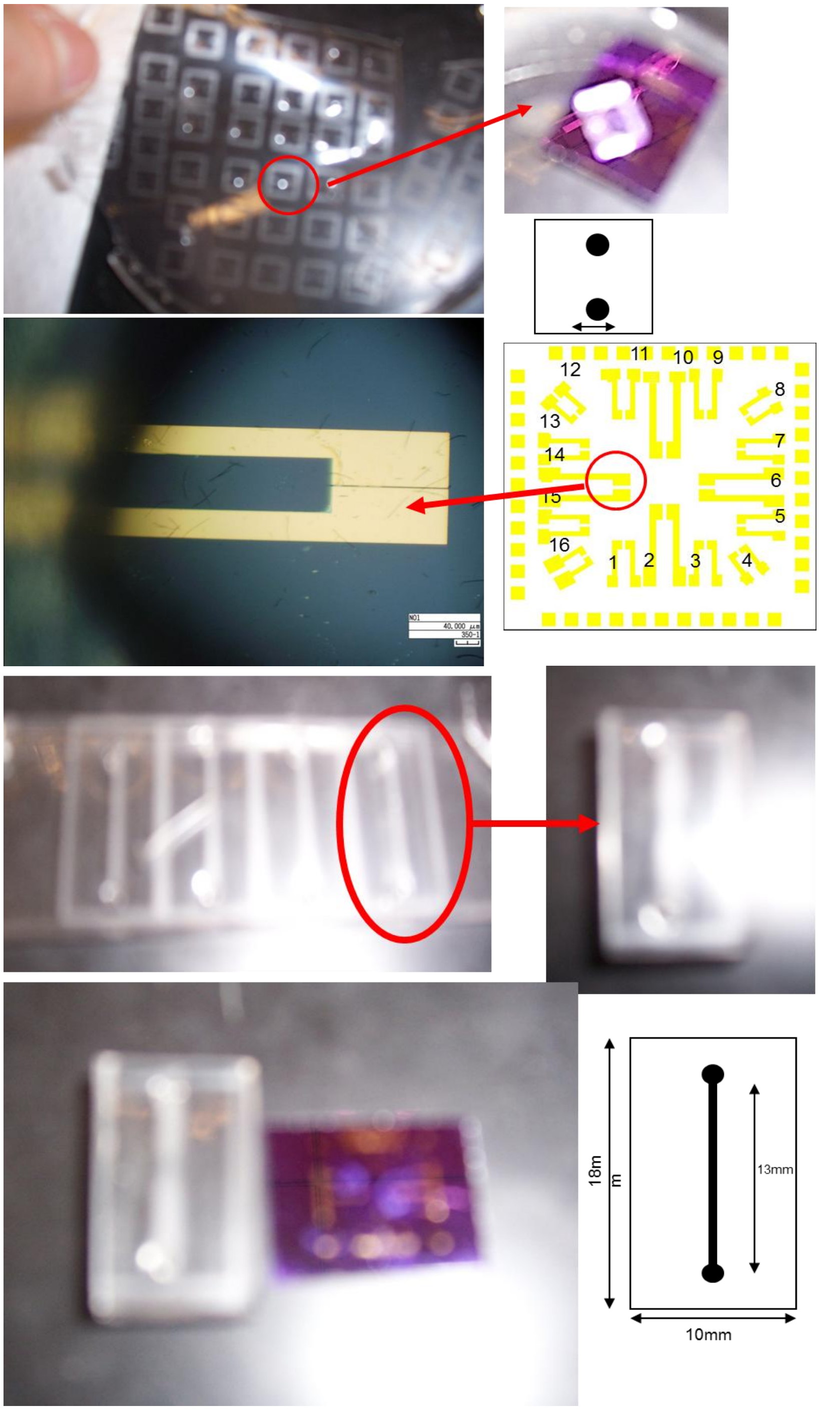

Figure A4.10. Optimal images and pictures of resulting PDMS molds and their compatibility to the silicon chip architecture.